

**Best  
Available  
Copy**

AD-A286 159



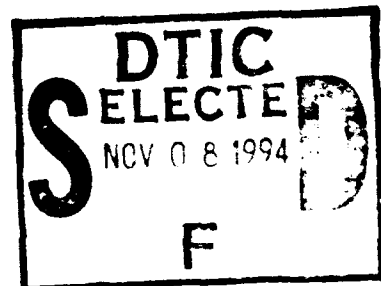
NASA  
Contractor Report 4607

Army Research Laboratory  
Contractor Report ARL-CR-144

(1)

# A Study of Dean Vortex Development and Structure in a Curved Rectangular Channel With Aspect Ratio of 40 at Dean Numbers up to 430

Phillip M. Ligrani



July 1994

This document has been approved  
for public release and sale; its  
distribution is unlimited

Prepared for  
Vehicle Propulsion Directorate  
U.S. Army Research Laboratory  
and  
Lewis Research Center  
under NASA Defense Purchase Requests  
MIPR DOC NR C-80019-F and MIPR DOC NR C-30030-P

94-34642



National Aeronautics and  
Space Administration



94 11 7 110

NASA  
Contractor Report 4607

Army Research Laboratory  
Contractor Report ARL-CR-144

# A Study of Dean Vortex Development and Structure in a Curved Rectangular Channel With Aspect Ratio of 40 at Dean Numbers up to 430

Phillip M. Ligrani  
*Naval Postgraduate School*  
*Monterey, California*

JF

|A-1|



National Aeronautics and  
Space Administration  
Office of Management  
Scientific and Technical  
Information Program  
1984



## FORWARD

This study was sponsored by the Propulsion Directorate, U. S. Army Aviation Research and Technology Activity-AVSCOM, NASA-Defense Purchase Requests C-80019-F and C-30030-P.

The material presented in this report represents technical contributions by a number of individuals at the Naval Postgraduate School over a six year period. The extents of their contributions are reflected in their co-authorship of the various archival journal papers written from the study. These include Dr. C. S. Subramanian, and Dr. B. A. Singer, both Adjunct Research Professors during the times of their respective contributions, and graduate students Mr. M. A. Siedband, Mr. R. D. Niver, Mr. L. R. Baun, Mr. D. W. Bella, Mr. J. M. Longest, Mr. W. A. Fields, Mr. M. R. Kendall, and Mr. S. J. Fuqua. Mr. Tom Clark of Jay-Edmund Enterprises deserves a word of mention for his construction of the channel including much detailed design of different channel components. Mr. Fred Lemos of NASA-Ames constructed many of the subminiature hot-wire sensors employed in the study, and supervised the construction of the miniature five-hole pressure probe. Professors Warren H. Finlay, Joel H. Ferziger and M. D. Kelleher are also acknowledged for the ideas which they contributed during discussions on various aspects of the research effort.

## TABLE OF CONTENTS

	<u>Page</u>
<b>LIST OF SYMBOLS</b>	1
<b>1.0 SUMMARY</b>	5
<b>2.0 INTRODUCTION</b>	7
<b>3.0 EXPERIMENTAL APPARATUS AND PROCEDURES</b>	14
<b>3.1 CURVED CHANNEL</b>	14
<b>3.2 MEASUREMENT OF THREE MEAN VELOCITY COMPONENTS AND THREE COMPONENTS OF MEAN VORTICITY</b>	18
<b>3.2.1 Experimental Details for the Miniature Five-Hole Probe</b>	20
<b>3.2.2 Miniature Five-Hole Pressure Probe Calibration</b>	24
<b>3.2.3 Corrections to Account for Finite Spatial Resolution and Induced Downwash Velocity</b>	27
<b>3.2.4 Five-Hole Probe Use in the Curved Channel</b>	31
<b>3.3 MEASUREMENT OF LONGITUDINAL VELOCITY FLUCTUATIONS</b>	35
<b>3.4 POWER SPECTRA APPARATUS AND PROCEDURES</b>	37
<b>3.4.1 Probes and Measurement Chain</b>	37
<b>3.4.2 Signal Processing and Analysis</b>	39
<b>3.5 FLOW VISUALIZATION APPARATUS AND PROCEDURES</b>	41
<b>3.5.1 Smoke Generators</b>	41
<b>3.5.2 Cameras and Lighting Systems</b>	42
<b>4.0 EXPERIMENTAL RESULTS</b>	44
<b>4.1 SURVEYS OF TOTAL PRESSURE, THREE COMPONENTS OF MEAN VELOCITY, AND THREE COMPONENTS OF MEAN VORTICITY</b>	44
<b>4.1.1 Total Pressure and Streamwise Velocity Distributions</b>	44

4.1.2 Velocity Perturbation Distributions	46
4.1.3 Mean Vorticity Distributions	48
<b>4.2 SPECTRA OF HOT-WIRE SENSOR SIGNALS</b>	<b>52</b>
4.2.1 Spectral Behavior for Dean Numbers From 40 to 130	52
4.2.2 Spectral Behavior for Dean Numbers From 130 to 185-200	53
4.2.3 Spectral Behavior for Dean Numbers Greater Than 185-200	54
<b>4.3 FLOW VISUALIZATION OF DEAN VORTICES</b>	<b>55</b>
4.3.1 Smoke Patterns as Observed 115 Degrees From the Start of Curvature	58
4.3.2 Map of Smoke Patterns	61
4.3.3 Symmetric Dean Vortex Flow	63
4.3.4 Oscillating and Wavy Dean Vortex Flow	64
4.3.5 Small Secondary Vortex Pairs	67
4.3.6 Streamwise/Spanwise Plane Flow Visualization	68
<b>4.4 WAVY DEAN VORTEX FLOW</b>	<b>69</b>
4.4.1 Undulating Dean Vortices	70
4.4.2 Twisting Dean Vortices	77
4.4.3 Twisting and Transition	83
<b>4.5 SPLITTING, MERGING, AND SPANWISE WAVENUMBER SELECTION OF DEAN VORTEX PAIRS</b>	<b>85</b>
4.5.1 Dean Vortex Pair Merging Events	87
4.5.2 Dean Vortex Pair Splitting Events	92
4.5.3 Recurrent Splitting and Merging Phenomena	95
4.5.4 Spanwise Wavenumber Selection of Dean Vortex Pairs	97
4.5.5 Longitudinal Velocity Fluctuations Associated With Splitting and Merging	101

<b>5.0 SUMMARY AND CONCLUSIONS</b>	<b>103</b>
<b>REFERENCES</b>	<b>110</b>
<b>FIGURES</b>	<b>114</b>

## LIST OF SYMBOLS

$a'$	Radius of Pressure Probe Tip, Used for Downwash Velocity Correction
$b$	Streamwise Wavenumber, $2 \pi / m$
CCPF	Curved Channel Poiseuille Flow
$C_{pp}$	Probe Calibration Coefficient, Pitch
$C_{ps}$	Probe Calibration Coefficient, Static Pressure
$C_{pt}$	Probe Calibration, Total Pressure
$C_{pst}$	Probe Calibration Coefficient, Total-Static Pressure
$C_{py}$	Probe Calibration Coefficient, Yaw
$d$	Channel Height = $r_o - r_i$
$d$	Distance between central hole centerline and the centerlines of adjacent holes for the miniature five-hole pressure probe
$D$	Induced Downwash Velocity in the $s$ Direction
$De$	Dean Number, $(Ud/V) \sqrt{d/r_i}$
$De_c$	Critical Dean Number
$E$	Coefficient for Downwash Velocity Correction
$E_y$	Coefficient for Downwash Velocity Correction
$E_z$	Coefficient for Downwash Velocity Correction
$f$	Non-dimensional Frequency, $2 \pi n (d/2)/U$
$m$	Streamwise Wavelength in Radians
$n$	Frequency
$P_1$	Pressure Measured at Five Hole Port One
$P_2$	Pressure Measured at Five Hole Port Two
$P_3$	Pressure Measured at Five Hole Port Three
$P_4$	Pressure Measured at Five Hole Port Four
$P_5$	Pressure Measured at Five Hole Port Five
$\bar{P}$	Average Pressure $(P_2+P_3+P_4+P_5)/4$

$\rho$	Pitch Angle of Flow With Respect to the Miniature Five-Hole Pressure Probe
$\rho'$	Preliminary Pitch Angle
$P_{mean}$	Average of Maximum and Minimum Pressure Differentials
$P_{off}$	Pitch Angle Offset Resulting from Five-Hole Probe Mount
$P_0$	Ambient Pressure
$P_s$	Static Pressure
$P_t$	Total Pressure
$Re$	Channel Reynolds Number, $Ud/\nu$
$Re_c$	Critical Channel Reynolds Number
$Re_{probe}$	Probe Tip Reynolds Number, $Ua'/\nu$
$r$	Radial Coordinate, Measured from Center of Curvature
$r_i$	Convex Surface Radius, or Inside Radius of Channel Curvature
$r_o$	Concave Surface Radius, or Outside Radius of Channel Curvature
$s$	Coordinate in Direction of Induced Downwash Velocity
$t$	Time
$U_l$	Local Total Mean Velocity, $(u_\theta^2 + u_r^2 + u_z^2)^{1/2}$
$U$	Bulk Mean Velocity
$U_{CCPF}$	Streamwise Mean Velocity for Curved Channel Poiseuille Flow
$u$	Mean Velocity
$u_\theta$	Streamwise Mean Velocity
$u_r$	Radial Mean Velocity
$u_z$	Spanwise Mean Velocity
$u_{yu}$	Radial Mean Velocity, Uncorrected for Downwash Velocity Error
$u_{zu}$	Spanwise Mean Velocity, Uncorrected for Downwash Velocity Error
$\overline{u'^2}$	Square of the Root-Mean-Square of the Longitudinal Fluctuating Velocity

$X$	Streamwise Coordinate
$Y$	Expansion Coefficient
$Y$	Radial Coordinate, Measured from Concave Surface Radially Inwards
$y$	Yaw Angle of Flow With Respect to the Miniature Five-Hole Pressure Probe
$y'$	Preliminary Yaw Angle
$Z$	Spanwise Coordinate
$z_k$	Spanwise Coordinate of Miniature Five-Hole Pressure Probe
$\alpha$	Local, Instantaneous Spanwise Wavenumber
$\bar{\alpha}$	Overall Average (in Space and Time) Spanwise Wavenumber
$\alpha_c$	Critical Spanwise Wavenumber
$\bar{\alpha}_c$	Overall Average (in Space and Time) Critical Spanwise Wavenumber
$\beta$	Streamwise Wavenumber, $2 \pi / m$
$\Gamma_x$	Circulation of Streamwise Vorticity
$\delta$	Shear Layer Thickness
$\Delta$	Downwash Velocity Correction Coefficient
$\lambda$	Spanwise Distance Between Vortex Pairs
$\nu$	Kinematic Viscosity
$\eta$	Radius Ratio, $r_i/r_0$
$\rho$	Density
$\theta$	Angular Location Measured from the Start of Curvature
$\omega_\theta$	Mean Streamwise Vorticity
$\omega_r$	Mean Radial Vorticity
$\omega_z$	Mean Spanwise Vorticity

**Superscript**

- \* **Average of Maximum and Minimum Values**

## 1.0 SUMMARY

Flow in a curved channel with mild curvature, an aspect ratio of 40, and an inner-to-outer radius ratio of 0.979 is studied at Dean numbers from 35 to 430. The primary objective is to obtain new information on the development and structure of Dean vortex pairs as well as their influences on flow structure, including events leading to transition to turbulent flow. These data include cross-sectional plane surveys of pressure, streamwise velocity, and all three vorticity components to illustrate time-averaged vortex pair features for each Dean number investigated.

At any streamwise location from 95 to 145 degrees from the start of curvature, a variety of different types of behavior develop as the Dean number increases. At low Dean numbers (<40-60), the flow is fully laminar. As the Dean number increases to any value between 40-60 and 64-75, flow visualizations show unsteady, wavy smoke layers evidencing small amplitude secondary flows. Then, at higher Dean numbers (>64-75), vortex pairs develop as the primary instability, where the streamwise location of the initial appearance of these pairs is dependent upon the Dean number. Secondary instabilities then develop at Dean numbers from about 75 to 200 in the form of vortex pair undulations, vortex pair twisting, and in the form of events where vortex pairs split and merge.

When viewed in cross section, experimental visualizations of undulating and twisting vortex flows show rocking motion and changes in the direction of the flow between vortices that are like those observed in the simulations of the time-dependent, three-dimensional Navier-Stokes equations using periodic boundary conditions in the spanwise and streamwise directions. When undulating vortices are present, experimental power spectra and visualizations give frequencies that are somewhat lower than the most unstable frequencies predicted by linear stability analysis. Experimental spectra show that undulating vortices are replaced by the higher frequency, shorter streamwise

wavelength twisting vortices at higher Dean numbers. When twisting vortices are present, experimental power spectra give fundamental and harmonic frequencies in good agreement with simulated values and with values from linear stability analysis.

Twisting is evidenced by experimental spectra over the largest Dean number range in measurements near the concave wall within inflow regions and in measurements near the concave wall near individual vortices. Fundamental amplitudes in these spectra are strongly dependent upon Dean number as well as on the location within the vortex pair structure. Twisting is important because it leads to increases in longitudinal fluctuating intensities at Dean numbers above 160, particularly in upwash regions near the concave surface, which appear to be the most unstable part of the vortex pair structure. These fluctuating intensity increases are significant and strongly dependent upon the location within the vortex pair structure as the Dean number increases from 160 to about 400. Fully turbulent conditions then develop at Dean numbers greater than about 400.

Results illustrating the splitting and merging of Dean vortex pairs are also presented. When viewed in cross-section at Dean numbers from 75 to 220 and at angular positions as small as 85 degrees from the start of curvature, visualization results show two distinctly different types of splitting events, and four distinctly different types of merging events. These results indicate that local spanwise wavenumber values higher than  $\bar{\alpha}$ , the overall average spanwise wavenumber (in space and time) for a particular Dean number, are prelude to the merging of a vortex pair across the channel span, and that values lower than  $\bar{\alpha}$  are prelude to the splitting of a new vortex pair across the channel span. After either a splitting event or a merging event, the reoccurrence of the same type of event just afterwards is unlikely. Instead, readjustment of the spanwise positions of pairs occurs as a result of the opposite event or spanwise shifting of pairs so that local and spanwise-averaged wavenumbers eventually approach  $\bar{\alpha}$ . Because of this behavior, as well as variations observed in time-averaged distributions of the three components of vorticity, vortex pairs are believed to have preferred spanwise locations.

## 2.0 INTRODUCTION

When Reynolds numbers are low enough in curved channel flows, the most basic laminar flow occurs. This is called curved channel Poiseuille flow (CCPF). When Reynolds numbers are high enough, the flow in a curved channel is unstable to centrifugal instabilities. Secondary flows subsequently develop which eventually form into pairs of counter-rotating vortices. This flow is referred to as Dean vortex flow, and the accompanying pairs of streamwise-oriented vortices are referred to as Dean vortices. The parameter used to characterize Dean vortex flow is the Dean number, defined as  $De=Re (d/ r_i)^{1/2}$  (Dean, 1928), where Reynolds number  $Re$  equals  $Ud/\nu$ ,  $U$  is the mean (bulk) streamwise velocity,  $d$  is the channel height,  $\nu$  is kinematic viscosity, and  $r_i$  is the radius of the convex (or inner) curved surface.

Vortices which develop from centrifugal instabilities are present in a variety of practical applications. Near concave surfaces of turbine blades, centrifugal instabilities result in the formation of Taylor-Görtler vortices. Within curved cooling passages inside turbine blades, and within curved ducts and pipes used in components such as heat exchangers, vortices may again be present as a result of centrifugal instabilities imposed on the flow. This mechanism is initiated as faster moving fluid some distance away from a concave curved surface is subjected to greater centrifugal forces than the fluid near the surface. Faster moving fluid packets then move toward the concave wall to displace slower moving fluid first in a spanwise direction and then normal to and away from the wall. The resulting spanwise periodic regions of high and low speed flow then form into pairs of counter-rotating streamwise vortices. With more intense curvature, circulation magnitudes of the vortices increase. Such vortices are important since they may cause significant alterations to boundary layer structure and wall heat transfer distributions. In addition, they may have an important effect on transition from laminar to turbulent flow. In particular, Taylor-Görtler vortices may cause the onset of

transition to occur closer to the leading edge of a turbine blade pressure side compared to a situation in which no vortices are present.

Using analytic means for narrow height channels where  $r_i/r_o$  is about 1, where  $r_o$  is the radius of the concave (or outer) curved surface, Dean (1928) first demonstrated that curved channel flow is unstable to small amplitude disturbances for values of  $De$  greater than 35.92. With sufficient streamwise development and when Dean numbers are sufficiently higher than this value, Dean vortices then eventually fill the entire channel cross-section. If the spanwise spacing of vortex pairs is  $\lambda$ , then a non-dimensional spanwise wavenumber of the vortex pairs is  $\alpha = 2(d/2)\pi/\lambda$ . Defining radius ratio  $\eta = r_i/r_o$ , classical linear stability analyses, such as the one employed by Dean (1928), predict neutrally stable Dean numbers for given  $\alpha$  and  $\eta$  which set the lower limit where vortices may be present.

The curve of neutrally stable Dean numbers versus neutrally stable spanwise wavenumbers is called the neutral stability curve. The neutral stability curve then separates unstable flow at higher Dean numbers, from CCPF at lower Dean numbers. With CCPF, the velocity in the channel is purely streamwise with a profile similar to the parabola of plane channel flow. The main difference from straight channel flow is evident in the maximum velocity which is shifted slightly towards the concave wall. The minimum of the neutral stability curve for the primary instability then occurs at the critical Dean number  $De_c$  and critical wavenumber  $\alpha_c$ . For the radius ratio considered here ( $\eta = 0.979$ ),  $De_c = 36.92$  (Finlay, 1989).

Following Dean, Hammerlin (1958) and Reid (1958) provided additional definition of the neutral stability curve. In an experiment with a  $\eta = 0.923$  channel, Brewster *et al.* (1959) found pairs of steady counter-rotating vortices for experimental conditions when the channel is unstable to small amplitude disturbances. He also provided evidence supporting a critical value of Dean number at the onset of the instabilities which lead to vortex formation. In work presented by Kelleher *et al.* (1980), results from a hot-

wire moving spanwise across the channel at different radii show that the periodic secondary motion undergoes a phase shift as the probe crosses the midpoint between concave and convex walls. These results and flow visualization photographs also indicate the spanwise wavenumber to be approximately constant for Dean numbers from 79 to 113. Berger *et al.* (1983) present a review of experiments and analytical calculations for square or nearly square channels in a paper that focuses only on axisymmetric and time-independent Dean vortices. Much analytic work also took place before and after this last study, as reviewed by Finlay *et al.* (1987, 1988). Of these analytic studies, Finlay and Nandakumar (1990) show that the end vortices which form in the corners of finite aspect ratio curved channels are only weakly coupled to the ones resulting from centrifugal instabilities.

Additional characteristics of Dean vortices are given by Ligrani and Niver (1988), and Finlay *et al.* (1988) for different values of  $De$ , and different locations from the start of channel curvature  $\theta$ . At low Dean numbers (<40-60), Ligrani and Niver (1988) provide evidence of fully laminar, curved channel Poiseuille flow (CCPF) flow in their curved channel. As the Dean number increases to any value between 40-60 and 64-75, flow visualizations then show unsteady, spatially uneven smoke layers evidencing small amplitude secondary flows at any streamwise location from 95 to 145 degrees from the start of curvature. Then, at higher Dean numbers (>64-75), the flow is increasingly unstable to centrifugal instabilities, and secondary flows develop which eventually form into pairs of counter-rotating vortices, where the streamwise location of the initial appearance of these pairs is dependent upon the Dean number. These values of  $De$  are just greater than the neutral stability curve, and both Ligrani and Niver (1988) and Finlay *et al.* (1988) indicate that individual Dean vortices may be axisymmetric such that the two vortices in a pair are mirror images of one another. Such agreement coincides with other quantitative flow similarities (Ligrani *et al.*, 1992a, 1992b), which is interesting since one set of data is derived from observations of flow patterns

visualized using smoke (Ligrani and Niver, 1988), whereas the other is derived from a direct simulation of the time-dependent, three-dimensional Navier-Stokes equations (Finlay *et al.*, 1988). The results from Ligrani and Niver (1988) are different from those presented by Finlay *et al.* (1988) in several respects including the fact that slightly greater  $\theta$  and slightly higher De are required for formation of symmetric Dean vortex pairs in the former study than in the latter.

For De sufficiently greater than values on the neutral stability curve, Ligrani and Niver (1988) and Finlay *et al.* (1988) show that the Dean vortices may become wavy. Finlay *et al.* describe two different modes of waviness which manifest themselves as superimposed waves travelling in the streamwise direction at constant speeds. These modes are called undulating and twisting, and both produce vortices which are non-axisymmetric. The first mention of experimentally observed waviness is given by Kelleher *et al.* (1980), and the first photographic evidence of twisting was provided by Ligrani and Niver (1988) who indicate that initial De and  $\theta$  of twisting are in rough agreement with values estimated by Finlay *et al.* (1988). Additional experimental evidence of wavy vortex flow in a rotating curved channel is given by Matsson and Alfredsson (1990). Numerical evidence of wavy vortex flows in a rotating channel is presented by Finlay (1990). Experimental evidence of undulating Dean vortex flow in curved channel flow is given by Ligrani *et al.* (1992a) along with additional evidence of twisting Dean vortex flow. This paper also compares experimental results from undulating and twisting flows to data from direct simulations of the time-dependent, three-dimensional Navier-Stokes equations. Further details on the quantitative structure and development of wavy Dean vortex flows are additionally given by Ligrani *et al.* (1992a).

Another category of motions which has been observed is related to splitting and merging of Dean vortex pairs as they are viewed in spanwise/radial planes across the span of the channel. Evidence of such behavior for channel flow was first provided by

Ligrani and Niver (1988) in the form of photograph sequences showing small secondary vortex pairs observed temporarily in spanwise/radial planes for  $De$  ranging from 75 to 220. By examining the linear stability of nonlinear axisymmetric vortices to disturbances of different spanwise wavelength, Guo and Finlay (1991) also study such phenomena as they affect variations of the spanwise wavenumber of vortex pairs in curved and/or rotating channels. According to them, merging and splitting of vortex pairs results from the instability of vortex pairs to spanwise perturbations (Eckhaus instability). Accordingly, Guo and Finlay describe a closed Eckhaus stability boundary for curved channel flow with  $\eta = 0.975$ . Within this boundary, Eckhaus growth rates are negative and pairing and splitting of pairs is not expected to occur. Here, growth rate refers to the real part of the eigenvalue representing the perturbed flow component. Outside of the Eckhaus boundary, growth and decay rates of the disturbances that cause vortex pairs to split or merge are positive. They are lowest in proximity to an Eckhaus valley, defined to be where positive growth rates are locally minimum.

In flow visualization results from a rotating channel (Alfredsson and Persson, 1989), and from a curved channel which rotates (Matsson and Alfredsson, 1990), pairing and splitting of vortex pairs in streamwise/spanwise planes is evident from flow visualization photographs of water contaminated with titanium-dioxide platelets. Views of streamwise/spanwise planes show upwash and downwash regions as dark streaks with light streaks in between. Splitting is evidenced by the splitting of light streaks between existing light streaks, and merging is evidenced by the merging of light streaks. Similarly, Ligrani and Niver (1988) describe individual tubes of smoke which occasionally divide into two branches, or adjacent tubes which merge together. Splitting and merging of vortex pairs is also found in experimental results from a rotating flat plate boundary layer (Musuda and Matsubara, 1989), and from a concave wall boundary layer (Bippes, 1978), and in simulation results for a rotating channel (Yang and Kim, 1991). Other investigators have noticed splitting and merging phenomena in wall

bounded flows (Peerhossaini and Wesfreid, 1990), or discussed spanwise wavenumber selection in analysis of boundary layers developing over concave surfaces (Floryan and Saric, 1984) and in experiments of rotating Couette flow (Snyder, 1969). Ligrani *et al.* (1992b) present results which illustrate two distinctly different types of splitting events, and four distinctly different types of merging events when viewed in cross-section at Dean numbers from 75 to 220 and at angular positions as small as 85 degrees from the start of curvature. These results further indicate that local spanwise wavenumber values higher than  $\bar{\alpha}$ , the overall average spanwise wavenumber (in space and time) for a particular Dean number, are prelude to the disappearance of a vortex pair across the channel span by merging, and that values lower than  $\bar{\alpha}$  are prelude to the appearance of a new vortex pair across the channel span from splitting. After either a splitting event or a merging event, the reoccurrence of the same type of event just afterwards is unlikely. Instead, readjustment of the spanwise positions of pairs occurs as a result of the opposite event or spanwise shifting of pairs so that local and spanwise-averaged wavenumbers eventually approach  $\bar{\alpha}$ .

The motivation of the present study is to examine vortex structure and development in a curved channel. Attention is focussed on the vortices resulting from centrifugal instabilities as these ultimately have important influences on local shear layer structure, wall heat transfer distributions, and transition. Both streamwise development and structural changes with Dean number are considered to provide information for modelers attempting to develop schemes to account for the influences of curvature. All results are obtained for  $De$  less than 430. A channel was used to provide a well controlled experimental environment wherein shear layer thickness does not change with streamwise distance after sufficient development length. Because of this, the vortices in this study are different from Taylor-Görtler vortices which form in boundary layers developing over surfaces with concave curvature.

The curved channel employed for the study has 180 degrees of curvature, and an aspect ratio of 40 to 1 (ratio of width to height). A 40 to 1 aspect ratio was chosen to minimize side wall effects, provide sufficient space for spanwise periodic flow patterns, and because little other data is available in curved channels with large aspect ratio. Results for aspect ratios less than 5 are not necessarily always applicable to larger aspect ratio cases. Results are given for Dean numbers ranging from 35 to 430, and for angular positions from the start of curvature ranging from 65 to 145 degrees. The magnitude of the inner to outer radius ratio  $\eta$  is 0.979. According to existing criteria, the amount of curvature is mild since  $\delta/r_i$  is .011, where  $\delta$  is the shear layer thickness.

In order to measure flow characteristics, ordinary and subminiature sized hot-wire sensors, a miniature five-hole pressure probe, and flow visualization schemes are employed. With these techniques, a variety of results are obtained including spectra which show different frequency events occurring in the velocity field, surveys of distributions of streamwise mean velocity and all three components of time-averaged vorticity, and photo sequences which illustrate time-varying flow characteristics.

Subsequent to this introduction, experimental apparatus and techniques are presented in Chapter 3.0. This discussion includes information on the curved channel, techniques used to measure distributions of time-averaged velocity and vorticity, spectral measurement techniques, and procedures used for flow visualization. Experimental results are then given in Chapter 4.0. A summary and conclusions are lastly given in Chapter 5.0.

### **3.0 EXPERIMENTAL APPARATUS AND PROCEDURES**

#### **3.1 CURVED CHANNEL**

The curved channel is described in detail by Ligrani and Niver (1988) and by Ligrani *et al.* (1992a, 1992b). A schematic and a photograph are shown in Figs. 1 and 2, respectively. The facility is an open-circuit suction facility designed for low-speed transition studies, and was designed and constructed especially for flow visualization. To eliminate any discontinuities along the inside surface of the channel, the upper wall and the lower wall are each made of three pieces of transparent plastic sheet bonded together in one continuous piece so that no seams are present. The inside dimensions and cross sectional area of the channel are the same along its entire 6.77 m length. Side wall, longitudinal, and cross-beam supports are used to support the upper and lower walls so that the inside dimensions and their tolerances at any streamwise location are  $1.27 \pm .015$  cm for the height and  $50.80 \pm 0.05$  cm for the width.

The lip at the channel inlet is constructed of quarter circumference sections of 15.2 cm outside diameter pipe. Following this is the 25.4 cm by 50.8 cm rectangular inlet section for flow management, consisting of a honeycomb followed by three screens stretched across the cross section. The distance between screens and between the honeycomb and adjacent screen is approximately 10 cm, following suggestions given by Mehta and Bradshaw (1979). Following the last screen is a 20 to 1 contraction ratio nozzle, whose contour is given by a fifth-order polynomial.

After the nozzle, flow enters the 40 to 1 aspect ratio channel. The first part is a 2.44 m long straight duct. This length is used to provide fully developed laminar flow at its exit for Dean numbers up to 640 (Han, 1960). The corresponding mean velocity is 3.8 m/s. After the straight channel, the flow enters the curved test section. The concave interior duct surface has a radius of curvature of 60.96 cm and the convex surface has a radius of curvature of 59.69 cm. At the exit of the curved portion of the channel, the air enters another 2.44 m long straight duct. At the exit are four screens and a honeycomb

used to isolate the channel flow from any spatial non-uniformities in the outlet plenum. A 45.7 cm long diffuser, having a total angle of three degrees, is also used to provide some pressure recovery just prior to the exit plenum.

The flow rate through the channel is controlled by the pressure in plenum number 1, shown in Fig. 1. One of two blower and piping systems is used to set this pressure. The first system with blower number 1 is used to obtain Dean numbers from 150 to 500. This blower is a vortex type, capable of producing 152 cm of water vacuum at 3.97  $\text{m}^3/\text{min}$  volumetric flow rate. The second blower/piping system attached to plenum number 1 is connected to blower number 2. This blower produces 10.2 cm of water vacuum at 4.82  $\text{m}^3/\text{min}$  volumetric flow rate. The suction side is connected to plenum number 2 in Fig. 1. This plenum is used to mate the 14.0 cm diameter blower inlet to piping without significant pressure losses, and additionally helps isolate the channel from unsteadiness caused by the blower impeller. With this second blower/piping arrangement, Dean numbers between 40 and 220 are obtained.

Each blower/piping system may be used independently since each one can be isolated from the other. With the pressure in plenum number 1 as a reference, flow measurements from each system agree within one percent (Niver, 1987). The second system with blower number 2 was used for most results of the present study, and produced no noticeable unsteady oscillations for its entire range of operation. Flow rate changes in the second system are made by throttling valve 1 just upstream of plenum number 2 (see Fig.1) while bypass valve 2 is kept fully open.

The mass flow rate and Dean number are calculated from measurement of the pressure drop across the 1.5 inch ASME standard orifice plate. The results of these measurements are checked using a rotameter which is sometimes placed in series with the orifice plate upstream of blower number 1. The orifice pressure drop is measured using a differential pressure transducer and a carrier demodulator. The signal is collected and processed using a data acquisition system, and a computer. Additional

details on the transducers, acquisition system, and associated computer are found later in this report.

The channel coordinate system is shown in Figs. 3 and 4. ( $\theta$ ,  $r$ ,  $Z$ ) are the normal, streamwise, and spanwise directions respectively. The alternate radial coordinate  $Y=(r_0 - r)$  is measured from the concave wall, radially inwards. The alternate streamwise coordinate  $X$  is measured from the channel inlet located at the nozzle exit plane. The inner and outer walls of the curved channel have radii of curvature  $r_i$  and  $r_0$  and the two curved plates are spaced a distance  $d$  apart.  $r_c$  is the radius of curvature of the radial midplane of the channel, and thus,  $X = \theta r_c$ . Two non-dimensional measures of channel curvature are the radius ratio  $\eta$ , and the ratio of shear layer thickness to convex wall radius,  $(d/2)/r_i = \delta/r_i$ . As mentioned earlier, the latter parameter value is 0.011, indicating mild curvature. Fig. 3 also illustrates the spanwise spacing between vortex pairs  $\lambda$ , which, as mentioned earlier, is often given in non-dimensional form as  $\alpha = 2(d/2)\pi/\lambda$ .

Fig. 4 shows how the coordinate system (X, Y, Z) is displaced at different channel locations. The figure also shows a slot, 3.2 mm wide and 76.2 mm long, which is located in the convex wall of the curved channel. It is aligned in the spanwise direction 50.8 mm off of the centerline at a location 120 degrees from the start of curvature. A support block of polycarbonate (152.4 mm by 63.5 mm by 22.2 mm) is joined using epoxy to the wall surrounding the slot to maintain the convex wall's dimensional integrity, and to minimize the deflection of the curved wall in the vicinity of the slot. Flexible sealant foam is used to line the slot to allow probe insertion with no air leakage to the channel interior. This foam is carefully positioned to avoid any bumps or discontinuities in the flow so that probes can be inserted into the channel and moved freely in the spanwise and radial directions. It is attached to the slot walls using a layer of adhesive attached to its backing material. A schematic of the support block and the

foam sealing device is shown in Figure 5. This figure also shows how a probe is inserted into the channel. Additional details are given by Ligrani *et al.* (1992a, 1992b).

A series of tests were conducted to qualify the performance of the transparent curved channel. To measure the turbulence intensity at the nozzle exit, a single sensor hot-wire probe was mounted normal to the flow direction and operated in a constant temperature mode. For channel Dean numbers of 290 and 450, the turbulence intensities of the streamwise velocity are .0006 and .0010 respectively, based on local mean velocities of 3.4m/sec and 5.2m/sec.

The spanwise uniformity of the flow 120 degrees from the start of curvature is indicated by total pressure contours shown in Fig. 6. Fig. 6a shows measurements using a miniature total-pressure Kiel-type probe traversed across a plane with 5.08 cm span at a Dean number of 54. Fig. 6b shows total pressure distributions for a Dean number of 49 which measured using a miniature five-hole pressure probe (Ligrani *et al.*, 1989a, 1989b). Additional qualification of the five-hole pressure probe is provided because the results in Figs. 6a and 6b are comparable qualitatively and quantitatively. Radial traverses of the streamwise mean velocity at three spanwise locations are shown in Fig. 7. These profiles were obtained at a Dean number of 36 also using the miniature five-hole pressure probe (Ligrani, Singer and Baun, 1989b). The measurements in Fig. 7 show the profiles to be spanwise uniform and in general agreement with equations for CCPF as given by Finlay *et al.* (1987). Small differences and minimal scatter are due to the difficulty in measuring the low pressure levels associated with these velocities, and the fact that the computed result represents fully developed flow, whereas the experimental profile is only partially developed. The components of velocity in the radial and spanwise directions are expected to be zero. These were measured to be less than a few percent of the mean centerline velocity in the channel for  $De=36$  as a result of data scatter. The miniature five-hole pressure probe has a 1.22 mm tip diameter and is shown schematically in Figs. 8 and 9. This same probe is also described in detail in

the next section. The traverses were made using a two-dimensional automated traversing mechanism and a data acquisition system, both computer controlled. Pressures were measured using transducers having a full scale of 0.25 cm of water. Additional details are given by Baun (1988) and by Ligrani *et al.* (1989b).

Tests were also conducted to determine the effects of blockages placed at the inlet of the channel on observed flow visualization patterns. Because of the extremely low velocities through the flow management apparatus, blocking as much as 50 percent of the inlet caused no changes in observed visualization patterns or measured quantitative results. Thus, wakes from the smoke generation device were also not expected to cause any disturbances to the natural flow in the curved channel. Also tested were the effects of small geometric perturbations to the side walls, small changes in the dimensions of the top and bottom walls of both the straight and curved portions of the channel, strips of tape just downstream of the nozzle, and geometric perturbations to the channel at the locations where vortex formation initially begins. For Dean numbers less than 200, none of these had any effect on quantitative or qualitative results.

Perturbations to channel geometry which were important included leaks of any size and at most any location, especially near points where visualization or quantitative results were obtained. Also important was any unsteadiness produced by anything (flapping plate, laboratory activity, closing doors) in the laboratory which affected the flow at the inlet of the channel. To minimize this, test results were always obtained at night and other times when virtually no activity was present in the laboratory containing the curved channel.

### **3.2 MEASUREMENT OF THREE MEAN VELOCITY COMPONENTS AND THREE COMPONENTS OF MEAN VORTICITY**

Surveys of mean velocity in cross-sectional (spanwise/radial) planes at the location of the convex wall slot are measured using the miniature five-hole pressure probe described by Ligrani, Singer and Baun (1989b). This device was developed to

measure the three mean velocity components in the curved channel, where pressures are low, flow is three-dimensional and laminar, and spatial resolution and probe blockage effects are important considerations. The tip diameter of the five-hole pressure probe is 1.22 mm. Experimental and calibration procedures are given by Ligrani, Singer and Baun (1989b), except for techniques employed to account for spatial resolution and streamline displacement, which are described elsewhere (Ligrani, Singer and Baun, 1989a). Velocity components are determined from pressures using calibration coefficient data for yaw angle, pitch angle, total pressure, and total minus static pressure. For Reynolds numbers based on probe tip diameter, these probe calibration coefficients are independent of Reynolds number for values ranging from 80 to 400. Using finite difference equations, distributions of the three components of mean vorticity are determined from distributions of the three components of mean velocity. Magnitudes of secondary flow vectors are used to determine the streamwise component of vorticity, using the equation given by  $\omega_\theta = \partial u_r / \partial Z - \partial u_Z / \partial r$ . Spanwise and radial components of vorticity are calculated using equations of the form  $\omega_z = \partial u_\theta / \partial r + u_\theta / r$  and  $\omega_r = - \partial u_\theta / \partial Z$ , respectively, where  $u_\theta$ ,  $u_r$ , and  $u_z$  represent streamwise, spanwise, and radial components of velocity. Streamwise derivatives are neglected since measurements were taken in only one spanwise/radial plane. Some details of these procedures are now presented.

Procedures for the calibration and application of ordinary-sized five hole pressure probes are described by Treaster and Yocom (1979). Here, calibration coefficients for the yaw angle, pitch angle, and total pressure are independent of Reynolds number based on probe tip diameters for Reynolds numbers ranging from 2000 to 7000. The static pressure coefficient shows small Reynolds number dependence which, if unaccounted for, results in errors in magnitudes of measured velocity. Five hole probes similar in size to the ones used by Treaster and Yocom are used extensively throughout the fluid dynamics community and many results obtained from such probes are available in the

literature. Treaster and Houtz (1986) describe the fabrication and calibration of miniature five hole pressure probes with tip diameters ranging from 1.07 mm to 1.68 mm. Calibration coefficients are defined in the same manner as given by Treaster and Yocum and also show similar dependence on Reynolds number and wall proximity. In a companion paper, Weltz (1986) describes a double interpolation procedure to obtain velocity direction and magnitude from calibration data and measured pressures.

### **3.2.1 Experimental Details for the Miniature Five-Hole Probe**

Two schematics and a photograph of the miniature five hole pressure probe employed in the present study are shown in Figures 8, 9, and 10, respectively. The diameter of the probe tip is 1.22 mm, where the central tube is surrounded by four other tubes, where the end of each is tapered at a 45 degree angle with respect to the mouth of the central tube. Each of the five hole tubes is made from stainless steel hypodermic tubing with inner and outer diameters of .203 mm and .406 mm, respectively. The probe was constructed by first spot welding together these five tubes. The five were then bent in a 90 degree turn with a radius of 1.52 mm to avoid any tube crimping. Silver solder was then used to join the five tubes together continuously along their length. Finally, the portions of the probe tip were tapered to appropriate angles using a surface grinder. This approach is different from the one described by Treaster and Houtz wherein probe tips are ground and sanded into appropriate shapes after solder is used to completely encase all tubes. Additional details are given by Ligrani, Singer and Baun (1989b).

Figure 9 shows that the present probe tip extends 5.08 mm ( 4 tip diameters) beyond the bend in the stem to minimize the effects of stem flow blockage at the measuring location. Similarly, the tip is 22.9 mm (19 tip diameters) from the 9.53 mm diameter cylinder. Within this cylinder, each tube is connected to a 1.60 mm diameter tube using a small manifold for each tube connection. The mounting cylinder was sized for easy handling and mounting. On top of the cylinder is a second set of

manifolds with five male connectors for attachment to 6.35 mm outer diameter/ 4.67 mm inner diameter tubing.

The miniature five hole probe was designed to minimize the adverse effects of flow blockage and spatial resolution when used for measurements in the curved channel. When in place for measurements at the centerline of the channel, the mounting cylinder is not exposed to the flow, and the probe produces 4.8 percent blockage over a 12.7 mm x 12.7 mm area. The tip is conical rather than a prism type to minimize near-flow blockage effects which are particularly severe for prism type probes.

The tubing used to connect the probe to transducers influences the pressure detected at the transducer. In particular, low amplitude pressure oscillations may result when there is a large volume of air in the tubes relative to that in the probe. With zero differential pressure applied across the transducer, these oscillations have peak to peak pressure amplitudes about .0003 cm of water. The period of oscillation is approximately one minute. These variations are believed to result due to compressibility of the gas and the constriction provided to the air as it passes through the 0.20 mm inner diameter holes in the probe tip from the larger diameter tubing. The motion of the air and the constriction result in the pressure waves which seem to initiate from small disturbances to the tubing. As the volume of air in the tubes increases, the pressure detected at the transducer becomes more unsteady and longer decay times are required before the measurement reaches a steady state. Ordinarily, to overcome such effects, tubing is fixed in place so that it may experience minimal vibration. Another alternative, used in the present study, is to minimize the volume of air in tubes. Flexible plastic tubing with 3.16 mm outer diameter and 2.66 mm inner diameter, less than 20 cm long, is employed for this purpose along with plastic adapters to connect the tubes to the male connections of the probe manifold. For differential pressures less than 0.2 cm of water, the pressure unsteadiness is then reduced considerably (Ligrani, Singer and Baun, 1989b).

Two different sets of transducers are used to convert pressure to an electrical signal. For differential pressures less than 0.25 cm of water, variable reluctance differential transducers are employed. For higher pressures, another type of variable reluctance transducers are used. A separate transducer is used to measure pressure relative to the atmosphere for each port of the five hole probe.

For low pressure measurements, the five transducers each have a full scale range of 0.25 cm of water differential pressure, and are used to measure pressures as low as 0.013 cm of water or five percent of the full scale range. These devices are quite sensitive, requiring extra care as they are used, particularly as tubing from the probe is connected or disconnected. This is done very slowly while monitoring transducer output to avoid pressure overload. Each transducer is supported in a vertical position by a plexiglass mount slightly above the probe. This mount minimizes gravitational effects, vibration, and orients transducers to minimize the influence of magnetic fields from two nearby stepping motors. Shielded cables connect the transducers to carrier demodulator units. The shields extend to the transducer cases to provide a ground connection to the demodulators and significantly reduce electronic noise. Further reductions are achieved by mounting the demodulators on a thick metal plate to further isolate them from the stepping motors. The carrier demodulator units are essentially AC bridge circuits which produce a DC voltage output proportional to the pressure signal from the transducers.

The signal to noise ratio of the transducer/carrier demodulator system for low pressure measurements ranges from 100 to 5000. The amount of temperature drift for zero differential pressure is typically less than 0.01 volts over an eight hour period. This drift was recorded to be as high as about 0.1 volt, but only for one transducer. This is still quite low considering that the maximum voltage produced from a demodulator is typically 10 volts. Demodulators are adjusted to maximize output voltage in order to minimize the adverse effects of zero drift and to maximize the signal to noise ratio.

For measurement of differential pressures higher than 0.25 cm of water, the other type of variable reluctance differential pressure transducers are supported by the short tubes extended from the mouth of the probe. The full scale range of each transducer is 2.0 cm of water. Carrier demodulators are again employed to convert electrical output to DC voltage. When compared to the low-pressure range transducers, these devices have higher noise levels, and for differential pressures less than 0.2 cm of water, more significant calibration non-linearities.

Each transducer/demodulator system is calibrated by first adjusting the zero so that the output with no applied pressure is less than 0.01 volts. This small offset voltage is determined from the average of 50 samples taken by the data acquisition system, recorded and then accounted for in subsequent signal processing. Next, a constant pressure, close to the value expected during measurement, is applied simultaneously to the unused orifice of the transducer and to a horizontal manometer, which can be read to an accuracy of 0.005 cm of water. A calibration coefficient is then determined to be the ratio of the manometer pressure and the difference between the average voltage and offset voltage. This procedure is repeated three times to give three calibration coefficients which are averaged to reduce experimental uncertainty. A typical value for high pressure transducers is 0.15 cm of water differential pressure per volt. Calibration coefficients for low pressure transducers are typically about .015 cm of water per volt.

Each transducer/demodulator system is connected to a data acquisition/control unit equipped with analog multiplexing and a digital voltmeter with  $\mu$ V sensitivity. The control unit is controlled by a computer, which also processes the data. The computer is equipped with a 8 MHz 16/32 bit processor, dual 5.5 inch floppy disk drives, and a memory of 1M bytes.

When data are acquisitioned from the probe, voltage samples are recorded sequentially from the five channels until 50 samples are accumulated for each channel.

The mean and standard deviation are subsequently calculated for each channel. One hundred additional samples are then recorded for each channel provided each is within three standard deviations of the current mean value. The overall sampling rate is about 5Hz.

### **3.2.2 Miniature Five-Hole Pressure Probe Calibration**

The wind tunnel used for probe calibration is an open circuit blower tunnel which provides uniform flow at the nozzle exit with a free stream turbulence intensity of approximately 0.1 percent at 30 m/s. Air enters the fan inlet from the surrounding air through a coarse filter. A 1.6 mm clearance between the fan and diffuser isolates vibrations from the fan to the wind tunnel body. The diffuser contains a second fine filter to remove small particles from the air as well as four baffle vanes to reduce spatial nonuniformities. A 16:1 contraction ratio nozzle leads to the 3.05 m long, 0.610 m wide test section. The height of the top wall is adjustable. For this work, a zero pressure gradient is maintained to within 0.013 cm of water differential pressure along the length of the test section. The exit of the tunnel vents of the laboratory.

To set probe angles during calibration, the probe is positioned in a manually operated traversing unit. The unit has been modified to include a protractor to facilitate positioning the probe to an accuracy of 0.5 degrees over a range of yaw angles from -40 degrees to +40 degrees. The traversing device is mounted on a horizontal sled which fits on top of the wind tunnel side walls. The mounting sled can be rotated through a range of pitch angles from -45 to +45 degrees to an accuracy of 0.5 degrees. The pressure transducers rotate with the probe and are sensitive to the direction of gravity and thus to the pitch angle. To account for diaphragm deflection from gravity as the transducers are rotated, a constant multiplied by the sine of the pitch angle is added to the pressure signal. Figure 11 shows a photograph of the calibration sled mounted on the top of the wind tunnel with probe, traversing device, protractor, and transducers.

The probe is calibrated in the uniform free stream flow of the wind tunnel. The right handed coordinate system shown in Figure 8 is employed. Positive yaw angles exist when the pressure at port two is greater than that at port three. Pitch is considered positive when the pressure at port four is greater than that at port five.

The probe is first aligned in the wind tunnel. Zero yaw is defined to be that angle where the pressures at ports two and three are equal. The calibration sled is constructed so that at zero pitch angle, the probe mounting cylinder is vertical within 0.5 degrees. Here, the difference in the pressures at ports four and five produces a nonzero pitch coefficient, which is also used to designate zero pitch when measurements are made.

To obtain calibration data, the probe is manually fixed at a known yaw angle and then rotated through the pitch plane. Similar procedures are employed by Treaster and Yocum (1979) and Treaster and Houtz (1986). A total of 25 angle combinations are used, five pitch angles at five different yaw angles. In addition to the pressures at the probe's five holes, the total and static pressures are required. The total pressure is measured with a Kiel-type total pressure probe; the static pressure is measured at the same streamwise position with a pressure tap in the side wall of the tunnel. To account for small changes in the free stream velocity, the static and total pressures are updated periodically. Typically, they vary less than 0.0005 cm of water during a three hour calibration session.

For each probe position during calibration, yaw, pitch, total, and total minus static pressure coefficients are calculated using:

$$C_{Py} = (P_2 - P_3)/(P_1 - \bar{P})$$

$$C_{Pp} = (P_4 - P_5)/(P_1 - \bar{P})$$

$$C_{Pt} = (P_t - \bar{P})/(P_1 - \bar{P})$$

and

$$C_{Pts} = (P_t - P_s)/(P_1 - \bar{P})$$

respectively.  $C_{pp}$  and  $C_{py}$  have the same form as the coefficients employed by Treaster and Yocum (1979).  $\bar{P}$  equals  $(P_2 + P_3 + P_4 + P_5)/4$ . New expressions for  $C_{pt}$  and  $C_{pts}$  are used to produce coefficients which do not approach zero as the yaw angle and pitch angle approach zero.

Calibration coefficients are presented in Figures 12-16 for a mean speed of 1.9 m/s, which corresponds to a Reynolds number based on probe tip diameter  $Re_{probe}$  of 86.  $C_{py}$  in Figure 12 increases with yaw angle and is close to zero and zero yaw angle. Some slight dependence on pitch angle is evident.  $C_{pp}$  variation with yaw and pitch in Figure 13 shows similar behavior, except it is about equal to -0.15 at zero pitch angle for all values of the yaw angle tested. In Figures 14-16,  $C_{pt}$ ,  $C_{pts}$ , and  $C_{ps}$  show significant dependence on yaw angle at a given pitch angle. Here,  $C_{ps} = (P_1 - P_s)/(P_1 - \bar{P})$ . The  $C_{pt}$  and  $C_{pts}$  curves are somewhat non-symmetric about zero pitch angle indicating a slightly non-symmetric probe tip.

The dependence of the yaw coefficient on probe Reynolds number is illustrated by results presented in Figures 17-20. These results correspond to mean speeds ranging from 1.1 to 5.0 m/s and probe Reynolds numbers ranging from 86 to 391. Except for some differences for  $Re=86$  due to scatter resulting from measurements of extremely low pressure levels, the yaw coefficient calibration curves are repeatable with minimal scatter and are independent of Reynolds number. This includes the value of  $C_{py}$  at zero yaw angle and zero pitch angle. Other coefficients show similar behavior, in contrast to the results of Treaster and Yocum (1979), where the static pressure coefficient shows significant dependence on the probe Reynolds number. The forms of the presently used coefficients were chosen to avoid this problem.

Calibration results and data reduction procedures were checked by placing the probe in the wind tunnel at known yaw and pitch angles and then determining these angles using the measurement procedures. At a mean speed of 2.7 m/s, both measured angles were

generally within 0.3 degrees of preset angles. Differences of about 0.5 degrees occurred only when the yaw angle was greater than 15 degrees.

Based on a 95 percent confidence level, the uncertainties of  $C_{Py}$  and  $C_{Pp}$  are both estimated to be plus or minus about 0.02. The uncertainty of  $C_{Pt}$  is typically plus or minus 0.04. The uncertainties of the slopes of the yaw and pitch calibration curves are approximately plus or minus 4.4 percent.

### **3.2.3 Corrections to Account for Finite Spatial Resolution and Induced Downwash Velocity**

Adjustments must be made to account for pressure and velocity gradients measured in three-dimensional flow fields using probes of finite size. Two of the most important adjustments result from finite spatial resolution and induced downwash velocities. The techniques described here are generally applicable, and discussed in additional detail by Ligrani, Singer and Baun (1989a).

Accounting for spatial resolution of multi-hole pressure probes is necessary since different pressure ports are at different locations. The simplest accounting corrects pressures so that all appear to be measured at the same physical location. For five hole probes, if this common point is chosen to be the location of the central hole, then four pressures require adjustment.

Figure 21 illustrates how the spatial resolution scheme is applied. Here, locations of the five pressure ports are shown as the probe is moved to different Z locations at a constant value of Y. For this case, to simplify discussion, corrections are applied only to ports two and three. In most real applications, the scheme is also used simultaneously for ports four and five, provided probe data are available for at least three locations in different planes normal to the wall. Spanwise gradients in total pressure appear as differences in pressures measured at ports two and three. Thus, for the situation of Figure 21, pressures from ports one, four, and five are not affected by spanwise gradients. Only pressures from ports 2 and 3 require adjustment.

The correction is implemented after pressures from each of the five holes are recorded at measurement locations  $k=1, 2, 3, \dots, n$ . As a first step, cubic spline curves are fit to pressures measured at port two for probe positions  $k=1, 2, 3, \dots, n$ . The exact spanwise position of this port is used and not the location of the center hole. In figure 21, these locations of  $P_2$  measurement are  $Z_k + d$ , where  $d$  is the distance between the center hole (port one) and the center position of each adjacent hole. A similar procedure is used for  $P_3$  measured from port three, except that its locations are  $Z_k - d$ . One smooth curve is constructed for each port, each of which is then used to calculate the value of  $P_2$  and  $P_3$  at the location of port one. In Figure 21, these pressures are designated  $P_{2,k}$  and  $P_{3,k}$ , and evaluated at  $Z_k$  and fully corrected to account for finite spatial resolution. They may then be used to calculate the yaw coefficient for determination of the yaw angle at location  $Z_k$ . If pressures from ports 4 and 5 had been corrected to give  $P_{4,k}$  and  $P_{5,k}$ , then these pressures could then be used to calculate pitch coefficients for pitch angle determination at  $Z_k$ .

With this approach there are no adjustable coefficients. Required are  $Y$  and  $Z$  locations of port one and  $d$ , the distance between port one and the center of the other probe pressure ports. For the custom-made miniature probe,  $d=0.041$  cm. The scheme assumes that pressures vary smoothly without significant discontinuities between pressure port locations and measurement locations. At the end points of any traverse, satisfactory results may be obtained by extrapolation. For optimal accuracy, in the present study, endpoints are discarded after interpolation for their neighbors is completed.

This scheme is physically more realistic than others which employ streamwise velocity gradients as a basis to account for spatial resolution. Finite spatial resolution is caused by variations of pressure, and thus, pressures must be corrected and not velocities or velocity gradients.

The downwash velocity is part of induced secondary flow which occurs as a result of the blockage of blunt bodies within transverse gradients of mean streamwise velocity. Young and Maas (1936) show that velocities measured in boundary layers using flat-faced pilot probes correspond to positions farther from the wall than where the measurements are actually made. Livesey (1956) obtains similar results for flat-faced probes, but finds that apparent streamline displacement depends strongly on probe shape. Lighthill (1957) describes a theoretical model for flow around a sphere in a uniform velocity gradient. He finds that the displacement of the stagnation streamline is caused by downwash velocity near the sphere with flow from regions of high streamwise velocity to regions of lower streamwise velocity. He also confirms earlier work showing that downwash velocity can be quite significant and depends strongly on the shape of the probe. For multiple hole probes that are used to determine flow direction as well as speed, the induced downwash velocity, if uncorrected, causes larger errors than displacement of the stagnation streamline.

After pressures and pressure coefficients are corrected for effects of finite spatial resolution, the velocity distribution is determined using data reduction procedures given later in this chapter. With this velocity field in the computer memory, adjustment for downwash velocity effects can proceed.

The present correction for induced downwash velocity is based on the work of Lighthill (1957). He shows that  $D/(a'du/ds)$  is of the order of one near a sphere. Here,  $a'$  is the sphere radius, and  $D$  is the induced downwash velocity in the  $s$  direction, which is normal to the direction of  $u$ . The gradient of the  $u$  component of velocity with respect to the  $s$ -direction is  $du/ds$ . For probe tips, downwash velocities in the normal and spanwise directions may then be estimated using:

$$D_y = (du_\theta/dY)(a'E_y) \quad \text{and} \quad D_z = (du_\theta/dZ)(a'E_z)$$

where  $a'$  is the probe tip radius and dimensionless quantities  $E_y$  and  $E_z$  are coefficients which depend on probe geometry. These may be different from each other, especially for

non-axisymmetric probe tips. In the present study, however, these two coefficients for the normal and spanwise directions are assumed to be the same and equal to  $E$ . Normal and spanwise velocity components  $u_r$  and  $u_z$  corrected for the effects of downwash velocity are then given by:

$$u_r = u_{ru} + (du_\theta/dY)\Delta \quad \text{and} \quad u_z = u_{zu} + (du_\theta/dZ)\Delta$$

where  $\Delta = a'E$ . In the above two equations,  $u_{ru}$  and  $u_{zu}$  represent velocities uncorrected for the downwash effect. By fitting  $u_\theta$  with cubic spline curves in the  $Y$  and  $Z$  directions,  $du_\theta/dY$  and  $du_\theta/dZ$  can be determined. The cubic splines are differentiated analytically and the values of the derivatives at every measurement point are then calculated.

In the present application, the final velocity components are corrected by numerically fitting the cubic splines and differentiating them. The corrected velocities are stored to be used for later plotting and vorticity computations.

Figure 7 shows measurements of streamwise velocity after corrections are applied, plotted at three radial traverse locations and compared to the curved channel Poiseuille flow (CCPF) profiles of Finlay *et al.* (1988). The profiles were taken at a Dean number of 36 and are generally in excellent agreement with the CCPF profile for this Dean number. Small differences are due to scatter caused by difficulty in measuring the low pressure levels associated with these velocities.

Another example of the application of pressure and velocity corrections is presented in Fig. 22. At a Dean number of 100, secondary flow velocities are reasonably steady and spanwise periodic, and result because of the presence of pairs of counter-rotating Dean vortices. Because of these vortices, pressure gradients exist in both spanwise and radial directions. Resulting streamwise velocity variations, which depend only weakly upon the corrections, are shown in Fig. 22a. Corresponding secondary velocity vectors when no corrections are made are presented in Fig. 22b. In this figure, vectors point away from regions of high streamwise velocity to regions of lower streamwise velocity, which is a physically unrealistic situation, especially near surfaces. Figure 22c then

shows secondary flow vectors from the same flow after the pressures are corrected only for spatial resolution. These vectors are substantially different from those in Figure 22b, even though vectors near walls still point away from the regions of high streamwise velocity. The largest vector in Figure 22b is 0.14 m/s, whereas the largest vector in Figure 22c is 0.10 m/s. In Figure 22d, both spatial resolution and downwash corrections are applied. Here, the value of  $\Delta$  employed in the induced downwash velocity corrections is 0.025 cm or  $0.4a'$ , and velocity vectors follow expected behavior. Well defined vortices are evident and vectors show no consistent tendency to point into walls or away from regions of high streamwise velocity. Secondary flow vectors indicate upwash from the concave to the convex surfaces over the same areas where streamwise velocity deficits are present in Fig. 22a.

### **3.2.4 Five-Hole Probe Use in the Curved Channel**

In this section, the traversing mechanism, measurement procedures, data reduction schemes, and qualification of the miniature five-hole probe are discussed as the device is employed to measure mean velocities in the curved channel. Additional details are given by Baun (1988) and by Ligrani, Singer and Baun (1989a, 1989b).

When measurements are made in the channel, the probe is oriented using a mount attached to a travelling block which is part of an automated two-dimensional traversing mechanism. The set-up is shown in Fig. 23. The travelling block moves in the spanwise and radial directions. These parts are driven by 20-thread per inch drive screws and guided by ground steel, case-hardened support shafts. The drive screws are rotated by stepping motors. These motors are controlled by a motion controller, which directs the movement of the probe according to instructions from the computer through a data interface.

The mount used to orient the probe is also evident in Figure 23. This mount consists of two collars. The first may be rotated relative to the radially mounted travelling block to allow the pitch angle of the probe to be set relative to the channel flow. A second

collar is attached to the probe by means of a set screw, which allows the yaw angle of the probe to be adjusted. Changes to the yaw angle as small as plus or minus 0.1 degree and to the pitch angle as small as plus or minus 0.5 degrees are possible with this mechanism.

The probe is positioned and aligned before measurements are made. This is accomplished by first inserting the probe into the channel at a spanwise location 5.08 cm from the centerline so that part just touches the concave wall. It is then visually aligned with the flow and subsequently moved to the channel centerline using the controller for the two-dimensional traversing mechanism. Small adjustments to the probe yaw angle and pitch angle are now made using the probe mount to obtain a zero yaw coefficient and a small pitch coefficient. A bulk flow velocity of 0.3 m/s is used for alignment since flow at this experimental condition is in the streamwise direction with minimal secondary flows. The low speed also means that the pressure differences between the ports are small. Hence, there is some scatter in the pitch and yaw coefficients. The final orientation of the probe gives a yaw coefficient of 0.00 plus or minus 0.01 and a pitch coefficient of -0.60 plus or minus 0.01. This is equivalent to +4.5 degrees offset accounting for the pitch coefficient of -0.15 obtained during calibration alignment. More accurate pitch alignment forces the probe against the edge of the slot, hence, the pitch offset is corrected during data reduction. No offset is applied or needed for the yaw angle.

In a typical spanwise/radial plane traverse, the probe moves in the radial direction from the concave wall to the convex wall as measurements are made. To begin measurements at a new spanwise location, the probe first moves 0.254 cm in the spanwise direction, then in the reverse span direction 0.127 cm, and finally toward the convex wall until it is 0.254 cm away. A new radial measuring traverse then begins. This procedure is used for positioning to reduce the adverse effects of backlash and give repeatable data regardless of the direction of spanwise probe motion.

When measurements are made at a particular location, 150 samples of each pressure are averaged. This is done by sampling pressure signals from probe ports in sequence so that a longer averaging time is provided for each channel, thereby minimizing the influence of short duration unsteadiness in the channel. For each probe location, about two minutes of acquisition and processing time is required. A traverse over an entire plane requires about eight hours. The entire process is computer controlled and generally performed at night when there is minimal unsteadiness at the channel inlet resulting from laboratory disturbances.

Measured pressures from each probe port are stored by the computer until an experiment is completed. These data are then corrected to account for the effect of finite spatial resolution using procedures described in section 3.2.3.

The next step is to determine the values of  $C_{py}$  and  $C_{pp}$  for each location using measured pressures. A four step procedure is used to determine the yaw angle and the pitch angle. First, a preliminary pitch angle  $p'$  is calculated using:

$$p' = 9.8 (C_{pp} + 0.15) - p_{off}$$

This equation provides a reasonable fit to pitch angle calibration data such as that shown in Figure 13 for a mean velocity of 1.9 m/sec. Here,  $p_{off}=4.5$  degrees, the pitch angle offset resulting from the probe mount. Referring to yaw angle calibration data in Figure 12, the second step requires the determination of a preliminary yaw angle  $y'$  by interpolation using  $p'$  and the measured value of  $C_{py}$ . In the third step, pitch angle is determined using the measured value of  $C_{pp}$  and  $y'$ , again interpolating from results such as the ones presented in Figure 13. The final pitch angle  $p$  is then determined by subtracting  $p_{off}$ . In the fourth step, the final yaw angle  $y$  is determined from  $C_{py}$  and  $p$  by interpolating results such as those in Figure 12.

Now that the yaw angle and pitch angle are known,  $C_{pts}$  is computed using a double linear interpolation procedure. A plot of  $C_{pts}$  versus yaw angle and pitch angle at a mean

speed of 1.9 m/s is shown in Figure 15. Knowing  $C_{pts}$ , the total velocity magnitude  $u$  is determined using:

$$u = (2 C_{pts} (P_1 - \bar{P}) / \rho)^{1/2}$$

where  $\rho$  is the fluid density. This approach gives less uncertainty for  $u$  than one which employs two separate coefficients for the total pressure and static pressure (i.e. Treaster and Yocom, 1979). The total pressure relative to atmospheric pressure  $P_0 - P_t$  at each location then follows using:

$$P_0 - P_t = (P_0 - \bar{P}) - C_{pt} (P_1 - \bar{P})$$

$C_{pt}$  is obtained using a double linear interpolation scheme from results such as the ones given in Figure 14. A coefficient for static Pressure  $C_{ps}$  is not used for data reduction. The three velocity components are subsequently given by:

$$u_\theta = u \cos(y) \cos(p)$$

$$u_r = u \sin(y)$$

$$u_z = u \cos(y) \sin(p)$$

In the final phase of data reduction, corrections are made to account for the downwash velocity correction using techniques described in section 3.2.3.

In order to qualify the behavior of the miniature five hole pressure probe, the total pressure distribution was measured and compared with measurements from the miniature Kiel probe. Total pressure measurements for a Dean number of 49 are shown in Figure 6b. Comparison with the Kiel probe measurement (Figure 6a) shows excellent agreement providing evidence of accurate five hole probe alignment and measurement procedures. Comparison is made at this Dean number since minimal secondary flows are present and because gradients of mean streamwise velocity are very small in the spanwise direction. For the data presented in Figure 6a, 40 spanwise locations and 8 vertical ones are used with a spacing between locations of 0.127 cm. The measurement area begins 0.127 cm from the concave wall, 5.08 cm from the channel

centerline, and extends to 0.254 cm from the convex wall and 10.16 cm from the channel centerline.

### **3.3 MEASUREMENT OF LONGITUDINAL VELOCITY FLUCTUATIONS**

Techniques are now described for measurement of longitudinal velocity fluctuations using hot-wire anemometer probes. These results were obtained at different Dean numbers over a spanwise/radial plane located 120 degrees from the start of curvature to obtain information on the growth of small scale disturbances and development of turbulence in the channel. To prevent any air leakage from the interior of the channel as each probe was traversed through the spanwise/radial plane, probes were inserted into the channel with the stem between two strips of foam.

The sensor of each probe was made of 90% platinum and 10% rhodium wire with a 5  $\mu\text{m}$  diameter. The active length of each wire was 1.25 mm, and the cold resistance of each sensor varied between 4 to 5 ohms. The hot-wire probes were calibrated in an open circuit subsonic wind tunnel using procedures for low velocity measurement described by Ligrani and Bradshaw (1987). During calibration and operation, wires were operated using constant temperature anemometer bridges set with overheat ratios of 1.8. Dynamic response of the hot-wire circuitry was established using a square wave generated within the anemometer bridge. Corrections to account for temperature drift were implemented using procedures described by Perry (1982) and Green (1989). From the bridge, the signal was sent to a signal conditioner as well as to an oscilloscope. The signal conditioner was used to amplify and low-pass filter the bridge output prior to analog-to-digital conversion. A gain of 2 (with zero offset voltage) is used to provide a dynamic signal within the +10 volt range of the analog-to-digital converter. The filter passed only the fluctuating portion of the signal at frequencies up to 1 kHz for Dean numbers up to 275 and up to 3 kHz for Dean numbers greater than 275.

The analog-to-digital converter was capable of 12-bit binary resolution. Although the device was configured for two channels, only one channel was used to obtain the

present results. Sample size and sampling frequency were set to obtain accurate time-averaged magnitudes of flow properties. A total of 20,000 samples were acquisitioned at each data point at a frequency of 2.5 kHz for Dean numbers less than 275, and at a frequency of 5.0 kHz for Dean numbers greater than 275. A total of 8 seconds of sampled data were thus obtained at the lower Dean numbers, and 4 seconds of data were obtained at the higher Dean numbers. The offset of the entire acquisition system was determined by shorting the signal conditioner input, and then recording the output from the analog-to-digital converter. The gain for a particular channel was found by inputting a 1.5 kHz sinusoidal signal of known root-mean-square amplitude and then comparing this to the amplitude of the root-mean-square of the signal at the output of the analog-to-digital converter. Typical values for offset and gain were -0.006 and 1.918, respectively. The signal for the converter was collected and processed using a laboratory computer which stored and processed 5000 sample sets of data in batches of 4 to obtain a total of 20,000 samples for each measurement point. The computer is also used to control the probe traversing equipment.

Each survey of mean velocity and longitudinal velocity fluctuations was made over a 0.89 cm by 5.08 cm spanwise/radial plane divided into 328 grid locations (8 radial and 41 spanwise) spaced 0.127 cm apart in both directions. The traversing device was fully automated, and as such, was operated so that measurements were delayed 10 seconds at each new position to allow any perturbations introduced into the flow by probe movements between measurement stations to dissipate. Within the device, the probe was attached to a mount which was secured to a travelling block that was moved in the radial and spanwise directions using two 20 thread-per-inch lead screws. Each screw was rotated using D.C. stepping motors connected to a drive and a controller, which was linked to the microcomputer through a data interface.

### **3.4 POWER SPECTRA APPARATUS AND PROCEDURES**

Techniques are now described for measurement of spectra of voltage fluctuations from hot-wire anemometer probes sensing velocity fluctuations. Both subminiature crossed-wire sensors (Ligrani *et al.*, 1987a, 1987b, 1989c) as well as conventional sized single hot-wire sensors were employed. In some cases, the probes were mounted by means of a plug in the channel side wall. With this mounting, single sensors were oriented in the radial direction and normal to the flow at a streamwise location 112 degrees from the start of curvature at  $Z/d=12.00-12.40$  and  $Y/d=0.5$ . These spanwise locations are equivalent to 9.60-10.16 cm from the channel side wall. These spanwise positions were chosen because flow visualization showed that this was an adequate distance to avoid side wall effects. Baun (1988) and Fields (1990) provide additional details.

#### **3.4.1 Probes and Measurement Chain**

The subminiature crossed-wire probes were chosen to take advantage of the excellent spatial resolution associated with this type of probe. These probes were manufactured using fabrication techniques described by Ligrani, Westphal, and Lemos (1989c) and by Westphal, Ligrani and Lemos (1989). The type of probes used were developed from techniques described by Ligrani and Bradshaw (1987a, 1987b). The sensors of the subminiature crossed-wire probes are 90% platinum/10% rhodium wire with a nominal diameter of 0.625  $\mu\text{m}$ , and a length of about 160  $\mu\text{m}$ .

The conventional-sized horizontal hot-wire probes employed were fabricated of platinum-plated-tungsten with diameters and wire lengths of 5.0  $\mu\text{m}$  and 1.25 mm, respectively. The single wire probes were used to measure spectra averaged over a larger portion of the channel height compared to the subminiature sensors.

The Reynolds numbers of the largest hot-wire sensors based on the maximum velocities experienced were less than one. For the prongs of the largest hot-wire sensors, the maximum Reynolds number attained was 4.9. According to Schlichting's

(1979) results for cylinders in cross flows, both Reynolds number ranges produce Strouhal numbers which are small enough to insure that there is no vortex shedding off of the hot-wire filaments or prong supports.

Probes were operated at elevated temperatures using standard commercially available hot-wire bridges operated in the constant-temperature mode. Hot-wire sensors were connected to the bridges using five meter coaxial cables. For the conventional-sized sensor, the time response of the sensor-bridge combination was adjusted using the square wave test function of the bridge. Using an overheat ratio of 1.5, a response time of 12.5  $\mu$ sec was achieved. The subminiature hot-wire sensor has much higher resistance than a standard hot-wire. Due to this, the commercially manufactured bridge was modified by adding a 2000 ohm metal-foil resistor at the location of the 0.09 ohm resistor setting. Recalibration of the bridge against an ohmmeter indicated that 98.90 ohms should be added to the bridge reading when the decade controller was switched to the 0.09 ohm position. Adjustment of cable impedance was accomplished by setting the cable compensator to the 5 m position. For subminiature hot-wire measurements, the bridge gain was then set at "1". For the conventional-sized wire measurements, the bridge gain was set at "2". With these arrangements, subminiature and conventional wire sensors were operated at overheat ratios of 1.2 and 1.5, respectively. Ligrani *et al.* (1987a, 1987b) provide additional details on the operation and maintenance of subminiature hot-wire probes.

Before passing to the signal analyzer, the output from the bridge was routed through a signal conditioner, employed to filter and amplify the voltage signal from the hot-wire bridge. The high-pass filter of the unit was set to 0.1 Hz in all cases to remove the DC signal. To prevent aliasing, the low-pass filter was set depending on the frequency range being investigated. Gain settings were maximized depending on the type of wire and flow velocity. Typically, a gain of 100 was used with the subminiature wire at all flow conditions. A gain of 100 was also used with most experimental conditions when the

conventionally sized hot-wire probe was employed. The output from the signal conditioner was sent simultaneously to the signal processor equipment as well as to an oscilloscope.

### **3.4.2 Signal Processing and Analysis**

Two different methods were used to obtain spectra of signals from the hot-wire sensors. With the first of these, a high speed data acquisition system was employed to acquire data into computer memory. Spectra were then computed using fast Fourier transform software. With the second method, a real-time signal analyzer was employed to compute spectra. Results from both methods were compared in order to check software and to identify spectral variations from digital and electronic noise (Baun, 1988).

Referring to the first method, a multiprogrammer was used for digital processing and acquisition of hot-wire time signals. This unit utilizes a four channel high speed data acquisition card in conjunction with a scanner control card. Each channel has a maximum sampling rate of 25 KHz. In the present study, one channel was used. A 12-bit analog to digital converter digitizes and passes data via a buffered cable and random-access-memory card to the computer. Data were gathered and sent to the computer in blocks of 2048 integers. A complete sampling of data then consisted of sixteen blocks of data. The acquisition of data, including acquisition rate, was controlled by the computer using parameters input by the user. The digitized time signal was stored on floppy disk for analysis at a later time.

The time domain signal was transformed to frequency domain using a fast Fourier transform routine adapted from Brigham (1974). The transform and acquisition software were written in Basic software language. The transform routine software read and processed each of the sixteen blocks of data separately and then ensemble averaged individual spectra from each of the sixteen blocks. The Hanning Window weighting parameter was used to treat the side lobes for each block of data. Before plotting, the

amplitudes of the signal were converted to (Volts<sup>2</sup>/Hz). These were then normalized so that the integral of the power over the frequency range was one. The digital processing equipment and transform were tested by processing sinusoidal voltage signals produced by a function generator.

With the second method, a signal analyzer is used to obtain spectra from the hot-wire anemometer. The device employed is a dual-channel fast Fourier transform (FFT) based analyzer with a 26.5  $\mu$ Hz-to-100 kHz frequency range and a 150 dB measurement range. The nominal sampling rate for all channels is 256 kHz. For the measurements of the present study, one channel is employed. The analog-to-digital conversion (ADC) portion of the analyzer works in two steps. First, it records a portion of the time history of the signal. Second, this analog sample is converted into 14-bit digital words in a time record which is 2048 samples long. The measurement stage then begins after the analog signal is converted to digital data and properly scaled. In this part of the measurement process, data are filtered to an appropriate frequency span. Windowing is then performed using software and two specialized processors. A Hanning data window is utilized in the present study to attenuate the input signal at both ends of the record, forcing the signal to appear periodic. The fast Fourier transform is subsequently implemented to convert the time varying signal to a frequency varying one. Next, the floating point processor (FPP) of the signal analyzer averages and calculates the final results. Continual measurements are made with one average, erasing the result of each previous measurement. Computed power spectra are plotted with axes of (Volts<sup>2</sup>/Hertz) versus frequency in Hertz.

Results presented in Baun (1988) show that results from both types of systems produce nearly identical results when probe spatial resolution effects are negligible. Additional information is provided later in this report.

### **3.5 FLOW VISUALIZATION APPARATUS AND PROCEDURES**

In order to obtain information on secondary flow motions resulting from the vortices, air in the channel was partially contaminated with smoke and then photographed. Smoke patterns in both spanwise/radial planes and streamwise/spanwise planes (viewed from outside of the concave side) were observed and photographed.

#### **3.5.1 Smoke Generators**

The device used to generate the smoke for visualization in radial/spanwise planes was a wood burning device. It is described by Ligrani and Niver (1988) and contains a steel pipe within which hickory or mesquite wood is burned (also see Ligrani *et al.*, 1992a, 1992b). The smoke exits the pipe and then passes into a large glass jar used to collect particulates which is followed by a cooling system used to lower the smoke temperature to a value near ambient conditions. The smoke was injected into the channel inlet using a manifold and a rake of tubes to produce an array of laminar jets which were employed to fill the nozzle and inlet of the channel about half full of smoke. The smoke produced by this system was ideal for the present visualization because it is dense, white, neutrally buoyant, and easily visible against the black paper used to line the outside of the channel as tests are conducted. The smoke was in sufficient quantity to permit detailed observations of flow structures for as long as 10 to 15 minutes. The smoke filled the bottom half of the channel at the inlet of the curved portion such that it enters near the convex surface. Consequently, events emanating from the proximity of the convex wall were smoke rich, whereas secondary flows which begin near the concave side were relatively free of smoke.

The device used to generate particulates for visualization in streamwise/spanwise planes was a commercial fog machine. This device is more compact and more convenient than the wood burning smoke generator. It uses a mixture of glycols of low molecular weight to produce the fog. During operation, fluid is drawn into the machine, heated to near its vaporization point, and then atomized by forcing the fluid through an orifice.

During experiments, the smoke was then injected into the entrance of the channel using the same manifold and 1.27 cm inside diameter tubes as employed for the wood burning generator. The fog generator was employed by injecting a single puff of fog into the channel entrance in amounts which increased with Dean number. After a short period of time, the fog then passed through the curved portion of the channel allowing pictures to be taken over about a ten second period. Fog from the generator eventually collected on the inside walls of the channel which obscured light, resulting in the need for frequent channel cleaning.

### **3.5.2 Cameras and Lighting Systems**

Smoke patterns were illuminated in spanwise/radial planes using spot lights directed at 2 mm by 46 mm spanwise slits located 5 cm off the centerline in the black paper used to line the exterior of the convex surface of the channel. This paper helped to illuminate a thin plane of smoke and to minimize reflections and stray light. When spot lights were not used, spanwise/radial planes were illuminated using a strobe light employed with a strobe rate of 2400 flashes per minute. The strobe light was mounted near the channel center of curvature with a collimator lens having a 75 mm focal length. These arrangements allowed photographs to be made of smoke patterns at different angular positions in the curved portion of the channel.

For some of the experiments conducted (Ligrani *et al.*, 1992a, 1992b), a video camera with a zoom lens was used to record the illuminated, time-varying patterns in spanwise/radial planes. The video camera was connected to a portable videocassette recorder which collects images at rates as high as 60 frames per second. Recorded images were then played back using a videocassette recorder connected to a color monitor. By employing the scan/stop action feature of this recorder, photographs of instantaneous images were then obtained using a still camera with a 55mm, f2.8 lens, motor drive, and intervalometer. Resulting photographs were then arranged in

sequences spaced either 1/10 second or 1/30 second apart to show time-varying phenomena.

In other experiments, the still camera was used directly to make still photographs of the smoke patterns which were illuminated in spanwise/radial planes (Baun, 1988; Ligrani and Niver, 1988). With this arrangement, lighting was supplied by a camera flash system. The best results were obtained with an aperture setting of f4.0, a shutter speed of 60, and an ASA of 1600. For Baun's (1988) study, photographs were taken in sequence with the camera intervalometer set for a pulse time of 0.1 secs. and an interval time of 0.1 secs. in the repeat mode. The still camera was ideal for this procedure since it contained a through-lens metering system which allowed the camera to measure the amount of light entering the flash unit and then automatically adjust the shutter speed for the best exposure.

When photographs were taken of streamwise/spanwise planes, the still camera was located outside of the concave surface and then focussed over half the channel width at locations encompassing 50-80 degrees, 80-110 degrees, and 110-140 degrees streamwise positions from the start of curvature. These photographs were taken in sequence using the same intervalometer setting, pulse time, and repeat mode interval time as for Baun's (1988) still photographs. The total time between photographs was 0.2 seconds. For illumination, large incandescent lights were employed instead of an automatic flash. With this arrangement, the best results were obtained using an ASA setting of 1600 on the still camera. The aperture and shutter speed were adjusted manually for different lighting conditions. Typical settings were f4.0 and 30, respectively.

## 4.0 EXPERIMENTAL RESULTS

This section presents surveys of the three components of mean velocity, the three components of mean vorticity, power spectra, and photographs of visualized flow, as well as results based on analysis of these different quantities. All of these results were obtained at Dean numbers from 35 to about 440.

### 4.1 SURVEYS OF TOTAL PRESSURE, THREE COMPONENTS OF MEAN VELOCITY, AND THREE COMPONENTS OF MEAN VORTICITY

The three mean velocity components and the three components of mean vorticity were determined from pressure measurements made using the miniature five-hole pressure probe described earlier. All of these pressure measurements were taken 120 degrees from the start of curvature in the spanwise/radial plane located at  $Z/d$  from 4.0 to 8.0, or 5.08 cm to 10.16 cm off the channel centerline. Contour plots presented in Figs. 24-27, 30-33, 35-42, 49-52, and 56-59 were obtained from surveys of a grid of 8 by 40 data points spaced 0.0127 cm apart. In these plots,  $Y$  and  $Z$  are normalized by the channel height,  $d$ , so that  $Y/d=0.0$  represents the concave surface and  $Y/d=1.0$  represents the convex surface.  $Z/d$  is measured with respect to the channel centerline.

#### 4.1.1 Total Pressure and Streamwise Velocity Distributions

Total pressure measurements normalized by  $(P_0 - P_1)^*$  are given in Figures 24-27 for  $De=35$  through 429, where  $(P_0 - P_1)^*$  is the average of the maximum and minimum pressure differentials measured. A graph of these maximum and minimum pressures measured at each Dean number is presented in Fig. 28. This figure shows that the range of total pressures measured increases nearly linearly with Dean number. Figure 29 then shows profiles of  $(P_0 - P_1)$  at Dean numbers from 250 to 426. Time-averaged streamwise velocity distributions are given in Figs. 30-33. In these figures, streamwise mean velocities  $u_0$  are normalized by  $U$ , the bulk mean velocity used to calculate the Dean number. Profiles of  $u_0$  at Dean numbers from 250 to 426 are then given in Fig. 34.

At Dean numbers of 35.0 and 51.4, the total pressure distributions in Fig. 24, and the streamwise mean velocity distributions in Fig. 30 are reasonably spanwise uniform compared to results at higher  $De$ . As Dean number increases, areas of low streamwise velocity and low total pressure are evident near the concave surface. At  $De=61.9$ , each velocity/total pressure deficit extends over about half of the channel height. However, at  $De$  from 73.6 up to 138.7, most of the low velocity regions extend over most of the channel height up from  $Y/d$  of 0.1 up to about 0.8. The time-averaged distributions for these  $De$  show several areas of low velocity near the concave surface in Figs. 30-31 which correspond to regions of low time-averaged total pressure in Figs. 24-25. Each of these corresponds to a region where secondary flows are directed from the concave surface to the convex surface. These are referred to as upwash regions (with respect to the concave surface), and are located between the two vortices in each vortex pair. At  $De$  higher than 175.5 in Figs. 25-27, velocity deficits extend over smaller radial distances and are somewhat smeared in the spanwise direction.

Examination of Figs. 24 and 30 reveals the replacement of one vortex pair with two vortex pairs on the left-hand sides of the two surveys at  $De$  of 73.6 and 86.7. Two pairs are replaced by one pair on the right-hand sides of the surveys as  $De$  increases from 162 to 187.7 in Figs. 25 and 31. From channel results which show spatial evolution, Bottaro *et al.* (1991) provide evidence that vortex pair merging and splitting occur in the time-averaged flow field as it convects downstream. Similar events are probably responsible for the events at  $De$  of 86.7 and 187.7 in Figs. 24, 30, 25, and 31. If so, the present author believes that this behavior is occurring because of repeated *instantaneous* splitting and merging of pairs near the same locations where the time-averaged results indicate splitting and merging. This is discussed in more detail later in this report.

As Dean number increases above 237 to 250, Figs. 26, 27, 32 and 33 show spanwise uniform time-averaged distributions of pressure and velocity. Simulations (Finlay, *et*

al., 1988) and flow visualization (Ligrani and Niver, 1988) results show vortices at these Dean numbers which are much more unsteady, especially in the spanwise direction, than at lower Dean numbers. Because the spanwise lengthscale of the amplitude of the unsteadiness is greater than the spanwise spacing between vortex pairs, time-averaged results show gradients only in the radial direction without any evidence of individual vortex pairs.

#### **4.1.2 Velocity Perturbation Distributions**

Curved channel Poiseuille flow (CCPF) is present when flow in the curved channel is two-dimensional and laminar, without secondary flows. This type of flow generally exists for Dean numbers less than about 36.92. CCPF profiles differ from straight channel Poiseuille flow velocity profile in that the maximum velocity is shifted slightly closer to the concave wall. Figures 35 through 38 show plots of the difference between measured streamwise velocity and mean velocity from the CCPF solution. The CCPF solution for streamwise velocity,  $U_{CCPF}$ , is obtained by determining the mass flow rate (and  $U$ ) from measured data and matching this  $U$  to the CCPF velocity profile. The data is plotted here, using  $u_g - U_{CCPF}$  normalized by  $U$ , to illustrate streamwise velocity perturbations with respect to curved channel Poiseuille flow caused by time-averaged secondary flows.

The normalized velocity perturbation contours in Figs. 35-38 were calculated using the data shown in Figs. 30-33. At  $De=35.0$  and  $De=51.4$ , results in Fig. 35 evidence approximate spanwise uniform CCPF behavior. At  $De=61.9$ , the negative perturbation contours are circular in shape. In this case, these contours correspond to newly developed vortex pairs. This is confirmed by the partially developed velocity deficits at this  $De$ , and by flow visualization results which show that vortex pairs at this  $De$  begin to develop only a short distance upstream. Bottaro *et al.* (1991) also note similar perturbation contours at streamwise positions where vortex pairs are first seen. As the Dean number increases to 73.6, the negative perturbations in Fig. 35 form into inverted

triangular shapes, and become narrower (in the spanwise direction) as the positive perturbations become wider. These narrower negative perturbations correspond to regions where secondary flows directed radially inwards from the concave surface (upwash regions) are intensified and narrower in the spanwise direction. At this and higher  $De$ , maximum perturbation amplitudes are locally sometimes greater than 60 percent of the bulk mean velocity. At  $De=86.7$ , the perturbation distributions show close agreement with ones presented by Bottaro *et al.* (1991) measured 112 degrees from the start of curvature at about the same Dean number. The radial position of the most negative perturbation for  $De=61.9$  in Fig. 35 is  $Y/d=0.3$ . As Dean number increases, the present results show that the radial location of the peak velocity deficit then moves toward the convex wall. At  $De=138.7$ , Fig. 36 shows that the most negative perturbation is centered at  $Y/d=0.5$ . The  $(u_\theta - U_{CCPF})/U$  variations evident at this Dean number continue for  $De$  up to 175.5. For  $De$  greater than 175.5 to 237.3, the results in Figs. 36 and 37 show deviations from CCPF which are spread over larger portions of the spanwise/radial plane where measurements were made. At Dean number greater than about 237.3, results in Figs. 37 and 38 show that contours of velocity deficit and surplus magnitudes become more spanwise uniform. This is consistent with spanwise uniform pressure and velocity data previously presented for the same Dean numbers.

From results like the ones presented in Figs. 35-38, magnitudes of  $e$ , the streamwise velocity perturbation across the spanwise/radial measurement plane can be determined. This quantity  $e$  is given by

$$e = (1/A \int_A (u^*)^2 dA)^{1/2}$$

where  $u^* = (u - U_{CCPF})$ , and  $A$  is the area of the cross-section where measurements are made. Magnitudes of  $e$  show a steadily increasing trend as Dean number increases (Ligrani *et al.*, 1992c). When compared with results from Bottaro *et al.* (1991) for the same  $De$  and approximately same streamwise location, the present results are lower.

This is probably because the present results are obtained from integrations only over the area within the spanwise/radial measurement plane where measurements were made, and not over the entire channel cross section.

#### 4.1.3 Mean Vorticity Distributions

Figures 39 through 63 present time-averaged vorticity distributions measured in the spanwise/radial plane located 120 degrees from the start of curvature. Of these, figures 39-48 present streamwise vorticity data, Figs. 49-55 give radial vorticity data, and Figs. 56-63 present spanwise vorticity data.

In the streamwise mean vorticity contour plots in Figs. 39-42, contours of positive vorticity are shown as dashed lines, and contours of negative vorticity are shown as solid lines. At the lower Dean numbers (35.0-61.9), distinct patterns of positive and negative vorticity are not evident except near  $Y/d=0.2$ . As the Dean number increases, streamwise vorticity distributions show spanwise alternating regions of positive and negative vorticity, where one pair of vortices is evidenced by a region of positive vorticity immediately adjacent to a region of negative vorticity. Each vortex is evidenced by contour lines which are approximately circular in shape, and vorticity regions are seen as concentric circles with higher magnitudes of vorticity closer to the center of the circles. About three complete pairs are evident for each Dean number for Dean numbers from 99.9 to 162. Only two complete pairs are then evident in the measurement plane areas shown for  $De=175.5$  and  $De=226.8$ . In all cases, the spanwise locations between the two vortices within each pair correspond precisely to the negative velocity perturbations in Figs. 35-38. Thus, areas of positive and negative vorticity lie on either side of upwash regions, or regions where low pressure/low velocity fluid has accumulated after being convected away from the concave wall by local secondary flows. According to Swearingen and Blackwelder's (1987) results from a Görtler vortex flow, elongated streaks of low-speed fluid exist in these upwash regions, which are separated in the spanwise direction by regions of higher-momentum fluid induced towards the wall

from the outer flow. Distributions of the streamwise mean velocity perturbation and the mean vorticity components are important since they indicate that Dean vortex pairs have preferred spanwise locations and preferred spanwise spacings in spite of some unsteadiness in the flow. This is evident since vortex signatures are readily apparent in the time-averaged flow field, a conclusion also consistent with Swearingen and Blackwelder (1987).

Magnitudes of the peak streamwise mean vorticity are plotted against Dean number in Figs. 43-45. Peak vorticity is the maximum of the absolute value of vorticity over the spanwise/radial plane area covered by each vortex within each vortex pair. Peak streamwise magnitudes in Figs. 43-45 were determined from the streamwise vorticity data in Figs. 39-42, where three vortex pairs are typically present across the span of the measurement plane for each Dean number. To distinguish the vortex pairs from each other, these are now referred to as the left, middle, and right pairs. Figures 43-45 show that peak vorticity values increase with Dean number for all six vortices when  $60 < De < 150$ . Peak vorticity values then show increasing scatter for Dean numbers above 150. The slightly different values of both components of peak vorticity at a particular  $De$  are present because vortex pairs are triggered by small-scale disturbances originating at the channel inlet which sometimes vary across the channel span (Ligrani *et al.*, 1992b). The random initiation of the vortex pairs thus results in vortices with different amounts of streamwise development and hence, different strengths.

Circulation of streamwise vorticity,  $\Gamma_x$ , is plotted as a function of Dean number in Figs. 46-48. Streamwise circulation is calculated by summing streamwise vorticity values over an area of positive or negative vorticity and then multiplying this sum by  $(0.0127 \text{ cm})^2$ , where  $0.0127 \text{ cm}$  is the spatial spacing between adjacent data points. Values of  $\Gamma_x$  plotted in Figs. 46-48 include absolute values for the positive vortex and the negative vortex for the right, middle and left vortex pairs. Circulation values for the two vortices in the right pair and the positive vortex in the left pair increase with

Dean number for values up to  $De=240$ . Circulation values for the other vortices show less definite trends and more scatter as the Dean number increases to 240.

Figures 49 through 52 show contours of the radial component of mean vorticity. Here, adjacent contours of positive and negative radial vorticity provide particularly clear indications of time-averaged Dean vortex pairs. According to Finlay, *et al.* (1988), locations of radial vorticity maxima and minima also identify locations of shear layer instabilities. Fig. 49 shows uniform streamwise flow for Dean numbers up to 51.4. At higher Dean numbers up to 162, pairs of vortices which are indicated by positive and negative radial vorticity regions are readily apparent, and magnitudes of absolute values of radial vorticity for each vortex pair increase. Upwash regions between the two vortices in a pair are evident where radial vorticity gradients are quite large and an abrupt change in the sign of this vorticity component occurs as one moves in the spanwise direction at constant  $Y/d$ . In Fig. 50, at a Dean number of 127.4, central portions of upwash regions are located at  $Z/d$  of about 5.1, 6.1 and 7.0. Distinct contours of positive and negative radial vorticity continue to be present at Dean numbers from 175.5 to 237.3, but they less clearly defined and cover smaller spanwise/radial measurement plane areas compared to the contours at lower Dean numbers. At Dean numbers greater than 250.3 in Figs. 51 and 52, radial vorticity regions are not evident in the time-averaged flow field due to large scale unsteadiness.

Peak radial vorticity values for the vortices contained in the left, middle, and right vortex pairs are presented as dependent on Dean number in Figs. 53-55. Here, as before, peak vorticity is the maximum of the absolute value of vorticity over the spanwise/radial plane area covered by each vortex within each vortex pair. Peak radial vorticity values increase with Dean number at about the same rate for all six vortices for Dean numbers up to about 162. At higher Dean numbers, peak radial vorticity values generally decrease with Dean number.

Figures 56 through 59 show spanwise vorticity distributions over the range of Dean numbers where measurements were made. Vorticity contours at Dean numbers of 35.0 and 51.4 evidence spanwise uniform mean flow field behavior. At higher Dean numbers up to 237.3, local upwash regions are evidenced by local regions of positive vorticity which emanate from the concave surface and begin to move closer to the convex surface. These result because low momentum fluid is moved away from the concave wall by upwash secondary flows. The locations of these secondary flow regions are consistent with distributions of the other two components of vorticity since they are located between the two vortices in each vortex pair. Regions of negative spanwise vorticity exist between these upwash regions resulting in spanwise periodic distributions which become more intense as the Dean number increases up to about 237. At Dean numbers of 250.3 and above, time-averaged spanwise vorticity distributions are then spanwise uniform, as expected. Profiles of spanwise vorticity for Dean numbers from 250 to 428 are given in Fig. 60.

Figures 61 through 63 show peak spanwise vorticity changes with Dean number. As with the other vorticity components, peak magnitudes are plotted separately for each vortex in the three different vortex pairs. For Dean numbers up to about 240, peak positive vorticity values increase (near the concave surface) with Dean number at a faster rate than peak negative vorticity values (near the convex surface). Magnitudes of positive spanwise vorticity are not only higher than absolute values of negative spanwise vorticity, but are also higher than the largest values of streamwise and radial vorticity measured. The variations and scatter for all three vorticity components at Dean numbers higher than about 240 are associated with significant unsteadiness and with significant increases of the longitudinal velocity fluctuations (Ligrani et al., 1992a).

Magnitudes of circulation and maximum vorticity are determined over a  $Z/d$  range specified for each individual vortex, and over a  $Y/d$  range covering the radial extent of the measurements, ie. from 0.1 to 0.8. This is important in regard to all three

components of vorticity, but especially in regard to spanwise vorticity distributions because absolute value magnitudes are probably significantly higher at  $Y/d$  outside of the range covered by the survey used to produce the results in Figs. 61-63.

#### **4.2 SPECTRA OF HOT-WIRE SENSOR SIGNALS**

Spectra of voltage fluctuations from hot-wire probes are presented to provide information on frequencies of events in Dean vortex flow. The voltage fluctuations were taken from hot-wire bridges, and result because of velocity fluctuations which change instantaneous convective heat rates to and from the hot-wire probes. Tests conducted with no flow in the channel showed maximum levels of most background electronic noise to be about four to five orders of magnitude less than spectral peak amplitudes with flow.

Three different regimes of behavior are observed, each involving phenomena at different frequencies. This first regime exists at Dean numbers from 40 to about 130, the second regime is present at Dean numbers from about 130 to 185-200, and the third regime is evident for  $De$  greater than 185-200. Observations end at a Dean number of about 435. Details which characterize these different regimes are now described.

##### **4.2.1 Spectral Behavior for Dean Numbers From 40 to 130**

Spectra typical of results obtained at Dean numbers from 40 to 130 are presented in Figs. 64 and 65. The results in Figs. 64a and 64b were obtained at a Dean number of about 60, and the results in Figs. 65a and 65b were obtained at a Dean number of about 100. For both sets of data, hot-wire sensors were located at a streamwise location 112 degrees from the start of curvature at  $Z/d=12.2 - 12.4$  and  $Y/d=0.5$ . These spanwise locations are equivalent to 9.65 - 9.91 cm from the channel side wall. For each  $De$ , spectra at these experimental conditions are qualitatively typical of spectra measured at other  $Y/d$  and  $Z/d$  and similar  $\theta$ . The results occasionally show locally higher humps (broad, small amplitude local maxima) at frequencies of 0.5-2 Hz, 4-7 Hz, 7-9 Hz, 10-12 Hz, 12-15 Hz, and 17-21 Hz. The oscillations at 0.5-2 Hz correspond to the

highest energy levels in the frequency plots, and are believed to be due to undulating vortex motions (Ligrani et al., 1992a). Spectral variations at other frequencies may also be partially related to undulating vortex motions, as well as to splitting and merging, and to the fact that channel inlet conditions are not precisely constant with time. Most of this unsteadiness occurs about vortex pair upwash regions, providing additional evidence that the vortex pairs have preferred locations across the channel span.

The spectra in Figs. 64a and 65a were obtained using the signal analyzer, and the ones in Figs. 64b and 65b were obtained using digital sampling and fast Fourier transforms. When spectra in Figs. 64a and 64b for  $De=60$  are compared, two additional rather sharp spectral peaks are seen at 21 Hz and 38 Hz in the plot in Fig. 64b. These are attributed to digital processing "noise" since they are not seen in the spectrum obtained with the signal analyzer. Comparison of the results in Figs. 65a and 65b for  $De=100$  leads to a similar conclusion since the latter plot also shows evidence of digital "noise" at 21 Hz and 38 Hz.

A summary of spectra at Dean numbers from 50.5 to 435.0 is presented in Fig. 66. These results were obtained from a hot-wire sensor located at a streamwise location 112 degrees from the start of curvature at  $Z/d=12.25$  and  $Y/d=0.5$ . This spanwise location is equivalent to 9.84 cm from the channel side wall. The low energy levels in spectra measured at  $De$  equal to 50.5 and 100.3 are apparent when the results at these  $De$  are compared to ones at higher  $De$ . A spectral peak at 60 Hz is apparent in both of these spectra which is due to electronic noise.

#### **4.2.2 Spectral Behavior for Dean Numbers From 130 to 185-200**

At Dean numbers from 130 to 185-200, twisting Dean vortex flow is present in the curved channel (Ligrani and Niver, 1988). Twisting is the result of a periodic signal imposed on the vortex pairs in the form of rocking motion (as observed in

spanwise/radial planes) at fundamental frequencies ranging from about 55 Hz to 100 Hz (Finlay *et al.*, 1988; Ligrani and Niver, 1988; Ligrani *et al.*, 1992a).

Power spectra obtained during twisting show evidence of this periodic signal, as illustrated by the spectrum for  $De=150.1$  in Fig. 66. This spectrum shows a broad peak at 80 Hz which corresponds to the principal frequency of twisting vortices, along with two harmonics at 160 Hz and 240 Hz. The broadness of the principal peak is caused by twisting frequencies which vary somewhat with time due to mergings and splittings of vortex pairs and the convective nature of curved channel flow. On the high frequency side of the principal peak, flow background noise levels are about two orders of magnitude lower than the local maximum. The measurement location for the  $De=150.1$  spectrum in Fig. 66 is near an upwash region within a vortex with negative vorticity levels.

Spectra which are qualitatively similar to the one in Fig. 66 for  $De=150.1$  are observed at a variety of locations in spanwise/radial planes located from 112 to 120 degrees for  $De$  from 130 to 185. As  $De$  increases, principal and harmonic peaks become higher in magnitude and more apparent relative to power levels of background fluid motions. Also present for  $De$  lower than about 150 within the twisting range are motions associated with a spectral peak at 7-8 Hz (Ligrani *et al.*, 1992a). For  $De$  higher than 150, there is no evidence of the 7-8 Hz motions.

#### **4.2.3 Spectral Behavior for Dean Numbers Greater Than 185-200**

For  $De$  higher than 185-200, no evidence of twisting motion is apparent from experimental measurements made thus far. Spectra at  $De$  from 200.1 to 435.0 in Fig. 66 illustrate this fact. All are broad band with no local maxima or spectral peaks. The results at  $De$  near 435.0 additionally show many characteristics found in fully turbulent flows.

### 4.3 FLOW VISUALIZATION OF DEAN VORTICES

The view seen in individual photographs which show flow visualization results is evident from the schematic shown in Fig. 67. Photographs show smoke patterns in spanwise/radial planes such that flow is moving away from the observer. The concave surface is then on the bottom and the convex surface on the top of each individual photograph. The concave surface is the outer wall with the 60.96 cm radius and the convex surface is the inner wall with the 59.69 cm radius. The left hand side of each photograph is 5.08 cm from the channel centerline, and the right side is 10.16 cm off of the channel centerline. Thus, the width of each photograph spans a distance of about 5.08 cm, and the field of view is 1.27 cm by 5.08 cm such that the spanwise direction is horizontal and the negative radial direction is vertical.

The smoke patterns in Figs. 68-71, 73-77, 92, 95, 98-99, and 102 are influenced by the temporal and spatial history of the flow from the smoke injection location at the channel inlet to the downstream cross-section of observation. Fortunately, significant secondary flows over this portion of the channel are generally non-existent until just upstream of the observation location. After initial injection, the smoke fills the bottom half of the inlet located just upstream of the nozzle. In the straight portion of the channel downstream of the nozzle and prior to the curved segment, flow is steady and laminar, diffusion is minimal, no significant or discernible secondary flows are present, and flow streak lines, path lines, and streamlines are all the same. Consequently, the smoke then enters the curved section as a spanwise uniform layer next to the convex surface (Fig. 68,  $De=42, 53$ ). The streak lines followed by smoke trajectories then continue to follow flow streamlines until small-scale unsteady secondary flows develop and the vortices begin to form (Fig. 68,  $De=64, 73$ ). After this occurs, vortex pairs are very coherent as they develop downstream (Fig. 68,  $De=90, 100$ ), and smoke particles follow the same vortex pairs from their inception. This is also apparent in results presented by Alfredsson and Persson (1989) and Matsson and

Alfredsson (1990), and occurs partially because vortex pairs have preferred spanwise positions with preferred spanwise spacings (Figs. 49-52), and partially because spanwise unsteadiness is not large enough to disrupt individual vortex pairs at low  $De$  (ie. Fig. 68,  $De=90, 100$ ). Thus, arrangement of smoke patterns from the spanwise uniform layer which exists at the entrance of the curved section occurs due to significant secondary flows in the channel, such as the ones associated with the vortices.

The initiation of vortex pairs is connected to infinitesimal scale disturbances which originate at the channel inlet. However, in spite of their effects on initial vortex pair development, the disturbances do not appear to influence the smoke layer upstream of vortex initiation locations (ie. at the inlet of the curved portion of the channel) by perceptible amounts. This is because they are probably not large enough to affect the smoke until it is rearranged by the secondary flows within the vortex pairs. Such ultra small disturbances are present in all convective flows and their imperceptible influences on the smoke layer is not surprising since they are *undetectable* to observation and measurement with most *any* technique.

A test was conducted to confirm that the smoke layer upstream of vortex initiation locations is not dependent upon these time and spatially varying infinitesimal scale disturbances. In this test, smoke was added to the channel inlet so that it filled the top half of the inlet located just upstream of the nozzle, instead of the bottom half. With this situation, the smoke entered the curved portion of the channel as a spanwise uniform layer near the *concave* surface, instead of as a spanwise uniform layer near the *convex* surface, as is done nominally. The result of this test showed the same flow visualization patterns as for nominal test conditions, except the patterns appeared so that what was dark before was now light, and visa versa. Because the flow visualization patterns were qualitatively and quantitatively the same for both situations even though the smoke originated at different portions of the channel inlet, the infinitesimal inlet disturbances do not appear to provide perturbations to the upstream smoke layer which are large

enough to be observed in the vortex pairs farther downstream. Thus, the small scale disturbances which trigger initial vortex development appear to alter smoke patterns only as they alter the initiation and development of vortex pairs, and not as they alter the smoke layer upstream. This test also confirmed the neutral buoyancy characteristics of the smoke. Other tests conducted with artificially induced disturbances at the channel inlet (Ligrani and Niver, 1988) also showed these to have no discernible effects on the smoke layer upstream of vortex initiation locations.

In spite of the fact that the initial development of individual vortex pairs depends upon infinitesimal disturbances that seem to vary in time and space, specific vortex pair features, specific splitting and merging events, and overall observations of vortex behavior including splitting and merging are very repeatable over long time periods. If the random timewise disturbances which trigger initial vortex development were qualitatively or quantitatively different over the long term, such repeatability could not have been achieved. This was partially because considerable care was taken to conduct the present investigation when the inlet conditions of the facility were as quiet as possible. The validity of the present results is additionally supported by their agreement with some specific experimental results obtained in other laboratories (Alfredsson and Persson, 1989; Matsson and Alfredsson, 1990), as well as with numerous analytic and numerical results (Finlay *et al.*, 1988; Guo and Finlay, 1991; Yang and Kim, 1991).

Smoke distributions thus give good qualitative indications of vortex locations because these are associated with significant secondary flows which remain fairly coherent within individual vortex pairs as they are convected downstream. The smoke, of course, does not indicate exact quantitative distributions of vorticity or exact vortex outlines because its locations are not directly due to vorticity. The smoke also does not follow the instantaneous streamlines in the flow during transient events. However, the smoke does indicate locations of vortex core regions, upwash regions and downwash regions such that

stronger secondary flows correspond to smoke patterns which are more developed (ie.

Fig. 68,  $De=90$  as compared to Fig. 68,  $De=73$ ).

#### **4.3.1 Smoke Patterns as Observed 115 Degrees From the Start of Curvature**

Smoke pattern development is now described for Dean numbers ranging from 42 to 218 (Ligrani and Niver, 1988). The patterns were photographed at the spanwise/radial plane located 115 degrees from the start of curvature, chosen since a wide variety of smoke patterns and pattern unsteadiness are seen.

For Dean numbers of 42 and 53, Fig. 68 shows smoke in a thick layer near the convex surface. Either because the flow is not fully developed or because the smoke has not yet followed part of a vortex rotation, evidence of Dean vortices is not apparent even though the Dean number is greater than the critical value. Flow visualization photographs show similar uniform layers of smoke at streamwise locations up to 125 degrees from the start of curvature for Dean numbers less than about 53, and at locations closer to the start of curvature at slightly higher  $De$  (Ligrani and Niver, 1988). These eventually develop randomly uneven appearances over the channel span near the concave surface at any particular streamwise location as the Dean number increases (Ligrani and Niver, 1988). Very small magnitudes of such spanwise waviness are evident in the smoke layer at a Dean number of 53 (in Fig. 68). It becomes more pronounced at a Dean number of 64 where a comparison of photographs at different times evidences some radial unsteadiness. The dark, circular shaped regions for  $De=64$  probably correspond to upwash regions between the two vortices in a pair during their initial development. Such behavior is somewhat similar to initial Görtler vortex development over concave surfaces, where wavelength selection mechanisms and vortex growth are very receptive to small departures from ideal flow conditions and to disturbances in the oncoming stream (Floryan and Saric, 1984). Results for both  $De$  of 53 and 64 in Fig. 68 were obtained at a spanwise/radial plane 115 degrees from the start of curvature. At higher

Dean numbers in the vicinity of 75, spatially non-uniform smoke layers are evident at locations only up to 75 to 90-95 degrees from the start of curvature (Ligrani *et al.*, 1992b).

When the Dean number reaches 73, mushroom-shaped smoke patterns for the 115 degree spanwise/radial plane in Fig. 68 provide evidence of Dean vortices. Such patterns form due to spanwise variations resulting from the different upwash and downwash regions associated with pairs of counter-rotating vortices. The vortices evidenced by these patterns appear to be symmetric (Ligrani and Niver, 1988) but not all the same height across the span of the channel. The region of radially inward flow between two vortices is called the upwash region (with respect to the concave wall) and corresponds to the bright "stem" of a mushroom-shaped smoke pattern (Ligrani and Niver, 1988). This sometimes lies on either side of a thin dark region relatively void of smoke. The downwash regions between adjacent pairs of vortices are seen as bright lines extending across the channel also in the approximate radial direction. Central portions of each vortex then lie in the dark areas between upwash and downwash regions, and are evidenced by the broad, dark "petal" portions of the mushroom-shaped patterns (Ligrani and Niver, 1988; Ligrani *et al.*, 1992b). Fig. 69 gives some information as to how these patterns change with time for  $De=73$ . These photographs, taken about 1 second apart, show mushroom patterns with discernible unsteadiness, changing radial height as they develop in time at this streamwise station. At each instant of time, mushroom-shaped smoke patterns of significantly different height co-exist together. Such behavior probably indicates variations of the streamwise locations where vortex pairs are initiated. The spanwise locations of mushroom patterns also change with time in Fig. 69 providing evidence of some spanwise unsteadiness.

At a Dean number of 77, Fig. 68 shows that adjacent smoke patterns again have different shapes and different heights. However, here, less spanwise unsteadiness is observed than for  $De=73$ . The smoke patterns at a Dean number equal to 90 in Fig. 68

are more fully developed than at lower Dean numbers. At most times, these cover most of the radial height of the channel with small amounts of radial unsteadiness. Spanwise unsteadiness is also observed, especially when small, intermittent secondary vortices are present or when splitting and merging of vortex pairs are occurring. The mushroom-shaped patterns for a Dean number of 100 take up the full radial height of the channel. These well-developed patterns show good spatial periodicity with an unusually small amount of unsteadiness in any direction. Thus, as Dean number increases from 73 to 100, observations in the spanwise/radial plane located 115 degrees from the start of curvature show that unsteadiness subsides in magnitude as the radial extents of mushroom-shapes become larger and smoke patterns become more fully formed.

At a Dean number of 123, Fig. 68 shows smoke patterns again with clearly defined mushroom-shapes. At this experimental condition, oscillations are most significant in the spanwise direction mostly in the form of a rocking-type motion. As the Dean number increases to 163, this unsteadiness and the pattern distortion which occurs with the oscillations are both more pronounced in the radial and spanwise directions. A sequence of photographs clearly illustrating the unsteady rocking motion at this Dean number is presented Fig. 70, where vortex pairs also seem to become non-symmetric with respect to upwash regions. This is evidenced by mushroom-shaped patterns with different shapes on either side of the stem which may mean that each individual vortex is no longer a mirror image of the opposite vortex within each pair (Ligrani and Niver, 1988). Fig. 68 shows that mushroom-shaped patterns are more difficult to distinguish at higher Dean numbers of 192 and 218 as a result of even greater unsteadiness and distortion of smoke. This is particularly evident from the time variation of smoke patterns in Fig. 71 for  $De=192$  which shows spanwise and radial oscillations with length scales on the order of the half-channel width.

In spite of the unsteadiness of the vortex pairs at Dean numbers from 53 to 218 at the 115 degree streamwise station, Figs. 24-63, which were discussed earlier, show

that important time-averaged features of vortex pairs are still apparent. This is because the vortex pairs not only have preferred spanwise spacing, but also prefer specific spanwise locations where they are readily apparent across the span of the channel in the time-averaged flow field (Ligrani *et al.*, 1992b). Most of the unsteadiness thus occurs about these time-averaged vortex pair positions. Referring again to Figs. 30-33, which shows time-averaged streamwise velocity distributions, several areas of low streamwise velocity (which also correspond to regions of low time-averaged total pressure) are present near the concave surface in individual surveys for Dean numbers from 61.9 to 237.3. These are located between the two vortices in each vortex pair and thus represent the same portions of the vortex pairs as the mushroom "stems" evident in Fig. 68. Each of these velocity deficits thus corresponds to an upwash region, i.e. a region where time-averaged secondary flows are directed from the concave surface to the convex surface. It should be mentioned that direct comparison of the precise spanwise positions of the time-averaged pairs with the flow visualization results in Fig. 68 is not possible because the two types of results were obtained at different spanwise portions of the channel.

#### **4.3.2 Map of Smoke Patterns**

An experimental domain map illustrating the conditions where different types of smoke patterns are observed is presented in Fig. 72. These were obtained from results such as the ones just described, and are given for Dean numbers ranging from 40 to 220 and for angular positions from 65 to 145 degrees from the start of curvature. Symbols in Fig. 72 indicate the experimental conditions at which photographs are available. In a similar study, Matsson and Alfredsson (1990) produced a map from flow visualization results in good agreement with the one in Fig. 72.

Experimental points labelled "smoke layer" are present at lower Dean numbers and smaller  $\theta$ . These points indicate photographs which show spanwise uniform smoke without significant distortion or waviness. "Wavy smoke layers" are present when

smoke layers are distorted with a wavy appearance near the concave side of the channel. These layers are sometimes observed to have discernible unsteadiness in radial or radial and spanwise directions.

Pairs of counter-rotating Dean vortices are believed to be present whenever mushroom-shaped smoke patterns are observed. These "mushrooms" often exist with periodic spacing across the channel span. Unless significant unsteadiness is present which prevents identification of clearly defined patterns, about 3.0 to 3.5 mushroom patterns are evident in photographs much of the time.

As Dean vortices initially form at lower Dean numbers, they are symmetric with respect to spanwise/radial planes. Such vortex pairs are indicated by mushroom "stems" which form radial lines of symmetry with smoke patterns which are mirror images on each side of the line. In other words, the two vortices in each pair are similar. For higher Dean numbers and larger downstream locations, Dean vortices become nonsymmetric. Nonsymmetric patterns are distorted (when viewed in spanwise/radial planes), generally by spanwise or radial unsteadiness in the flow, such that no line of symmetry exists. For Dean numbers greater than 120 to 160, and  $\theta$  locations greater than 115 to 125 degrees, smoke patterns are generally so distorted by unsteadiness that no mushroom-shaped smoke patterns can be discerned. This region is labelled "no identifiable vortex pattern" in Fig. 72.

Another important feature clearly identifiable from photographs are the heights of mushroom-shaped smoke patterns and smoke layers. Mushroom-shaped patterns which identify Dean vortices are either full height or mixed height. Full height patterns exist for higher Dean numbers and larger downstream locations, and are indicated by patterns at different span locations which extend the complete radial channel width from concave surface to convex surface. Mixed height patterns are present when photographs show mushroom-shaped smoke patterns which vary in height across the channel span. Experimental conditions for this are indicated by the shaded region in Fig. 72. Mixed-

height behavior seems to be present for roughly the same experimental conditions as where symmetric Dean vortex pairs and wavy smoke layers are present.

#### 4.3.3 Symmetric Dean Vortex Flow

Figure 72 shows that symmetric Dean vortex pairs are observed for a range of conditions. For  $De < 100$ , the streamwise distance required for mushroom-shaped patterns to first appear depends strongly on  $\theta$ . For higher Dean numbers from 100 to 200, clear evidence of symmetric vortices is evident usually after about 95 degrees after the start of curvature. For some visual observations over this  $De$  range, this boundary is slightly upstream. The overall minimum Dean number where evidence is obtained is 64 for  $\theta$  ranging from 125 to 145 degrees. Because of the transitional nature of these flows, these boundaries are not distinctly defined. The same can be concluded regarding boundaries between other regimes of curved channel flow behavior.

Examples of smoke patterns of symmetric Dean vortices are presented in Fig. 73. These were obtained at a  $\theta$  equal to 95 degrees and a Dean number of 123. The patterns show only a small amount of unsteadiness. The slight differences in shape and spacing at different spanwise positions may be due to differing amplitudes and locations of the small upstream disturbances which trigger initial vortex development. The narrow "mushroom stems" evidence narrow upwash regions from the concave wall. The large "mushroom petals" evidence the sizes of the vortices themselves. The spacing between "mushrooms" then indicates large, spread-out side-wash and downwash regions.

A comparison of the smoke patterns in Fig. 73 with ones in Fig. 68 for Dean numbers of 90 and 100, also for symmetric Dean vortex flow, shows the three sets to be qualitatively and quantitatively significantly different in shape. Such behavior is consistent with results presented by Finlay, *et al.* (1987, 1988), which indicate that vortex shape changes occur with spanwise wavenumber and Dean number. However, the present visualization results indicate that important shape changes also occur with streamwise development.

In the qualitative streamwise development analysis of Finlay, *et al.* (1987), Fourier expansions are used to represent spatial velocity perturbations of an axisymmetric Dean vortex pair relative to curved channel Poiseuille flow. The locations where the first Fourier mode of this approximate expansion reach 90 percent of full amplitude are shown in Fig. 72. The corresponding Dean numbers are interpreted to be the ones where velocities of Dean vortices are nearly fully developed also at 90 percent of their full amplitudes. These  $De$  are provided in Fig. 72 for moderate initial disturbances (turbulence intensity approximately 0.0004) located at the start of curvature. The curve for moderate disturbances approximately follows the boundary between smoke layers and wavy smoke layers at Dean numbers lower than where symmetric vortex pairs are present. The curve for low disturbances is at higher Dean numbers just below where mushroom-shaped patterns are first observed. If these first observed patterns represent vortices at 90 percent of their full amplitudes, then there is reasonable agreement. However, mushroom patterns probably require some additional streamwise development before they correspond to fully-developed vortices.

#### 4.3.4 Oscillating and Wavy Dean Vortex Flow

Figure 69 shows Dean vortices with significant unsteadiness in the radial direction for  $De=73$ . Another good example is presented in Fig. 13 of Ligrani and Niver (1988) for  $\theta=125$  degrees and  $De=64$ . In this latter case, very little spanwise oscillation is present and mushroom patterns seem to move almost exclusively in the radial direction. The experimental conditions for radial oscillations are indicated in Fig. 72. When these oscillations occur by themselves, they are mostly where symmetric Dean vortices are observed, or in smoke layers near the onset of symmetric Dean vortex flow. As indicated earlier, for  $\theta=115$  degrees, radial unsteadiness decreases in magnitude as overall average vortex height increases and  $De$  increases from 73 to 100.

When oscillations occur only in the radial direction, different heights at different spanwise positions may result because vortices initiate at different streamwise locations

across the span of the channel. These initial initiation locations probably also change with time which makes vortex heights appear to oscillate in the radial direction in spanwise/radial planes at locations farther downstream.

Such variations of vortex pair height and unsteadiness are clues that the amplitudes and levels of unsteadiness of the small disturbances which trigger initial vortex development also vary across the span. Clearly, if large amplitude or spanwise uniform disturbances are present, vortex initiation would probably also be more spanwise uniform and steady, and occur just after the imposition of curvature. However, in reality, because qualification tests indicate low initial turbulence levels and little spanwise variation at lower Dean numbers, initial disturbances must be very small, and initial vortex development must be very sensitive to the amplitudes of these small disturbances. Thus, radial unsteadiness is likely to be present whenever Dean vortices are allowed to develop naturally. Other observed oscillations may be due to transients which have not completely decayed. In Taylor-Couette flow, Swinney (1983) indicates that decay times are longer and susceptibility to small external perturbations is greater as aspect ratio increases.

Less sensitivity to initial disturbances seems to result after Dean vortices become fully developed at larger downstream locations. Here, vortex heights at different span positions show relatively small variations in height and spacing. This is certainly, in part, due to the limitations imposed on vortex pair growth by the channel walls and aspect ratio. However, it is also additionally a result of the fact that, once initiated, vortex behavior and development are strongly controlled by the centrifugal instability from concave curvature.

Another type of oscillating Dean vortex flow is twisting. Twisting is different from the radial oscillating modes just described because it produces vortices that are wavy. Twisting Dean vortex flow (TDVF) was observed in results from numerical work by Finlay, *et al.* (1987), and is evidenced in flow visualization results by mushroom-

shaped smoke patterns which have a rocking type of motion. It is also discussed in more detail later in this report. Twisting motion is observed mostly near the onset of non-axisymmetric Dean vortex flow for experimental conditions in Fig. 72 where smoke patterns are denoted to have spanwise oscillations or spanwise and radial oscillations. Rocking motion associated with twisting is rarely observed alone, rather it is most often observed in conjunction with at least one other mode of oscillation. In many cases, rocking vortex pairs are adjacent to pairs with a different type of motion. Examples believed to represent TDVF are shown in Fig. 70 for  $De=163$  and  $\theta=115$  degrees. The vortex pairs in these figures and for TDVF in general are nonsymmetric, which is consistent with Fig. 72 and the simulation results of Finlay, *et al.* (1987, 1988).

Also included on Fig. 72 is a curve which indicates the experimental conditions where TDVF reaches 90 percent of its full amplitude (Finlay, *et al.*, 1987) determined from an approximate estimate where the first Fourier mode for twisting reaches 90 percent of its fully developed amplitude. The associated Fourier expansion is for the perturbation provided by TDVF relative to fully developed symmetric Dean vortex flow. The line is given for a moderate level of disturbance at the initial development location within the channel. It shows some consistency with the present results in that most observations of nonsymmetric patterns with spanwise oscillations and/or rocking motion occur for higher Dean numbers. When making this comparison, it is important to note that, in our visualization, it is not clear whether the twisting patterns represent partially developed or fully developed flows.

Mushroom-shaped smoke patterns with oscillations simultaneously in the spanwise and radial directions are also present without twisting motion. Some evidence of the range of conditions is indicated in Fig. 72. These generally have larger-scale oscillations and greater unsteadiness than smoke patterns identified with twisting or radial modes. In some cases, the oscillations also appear to be so chaotic that mushroom-shaped patterns are barely distinguishable or cannot be identified. It is

additionally not clear whether these oscillations are generic to curved channel flow or a result of transient disturbances which have not completely decayed (Swinney, 1983). Photographs of such patterns are shown in Fig. 71 for  $De=192$  and  $\theta=115$  degrees.

#### 4.3.5 Small Secondary Vortex Pairs

Photographs of smoke patterns in spanwise/radial planes which provide clear evidence of the presence of small secondary vortex pairs are presented in Fig. 74. Figure 72 shows experimental conditions where these are seen in the study of Ligrani and Niver (1988). Because of their nature and rapid growth rates, these small secondary vortex pairs are always associated with spanwise and radial oscillations. They are also discussed in more detail later in this report.

The example in Fig. 74 is for  $De=100$  and  $\theta=95$  degrees. Here, two mushroom-shaped patterns seem to have been replaced by one pattern between the first and second photographs. By the time of the third photograph, the middle mushroom pattern again seems to have been replaced by two smaller patterns. In the study of Ligrani and Niver (1988), such behavior was believed to result from either of two different phenomena. The first of these possibilities was considered to be a situation in which vortex pairs are present with radial oscillations in combination with significant spanwise motion. However, more recent work indicates that the second possibility suggested by Ligrani and Niver (1988) is the more likely explanation. With this possibility, new vortex pairs are forming near the concave wall between other pairs, followed by a readjustment of the spanwise wavenumber (Ligrani *et al.*, 1992b). The disappearance of a vortex pair may be a result of this process in reverse. Additional evidence of formation is indicated by mushroom-shaped patterns observed in spanwise/radial planes, which suddenly appear to "pop" out of the concave wall. When viewed from outside of the concave surface, vortex pairs appear to be surrounded by tubes of smoke with non-circular interior cross sections which are relatively void of smoke. Appearances and disappearances or splittings and mergings of vortex pairs are indicated by adjacent tubes

which occasionally divide into two branches or merge together. Similar observations were made by Nakabayashi (1983) in spherical Couette flow. For square and rectangular ducts, respectively, Hille, *et al.* (1985) and Komiyama, *et al.* (1984) also give evidence of secondary vortices for certain Dean numbers, angular positions, and inlet flow conditions. However, the secondary vortices in these studies are different from the present one since they are not intermittent when present at a particular Dean number.

Finlay *et al.* (1987, 1988) also observed secondary vortex pair formation with decreasing spanwise wavenumber. After the new vortices are formed, steady-state vortex pairs are double in number across the span, and increase in strength as the spanwise wavenumber is decreased further or as  $De$  is increased. Our results are different since the original number, sizes and spacing seem to be resumed a short time following formation. This sudden flow readjustment may occur as a result of the merging of vortex pairs at some position away from the original appearance site, followed by an adjustment of the spanwise pair positions across the span. The vortices which are originally formed must then increase in size and strength to quickly resume the height and spacing of the original vortices.

#### 4.3.6 Streamwise/Spanwise Plane Flow Visualization

Figures 75 and 76 present photographs of a portion of flow, as viewed from exterior to the concave surface of the channel. All photographs for a particular Dean number and location were taken in sequence 0.2 seconds apart. In Figs. 75 and 76, photographs are shown in the sequence they were taken, clockwise from upper left. The left side of each photo represents the channel centerline and the right side is the channel side-wall. Streamwise distance increases from the top to bottom of each exterior view photograph.

The secondary flows evident in the photographs of Figs. 75 and 76 for respective Dean numbers of 145.2 and 104.8 appear as tubes of smoke. These tubes of smoke surround vortex pairs which are relatively void of smoke (Ligrani and Niver, 1988).

These photographs clearly show that the tubes of smoke are not always spanwise periodic. In Figs. 75 and 76, a merging event and a splitting event are evidenced by tubes of smoke which join and divide, respectively. Shortly after this activity, the streamwise oriented vortex pairs tend to resume their nominal spanwise spacing.

#### 4.4 WAVY DEAN VORTEX FLOW

In this section, experimental features of undulating Dean vortex flow and twisting Dean vortex flow are presented and discussed. Certain results are compared to wavy vortex results obtained from direct simulations of the time-dependent, three-dimensional Navier-Stokes equations. Additional details on the numerical method used for these simulations are given by Ligrani *et al.* (1992a).

Finlay *et al.* (1988) first calculated the linear stability of Dean vortex flow to disturbances that cause the vortices to become wavy in the streamwise direction. For a channel radius ratio of 0.975, it was found that as the Dean number increases above 1.2 times the critical Dean number, Dean vortices become unstable to low frequency, long streamwise wavelength wavy disturbances that produce a temporally periodic wavy vortex flow that Finlay *et al.* (1988) termed "undulating vortices". Undulating vortices are similar to wavy Taylor vortices that occur in Taylor-Couette flow. At higher  $De$ , a second mode of wavy instability sets in that has considerably higher frequency and shorter wavelength than the undulating mode. This second mode produces another temporally periodic wavy vortex flow called "twisting vortices" (Finlay, *et al.*, 1988; Ligrani and Niver, 1988; Ligrani *et al.*, 1992a). Some of the rocking motion mentioned earlier is believed to be associated with twisting. The first mention of experimentally observed twisting is given by Kelleher *et al.* (1980), and the first photographic evidence of vortex motions believed to be twisting is presented by Ligrani and Niver (1988). Additional evidence of wavy vortex flow is given by Matsson and Alfredsson (1990) for a rotating, curved channel, and in simulations by Yang and Kim (1991) for a rotating channel. Some of their observations are similar to ones from three-

dimensional nonlinear simulations (Finlay *et al.*, 1990), which show that both twisting and undulating wavy vortices consist of waves travelling in the streamwise direction at constant speed, superposed on the vortices. Some of the major qualitative features associated with one period of these wavy vortex flows are defined by Finlay (1990).

#### 4.4.1 Undulating Dean Vortices

Fig. 77 shows smoke visualization photographs of typical experimental undulating vortices for  $De=3.4De_C$  at a streamwise location  $115^{\circ}$  from the start of curvature. Such behavior sometimes occur intermittently for  $1.1De_C < De < 3.5De_C - 3.8De_C$  and at streamwise positions far enough from the start of curvature. The photographs are separated by 1/30 second and time increases as one proceeds down the page. The streamwise direction is into the plane of the paper. The convex surface ( $r=r_i$ ) is at the top of each photograph and the concave surface ( $r=r_o$ ) is at the bottom of each photograph. One pair of counter-rotating vortices is seen centered just to the left of center in the first photograph, with two other pairs partially appearing on each side of the central pair.

The inflow region of the left hand pair of vortices in Fig. 77 is seen tilted to the left at the left hand side of the top photograph of Fig. 77. Shortly thereafter, it tilts to a nearly vertical orientation followed by tilting to the right and then back to a vertical position by the end of the sequence. Each of the vortices on each side of the inflow region rocks in the radial direction in phase with the changes in direction of the inflow region. The central pair of vortices in Fig. 77 is seen to undergo similar motion. Observations of many other flow visualization sequences show this type of motion occurs frequently in the experimental channel, however in most cases it is transient, lasting locally only about  $70-100 d/(2U)$ .

Vortex rocking coupled with changes in direction of the inflow region that are in phase with the rocking are two of the key qualitative features of numerically simulated undulating vortices (Finlay *et al.*, 1988; Ligrani *et al.*, 1992a). When viewed in

cross-section (i.e. in an  $r, Z$  plane), numerically simulated undulating and twisting modes both cause the vortices to rock such that the line joining the center of any two vortices rocks back and forth from positive to negative slope. The direction of the flow in the inflow region between a pair of vortices remains aligned roughly perpendicular to the line joining the vortex centers across the inflow region, i.e. the changes in the direction of the inflow region occur in phase with the rocking of the vortices. Both twisting and undulating modes have these features, but numerically simulated undulating vortices also slip back and forth considerably in the spanwise direction during one cycle.

According to Finlay *et al.* (1988), this periodic spanwise sideslipping motion is one of the principal qualitative features of numerically simulated undulating vortices. Such periodic sideslipping is often observed experimentally, but not during all undulating events. The present results in Fig. 77 show sideslipping which is probably partially a result of undulation, but certainly also due to other types of events at other locations across the span of the channel. In particular, splittings and mergings of pairs of vortices may be disrupting the undulating motions since these also result in significant spanwise motions at particular streamwise locations in the channel. In addition, individual pairs of vortices in the curved channel probably become unstable to waviness at a different streamwise locations. Consequently, waviness of adjacent pairs is sometimes not in phase, as it would be when spanwise periodicity is imposed, and the vortices cannot sideslip easily because neighboring pairs may be sideslipping somewhat out of phase. Finally, conditions at the channel inlet that cannot be maintained precisely constant with time may also cause undulation to exist at a particular frequency for limited periods of oscillation. Thus, the convective nature of the curved channel produces flow patterns which are much less regular temporally and spatially than those occurring in Taylor-Couette flow. The situation is also different in simulated channel flows because periodic spanwise boundary conditions are not imposed experimentally.

Shown in Fig. 78 is a sequence of plots showing the cross flow velocities associated with one pair of numerically simulated, fully developed undulating vortices at  $De=1.776$   $De_C$ ,  $\eta=0.979$ . The spanwise wavenumber is  $\alpha=2.5$ , which is near that observed in Fig. 77. (The spanwise wavenumber of the left hand pair of vortices in Fig. 77 varies between 2.3 to 2.5. The central pair in the first photograph of Fig. 77 has  $\alpha\sim2.5$ .) The streamwise wavenumber is  $\beta=15$ , which is near that of the most unstable undulating mode based on the linear stability analysis of Finlay *et al.* (1988). Here, streamwise wavelength of the waviness is  $m$  radians and the streamwise wavenumber is defined as  $\beta=2\pi/m$ . Thus,  $\beta$  is the number of waves in a  $2\pi$  circumference of the curved channel. The streamwise direction is into the plane of the plot. Fully developed numerical undulating vortices are exactly periodic in time, since the flow is due to a travelling wave that is periodic in  $Z$  and  $\theta$  and that travels at constant speed in the streamwise direction. One period of oscillation is shown in Fig. 78. The characteristic rocking and directional changes in the inflow region are strikingly similar to those observed experimentally.

Wavy vortices simulated numerically have shift-and-reflect symmetry within round-off error, even though this symmetry is not imposed (Ligrani *et al.*, 1992a). In the shift-and-reflect symmetry equations,  $Z=0$  is the location of either the outflow or inflow plane when the flow is averaged over one temporal period or one streamwise wavelength. This symmetry is apparent in Fig. 78 where plots separated by half a streamwise wavelength (or half a period in time since the flow is due to a travelling wave) are just a reflection about their midplane of those half a wavelength upstream (or half a temporal period earlier).

Shift-and-reflect symmetry is not observed in experiments since the removal of streamwise periodicity is symmetry breaking. However, prior to the onset of waviness, Ligrani and Niver (1988) observe that Dean vortices often appear nearly symmetric about their inflow region, indicating they approximately satisfy the axisymmetric

version symmetry that is also observed for numerically simulated axisymmetric Dean vortices (Finlay, *et al.*, 1988). At higher  $De$ , appearance and disappearance events occur frequently in experiments. These events and finite streamwise length effects preclude shift-and-reflect symmetry.

The frequencies of undulation observed experimentally are now compared with the values expected from the linear stability analysis of axisymmetric Dean vortices given by Finlay *et al.* (1988). Shown in Fig. 79 is the frequency of undulation  $n$  (in Hz) at various  $De/De_C$  obtained from flow visualization records like that in Fig. 77. Also shown in Fig. 79 are data obtained from Finlay *et al.* (1988) from linear stability analysis of axisymmetric vortices (with spanwise wavenumber  $\alpha=2.5$ ) subject to wavy disturbances. For the range of  $De/De_C$  shown, the experimental data deduced from flow visualization results are at lower frequencies than those associated with wavy disturbances having maximum linear growth rates.

Frequencies of undulation observed experimentally may be converted into streamwise wavenumbers  $\beta$  if one assumes the undulating waves travel at the roughly constant angular speed of  $0.0155 U/(d/2)$  (Ligrani *et al.*, 1992a). This is possible because the streamwise speed at which undulating waves travel is approximately independent of their streamwise wavelength. Shown in Fig. 80 is the same data as in Fig. 79 but the experimental frequencies have been converted into streamwise wavenumbers using this approach. (The simulation data in Fig. 3 have actually been converted from wavenumbers to frequencies in the opposite manner.)

The experimental frequencies converted into wavenumbers in Fig. 80 lie approximately between two and four, which means that there are between one and two streamwise wavelengths lying inside the  $180^\circ$  curved section of the channel. Wavenumbers in this range probably correspond to the lowest wavenumbers which can be observed experimentally because of the finite streamwise extent of the channel. Because of the low wavenumbers, the streamwise wavelength selection of the undulating

vortices is probably strongly affected by spatially nonperiodic experimental boundary conditions at the inlet and outlet of the curved channel, as well as any temporal variations of inlet conditions. In addition, differences shown in Figs. 79 and 80 are likely due to the fact that the linear stability analysis applies only to fully developed vortices, whereas experimentally, waviness likely sets in before the vortices are fully developed. (Partially developed vortices are indicated by flow visualization results which show vortex patterns that do not span the entire width of the channel.) With these considerations, it is not surprising that experimentally observed frequencies and streamwise wavenumbers are different from those of the most unstable undulating mode from the linear stability theory of Finlay *et al.* (1988).

Fig. 81 shows a spectrum obtained at  $De/De_C=1.35$ , and  $Y/d=0.10$  in a spanwise/radial plane 120 degrees from the start of curvature. These data were obtained within the inflow region near the concave surface between two vortices which make up a pair. A broad hump (with numerous local maxima) is evident at frequencies ranging from 0.8 Hz to 2.0 Hz, which is believed to correspond to wavy undulating events like the ones in Fig. 77. The broad non-spikey character of the hump results because of variations of the undulation frequency with time, and because the undulations were probably present for only a few periods during the time that the spectrum was sampled. Similar humps are evident in spectra obtained for  $1.1De_C < De < 5.0De_C$  -  $5.4De_C$  throughout the channel spanwise/radial plane located 120 degrees from the start of curvature. However, flow visualizations indicate that these humps are associated with undulations only for  $De$  up to about  $3.4De_C$ . Humps near 1-2 Hz are apparent in spectra at locations which include probe positions at  $Y/d=0.5$  within inflow regions (position 2),  $Y/d=0.1$  and  $Y/d=0.5$  within outflow regions (positions 3 and 5), and at  $Y/d=0.1$  beneath individual vortices (position 4). The position of the Fig. 81 results ( $Y/d=0.1$  within an inflow region) is denoted position 1. These positions with respect to the vortex pairs are determined from measurements of vortex pair structure at a Dean

number of  $2.82De_C$ . Because the positions of pairs are altered slightly as the Dean number varies, these five positions are somewhat approximate in regard to their locations with respect to vortex pair structure at other Dean numbers. The vortex pair structure within which positions 1-5 are located was chosen because it does not change its spanwise position significantly as  $De$  varies from  $1.0De_C$  to  $5.5De_C$ .

A local maximum near 8 Hz is also apparent in Fig. 81. Although this result corresponds approximately to the highest possible frequency for which axisymmetric vortices are unstable to undulating disturbances (Fig. 79), observations in the flow visualizations indicate that this is not associated with undulations. Similar frequency local maxima are not evident at other  $De$  for position 1. At positions 3, 4, and 5, the 7-8 Hz local maximum is again present only for  $De=1.35De_C$ . However, at position 2, which corresponds to  $Y/d=0.5$  within inflow regions, local maxima associated with these frequencies are present over a range of  $De$  from  $1.35De_C$  to  $4.06De_C$ .

Contour plots obtained from experiment and simulation, which show characteristics of the time-averaged flow field when undulation is present, are given in Figs. 82 and 83, respectively. The figures show distributions of the time-averaged streamwise velocity perturbation, streamwise vorticity, radial vorticity and spanwise vorticity in the  $(Y, Z)$  plane. Results are presented in Fig. 82 that are typical of spanwise periodic pair characteristics measured over an area encompassing about two and one-half vortex pairs. Results in Fig. 83 show one vortex pair from a simulation with spanwise periodic boundary conditions. In Fig. 82a and 83a the curved channel Poiseuille flow velocity profile has been subtracted from the streamwise mean velocity and then normalized using the bulk mean velocity  $U$ . All vorticity distributions are normalized using the channel half-height  $d/2$  and  $U$ . The heavy horizontal dashed lines in Fig. 83 show the vertical extent of the data in Fig. 82. Dashed contour lines in each of these figures correspond to negative values, whereas solid lines correspond to positive values.

Experimental results in Fig. 82 were obtained 120 degrees from the start of curvature

for  $De=1.68De_C$ , and  $\eta=0.979$ . The measured spanwise periodicity of streamwise velocity, streamwise vorticity, radial vorticity, and spanwise vorticity distributions from one vortex pair to another is evident in this figure. Simulation results in Fig. 83 are for  $De=1.776De_C$ ,  $\alpha=2.5$ ,  $\eta=0.979$ , and streamwise wavenumber  $\beta=15$ .

Comparison of results in Fig. 83 to ones in Fig. 82 for  $4.7 < Z/d < 6.3$  shows that the time-averaged distributions of streamwise velocity, radial vorticity, and spanwise vorticity are in good qualitative agreement. Normalized streamwise velocity distributions in Figs. 82a and 83a also show quantitative levels to be in good agreement, especially near the concave wall ( $Y/d < 0.4-0.5$ ). The same can be said for the radial vorticity distributions. Experimental results show higher local gradients of radial vorticity and higher vorticity levels occurring over larger portions of the time-averaged vortices. Experimentally determined spanwise vorticity distributions in Figs. 82d show good quantitative and qualitative correspondence to simulation distributions in Fig. 83d. Such agreement as well as radial vorticity trends provide some justification for neglecting streamwise derivatives of  $u_z$  and  $u_r$  in the experimental determination of radial and spanwise vorticity components. The agreement also validates the numerical approach employed. Simulated streamwise vorticity contours in Fig. 83b show two significant regions of negative vorticity and two significant regions of positive vorticity. The experimentally determined distributions of streamwise vorticity in Fig. 82b show a large region of positive vorticity and a large region of negative vorticity for  $Z/d$  between 4.7 and 6.3. The large regions of opposite sign near the center of the channel correspond to the principal vortices of the simulated pair, while those near  $Y/d=0$  (which are only apparent in the simulation results in Fig. 83b) are due to the shear layer near the wall. Because of the small magnitudes of secondary flow vectors in the curved channel at  $De=1.68De_C$ , the streamwise component of vorticity could not be measured experimentally to an accuracy which exceeded the experimental uncertainty of this data.

Consequently, some scatter is evident in Fig. 82b, and these results show qualitative trends which are somewhat different from the ones in Fig. 83b.

#### 4.4.2 Twisting Dean Vortices

Power spectra obtained experimentally show the addition of a much higher frequency periodic signal when the Dean number exceeds about  $3.5D_{eC}$ . This corresponds to the addition of twisting vortices to the flow, which are the other kind of wavy vortices observed numerically by Finlay *et al.* (1988) and experimentally by Ligrani and Niver (1988) and by Ligrani *et al.* (1982a). Also present for lower De within the twisting range (i.e. up to  $4.06D_{eC}$ ) are motions associated with the 7-8 Hz spectral peak shown in Fig. 81. For De higher than  $4.06D_{eC}$ , there is no evidence of the 7-8 Hz motions, and for De higher than  $5.0D_{eC}$ - $5.4D_{eC}$ , no evidence of twisting motion is apparent from experimental measurements made thus far.

Linear stability analysis of axisymmetric vortices shows that the appearance of the higher twisting frequencies is expected. The results from Finlay *et al.* (1988) show that only undulating vortices have positive linear growth rate when  $De < 1.96D_{eC}$ . Once  $De > 1.96D_{eC}$ , twisting vortices have positive growth rate. Undulating motion frequencies then have lower growth rates than twisting motion frequencies when  $De > 2.11D_{eC}$  for  $\eta = 0.975$  and  $\alpha = 2.5$ . Since the streamwise wavelength of the most unstable twisting vortices is much less than that of the most unstable undulating mode and both travel at approximately the same streamwise velocity, the frequency of the most unstable twisting mode is much higher than that of undulation.

The experimental onset of twisting at considerably higher De, near  $De=3.5D_{eC}$ , may be because fully developed Dean vortices are employed in the stability analysis, whereas in the experiment, twisting sometimes begins before the Dean vortices become fully developed. Shown in Fig. 84 are power spectra of time records of voltages from a hot-wire probe sensing velocity fluctuations (mostly in the longitudinal direction) sampled at one point in the flow at  $Y/d=0.5$  and  $Z/d=-12.25$  and a streamwise location  $112^0$

from the start of curvature. For  $De/De_C$  corresponding to 3.81, 3.93, 4.07, and 4.21, this location is within a vortex with negative vorticity levels and near an inflow region (near position 2). In this figure and in Fig. 85, non-dimensional frequencies are given as  $f=2\pi n(d/2)/U$  where  $n$  is the frequency in Hz, and values of  $U$  employed in Fig. 84 correspond to  $De/De_C=3.93$ . Referring to data in Fig. 84 at this  $De/De_C$ , the broad peak centered near  $2.5 U/(2\pi d/2)$  corresponds to the principal frequency of twisting vortices; two harmonics are seen at 4.9 and  $7.4 U/(2\pi d/2)$ . (For the experimental channel,  $U/(2\pi d/2)$  in Hz equals 0.211 $De$ .) On the high frequency side of the principal peak, flow background noise levels are about two orders of magnitude lower than the local maximum. All three peaks are considerably broader than observed in closed systems such as Taylor-Couette flow (Fenstermacher *et al.*, 1979) or Rayleigh-Bénard convection. Such behavior is caused by twisting frequencies that vary somewhat with time due to mergings and splittings of vortex pairs and the convective nature of the curved channel flow (Ligrani and Niver, 1988). As  $De/De_C$  increases from 3.81 to 4.21 in Fig. 84, principal and harmonic peaks become higher in magnitude and more apparent relative to power levels of background fluid motions.

Spectra which are qualitatively similar to the one in Fig. 84 are observed at a variety of locations in spanwise/radial planes located from 112 to 120 degrees from the start of curvature, and at a variety of  $De$  ranging from  $3.5De_C$  to  $5.0De_C$  -  $5.4De_C$ . This is illustrated by results presented in Fig. 86 which shows maximum amplitudes of principal spectral peaks associated with twisting vortices for this  $De$  range. These are given for probe positions 1-5, which are located with respect to vortex pair structure exactly as described in the previous section. Tick marks just above the abscissa in Fig. 86 show the  $De$  where spectra are available for all five probe positions 1-5. Data are also available for  $De/De_C=3.81$ , 3.93 and 4.21 but only for probe position 2 (i.e. Fig. 84 for a location 112 degrees from the start of curvature). Thus, if no data points are located above a tick mark for a particular  $De$ , measured spectra are qualitatively

different from the one presented in Fig. 84 in that clearly defined principal and harmonic peaks are not apparent. However, because amplitudes of spectral peaks from twisting may be lower than surrounding flow noise and turbulence levels, this does not necessarily preclude the existence of twisting. For some experimental conditions, twisting may not be present, and in others, it may not be fully developed as it is somewhat dependent upon the channel inlet turbulence intensity level (Ligrani and Niver, 1988).

Spectra which show some qualitative similarity to the one presented in Fig. 84 are measured at all experimental conditions indicated by data points in Fig. 86. For these data, it is apparent that the amplitudes of principal peaks from twisting are strongly dependent upon Dean number, as well as on the location within the vortex pair structure. Spectra measured near the center of the channel for  $Y/d=0.5$  (i.e. probe positions 2 and 5, inflow and outflow regions, respectively) show principal peak amplitudes with little dependence on  $De/De_C$ . However, spectra measured near the concave surface at  $Y/d=0.1$  contain principal peaks with amplitudes which are much more strongly dependent upon  $De/De_C$  with significant increases as this quantity increases which are about the same for probe position 1 (inflow regions), probe position 3 (outflow regions), and probe position 4 (beneath individual vortices). Of all five positions, twisting spectra are apparent over the largest range of  $De/De_C$  within inflow regions at  $Y/d=0.1$  (i.e. position 1). The principal frequency in the twisting portions of spectra usually lies between  $n=55$  Hz and 90 Hz (or  $f$  ranging from 1.6 to 3.3). For  $De > 5.0De_C - 5.4De_C$ , frequency peaks associated with twisting vortices are not apparent in measured spectra, even though twisting may be present at  $De$  just above  $5.0De_C - 5.4De_C$  along with some turbulence activity, as mentioned earlier.

Flow visualization sequences of photographs spaced 1/30 of a second apart are at too low a frequency (30 Hz) to observe the complete details of twisting motion. However, in spite of this, photographs taken at uncorrelated and random phases of different twisting

cycles show some characteristics of twisting motions. Such results in Fig. 70 (Ligrani and Niver, 1988) show that experimental twisting vortices rock back and forth in phase with directional changes of the inflow region in the same manner as illustrated by Finlay *et al.* (1988). However, both twisting and undulating vortices rock back and forth in phase with directional changes of the inflow region. In numerical simulations, twisting vortices are distinguished from undulating vortices by large periodic sideslipping of the undulating vortices (Finlay *et al.*, 1988), and the frequencies of oscillation of the two types of wavy motions. As mentioned earlier, this sideslipping motion does not always occur experimentally during undulations so this characteristic cannot always be used to distinguish undulation from twisting. However, the frequencies of the two different types of wavy motions can be used. As indicated in Figs. 79 and 80, the highest possible frequency of undulating vortices is an order of magnitude lower than fundamental frequencies observed experimentally for  $3.5De_C < De < 5.0De_C-5.4De_C$ . Thus, the peaks observed in experimental spectra for this range of  $De$  are not due to undulating vortices, but are instead due to twisting vortices.

The twisting vortices simulated by Finlay *et al.* (1988) at  $\eta=0.975$  and  $De=2.733De_C$  and  $De=5.466De_C$ , which have streamwise wavelength near that of the most unstable twisting mode, have fundamental frequencies of  $2.61U/(2\pi d/2)$  and  $2.69U/(2\pi d/2)$ , respectively. A power spectrum from a simulation of twisting vortices with  $\eta=0.979$ ,  $\alpha=3.0$ ,  $De=3.580De_C$ , and streamwise wavenumber  $\beta=200$  (near that of the most unstable twisting mode) is shown in Fig. 85. The fundamental frequency of  $2.33 U/(2\pi d/2)$  gives a frequency  $n$  of 64.7 Hz, which is within the range of the broad fundamental peak from experiment shown in Fig. 84. Also like the experiment, the spectrum shows a series of harmonic peaks at multiples of the fundamental frequency. However, the different peaks in Fig. 85 are more clearly distinguished than the ones in Fig. 84 because of much lower energy levels at locations away from the peaks, behavior resulting because the simulation does not capture all the

complexity present in the experimental flow. Despite different background noise levels, comparison of Figs. 84 and 85 shows that twisting frequencies from the simulation correspond closely to those observed experimentally.

We can convert the experimental frequency of twisting to an approximate streamwise wavenumber as done earlier for undulating vortices. Using the roughly constant angular speed of  $0.015 U/(d/2)$  given by Ligrani *et al.* (1992a) for twisting waves yields  $\beta=163$  for the twisting vortices of Fig. 84. From simulation results at  $De=2.733De_C$ , twisting vortices have positive linear growth rate for  $30 \leq \beta \leq 270$ . At this  $De$ ,  $\beta=180$  has largest linear growth rate. The range increases with  $De$  and so does the  $\beta$  of the most unstable mode. Thus, the streamwise wavenumbers observed experimentally are in the expected range for twisting vortices, but are at lower  $\beta$  than the mode with largest growth rate from axisymmetric vortices. The discussion in the previous section as to why the experimental wavenumbers are not the most unstable wavenumbers applies here. However, because streamwise wavenumbers associated with twisting vortices are large, the finite streamwise extent of the channel is believed to be much less significant in affecting the characteristics of twisting vortices than undulating vortices.

Results that illustrate some time-averaged flow characteristics of twisting vortices are presented in Figs. 87 and 88. These contour plots show distributions of streamwise velocity perturbation, streamwise vorticity, radial vorticity and spanwise vorticity in  $Y, Z$  planes. Results are normalized using the same procedures as employed in Figs. 82 and 83. Results in Fig. 87 are obtained experimentally for  $De=3.45De_C$ ,  $\eta=0.979$ , and  $120^0$  from the start of curvature, and results in Fig. 88 are from a simulation at  $\eta=0.979$ ,  $\alpha=3.0$ ,  $De=3.580De_C$ , and  $\beta=200$ . In the latter case, results are given for a single vortex pair. In the former case, results are given for three vortex pairs to illustrate the repeatability of results between different pairs, and to illustrate the spanwise periodicity of measured distributions of streamwise velocity, and the three

vorticity components. As for the contour plots presented earlier, heavy horizontal dashed lines in Fig. 88 show the vertical extent of the data in Fig. 87. Dashed contour lines correspond to negative values, and solid contour lines correspond to positive values.

Contour plots in Figs. 87 and 88 show reasonable qualitative and quantitative agreement. Both figures evidence radially inward flow regions that produce the large velocity deficits in the center of Fig. 88a, and at  $Z/d$  of about 5.1, 6.1 and 7.0 in Fig. 87a. Such inflow regions are located between the counter-rotating vortices which make up each vortex pair. Of the three components of vorticity, the spanwise component near the walls has the largest magnitude as result of the shear layers there. The low amplitude extremes near the convex wall in Figs. 87c, 88b and 88c are a consequence of the flow field produced the pair of counter-rotating vortices. Most large-scale features produced by the experiment and simulation correspond well, and the experimental results in Fig. 87 show comparable regularity and symmetry as the simulation results in Fig. 88. With the exception of some quantitative differences which exist near zero values, distributions of streamwise velocity, streamwise vorticity, radial vorticity, and spanwise vorticity shown in Figs. 87 and 88 show good quantitative and qualitative agreement including spatial sizes and extents of flow features. This provides additional validation of the simulation results.

Compared to the results in Fig. 82 for  $De=1.68De_C$ , the results in Fig. 87 for  $De=3.45De_C$  evidence vortex pairs with closer spanwise spacings resulting in a larger number of pairs across the span of the measurement plane. The time-averaged features of pairs during twisting are thus more compact with slightly higher spanwise wavenumbers. Compared to the undulating vortex pairs, they also contain larger velocity and vorticity gradients between the two individual vortices which make up each pair.

#### 4.4.3 Twisting and Transition

Twisting is connected to important increases of the square of the root-mean-square (RMS) of the longitudinal fluctuating velocity,  $\overline{u'^2}$ . This is apparent from surveys of the streamwise mean velocity and  $\overline{u'^2}$  which are presented in Figs. 89, 90, and 91 for a spanwise/radial plane located  $120^0$  from the start of curvature (Fuqua, 1991). In the first of these figures, dimensional  $\overline{u'^2}$  are presented as dependent upon  $De/De_C$  for three different locations within the vortex pair structure: (1) within an inflow region near the local streamwise mean velocity minima at  $Y/d=0.1$ , (2) within an inflow region at  $Y/d=0.5$  and the same  $Z/d$  as the open circled points, and (3) at the location where  $\overline{u'^2}$  is maximum. In contrast to the data presented earlier for positions 1-5 (i.e. Figs. 81 and 86) which were obtained using probes at fixed positions within the channel, these data were obtained from the survey results in Figs. 90 and 91 for the vortex pair evidenced by the velocity deficit located on the left-hand portion of each survey plot. Thus, the results correspond to specific locations within the vortex pair structure and not to fixed  $Z/d$  locations as  $De/De_C$  is changed.

Fig. 89 indicates that dimensional  $\overline{u'^2}$  magnitudes are quite low for  $De/De_C < 4.0$ . As  $De/De_C$  increases above this value up to about 5.0-5.4, twisting is clearly evidenced by spectral results (Fig. 84). For these conditions,  $\overline{u'^2}$  values increase for all three locations within the vortex pair structure, although magnitudes within the upwash region at  $Y/d=0.1$  and  $Y/d=0.5$  in Fig. 89 are significantly lower than maximum values. Here, the  $\overline{u'^2}$  increases are probably mostly due to the twisting motion itself, and partially a result of fluid which, in some cases, may be agitated by twisting. In the latter case,  $\overline{u'^2}$  are associated with the longitudinal Dean normal stress. As  $De/De_C$  then increases farther above 5.0-5.4 (where twisting is no longer evident because spectra become broad band),  $\overline{u'^2}$  increases abruptly, especially at locations where  $\overline{u'^2}$  is maximum within the vortex pair structure, which, for this range of measurement locations and  $De/De_C$ , corresponds  $Y/d=0.1$  within inflow regions. Under these

circumstances, the  $\overline{u'^2}$  variations are probably not due to twisting motions at the measurement location, but from fluid that has been agitated by twisting motions occurring upstream (Ligrani *et al.*, 1992a).

Surveys of the streamwise mean velocity normalized by the bulk velocities  $U$  are presented in Fig. 90 for  $De/De_C$  from 3.40 to 5.44. Velocity deficits are evident for each  $De/De_C$  at different locations across the span of the channel. These, of course, correspond to radial inflow regions between the two vortices which make up each vortex pair. The spanwise locations of different vortex pairs are then clearly evident in Fig. 90 along with the spanwise periodicity of corresponding velocity deficits. The time-averaged merging of two vortex pairs into one vortex pair as  $De/De_C$  increases is evident on the right-hand sides of the Fig. 90 plots. The merging is believed to appear in the time-averaged flow field because of repeated instantaneous merging at the same streamwise location (Ligrani *et al.*, 1992b). The changes in Fig. 90 may then result because this stationary position moves upstream as the Dean number increases. In Fig. 91, locally higher  $\overline{u'^2}/u_\theta^2$  magnitudes are evident at locations which correspond to inflow regions. At  $De/De_C=3.40$ ,  $\overline{u'^2}/u_\theta^2$  magnitudes are only minimally higher than for other parts of the survey. However, for  $De/De_C \geq 4.08$ , increased  $\overline{u'^2}/u_\theta^2$  magnitudes are quite apparent, especially for the inflow region associated with the velocity deficit on the left-hand sides of the plots. For  $4.35 \leq De/De_C \leq 5.17$ , the highest magnitudes of  $\overline{u'^2}/u_\theta^2$  within the left most inflow regions in Fig. 91 are measured at  $Y/d$  from 0.2 to 0.4, and not at the smallest  $Y/d$  measured, 0.1.

The regions where longitudinal velocity fluctuation levels are locally increased correspond closely to regions where twisting is most apt to be present (i.e. occurring over the widest range of  $De/De_C$  with the highest amplitudes, which is when spectra are measured at  $Y/d=0.1$  within inflow regions (probe position 1), and at  $Y/d=0.1$  beneath individual vortices (probe position 4)). The most compelling evidence that twisting is associated with increases of longitudinal fluctuating velocity (which may be associated

with longitudinal Reynolds normal stress) is that both occur at the same locations within a vortex pair structure and over nearly the same range of Dean numbers. Twisting energy levels in Figs. 84 and 86 are certainly high enough to stir up surrounding fluid and produce significant changes to fluctuating energy levels. Thus, twisting may play a significant role in the onset of turbulence (Bland and Finlay, 1991, Ligrani *et al.*, 1992a).

The regions of locally higher fluctuating velocity which exist for  $4.0 \leq De/De_C \leq 5.0$ -5.4 increase in intensity and spatial extent at higher  $De$  (Fig. 89). Eventually these regions merge together into a fully turbulent flow. Thus, the sequence of transition events (at one streamwise location as  $De$  increases) includes the development of Dean vortex pairs from curved channel Poiseuille flow, followed by wavy modes and splitting and merging. Then, the twisting wavy mode progresses into local turbulence regions and eventually higher turbulence levels occurs. These instability and transition events are thus much different from boundary layer flow, where early stages are dominated by the growth and eventual breakdown of two-dimensional Tollmien-Schlichting waves, and from plane channel flow, where transition often occurs through the growth of local three-dimensional disturbances (Ligrani *et al.*, 1992d).

#### **4.5 SPLITTING, MERGING, AND SPANWISE WAVENUMBER SELECTION OF DEAN VORTEX PAIRS**

Observations of instantaneous merging and splitting of Dean vortex pairs in the present channel have been made at  $De$  from 75 to as large as 220 and at angular positions as small as 85 degrees from the start of curvature (Ligrani and Niver, 1988). These maximum and minimum  $De$  correspond to  $De/De_C$  of 5.96 and 2.03, respectively, where  $De_C$  is the critical Dean number for an inner to outer radius ratio of 0.979 (Ligrani *et al.*, 1992a). Splitting and merging have important dynamical significance because of their alterations to spanwise vortex pair spacing, and because of the agitation which they impart to surrounding flow. These agitations influence other flow phenomena

during transition, such as undulations, and probably also result in local increases in instantaneous wall heat transfer and wall shear stress rates.

Smoke distributions during splitting and merging give good qualitative indications of vortex locations because these are associated with significant secondary flows which remain fairly coherent within individual vortex pairs as they are convected downstream (Ligrani *et al.*, 1992b). This is because there are few unsteady events *prior* to the splitting and merging observations presented which interrupt the coherence of the vortex pairs or cause the streamlines to differ from the flow streak lines. When significant unsteady events did occur upstream, they were transient which allowed the results to be video taped over time intervals with no other observable transient events (ie. merging and splitting) upstream. Thus, when the splittings and mergings occur, these are then shown by the same smoke which existed in the vortex pairs as they developed upstream. This is why this portion of this study focuses on *initial* vortex pair development, and on splitting and merging during the *initial* development of the vortex pairs upstream of experimental conditions when spanwise unsteadiness is large enough to disrupt smoke from the streak lines in individual vortex pairs. This is also why the flow visualization patterns in the present study and in other studies (Alfredsson and Persson, 1989; Matsson and Alfredsson, 1990) successfully depict these events.

In the photograph sequences which follow, photographs are separated by 1/10 second or 1/30 second intervals, where time increases as one proceeds down the page. The streamwise direction is into the plane of the paper. The convex surface is at the top of each photograph and the concave surface is at the bottom of each photograph. Scales are placed at the bottoms of each photograph sequence, with the smallest adjacent markings being 1 mm apart. The observations and photographs of visualized flow patterns which follow focus on splitting and merging of vortex pairs which occur at  $De$  of 75 and 100. Figs. 92-98 illustrate several different types of merging events. Figs. 99-102 then show two examples as to how vortex pairs may split.

#### 4.5.1 Dean Vortex Pair Merging Events.

Fig. 92 shows how a vortex pair may be engulfed by a larger adjacent vortex for  $De=100$  at a position 125 degrees from the start of curvature. This is followed by emergence of a new pair from the flow near the concave surface. Initially, in photograph number 1, about three and one-half vortex pairs are present each with a slightly different orientation. As time increases in photos 2-10, the middle vortex pair becomes smaller, and starts to tilt such that the upwash region reaches an angle of about 60 degrees from the plane of the concave wall (photos 11-14). This tilting and the motion of the smaller vortex pair towards the larger pair to its left are speculated to occur because of pressures in fluid redistributed by secondary flows. As this occurs, adjacent smoke patterns show significant spanwise expansion as well as some rocking motion from undulation. In photos 12-15, the right-hand vortex of the larger pair begins and continues to surround the entire smaller pair. In photos 16-19, the right-hand vortex of the larger pair is merging with the right-hand vortex of the smaller pair. Thus, the smaller pair is engulfed by the larger pair such that vortices (which make up one-half of each pair) with the same sign of vorticity merge together. The smaller pair is then completely undistinguishable in photos 20-24.

The type of merging event illustrated by Fig. 92 occurs because the net vorticity of each vortex pair is non-zero, and because net instantaneous vorticity magnitudes vary from one pair to another. Variations between individual vortices are so significant that they are even apparent in time-averaged results, as illustrated by Figs. 30-33. In the direct numerical simulation of a rotating channel by Yang and Kim (1991), vorticity variations between vortices often cause them to merge into quadruples due to self induction, which then leads to merging of vortex pairs and occasional cancellation of individual vortices. The initial step of merging (and splitting) processes involves instability of vortex pairs to spanwise perturbations (' and Finlay, 1991), a part of the process which may be described by linear theory. As the process continues, non-

linear effects become important. Pressures in fluid rearranged by secondary flows then cause the vortex pairs to further alter spanwise positions as they are convected downstream. Merging (or splitting) of pairs subsequently occurs, where the former is often due to the same type of vortex self induction observed in rotating channel flows. Thus, even though the photo sequence in Fig. 92 shows the timewise variation of flow patterns, the merging event is the result of a spatially evolving flow.

Z-locations of the vortex pairs of Fig. 92 are presented in Fig. 93. Spanwise locations of individual vortex pairs are determined from measurement of dark thin "mushroom stems" from left hand edges of photograph sequences using scales placed at the bottoms of each sequence. Such measurements are always made at the radial midplane of the channel ( $Y/d=0.5$ ). In Fig. 93 as well as in Fig. 92, the four pairs at  $4.4 d/(2.0 U)$  secs. (photo 1) are designated A, C, D and E from left to right. The new pair which emerges in photos 17-24 is denoted B. It begins to develop near the concave wall to the left of the large vortex pair which engulfed the smaller pair. The emergence of this new vortex pair occurs because of the merging event and subsequent spanwise wavenumber selection. This is illustrated by Figs. 92 and 93, which show that the adjustment of the spanwise spacing of vortex pairs during the engulfment of pair D by pair C is accomplished by the emergence of pair B. These two phenomena occur concurrently from 66 to 90 channel time scales and are accompanied by rapid growth of the emerging vortex pair B. Here, one channel time scale equals  $d/(2.0 U)$ . In the study of Ligrani and Niver (1988), such emerging pairs are referred to as small secondary vortex pairs. According to Guo and Finlay (1991), base vortices with secondary vortex pairs between them are much more unstable to spanwise perturbations than base vortices without secondary pairs present. Once secondary vortices reach nonlinear amplitude, the resulting flow is then even more unstable to occurrences leading to splittings and mergings. The radial growth of pair B is significant at  $0.036 \text{ m/s}$  or

about 4.3 percent of the bulk mean velocity  $U$ , as determined from measurements of pair heights in photos 20-24.

Spanwise wavenumbers between adjacent pairs are presented in Fig. 94. In this figure, the large increase of wavenumber between pairs C and D for  $(2.0 t U)/d$  from 35 to 70 results as the two pairs approach just prior to the engulfment of D. The subsequent discontinuity then results as D is engulfed by C. At about the same time, the wavenumber between A and C decreases just before pair B emerges. At  $75 d/(2.0 U)$  secs. after the start of the sequence, just after the emergence, values of  $\alpha$  between A and B, and between B and C are 3.9 and 4.9, respectively. As time increases, the values between these pairs then decrease. Thus, if certain pairs split or merge, the subsequent local readjustment of spanwise wavenumbers may change wavenumbers between other pairs along with their splitting/merging processes.

In some cases such as the one presented in Fig. 95, vortex pairs merge together in a different way. The data in this figure are for a Dean number of 100 at a streamwise position 125 degrees from the start of the curvature. In photos 1-15 of Fig. 95, three complete vortex pairs are evident with some rocking motion. Because of the frequency of the rocking motion in this particular sequence, this behavior is believed to be undulating Dean vortex flow (Ligrani *et al.*, 1992a), and it appears to be occurring concurrently with a merging event (photos 18-20). Finlay *et al.* (1988) also observe vortex pair merging and splitting when undulating motions are present. The competition between them is determined by the growth rate of the wavy instability compared to the growth rate of Eckhaus instabilities (Guo and Finlay, 1991; Eckhaus, 1965).

From left to right, the three pairs in photos 1-15 of Fig. 95 are denoted B, C, and D, respectively. The vortex pair which begins to appear on the far left-hand sides of all photos numbered 14 and upwards is denoted A. In photos 15-17, vortex pairs B and C become smaller and become reoriented such that the directions of upwash regions are oriented towards each other at angles of about 60 degrees from the concave wall. As the

upwash region of pair B becomes normal to the concave surface (Photo 18), the upwash region of vortex pair C tilts to the left. The left-hand vortex of pair C then merges into near-wall flow, and the right-hand vortex merges with the right-hand vortex of pair B (Photos 19-20). One vortex pair then replaces the two pairs in all photos after number 20. This type of event is considered to be the same type of merging as described by the results in Figs. 92, 93 and 94. In some other cases, vortex pairs merge together because of vortex cancellation. This occurs as two neighboring pairs approach each other such that adjacent vortices of opposite sign appear to collide and then cancel.

Spanwise locations of vortex pairs in Fig. 95, presented as a function of time in Fig. 96, illustrate the merging of vortex pairs B and C which occurs 0.6-0.7 secs. or 80-93 channel time scales after the start of the photo sequence. At times greater than or equal to 80-93 channel time scales, spanwise adjustment of the remaining vortex pairs is evident. In this case, vortex pairs move laterally towards the location of the merging event. Eventually, roughly the same spanwise spacing of vortex pairs is present as existed prior to the cancellation. This is evident in Fig. 95 since three complete vortex pairs exist in photos 21-28. Some spanwise expansion and shifting of smoke patterns to the right of these pairs is then evident in photos 29-37, probably because of some sort of simultaneous splitting/merging event at some other spanwise location in the channel.

Simultaneous spanwise wavenumbers between vortex pairs A, B, C and D are given as a function of time in Fig. 97. These values are determined from spanwise distances in plots such as the ones shown in Fig. 96, and represent variations at the radial midplane of the channel ( $Y/d=0.5$ ). As time becomes greater than 0.55 secs. (73.  $d/(2.0 U)$ ), the value of  $\alpha$  between pairs B and C in Fig. 97 increases drastically as a consequence of merging of two adjacent pairs just prior to the cancellation. Prior to this increase, values of  $\alpha$  between vortex pairs A and B, and between vortex pairs C and D range between 3.0 and 3.4. After the two vortices have cancelled,  $\alpha$  values between the same pairs vary between 2.2 and 3.0. The overall average (in space and time) at a particular

experimental condition is denoted  $\bar{\alpha}$ . At this experimental condition,  $\bar{\alpha}$  is 2.82-2.88 when no perturbation exists in the flow. Values of  $\alpha$  higher than this average, such as exist at times prior to  $60.0 d/(2.0 U)$  secs., are prelude to a merging event and the merging of a vortex pair across the channel span. Results later in this section will illustrate that  $\alpha$  values lower than  $\bar{\alpha}$ , such as exist at times larger than  $140.0 d/(2.0 U)$  secs., are often prelude to the splitting of a new vortex pair across the channel span even though this is not yet evident in the time sequence shown in Fig. 95.

The instantaneous flow visualization results in Figs. 92 and 95 may be compared to the time-averaged results in Figs. 30 and 39 for similar  $De$  (99.9) and streamwise location ( $\theta = 120^0$ ), but different spanwise portions of the channel. This comparison illustrates the presence of the vortex pairs in the time-averaged flow field in spite of the unsteadiness which results from merging events. In addition, because the vortex pairs are apparent within the time-averaged flow field, they have preferred spanwise locations about which the unsteadiness from merging (or splitting) must be occurring.

Results in Fig. 98 are presented for a Dean number of 75 and an angular position 135 degrees from the beginning of curvature to illustrate how a smaller vortex pair may be swept into the upwash region of a larger adjacent vortex pair. Three pairs are distinguishable in photos 1-9 which corresponds to time scales from the start of the sequence as large as 30.0. The smaller "mushroom shaped" smoke pattern previously in the middle of these photos then merges with the "stem" of the larger pattern to its left in photos 10-12. From measurements of the height of the smoke pattern corresponding to the engulfed pair, its decay rate in photos 6-11 is approximately -0.025 m/s which amounts to about 4 percent of the bulk channel velocity  $U$ . The merging event is accompanied by significant reorientation of the vortex pair on the right side of the photos, a type of motion which continues to the last photo shown.

All of the flow visualization data shown thus far illustrate the merging of two vortex pairs into one vortex pair. According to Guo and Finlay (1991), such two to one

merging is the most common merging event not only in curved channels but in rotating channels. Indeed, such behavior is evident in the flow visualizations of Alfredsson and Persson (1989) and Matsson and Alfredsson (1990) in straight rotating channels as well as in curved rotating channels, but from a plan view (streamwise/spanwise plane) not from a cross-sectional view (spanwise/radial plane). Plan views from outside of the concave surface in the present study, as well as in the study of Ligrani and Niver (1988), show results similar to theirs. Vortex pairs appear to be surrounded by tubes of smoke with non-circular cross sections that are relatively void of smoke. Mergings of vortex pairs are then indicated by adjacent tubes which occasionally merge into one tube.

Another type of event is observed in spanwise/radial plane views of visualized flow which involves the replacement of two vortex pairs by one vortex pair (Ligrani *et al.* 1992b). This type of event is different from the merging events described so far because it does not involve interactions between two vortex pairs. Instead, vortex pairs decrease in radial extent to eventually merge with flow very near the concave surface. Such collapses of vortex pairs are important because they are the most frequent mode in which two pairs are replaced by one pair, as shown by frequency results in Figs. 104 and 105, which are described later.

#### 4.5.2 Dean Vortex Pair Splitting Events

In Figs. 99-102, two different types of events are illustrated: (1) emergence of pairs from flow near the concave surface, and (2) abrupt development of two new vortex pairs from a single vortex pair. In the photograph sequences shown in Figs. 99 and 102, individual photographs are separated by 1/10 second intervals and 1/30 second intervals, respectively. All other layout details are the same as for the sequences discussed earlier.

In the photograph sequence shown in Fig. 99, the vortex pair which is only partially shown on the left sides of photos 1-8 is labelled A. The other pairs which exist across

the span (from left to right) in photos 1-4 and in most subsequent photos, are sequentially labelled B, D and F. The new pair which begins to emerge from near the concave surface in photos 6-10 is denoted C and the new pair which appears in photos 23-25 is denoted E. Spanwise spacings of these six different vortex pairs are shown as they vary with time in Fig. 100. Emergence of vortex pairs C and E are evident at  $(2.0 t U)/d$  about equal to 80 and 290, respectively. In Fig. 99, new pairs initially appear as a dark spot near the concave surface which grows in size in the radial direction to eventually appear mushroom shaped about 50  $d/(2.0 U)$  secs. later. In real time, mushroom-shaped patterns suddenly appear to "pop" out of the concave wall (Ligrani and Niver, 1988). As this occurs in Fig. 99, spanwise spacings of existing vortex pairs readjust such that these pairs move laterally away from the location of newly formed pairs. This motion is accompanied by some spanwise expansion of individual smoke patterns, as well as intermittent rocking and radial motion.

Instantaneous spanwise wavenumbers between vortex pairs B, C and D are shown in Fig. 101. Values between B and D for times less than 65  $d/(2.0 U)$  secs. from the start of the sequence are lower than 2.82-2.88, the overall average wavenumber for  $De=100$ . As the new pair emerges, instantaneous  $\alpha$  between pairs B and C, and C and D are 4.5 and 3.3, respectively. As the new pair begins to grow radially, spanwise spacings of existing vortex pairs readjust such that these pairs move laterally away from the location of the newly formed pair. Instantaneous  $\alpha$  then decrease with time to approach  $\alpha$ .

Magnitudes of  $\alpha$  prior to the emergence event at  $t=80.0 d/(2.0 U)$  provide evidence that values of the spanwise wavenumber lower than the overall average are prelude to the replacement of one vortex pair with two pairs across the channel span. After such events, the relaxation of vortex pair positions illustrated by Figs. 99-101 does not always occur. Instead, spanwise wavenumber readjustment may occur with some type of merging event. However, in either case, the intermittent flow adjustments seem to

occur so that local instantaneous wavenumbers subsequently approach the overall average wavenumber  $\bar{\alpha}$ .

Figure 102 shows how a splitting event results in the abrupt rearrangement of a single vortex pair into two vortex pairs. This time sequence begins in photo 1 with two vortex pairs along with a dark region near the concave wall to the left of the central pair. As time increases further in photos 6-8, the central pair becomes indistinguishable as two dark spots replace it to emerge as identifiable vortex pairs. In photo 9, the two newly formed pairs are evident along with the third pair to the right which is also present in photos 1-8. As time increases in the last photos of the sequence (10-14), the two newly formed vortex pairs reorient themselves such that upwash regions are directed normal to the concave surface with about equal spacing in the spanwise direction between adjacent pairs.

The most common event in which two vortex pairs replace one pair at a particular streamwise station is one where new vortex pairs emerge between existing pairs from flow very near the concave surface (Figs. 99-101). Guo and Finlay (1991) also observe similar phenomena. They describe smaller new pairs forming between existing pairs, which, in their secondary stability analysis, occurs between every second pair. The present experimental results are different from ones given by Guo and Finlay (1991) because the latter do not account for the finite span effects of the channel employed. In addition, spanwise periodicity is not imposed in experiments which allows considerable spanwise shifting, as seen in all of the flow visualization sequences presented. However, in the present results as well as those from Guo and Finlay (1991), new pairs start to appear near the concave surface in the downwash region between two existing pairs just before they grow radially inwards away from the concave surface. Such behavior appears as the division of one smoke tube into two tubes of smoke (Ligrani and Niver, 1988), or as the splitting of new bright streaks of titanium-dioxide between existing streaks, when viewed from outside of the concave

surface or from a plan view (Alfredsson and Persson, 1989; Matsson and Alfredsson, 1990).

Such events are more likely to occur at some locations instead of others because the Dean vortices develop freely without artificial disturbances. Their initial development is then triggered by small scale disturbances which occur unevenly and non-uniformly at the channel inlet. As a result, some vortex pairs begin to develop earlier and are therefore stronger as they develop to one particular streamwise location in the curved channel. The resulting variations of strengths of the different vortices and vortex pairs across the span of the channel cause some to be more likely to merge and split compared to others (cf. Yang and Kim , 1991, and Guo and Finlay, 1991).

#### **4.5.3 Recurrent Splitting and Merging**

The two types of splitting events observed include vortex pair emergence from flow near the concave surface, and splitting, which involves the abrupt development of two vortex pairs from a single pair. The four types of merging events observed include vortex pair engulfment, vortex cancellation, the sweeping of a vortex pair into the upwash of a neighboring pair, and the collapse of a vortex pair into flow near the concave surface. These are now discussed further in terms of recurrent events and frequencies of different events, which are presented in Figs. 103-105. This is followed by discussion of variations of the instantaneous spanwise wavenumber and overall average spanwise wavenumber (averaged in time and space), where variations of the latter quantity with Dean number are presented in Fig. 106.

Results in Fig. 103 show a time sequence of different types of splitting and merging events as they are observed at  $De=100$  in a spanwise/radial plane located 115 degrees from the start of curvature. The recurrent nature of splitting and merging phenomena is apparent. Close examination reveals that splitting type events generally follow merging type events, and visa versa, as described earlier. Such variations are important because they result in adjustments and readjustments of the spanwise

wavenumber with time. Evidence of such recurrent phenomena were first presented by Ligrani and Niver (1988) for curved channel flows. More recent studies indicate that such phenomena also occur in rotating channels (Alfredsson and Persson, 1989) as well as in curved channels which rotate (Matsson and Alfredsson, 1990). Recurrent phenomena are also discussed by Guo and Finlay (1991), who indicate that they are most apt to occur for  $1.7De_c < De < 2.2De_c$ .

Information on the frequencies of splitting and merging events is presented in Figs. 104 and 105. These data were obtained from measurements in video sequences photographed in 5.5 cm by 1.27 cm spanwise/radial planes located at different streamwise locations (Kendall, 1991). On these plots, non-dimensional frequencies  $f=2\pi n(d/2)/U$  are given, where  $n$  is the dimensional event frequency in Hz.

Results in Fig. 104 for different  $De$  for a spanwise/radial plane located 95 degrees from the start of curvature indicate that emergences are the most frequent type of splitting event, whereas collapses are the most frequent type of merging event. Non-dimensional frequencies decrease for Dean numbers less than 60 to 80 since frequencies are recorded only for identifiable vortex pairs, and not for less developed smoke patterns like the ones (Ligrani et al., 1992b). At higher  $De$ , strong dependence on Dean number is evident. In addition, overall frequency magnitudes of all splitting and merging events are about equal for each Dean number which indicates a balance between these two types of phenomena. Such behavior also provides additional evidence that vortex pairs have preferred spanwise locations and preferred spanwise wavenumbers across the span of the channel. The non-dimensional splitting and merging frequencies increase with Dean number for values up to around 125. At the Dean numbers increases further, decreases of these quantities with Dean number are evident.

Fig. 105 presents non-dimensional splitting and merging event frequencies at different streamwise stations for  $De=100$ . Higher values are generally evident at locations farther upstream. As for the results in Fig. 104, the most frequent splitting

events are emergences, and the most frequent merging events are collapses. In addition, a balance of overall splitting and merging events is evident.

The experimental results described so far indicate that local spanwise wavenumber values higher than the overall average are prelude to the merging of a vortex pair across the channel span, and that values lower than the overall average are prelude to the splitting of a new vortex pair across the channel span. After either an splitting event or a merging event, readjustment of the spanwise positions of vortex pairs may occur as a result of: (1) splitting of pairs, (2) merging of pairs, or (3) spanwise motions of pairs. Except when spanwise shifting of vortex pairs occurs afterwards, the occurrence of one particular type of event (splitting or merging) generally precludes the reoccurrence of the same type of event just afterwards to achieve readjustment. This is because of the alterations to the spanwise wavenumber which occur immediately following such events. With splittings,  $\bar{\alpha}$  is generally increased above the overall average so that additional splittings are unlikely, whereas with mergings, the spanwise wavenumber is generally decreased below the overall average which makes the occurrence of additional mergings unlikely. In either case, the subsequent flow adjustments seem to occur so that local and spanwise-averaged wavenumbers eventually approach  $\bar{\alpha}$  for a particular Dean number. This is discussed in more detail in reference to Fig. 106.

#### 4.5.4 Spanwise Wavenumber Selection of Dean Vortex Pairs

Figure 106 shows variations of  $\bar{\alpha}$ , the spanwise wavenumber averaged in time and space, as dependent upon  $De$ . In this figure, several different sets of experimental, numeric and analytic results are included. For the experimental results, values of  $\bar{\alpha}$  are given as determined from flow visualization results, from time-averaged vorticity distributions (Baun, 1988; Fields, 1990), as well as from the experimental study of Kelleher *et al.* (1980). These distributions are compared to the curve for maximum linear growth rate of the primary instability from Finlay *et al.* (1987, 1988), and to

the Eckhaus valley from Guo and Finlay (1991). The primary stability boundary of Finlay *et al.* (1987, 1988) is also included for reference.

Before these results are described and comparisons are made, determination of  $\bar{\alpha}$  values from time-averaged vorticity distributions is explained. The radial component of vorticity measured at a Dean number of 100 at a location 120 degrees from the start of curvature in Fig. 49 is employed for this purpose. Radial vorticity distributions in Fig. 49 show spanwise alternating regions of positive and negative vorticity. Pairs of vorticities are evidenced by a region of positive vorticity (solid contour lines) immediately adjacent to a region of negative vorticity (dashed contour lines). Three complete pairs are evident in the figure. Because these data were obtained at a different spanwise portion of the channel than where the flow visualization results were observed, a direct comparison between the two is precluded. Upwash regions between the two vorticities in a pair are located where gradients of radial vorticity are quite large and an abrupt change in the sign of this vorticity component occurs as one moves in the spanwise direction at constant  $Y/d$ . In Fig. 49, central portions of upwash regions are thus located at  $Z/d$  of about 5.1, 6.0 and 7.1. With this information, spanwise wavenumber values are determined between individual vortex pairs for a particular Dean number and channel location. These values are then averaged across the span in order to determine  $\bar{\alpha}$ .

We now return to our discussion of the results in Fig. 106. Here,  $\bar{\alpha}$  values from the flow visualization results and from vorticity distributions (ie. from Fig. 49 and from Baun (1988) and Fields (1990)) generally show remarkable consistency for the range of (De-Dec)/Dec shown. The Kelleher *et al.* (1980)  $\bar{\alpha}$  data are in the same general vicinity but show no variation as the Dean number varies. Such  $\bar{\alpha}$  variations from channel flows are dependent upon aspect ratio, and do not appear to be strongly dependent upon inlet flow conditions. In contrast, vortex development is much more strongly dependent upon inlet flow conditions in boundary layers developing over concave

surfaces (Floryan and Saric, 1984). There, magnitudes of  $\bar{\alpha}$  vary significantly as flow conditions change and do not follow a single curve (as the Görtler number varies) in the fashion of the present results in Fig. 106.

The Eckhaus valley is given by Guo and Finlay (1991) from an analysis of instabilities occurring with respect to spanwise perturbations which lead to the merging and splitting of Dean vortex pairs. The growth of these perturbations is denoted the Eckhaus growth rate (Guo and Finlay, 1991), which is the real part of the eigenvalue which determines the stability of the vortex flow. According to Guo and Finlay (1991), splittings of secondary vortex pairs observed by Ligrani and Niver (1988) are probably initiated by Eckhaus instabilities. In addition, the Eckhaus growth rate is positive for all experimental conditions examined in the present paper since they are outside of the Eckhaus stability boundary. The Eckhaus valley shown in Fig. 106 is then where the growth rate is the minimum in the unstable part of the  $(De-Dec)/Dec$  versus  $\bar{\alpha}$  plane. This curve indicates where vortex pairs are most likely to be observed in experiments since these are the ones which are least apt to split or merge. Such pairs may then be in place for longer time intervals than surrounding pairs partially because their splitting or merging is suppressed by splittings or mergings at some other  $\alpha$  where the value of the Eckhaus growth rate is greater than the minimum. Thus, for values of  $\alpha$  close to the Eckhaus valley, a relatively small number of vortices split and merge for a given number of base vortices. Further away, Eckhaus growth rates are higher and a large number of vortices split and merge.

Most experimental data in Fig. 106 are in close agreement with the Eckhaus valley for all  $(De-Dec)/Dec$  greater than 1.3 shown. This provides some evidence that  $\bar{\alpha}$  values over these conditions are influenced by splitting and merging phenomena. The differences between these data and the Eckhaus valley may suggest that the Eckhaus instability does not completely dominate flow behavior for all  $(De-Dec)/Dec$  greater

than 1.3. Instead, time and spatially averaged positions of the vortex pairs are probably also influenced, at least in part, by phenomena not leading to splitting and merging.

When no spanwise selection mechanism is imposed on the flow, the overall average of the spanwise wavenumber is determined by the maximum linear growth rate of the primary instability (Guo and Finlay, 1991). That is, the vortices themselves, rather than their responses to perturbations from different spanwise wavenumbers determine the spanwise spacing of adjacent vortex pairs. This is consistent with Fig. 106 for  $(De - De_c)/De_c$  less than about 1.2 where most of the present experimental results lie near the maximum growth rate curve.

*Instantaneous* values of the spanwise wavenumber may deviate significantly away from the  $(De - De_c)/De_c$  versus  $\bar{\alpha}$  curve shown in Fig. 106. When values of  $\alpha$  lie to the right of the  $\bar{\alpha}$  curve for a particular  $De$ , a merging event is likely to follow. Similarly,  $\alpha$  values to the left of the  $\bar{\alpha}$  curve are often subsequent to an splitting event. The observations of Guo and Finlay are similar, except they also refer to  $\alpha$  behavior on right and left sides of the closed Eckhaus stability boundary which extends only to  $(De - De_c)/De_c$  as high as 0.3. For  $De=75, 100$  and  $125$ , instantaneous values of the spanwise wavenumber from the present study are observed to be as low as 1.6, and as high as 6.2. Although the smallest values observed are quite far away from the primary stability boundary in Fig. 106, the largest values observed are certainly in close proximity to the right-hand side of this boundary. After  $\alpha$  deviates significantly from  $\bar{\alpha}$ , the trend is then to return to the  $(De - De_c)/De_c$  versus  $\bar{\alpha}$  curve either by an splitting event, merging event, or spanwise adjustment of pair spacings. Either mergings or splittings can cause an overshoot which then results in the likelihood of the occurrence of the opposite event, and then recurrent phenomena. Such perturbations occur with respect to the time-averaged flow field, and thus, with respect to time-averaged spanwise vortex positions and spanwise wavenumbers (averaged in space and time), as mentioned earlier.

#### **4.5.5 Longitudinal Velocity Fluctuations Associated With Splitting and Merging**

Surveys of time-averaged longitudinal velocity fluctuations measured in the spanwise/radial plane located at  $\theta = 120^0$  are given in Fig. 107 for experimental conditions when splitting and merging are present ( $De=50.2-125.4$ ). In this figure, the quantity of interest is  $\overline{u'^2}/u_\theta^2$ , the square of the root-mean-square (RMS) of longitudinal velocity fluctuations normalized by the local streamwise velocity. The spanwise locations of upwash regions are denoted by small arrows for each survey plot in Fig. 107. Locally higher fluctuation magnitudes are evident at locations which correspond to upwash locations between individual vortex pairs. Even though these magnitudes are only minimally higher than for other parts of the surveys, interesting and repeatable structural characteristics are apparent. At  $De$  of 60.2 and 70.2, individual regions of increased  $\overline{u'^2}/u_\theta^2$  show singular local maxima near the spanwise middle of each upwash region. However, at  $De$  from 80.3 to 125.4, individual regions of increased  $\overline{u'^2}/u_\theta^2$  show two local maxima on each side of upwash regions at locations where spanwise gradients of the streamwise mean velocity are highest (Fuqua, 1991). Values of  $\overline{u'^2}/u_\theta^2$  at the same streamwise location are much higher as Dean numbers increase above 150 and Dean vortex pairs are twisting (Ligrani *et al.*, 1992a).

Even though spectra of hot wire signals corresponding to the locations and experimental conditions of the data in Fig. 107 occasionally show locally higher humps (broad, small amplitude local maxima) at frequencies of 0.5-2 Hz, 4-7 Hz, 7-9 Hz, 12-15 Hz, and 17-21 Hz, there is no evidence at present to suggest that the time-averaged velocity fluctuations in Fig. 107 are associated with one particular frequency of fluid motions. Examples of spectra are shown in Fig. 108 along with corresponding time traces in Fig. 109. These data were measured using a hot-wire probe sensing longitudinal velocity fluctuations placed at  $\theta = 112^0$ ,  $Y/d=0.5$  and  $Z/d=12.25$ , and for each  $De$ , are qualitatively typical of spectra measured at other  $Y/d$  and  $Z/d$  and similar

θ . The oscillations at 0.5-2 Hz evidenced in Figs. 108 and 109 are believed to be due to undulating vortex motions (Ligrani *et al.*, 1992a). Spectral variations at other frequencies may also be partially related to undulating vortex motions, as well as to splitting and merging, and to the fact that channel inlet conditions are not precisely constant with time. Fig. 107 shows that most of this unsteadiness occurs about vortex pair upwash regions, providing additional evidence that the vortex pairs have preferred locations across the channel span.

Results from Fig. 104 indicate that the overall average dimensional frequency of splitting and merging events together increases with Dean number. Values for De of 75, 100, and 145 are 2.1 Hz, 4.4 Hz, and 5.8 Hz, respectively. Figure 108 shows low-amplitude spectral humps near 2.1 Hz for De=50.4 and near 4.4 Hz for De=100.2, however, there is no evidence, at present, which suggests that fluid agitations from splitting and merging occur at one particular frequency or wavenumber for a given location and De. This is because splitting and merging seem to occur somewhat randomly about the time-averaged vortex pair locations. In addition, the time trace in Fig. 103 provides evidence that splitting and merging frequencies are not stable with time, but varying continuously, which would make them unapparent in ensemble-averaged spectra.

## 5.0 SUMMARY AND CONCLUSIONS

The development and structural characteristics of Dean vortices in a curved channel were measured and evaluated. The channel has a 40 to 1 aspect ratio, a radius ratio of 0.979, and mild curvature. Results were obtained at Dean numbers ranging from 35 to 430, and at angular positions from the start of curvature ranging from 85 degrees to 145 degrees. Of particular interest are the sequence of events as transition proceeds from laminar flow to fully turbulent flow, and the roles and effects played by Dean vortex pairs during these events.

For positions from the start of curvature ranging from 85 to 145 degrees, the sequence of transition events begins with curved channel Poiseuille flow at Dean numbers less than 40 to 64. As the Dean number increases, observations show initial development of Dean vortex pairs, followed by symmetric vortex pairs which, when viewed in spanwise/radial planes, cover the entire channel height ( $De=90-100$ ). At Dean numbers from 40 to 125-130, the vortex pairs often develop intermittent waviness in the form of vortex undulations. Splitting and merging of vortex pairs is also observed over the same experimental conditions as well as at higher Dean numbers. When Dean numbers range from 130 to 185-200, the undulating wavy mode is replaced by a twisting mode with higher amplitudes of oscillation and shorter wavelengths. The twisting wavy mode results in the development of regions where turbulence intensity is locally augmented at Dean numbers from 150 to 185-200, principally in the upwash regions between the two individual vortices which make up each vortex pair. These turbulent regions eventually increase in intensity and spatial extent as the Dean number increases further, until individual regions merge together so that the entire cross section of the channel contains chaotic turbulent motions. When Dean numbers then reach 400-435, spectra of velocity fluctuations then evidence fully turbulent flow.

Time-averaged measurement surveys of the three components of mean vorticity, streamwise mean velocity, and total pressure in a spanwise/radial plane located 120

degrees from the start of curvature show that spanwise non-periodic disturbances develop near the concave surface of the channel at Dean numbers in the vicinity of 61.9. At  $De$  greater than or equal to 73.6, evidence of pairs of Dean vortices are apparent in these surveys which, in many cases, are fairly periodic across the span of the channel. These results confirm that Dean vortex pairs not only have preferred spanwise spacing, but also preferred spanwise locations since they are readily apparent in the time-averaged flow field. Streamwise vorticity distributions clearly show spanwise varying regions of positive and negative vorticity which correspond to different vortex pairs. Upwash regions (with respect to the concave surface) are present between the two vortices in each pair where fluid with low streamwise velocity (and low total pressure) is moved away from the concave wall by local secondary flows. In the radial vorticity distributions, these upwash regions are located where gradients of radial vorticity are quite large and an abrupt change in the sign of this vorticity component occurs as one moves in the spanwise direction at constant radial distance. In distributions of the spanwise component of vorticity, upwash regions are evidenced by local regions of negative vorticity emanating from the concave surface. Levels of maximum vorticity and circulation magnitudes of the streamwise vortices increase as the Dean number increases, until Dean numbers reach 150-240. Because the length scales of the spanwise unsteadiness at Dean numbers higher than 240 are greater than spanwise vortex spacings, time-averaged distributions are then spanwise uniform with gradients apparent only in the radial direction.

At experimental conditions where the Dean vortices first begin to develop for Dean numbers greater than 64 and angular positions at least 85 degrees from the start of curvature, observations and photographs of visualized flow patterns in spanwise/radial planes show evidence of pairs of counter-rotating Dean vortices indicated by mushroom-shaped smoke patterns. At Dean numbers and angular positions near these values, radial oscillations of smoke patterns are believed to result because of unsteadiness and

nonuniform spanwise positions of the infinitesimal amplitude disturbances which trigger initial vortex development. When vortex pairs are present at these low Dean numbers, radial heights vary considerably across the span of the channel. As the Dean number increases to values in the vicinity of 90-100, the sizes of smoke patterns which evidence pairs increase, radial extents become more uniform across the span, and the heights approach the full channel width. The radial unsteadiness is then much smaller, and the size, spacing, and behavior of the Dean vortex pairs appears to be much less sensitive to the presence and magnitude of initial disturbance levels. Most unsteadiness at  $De$  from 90 to 100 seems to be due to splitting and merging, which, as mentioned earlier, are also observed at higher and lower Dean numbers as well.

Detailed observations of splitting and merging have been made in spanwise/radial planes at angular positions from 95 degrees to 135 degrees from the start of curvature at Dean numbers of 75 and 100. Visualizations at these experimental conditions show two distinctly different types of splitting events: (1) vortex pair emergence from flow near the concave surface, and (2) splitting which results in the abrupt development of two vortex pairs from a single pair. In addition, four different types of merging events are observed. These include: (1) engulfment of a smaller vortex pair by a larger pair such that vortices having the same sign of vorticity merge together, (2) cancellation of adjacent vortices having opposite signs of vorticity in two adjacent pairs, (3) the sweeping of a vortex pair into the upwash of a neighboring pair, and (4) the collapse of a vortex pair into the flow near the concave surface. Of these, vortex pair emergence and collapse are most often observed. According to Ligrani and Niver (1988), similar behavior are observed at  $De$  as large as 220 and at angular positions as small as 85 degrees from the start of curvature.

Splitting and merging events observed in spanwise/radial planes are a consequence of phenomena occurring during the streamwise development of vortex pairs. As this occurs, splitting and merging agitate nearby flow. Undulating motions, in particular,

are disrupted and more intermittent because of splitting and merging (Ligrani *et al.*, 1992a). However, in spite of such disruptions, there is no evidence at present to suggest that such agitations occur continuously in the unsteady part of the flow at one particular frequency or wavenumber. This is apparent from spectra during splitting and merging, which mostly appear to be broad-band with several low-amplitude local maxima and no local sharp peaks. Thus, splitting and merging do not contribute disruptions at one particular wave number during transition, even though their overall effects are speculated to cause twisting to occur at lower Dean numbers than if no splitting and merging were present.

Overall average spanwise wavenumbers (in space and time)  $\bar{\alpha}$  are close to the Eckhaus valley (Guo and Finlay, 1991) for all  $(De-De_C)/De_C$  greater than 1.3. This suggests that splittings and mergings of Dean vortex pairs result because of Eckhaus instabilities to perturbations from different spanwise wavenumbers. Differences from the Eckhaus valley over this  $(De-De_C)/De_C$  range, and for  $(De-De_C)/De_C < 1.2$  suggest that positions of the vortex pairs (averaged in space and time) are probably also influenced by phenomena other than ones leading to splitting and merging (Ligrani *et al.*, 1992b). The present wavenumber results lie near the  $\bar{\alpha}$  curve which represents the maximum linear growth rate of the primary instability (Finlay *et al.*, 1988) when  $(De-De_C)/De_C$  is less than about 1.2, which suggests that the spanwise spacing of adjacent vortex pairs is determined mostly by the vortices themselves rather than their responses to perturbations from different spanwise wavenumbers (Ligrani *et al.*, 1992b).

The present results also indicate that instantaneous local spanwise wavenumber values higher than  $\bar{\alpha}$  are prelude to the merging of a vortex pair across the channel span, and that values lower than  $\bar{\alpha}$  are prelude to the splitting of a new vortex pair across the channel span. After either an splitting event or a merging event, the reoccurrence of the same type of event just afterwards is unlikely because of the

alterations to the spanwise wavenumber which occur immediately following such events. With splittings, local wavenumbers are generally increased above the overall average so that additional splittings are unlikely, whereas with mergings, the spanwise wavenumber is generally decreased below the overall average which makes the occurrence of additional mergings unlikely. In either case, subsequent flow adjustments seem to occur as a result of the opposite event, or spanwise shifting of pairs, so that local and spanwise-averaged wavenumbers eventually approach the  $\bar{\alpha}$  value for a particular Dean number. Such spanwise wavenumber variations and the overall balance of the frequencies of different splitting and merging events provide evidence that vortex pairs have preferred spanwise spacings across the span of the channel in spite of the unsteadiness from splitting and merging.

When viewed in spanwise/radial planes, visualizations of undulating and twisting vortex flows show vortex pairs with rocking motion and changes in the direction of the flow between vortices that are like those observed in the simulations. The spanwise sideslipping observed in numerical simulations of undulating vortices is present experimentally, but it is interrupted sometimes because of the convective nature of curved channel flow, as well as by vortex pair merging and splitting events at other locations across the span of the channel. Experimental frequencies of twisting vortices agree with values predicted by simulations, as well as with values from linear stability analysis of axisymmetric vortices given by Finlay *et al.* (1988). The numerical and experimental results also agree in that both indicate that undulating vortices have much lower frequencies than twisting vortices though the most unstable undulation frequencies from the linear stability analysis are somewhat higher than ones observed in the experiment (Ligrani *et al.*, 1992a).

Undulating streamwise wavenumbers estimated from frequencies by using constant angular speeds of wave motion indicate there are only a few streamwise wavelengths present in the 180° curved experimental section. Because of this, finite streamwise

length effects in the experimental channel are believed to be important if the accuracy of quantitative predictions of this flow are to be improved. Undulating Dean vortex flow is observed in the experimental curved channel mostly at streamwise positions some distance away from the point where curvature begins. Spectra obtained when undulations are present occasionally show locally higher humps (broad, small amplitude maxima) at frequencies of 0.5-2 Hz, 4-7 Hz, 7-9 Hz, 10-12 Hz, 12-15 Hz, and 17-21 Hz. The oscillations at 0.5-2 Hz correspond to the highest energy levels in the frequency plots, and are believed to be due to undulating motions. At  $De=105$  and a position 120 degrees from the start of curvature, evidence of undulating motions are present throughout the spanwise/radial measurement plane from  $Y/d=0.1$  to  $Y/d=0.5$ . Measured distributions of mean velocity and vorticity components at  $De=65$  illustrate the structural characteristics of the time-averaged flow field when undulation is present. Good agreement generally exists between experiment and simulation (Ligrani *et al.*, 1992a).

Experimental power spectra show that twisting vortices are associated with higher frequencies and shorter streamwise wavelengths compared to undulations. Fundamental and harmonic frequencies from experimental spectra during twisting are in good agreement with simulated values. Experimental spectra which evidence twisting over the largest  $De$  range are measured within inflow regions at  $Y/d=0.1$  and near individual vortices at  $Y/d=0.1$ . Fundamental amplitudes in these spectra are strongly dependent upon  $De$  as well as on the location within the vortex pair structure. Contour plots in a spanwise/radial plane of time-averaged vorticity and streamwise velocity evidence pairs of counter-rotating vortices on either side of upwash regions (with respect to the concave wall) which produce velocity deficits emanating from the concave surface. Distributions of streamwise velocity, streamwise vorticity, radial vorticity, and spanwise vorticity are in good quantitative and qualitative agreement with simulation results (Ligrani *et al.*, 1992a), including spatial sizes and extents of flow features.

Twisting is connected to local increases of the fluctuating longitudinal velocity (and probably also the longitudinal Reynolds stress), which, like twisting, are initially present near the concave surface within flow regions. When twisting is present for  $130 < De < 185-200$ , fluctuating longitudinal velocity magnitudes are significantly higher than for lower De values. When De increases above 185-200, additional longitudinal velocity fluctuation level increases are present at different spanwise/normal plane locations within the channel perhaps as a result of fluid having undergone breakdown after upstream twisting. At Dean numbers from 185 to 200, the spectral peaks which characterize twisting decrease in amplitude relative to surrounding energy levels. At higher Dean numbers, spectra are broad-band without spectral peaks or local maxima, and flow visualization observations show complex chaotic motions with large-scale oscillations in spanwise and radial directions. When Dean numbers reach 400-435, spectra then evidence fully turbulent flow.

To measure distributions of time-averaged velocity components, the present study also included the development of a miniature five-hole pressure probe. This probe was designed with a 1.22 mm tip diameter specifically for use in the curved channel where spatial resolution and blockage considerations are very important (Ligrani, Singer and Baun, 1989b). The device was calibrated in a separate wind tunnel at Reynolds numbers based on probe tip diameter ranging from 80 to 400. Spatial resolution and induced downwash velocity correction schemes were developed to correct results obtained from the curved channel (Ligrani, Singer and Baun, 1989a). After application of these corrections, pressure measurements from the probe were used to determine the three mean velocity components. From these, the three components of mean vorticity were also determined (Ligrani, Singer and Baun, 1989b).

## REFERENCES

Alfredsson P. H. and Persson H., "Instabilities in Channel Flow with System Rotation," Journal of Fluid Mechanics, Vol. 202, pp. 543-557, 1989.

Baun L. R., "The Development and Structural Characteristics of Dean Vortices in a Curved Rectangular Channel," M. E. Thesis, Department of Mechanical Engineering, Naval Postgraduate School, Monterey, 1988.

Berger S. A., Talbot L., and Yao L. S., "Flow in Curved Pipes," Annual Review of Fluid Mechanics, Vol. 15, pp. 461-512, 1983.

Bipps H., "Experimental Study of the Laminar-Turbulent Transition of a Concave Wall in a Parallel Flow," NASA TM 75243, 1978.

Bland S. B. and Finlay W. H., "Transitions Toward Turbulence in a Curved Channel," Physics of Fluids A, Vol. 3, pp. 106-114, 1991.

Bottaro A., Matsson O. J. E., and Alfredsson P. H., "Numerical and Experimental Results for Developing Curved Channel Flow," Physics of Fluids A, Vol. 3, No. 5, pp. 1473-1476, 1991.

Brewster D. B., Grosberg P., and Nissan A. H., "The Stability of Viscous Flow Between Horizontal Concentric Cylinders," Proceedings of the Royal Society of London. Series A, Vol. 251, pp. 76-91, 1959.

Brigham E. O., The Fast-Fourier Transform, Prentice-Hall Co., New York, 1974.

Dean W. R., "Fluid Motion in a Curved Channel," Proceedings of the Royal Society of London. Series A, Vol. 121, pp. 402-420, 1928.

Eckhaus W., Studies in Nonlinear Stability Theory, Springer, New York, 1965.

Fenstermacher P. R., Swinney H. L., and Gollub J. P., "Dynamical Instabilities and the Transition to Chaotic Taylor Vortex Flow," Journal of Fluid Mechanics, Vol. 94, pp. 103-128, 1979.

Fields W. E., "Study of the Effects of Centrifugal Instabilities on Transition from Laminar to Turbulent Flow in Curved Channels for Dean Numbers from 160 to Fully Turbulent Conditions," M. E. Thesis, Naval Postgraduate School, Monterey, 1990.

Finlay W. H., "Perturbation Expansion and Weakly Nonlinear Analysis for Two-Dimensional Vortices in Curved or Rotating Channels," Physics of Fluids A, Vol. 1, No. 5, pp. 854-860, 1989.

Finlay, W. H., "Transition to Oscillatory Motion in Rotating Channel Flow," Journal of Fluid Mechanics, Vol. 215, pp. 209-227, 1990.

Finlay W. H., Keller J. B., and Ferziger J. H., "Instability and Transition in Curved Channel Flow," Report TF-30, Dept. of Mech. Eng., Stanford University, Stanford, 1987.

Finlay W. H., Keller J. B., and Ferziger J. H., "Instability and Transition in Curved Channel Flow," Journal of Fluid Mechanics, Vol. 194, pp. 417-456, 1988.

Finlay W. H., and Nandakumar K., "Onset of Two-Dimensional Cellular Flow in Finite Curved Channels of Large Aspect Ratio," Physics of Fluids A, Vol. 2, No. 7, pp. 1163-1174, 1990.

Floryan J. M., and Saric W. S., "Wavelength Selection and Growth of Gortler Vortices," AIAA Journal, Vol. 22, No. 11, pp. 1529-1538, 1984.

Fuqua S. J., "Study of the Transition to Turbulence Within a Curved Rectangular Channel With 40 to 1 Aspect Ratio," M. S. Thesis, Naval Postgraduate School, Monterey, 1991.

Green J. G., "Turbulence Structure Resulting From Interaction Between an Embedded Vortex and Wall Jet," M. S. Thesis, Naval Postgraduate School, Monterey, 1989.

Guo Y., and Finlay W. H., "Splitting, Merging and Wavelength Selection of Vortices in Curved and/or Rotating Channel Flow Due to Eckhaus Instability," Journal of Fluid Mechanics, Vol. 228, pp. 661-691, 1991.

Hammerlin G., "Die Stabilitat der Stromung in Einem Gekrummten Kanal," Archive for Rational Mechanics and Analysis, Vol. 1, pp. 212-224, 1958.

Han L. S., "Hydrodynamic Entrance Lengths for Incompressible Laminar Flow in Rectangular Ducts," Journal of Applied Mechanics, Vol. 27, pp. 403-410, 1960.

Hille P., Vehrenkamp R., and Schulz-Dubois E. O., "The Development and Structure of Primary and Secondary Flow in a Curved Square Duct," Journal of Fluid Mechanics, Vol. 151, pp. 219-241, 1985.

Kelleher M. D., Flentie D. L., and McKee R. J., "An Experimental Study of the Secondary Flow in a Curved Rectangular Channel," ASME Transactions-Journal of Fluids Engineering, Vol. 102, 92-96, 1980.

Kendall M. R., "Effects of Centrifugal Instabilities on Laminar/Turbulent Transition in Curved Channels With 40 to 1 Aspect Ratios," M. E. Thesis, Naval Postgraduate School, Monterey, 1991.

Komiyama Y., Mikami F., Okui K., and Hori T., "Laminar Forced Convection Heat Transfer in Curved Channels of Rectangular Cross Section," Heat Transfer Japanese Research, Vol. 13, No. 3, pp. 68-91, 1984.

Lighthill M. J., "Contribution to the Theory of the Pitot-Tube Displacement Effect," Journal of Fluid Mechanics, Vol. 2, pp. 493-512, 1957.

Ligrani P. M., and Bradshaw P., "Subminiature Hot-Wire Sensors: Development and Use," Journal of Physics E-Scientific Instruments, Vol. 20, No. 3, pp. 323-332, 1987a.

Ligrani P. M., and Bradshaw P., "Spatial Resolution and Measurement of Small-Scale Turbulence in the Viscous Sublayer Using Subminiature Hot-Wire Probes," Experiments in Fluids, Vol. 5, No. 6, pp. 407-417, 1987b.

Ligrani P. M., Fields W. A., and Baun L. R., "Time-Averaged Features of Dean Vortex Pairs," Department of Mechanical Engineering, Naval Postgraduate School, Monterey, 1992c.

Ligrani P. M., Finlay W. H., Fields W. A., Fuqua S. J. and Subramanian C. S., "Features of Wavy Vortices in a Curved Channel from Experimental and Numerical Studies," Physics of Fluids A, Vol. 4, No. 4, pp. 695-709, 1992a.

Ligrani P. M., Longest J. E., Kendall M. R., and Fields W. A., "Splitting, Merging, and Spanwise Wavenumber Selection of Dean Vortex Pairs During Their Initial Development in a Curved Rectangular Channel," submitted to Physics of Fluids A, 1992b.

Ligrani P. M., and Niver R. D., "Flow Visualization of Dean Vortices in a Curved Channel with 40 to 1 Aspect Ratio," Physics of Fluids, Vol. 31, No. 12, pp. 3605-3617, 1988.

Ligrani P. M., Singer B. A., and Baun L. R., "Spatial Resolution and Downwash Velocity Corrections for Multiple-Hole Pressure Probes in Complex Flows," Experiments in Fluids, Vol. 7, No. 6, pp. 424-426, 1989a.

Ligrani P. M., Singer B. A., and Baun L. R., "Miniature Five-Hole Pressure Probe for Measurement of Three Mean Velocity Components in Low Speed Flow," Journal of Physics E-Scientific Instruments, Vol. 22, No. 10, pp. 868-876, 1989b.

Ligrani P. M., Subramanian C. S., Coumes T. M., Greco F. J., Koth H., and Longest J. M., "Study of the Imposition of Bulk Flow Pulsations on Plane Channel Flow at Moderate Stokes Numbers," Experimental Thermal and Fluid Science, Vol. 5, pp. 145-161, 1992d.

Ligrani P. M., Westphal R. V., and Lemos F. R., "Fabrication and Testing of Subminiature Multi-Sensor Hot-Wire Probes," Journal of Physics E-Scientific Instruments, Vol. 22, No. 4, pp. 262-268, 1989c.

Livesey J. L., "The Behavior of Transverse Cylindrical and Forward Facing Total Pressure Probes in Transverse Total Pressure Gradients," Journal of Aeronautical Science, Vol. 23, pp. 949-955, 1956.

Longest J. M., "Flow Visualization Studies in (1) a Curved Rectangular Channel with 40 to 1 Aspect Ratio and (2) a Straight Channel with Bulk Flow Unsteadiness," M.S. Thesis, Department of Mechanical Engineering, Naval Postgraduate School, Monterey, 1989.

Matsson, O. J. E., and Alfredsson, P. H., Curvature- and Rotation-Induced Instabilities in Channel Flow, Journal of Fluid Mechanics, Vol. 210, pp. 537-563, 1990.

Mehta R. D., and Bradshaw P., "Design Rules for Small Low Speed Wind Tunnels," Aeronautical Journal of the Royal Aeronautical Society, Vol. 83, pp. 443-449, 1979.

Musuda S., and Matsubara M., "Visual Study of Boundary Layer Transition on Rotating Flat Plate," IUTAM Symposium on Laminar-Turbulent Transition, Springer, New York, 1989.

Nakayabayashi K., "Transition of Taylor-Gortler Vortex Flow in Spherical Couette Flow," Journal of Fluid Mechanics, Vol. 132, pp. 209-230, 1983.

Niver R. D., "Structural Characteristics of Dean Vortices in a Curved Channel," M. S. Thesis, Naval Postgraduate School, Monterey, 1987.

Peerhossaini H., and Wesfreid J. E. (editors), Euromech 261: Colloquium on Gortler Vortex Flows, ISITEM, Nantes, France 1990.

Perry A. E., Hot-Wire Anemometry, Clarendon Press, Oxford, 1982.

Reid W. H., "On the Stability of Viscous Flow in a Curved Channel," Proceedings of the Royal Society of London, Series A, Vol. 244, pp. 186-198, 1958.

Schlichting H., Boundary Layer Theory, Seventh Edition, McGraw-Hill Book Company, New York, 1979.

Snyder H. A., "Wave-Number Selection at Finite Amplitude in Rotating Couette Flow," Journal of Fluid Mechanics, Vol. 35, No. 2, pp. 273-298, 1969.

Swearingen J. D., and Blackwelder R. F., "The Growth and Breakdown of Streamwise Vortices in the Presence of a Wall," Journal of Fluid Mechanics, Vol. 182, pp. 255-290, 1987.

Swinney H. L., "Observations of Order and Chaos in Nonlinear Systems," Physica 7D, Vol. 3, pp. 3-15, 1983.

Treaster A. L., and Houtz H. E., "Fabricating and Calibrating Five-Hole Probes," Proceedings Fluid Measurements and Instrumentation Forum (Edts. Bajura R. A. and Billet M. L.), Vol. 34, 1986.

Treaster A. L., and Yocom A. M., "The Calibration and Application of Five-Hole Pressure Probes," ISA Transactions, Vol. 18, No. 3, pp. 23-34, 1979.

Welz J. P., "An Algorithm for Using the Five-Hole Probe in the Non-Nulled Mode," Proceedings Fluid Measurements and Instrumentation Forum (Edts. Bajura R. A. and Billet M. L.), Vol. 34, 1986.

Westphal R. V., Ligrani P. M., and Lemos F. R., "Subminiature Hot-Wire Probes," NASA Tech Briefs Journal, Vol. 13, No. 10, pp. 40-41, 1989.

Yang K.-S., and Kim J., "Numerical Investigation of Instability and Transition in Rotating Plane Poiseuille Flow," Physics of Fluids A, Vol. 3, No. 4, pp. 633-641, 1991.

Young A. D., and Maas J. M., "The Behavior of a Pitot Tube in a Transverse Total Pressure Gradient," British R&M 1770, 1936.

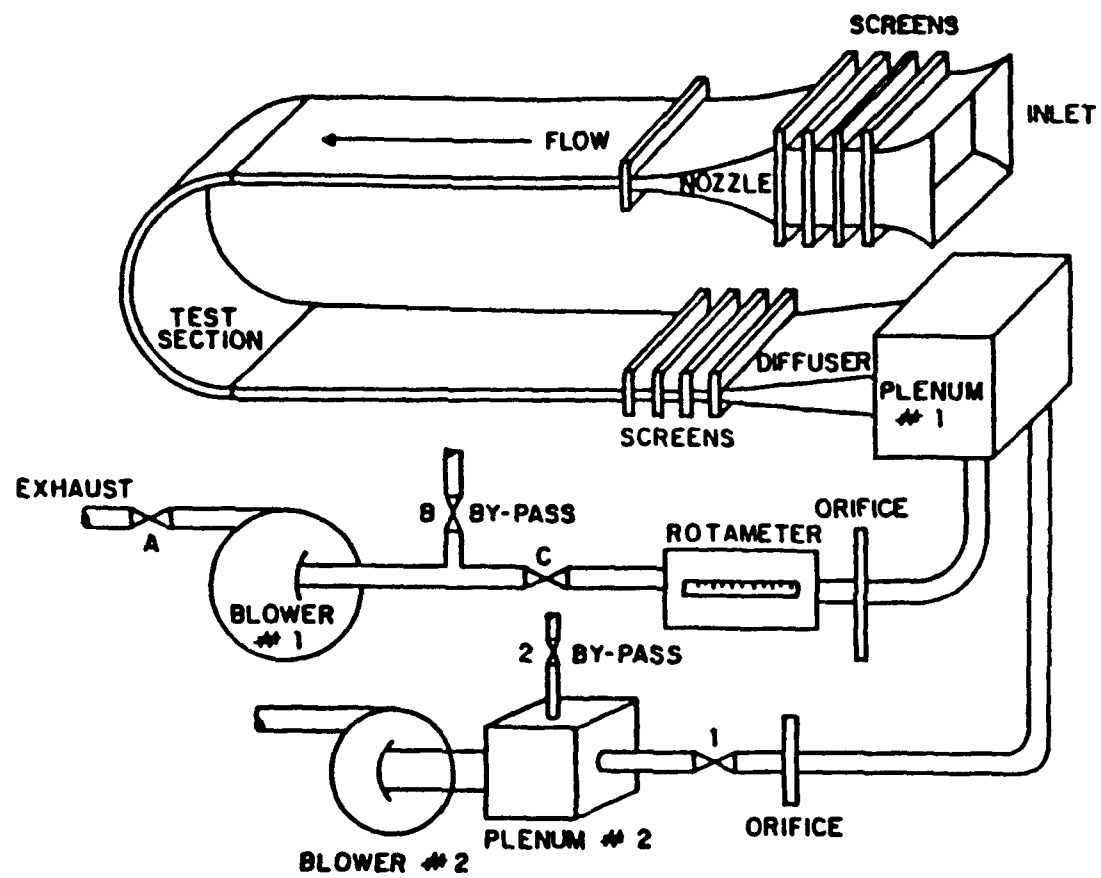


FIG. 1. Schematic of the transparent curved channel test facility.

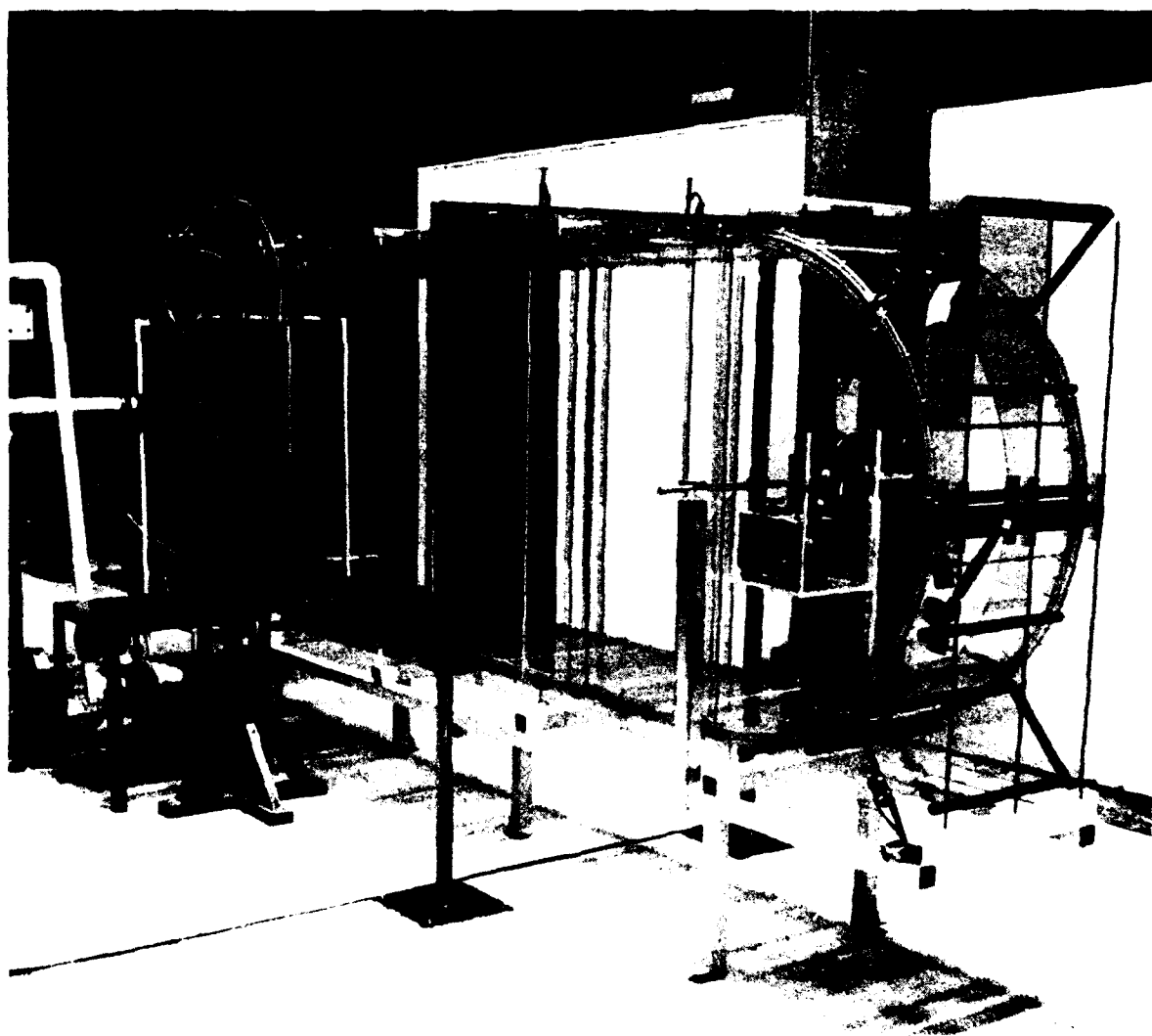


FIG. 2. Photograph of the transparent curved channel test facility.

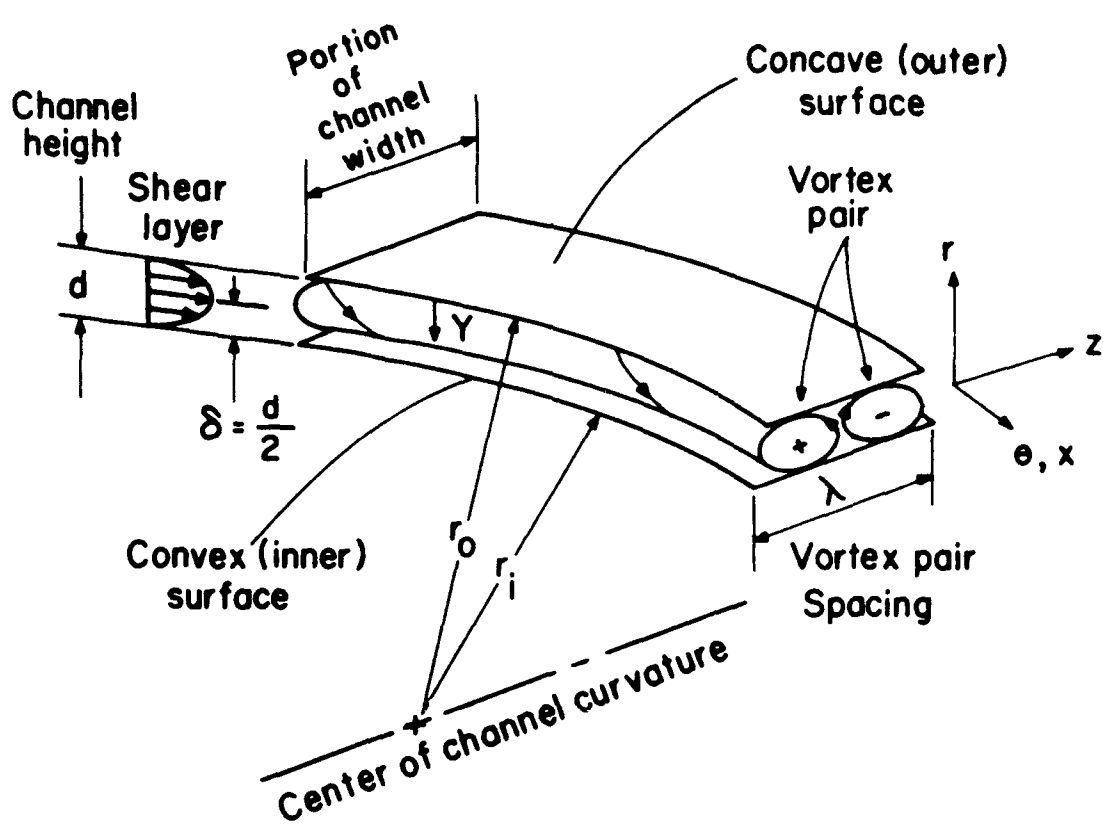


FIG. 3. Schematic of the curved channel coordinate system including one pair of Dean vortices. The flow is periodic in Z and only one period is shown.

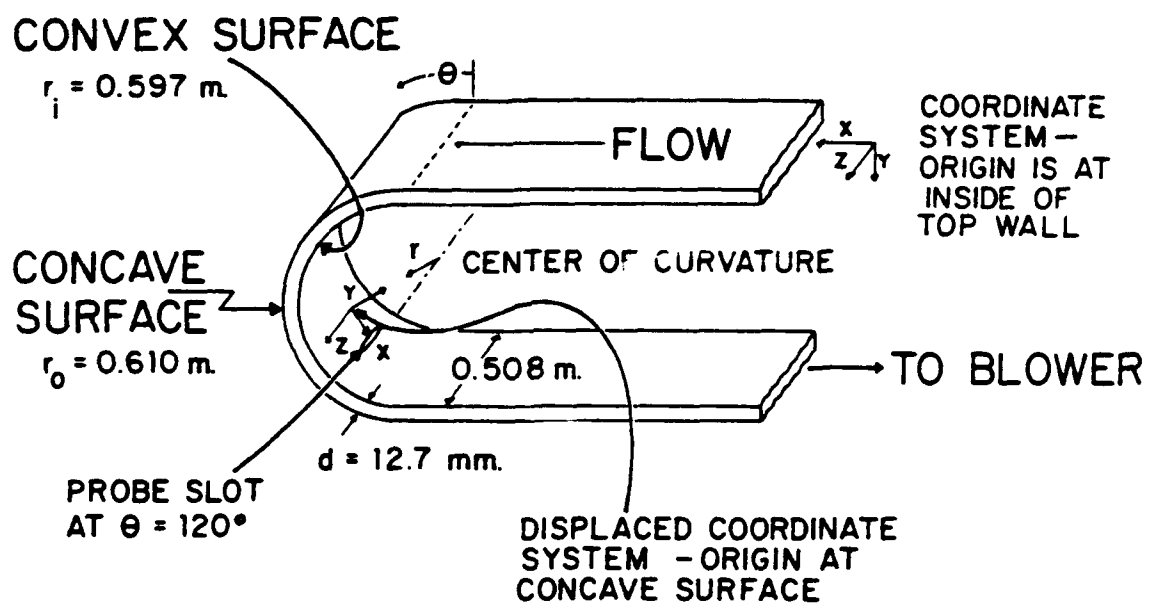


FIG. 4. Schematic of the curved channel coordinate system and dimensions.

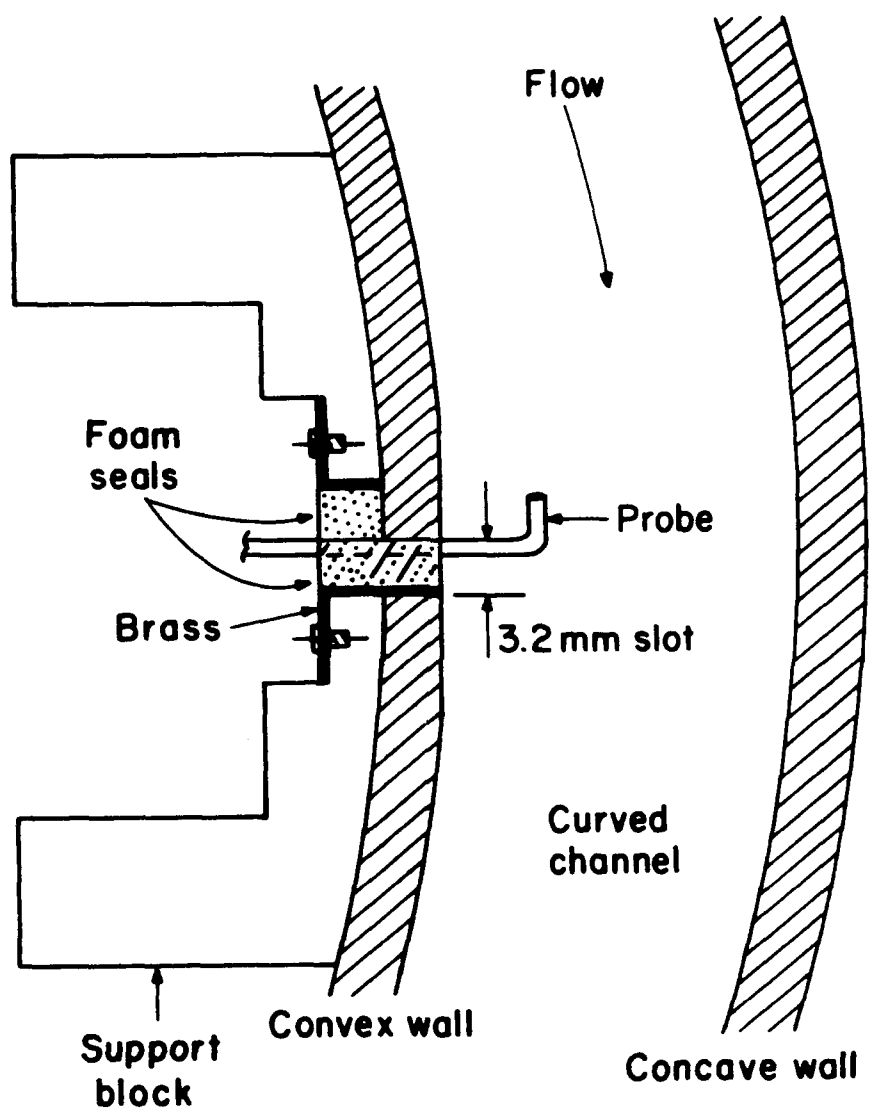
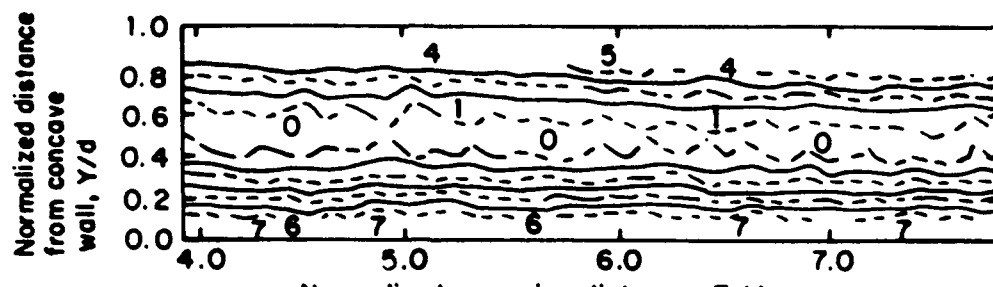


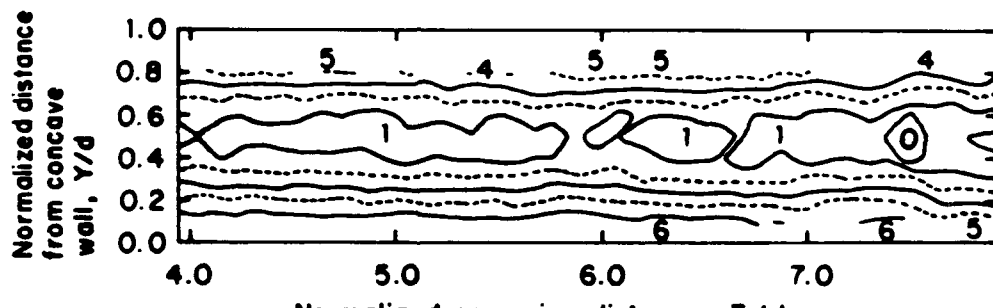
FIG. 5. Schematic of the arrangement employed to insert the miniature five-hole probe into the curved channel.



Differential pressure ranges,  $(P_o - P_t) (N/m^2)$

0	1.85 - 1.90	4	2.01 - 2.05
1	1.90 - 1.93	5	2.05 - 2.08
2	1.93 - 1.98	6	2.08 - 2.13
3	1.98 - 2.01	7	2.13 - 2.15

a)  $De = 54$ , Miniature Kiel probe survey



Differential pressure ranges,  $(P_o - P_t) (N/m^2)$

0	1.85 - 1.90	4	2.04 - 2.08
1	1.90 - 1.94	5	2.08 - 2.13
2	1.94 - 1.99	6	2.13 - 2.18
3	1.99 - 2.04	7	2.18 - 2.23

b)  $De = 49$ , Miniature five-hole probe survey

FIG. 6. Total pressure distributions measured 120 degrees from start of curvature: (a) miniature Kiel probe survey for  $De=54$ , (b) miniature five-hole probe survey for  $De=49$ .

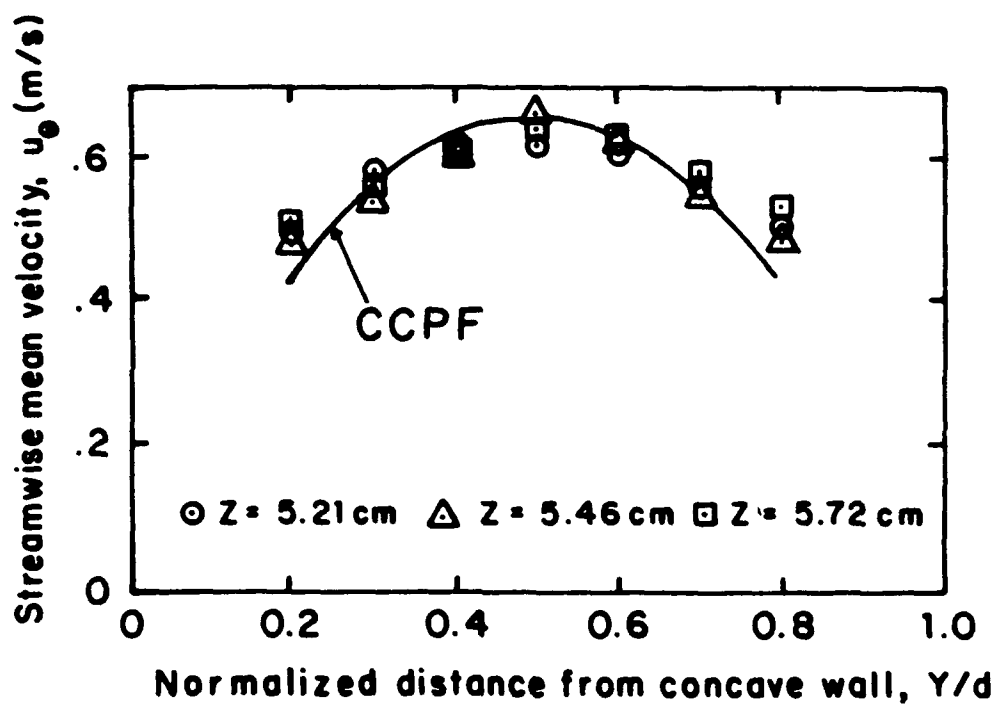


FIG. 7. Streamwise mean velocity profiles compared to curved-channel Poiseuille flow profiles,  $De=36.6$ .

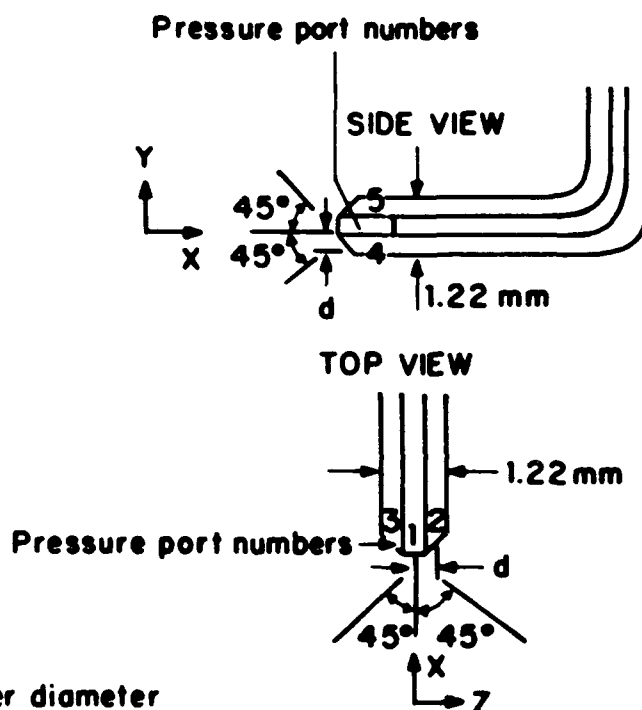
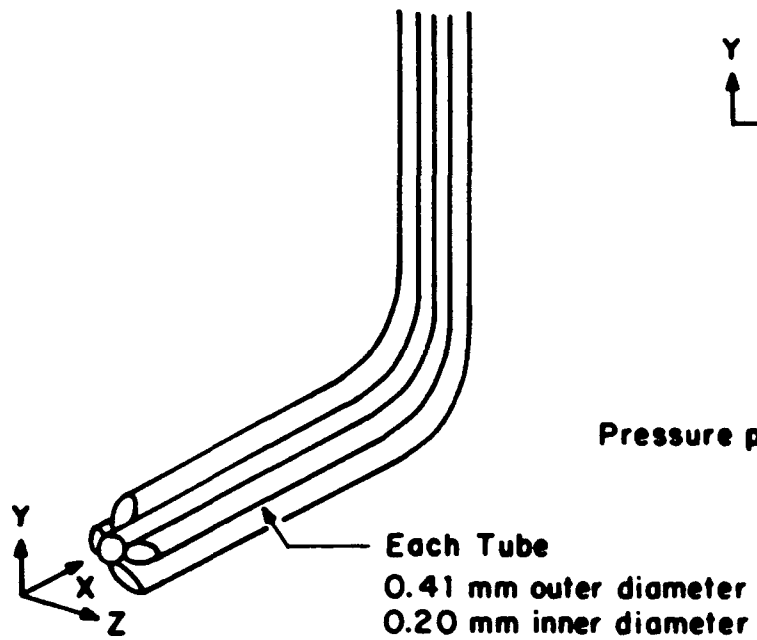


FIG. 8. Schematic drawings of the miniature five-hole pressure probe.

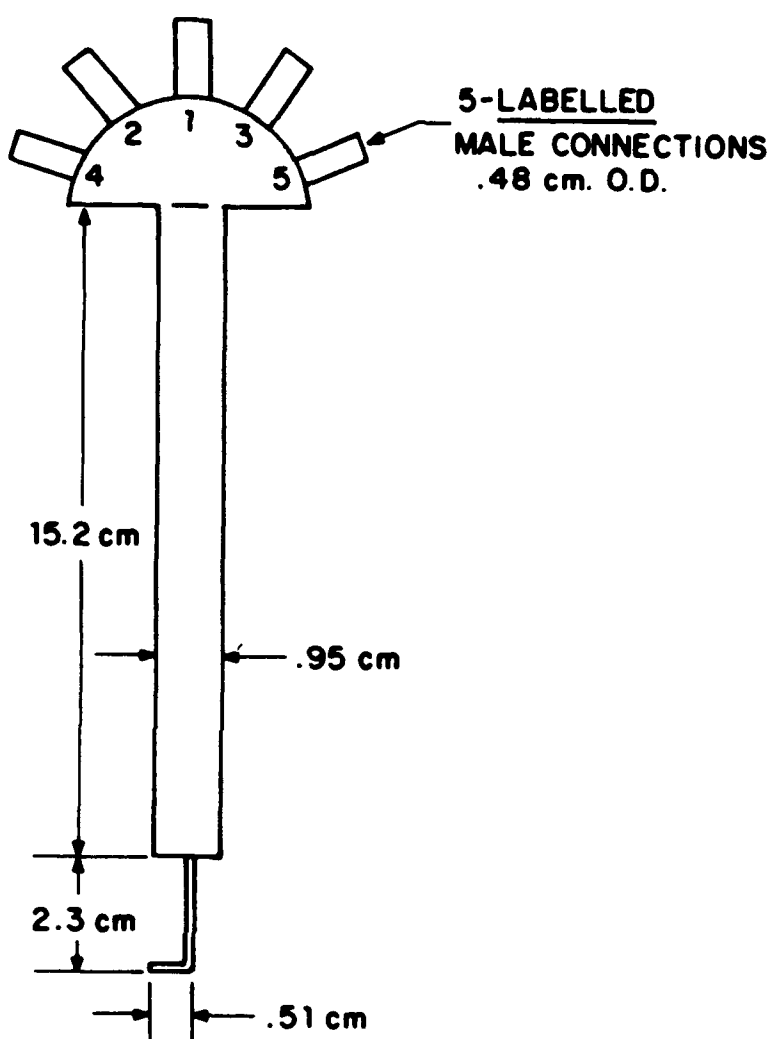


FIG. 9. Schematic of miniature five-hole pressure probe.

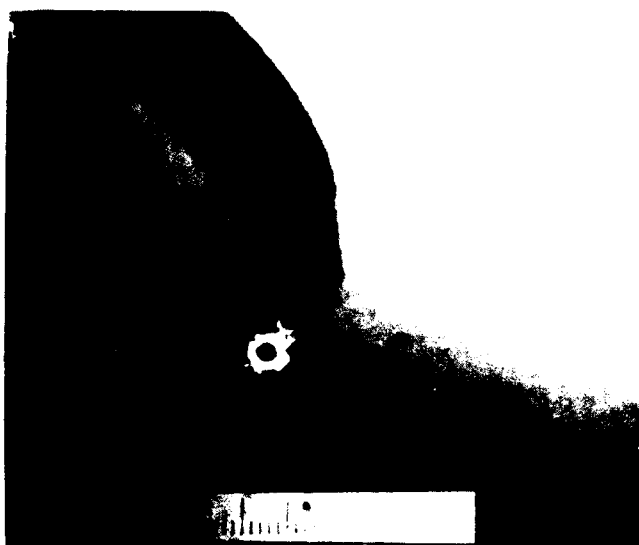


FIG. 10. Photograph of miniature five-hole pressure probe. Distance between adjacent scale markings is 0.10 mm.

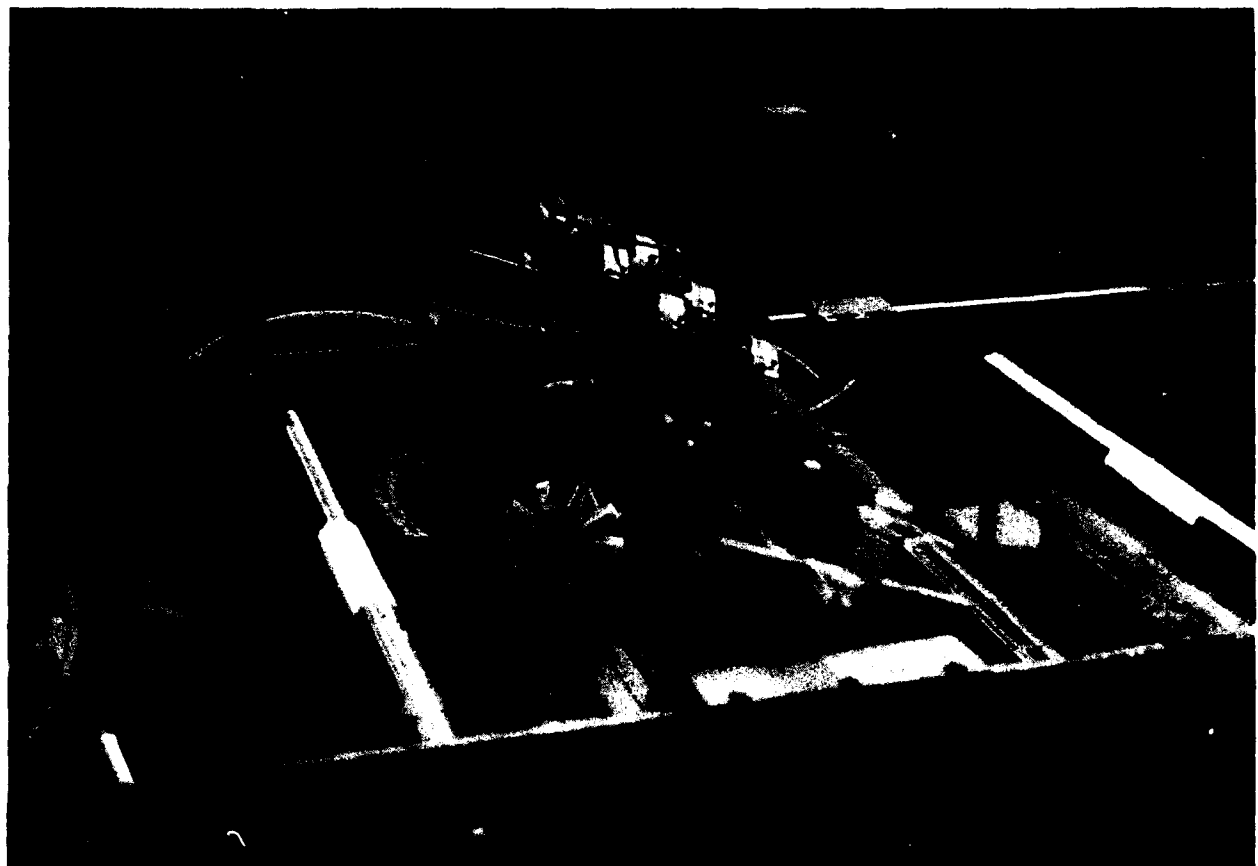


FIG. 11. Photograph of miniature five-hole pressure probe calibration sled.

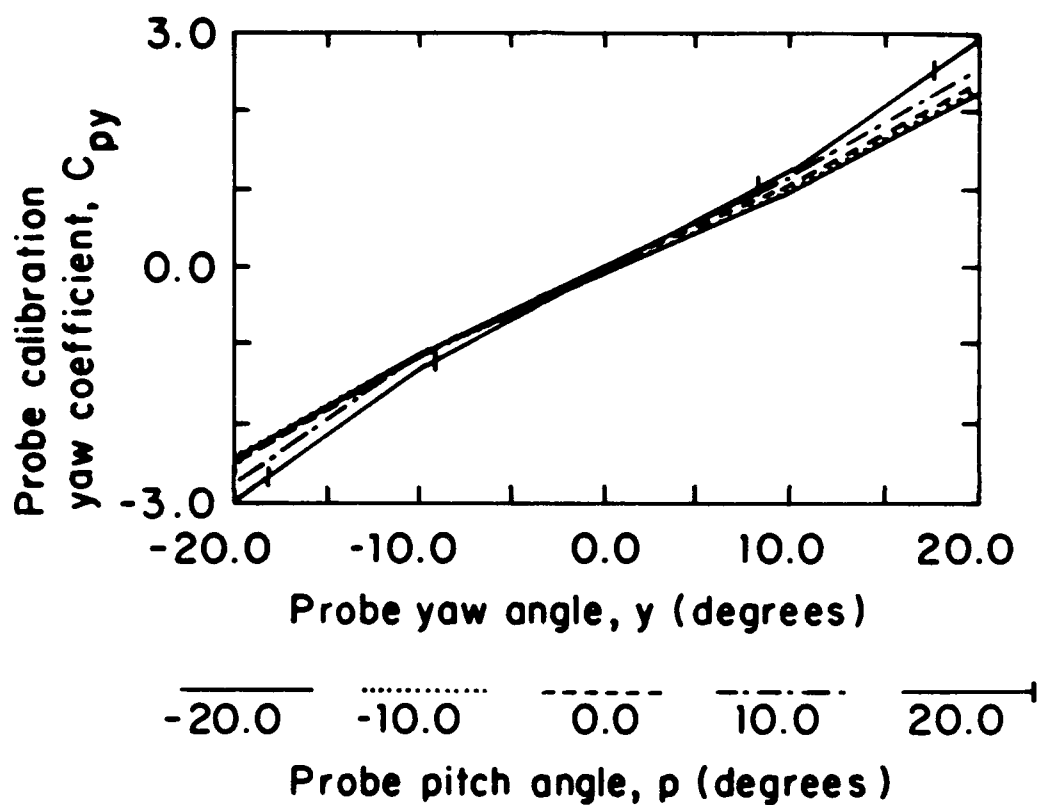


FIG. 12. Calibration characteristics of the miniature five-hole pressure probe, yaw pressure coefficient versus yaw angle, 1.9 m/s.

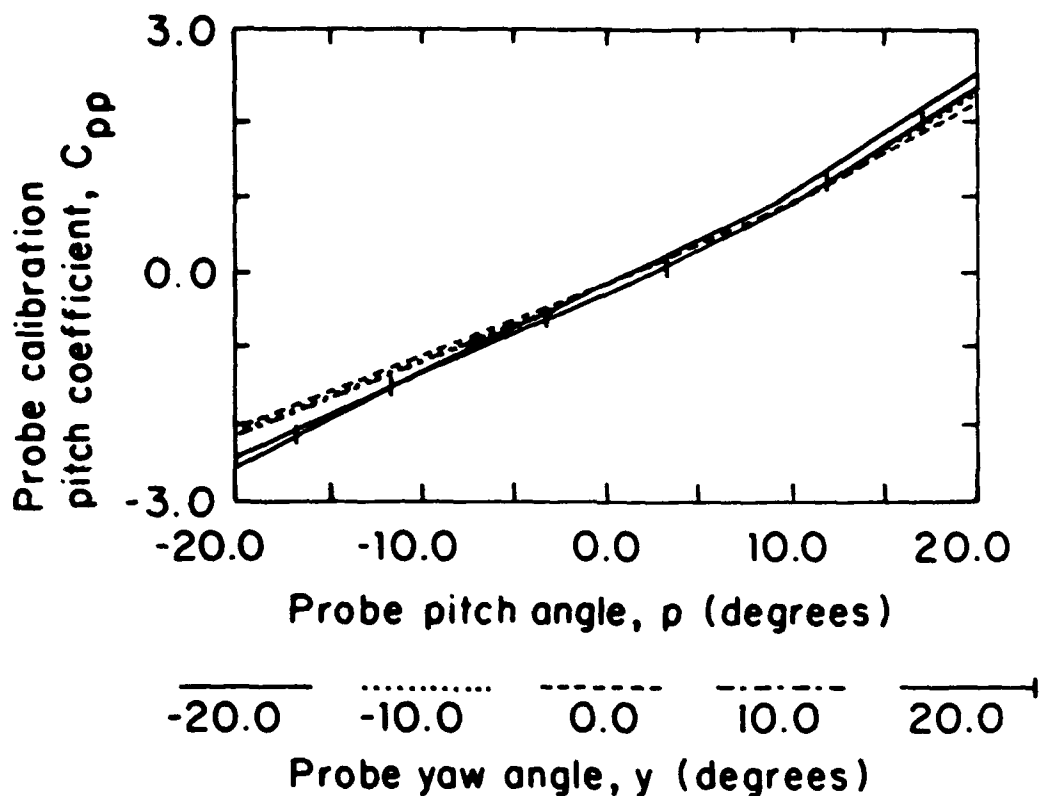


FIG. 13. Calibration characteristics of the miniature five-hole pressure probe, pitch pressure coefficient versus pitch angle, 1.9 m/s.

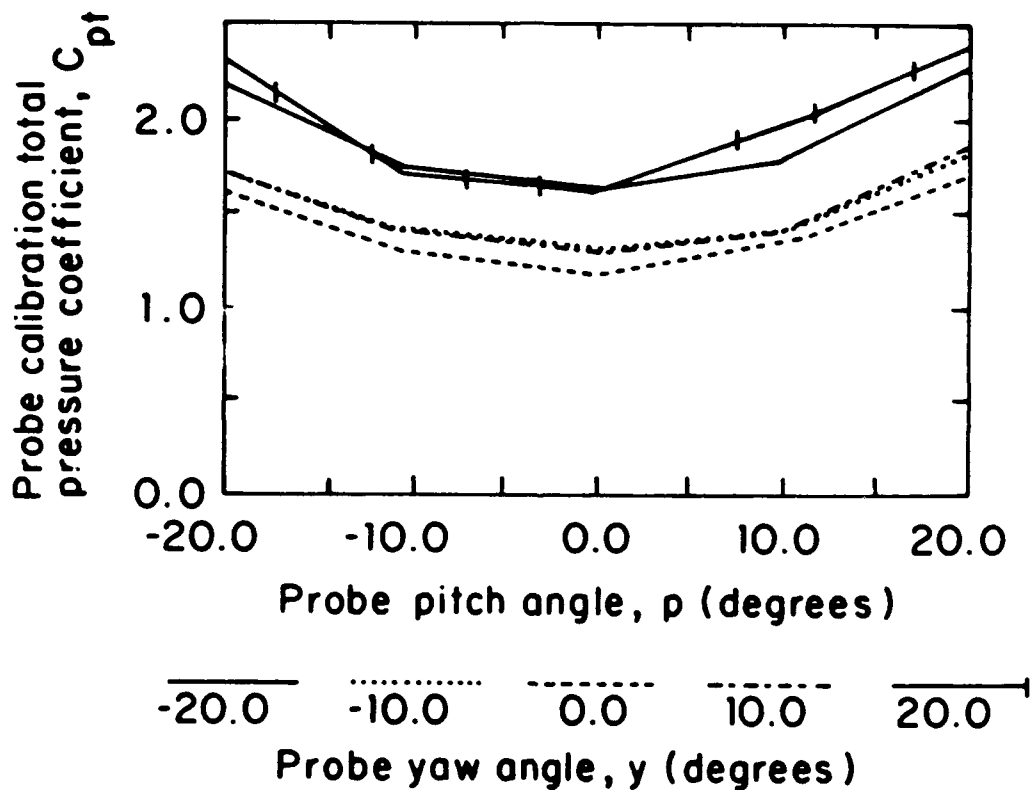


FIG. 14. Calibration characteristics of the miniature five-hole pressure probe, total pressure coefficient versus pitch angle, 1.9 m/s.

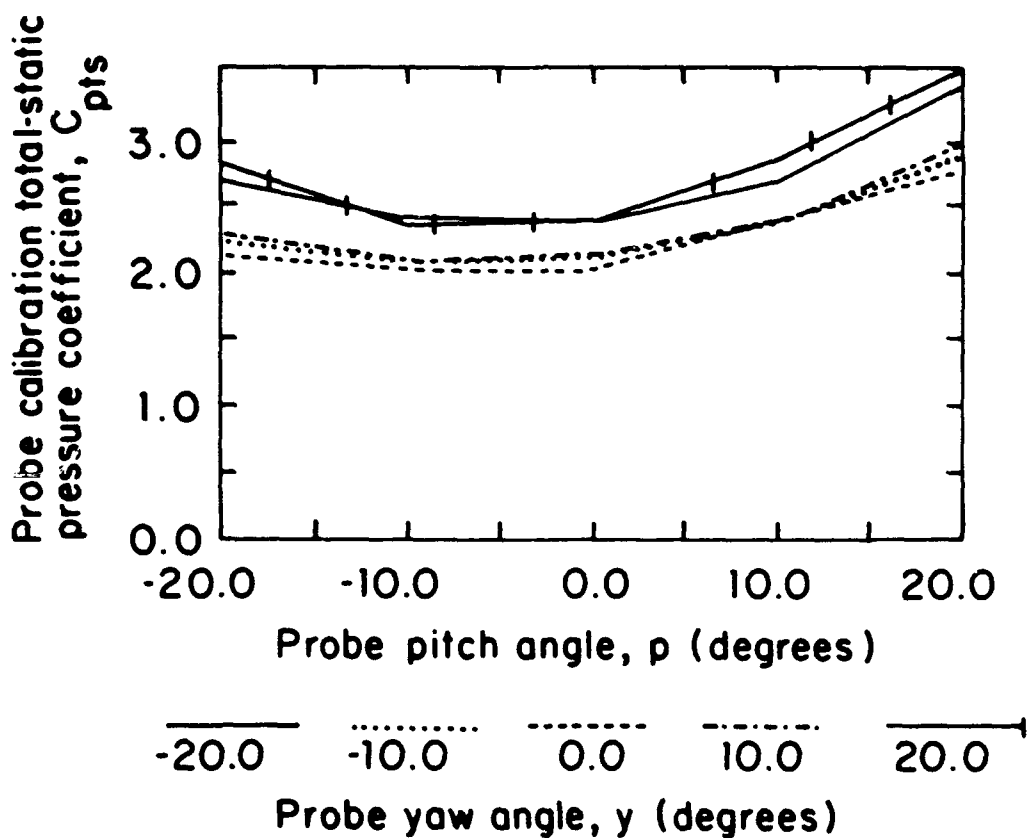


FIG. 15. Calibration characteristics of the miniature five-hole pressure probe, total pressure minus static pressure coefficient versus pitch angle, 1.9 m/s.

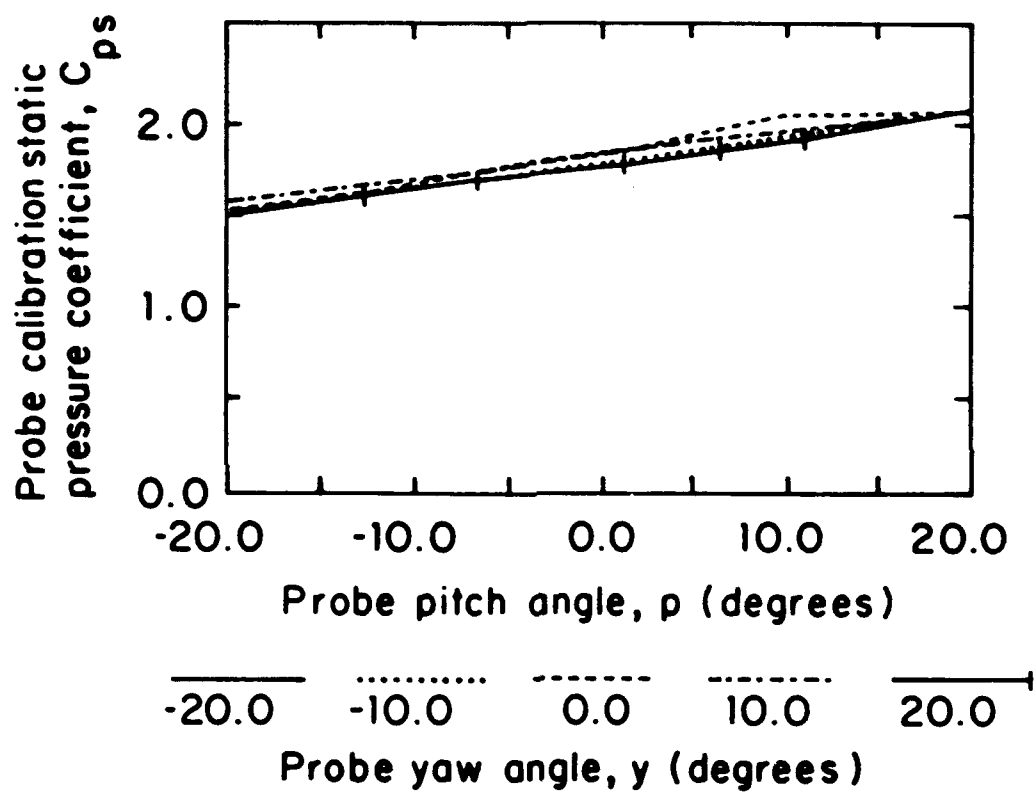


FIG. 16. Calibration characteristics of the miniature five-hole pressure probe, static pressure coefficient versus pitch angle, 1.9 m/s.

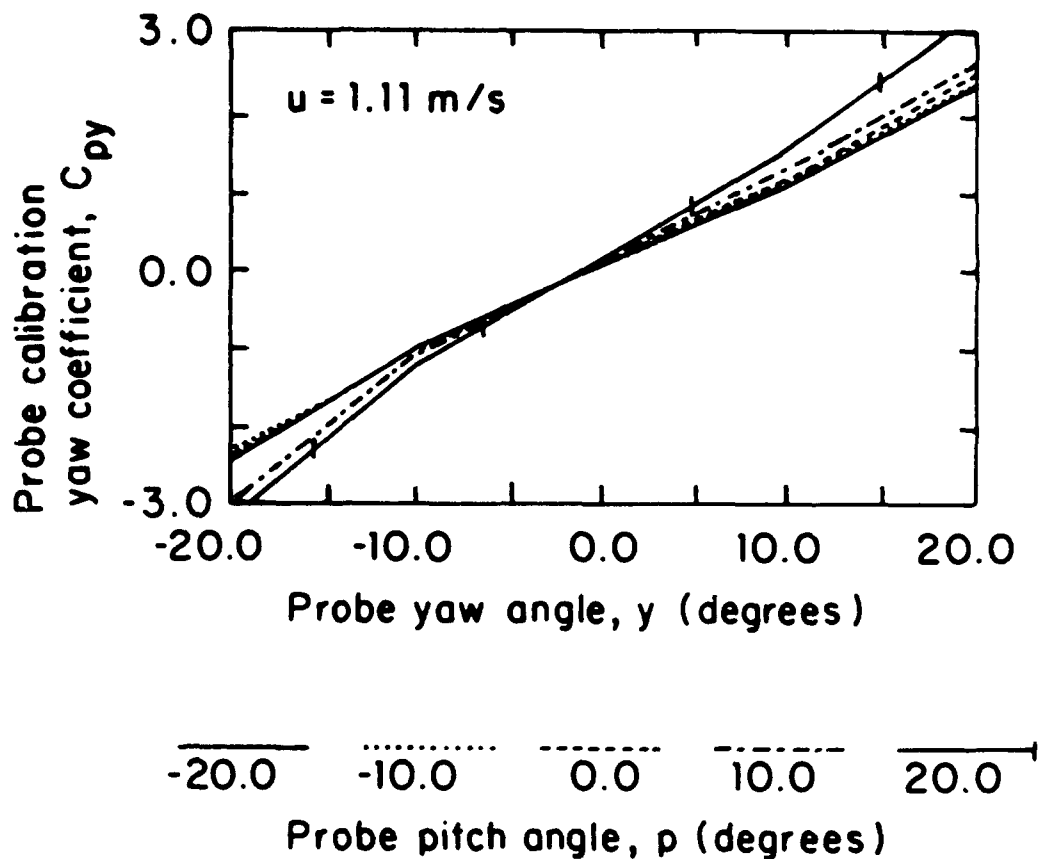


FIG. 17. Calibration characteristics of the miniature five-hole pressure probe, yaw pressure coefficient versus yaw angle, 1.11 m/s.

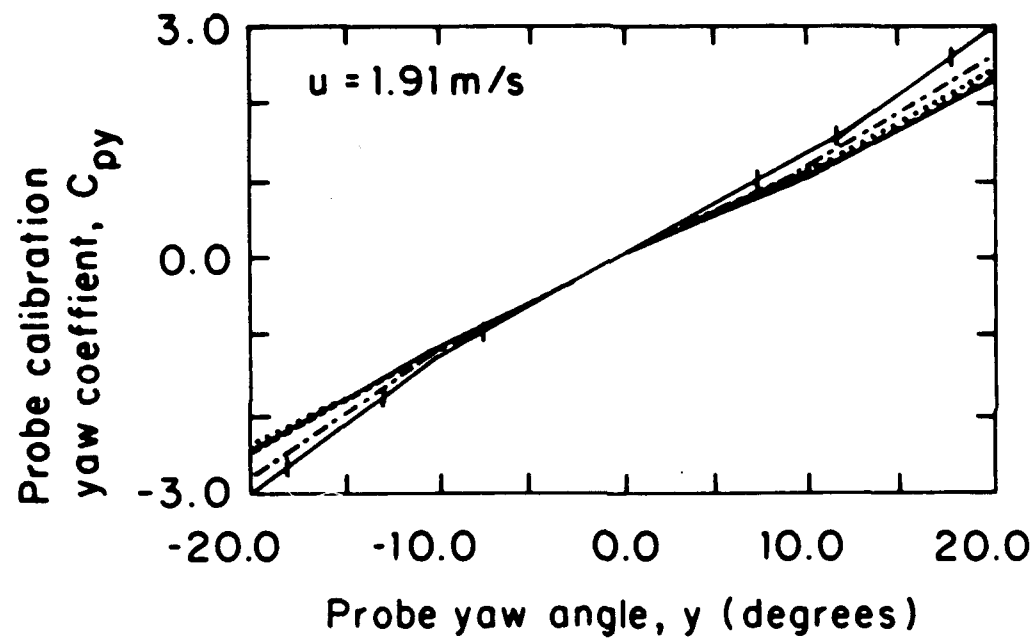


FIG. 18. Calibration characteristics of the miniature five-hole pressure probe, yaw pressure coefficient versus yaw angle, 1.91 m/s.

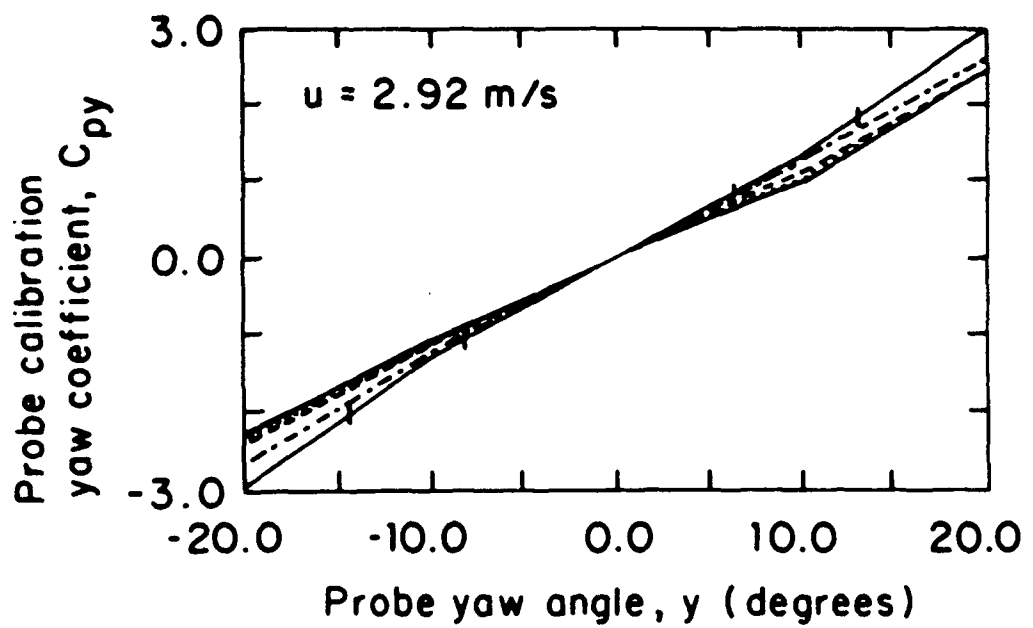


FIG. 19. Calibration characteristics of the miniature five-hole pressure probe, yaw pressure coefficient versus yaw angle, 2.92 m/s.

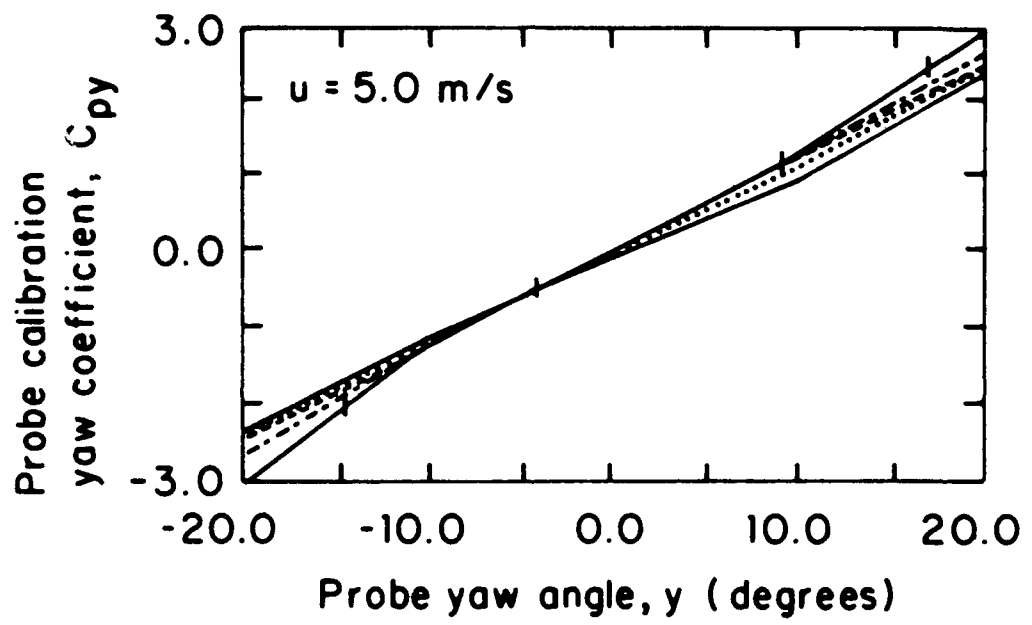


FIG. 20. Calibration characteristics of the miniature five-hole pressure probe, yaw pressure coefficient versus yaw angle, 5.0 m/s.

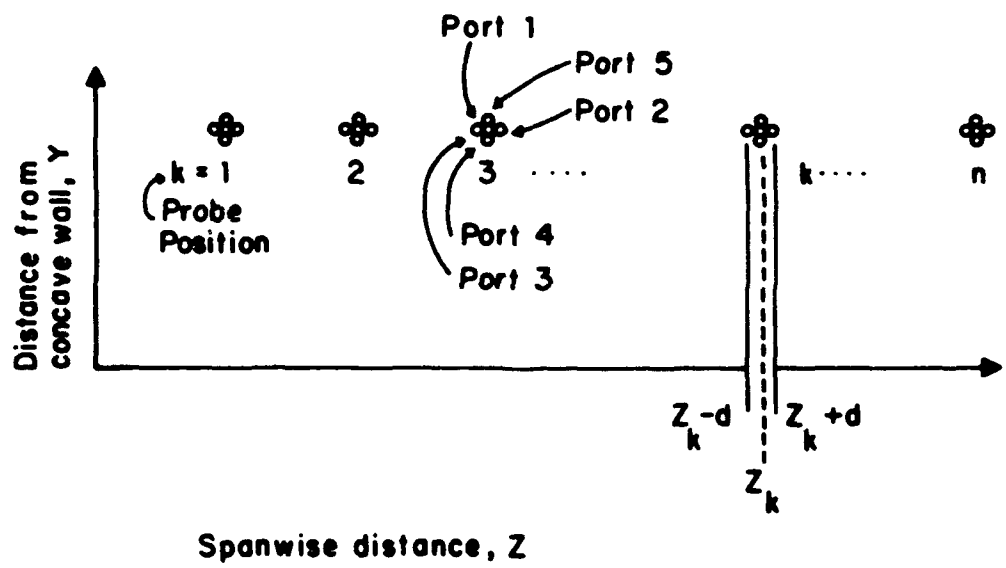


FIG. 21. Successive positions of the five-hole pressure probe and probe ports, looking downstream.

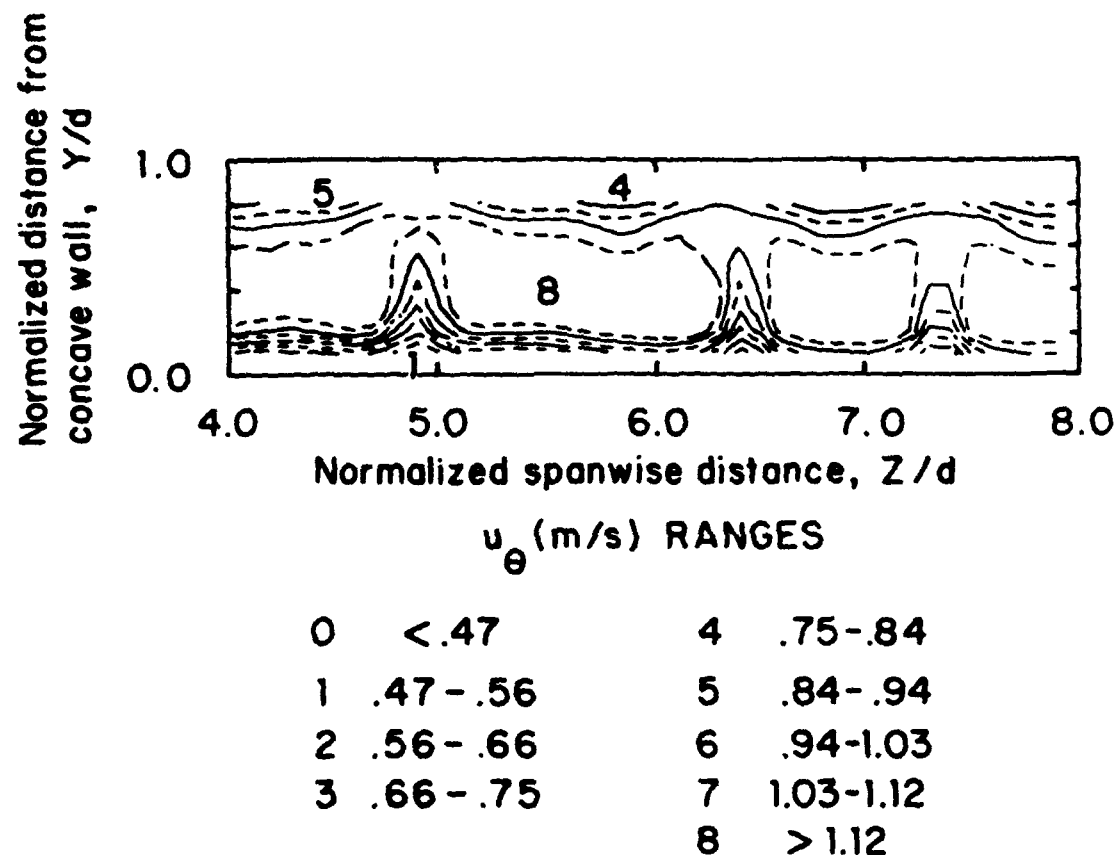


FIG. 22. Miniature five-hole pressure probe qualification results for  $De=100$ . (a) Streamwise velocity contours.

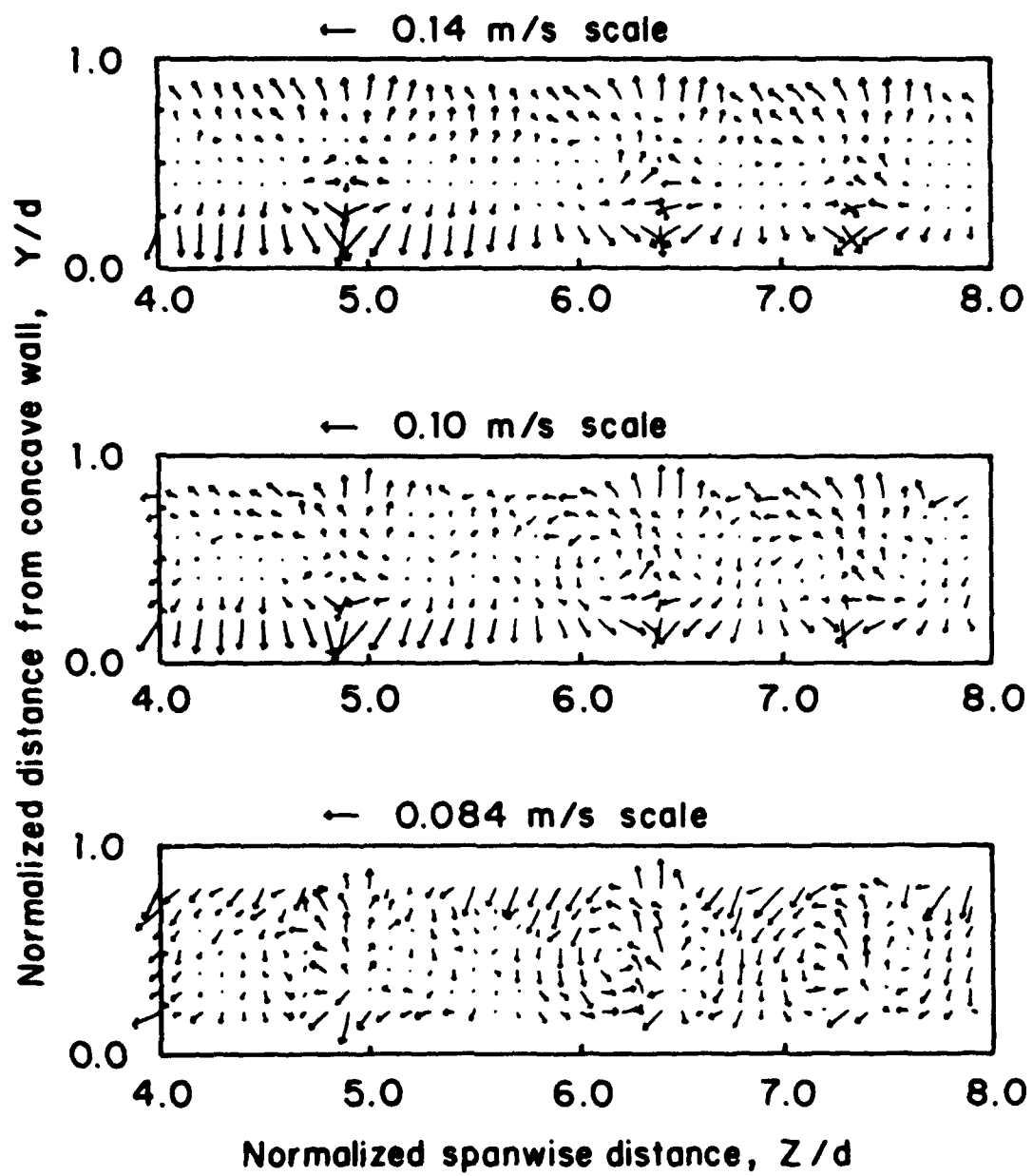


FIG. 22. Miniature five-hole pressure probe qualification results for  $De=100$ . (b) Secondary flow vectors, no corrections applied, (c) secondary flow vectors, spatial resolution correction only, (d) secondary flow vectors, spatial resolution correction and downwash velocity correction.

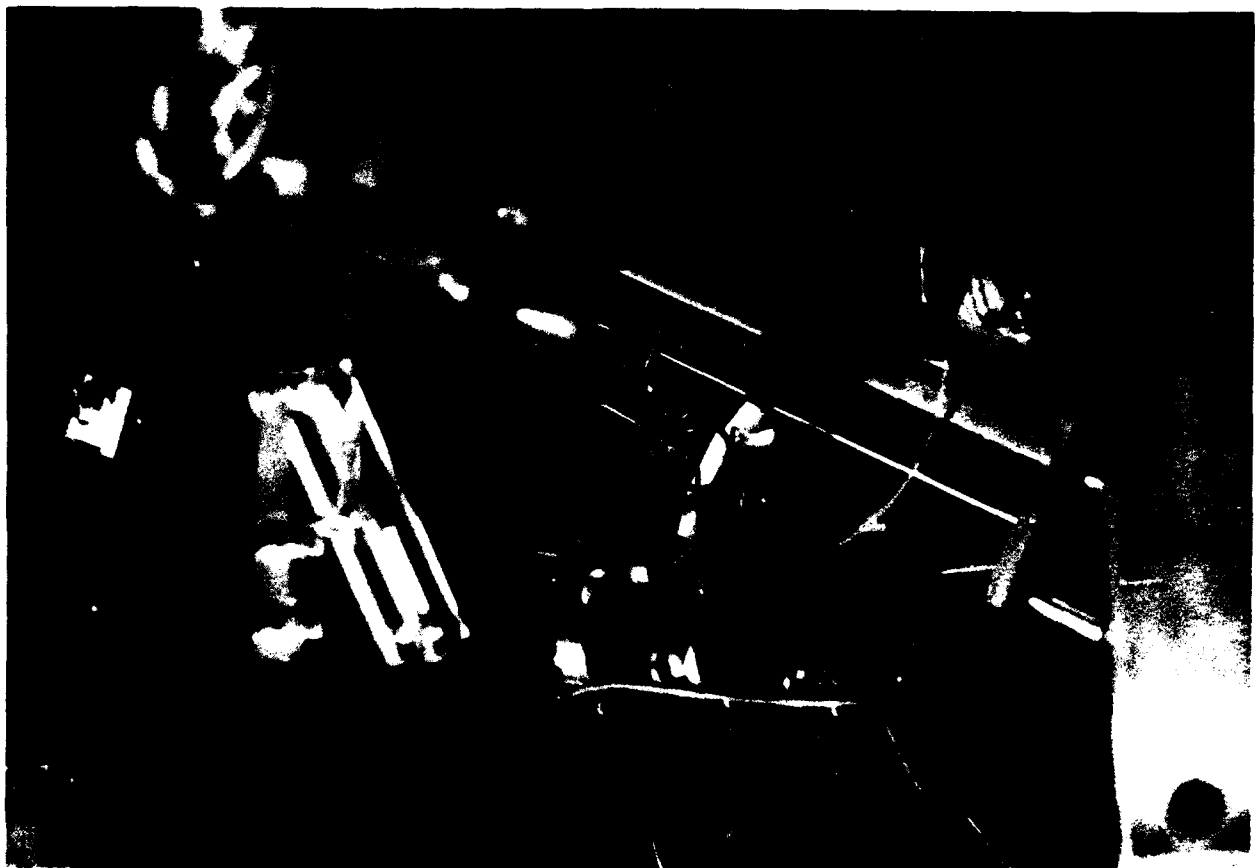


FIG. 23. Curved channel traversing mechanism, transducers, miniature five-hole pressure probe, and probe mount.

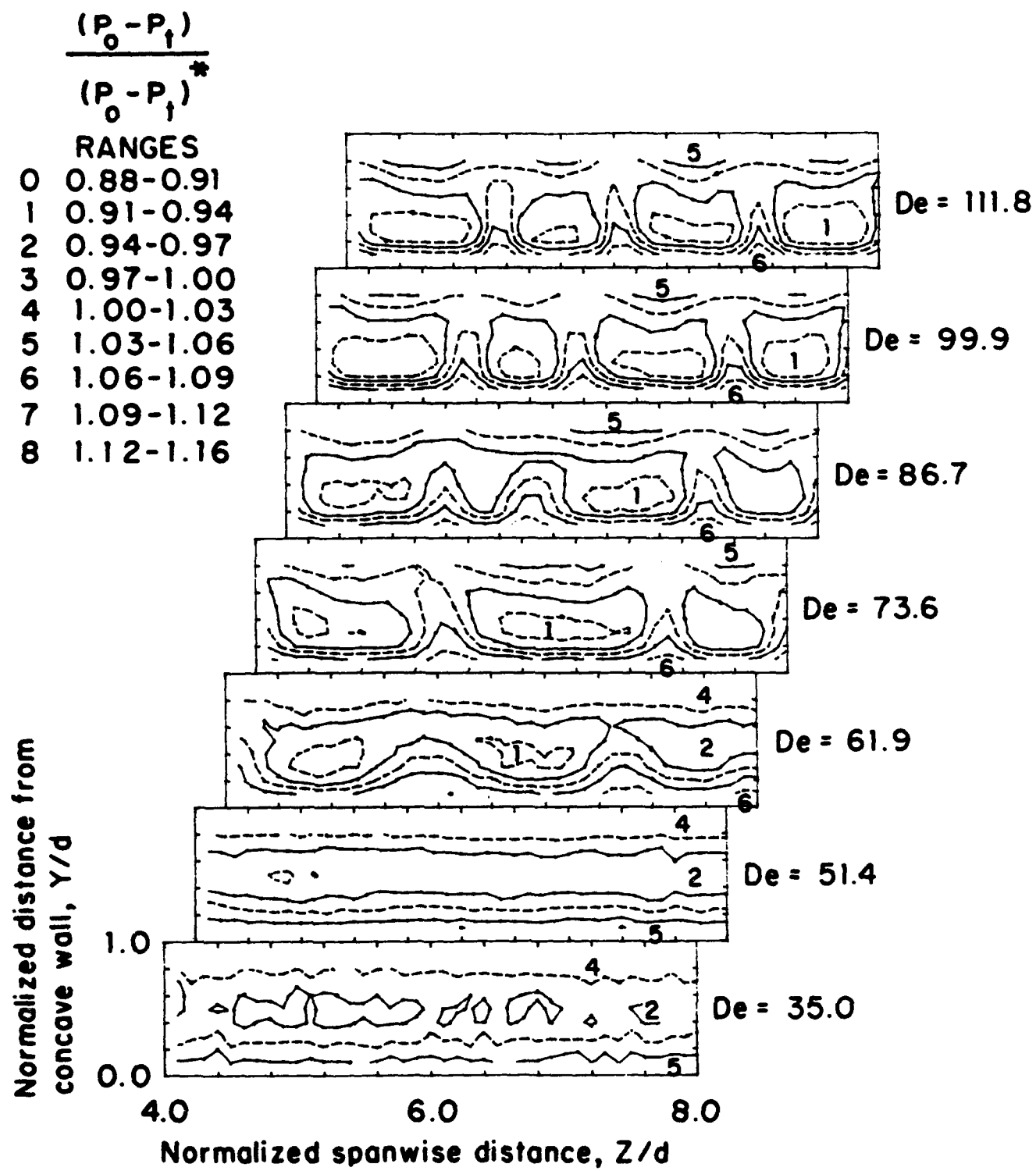


FIG. 24. Total pressure contours,  $De=35.0$  to  $De=111.8$ .

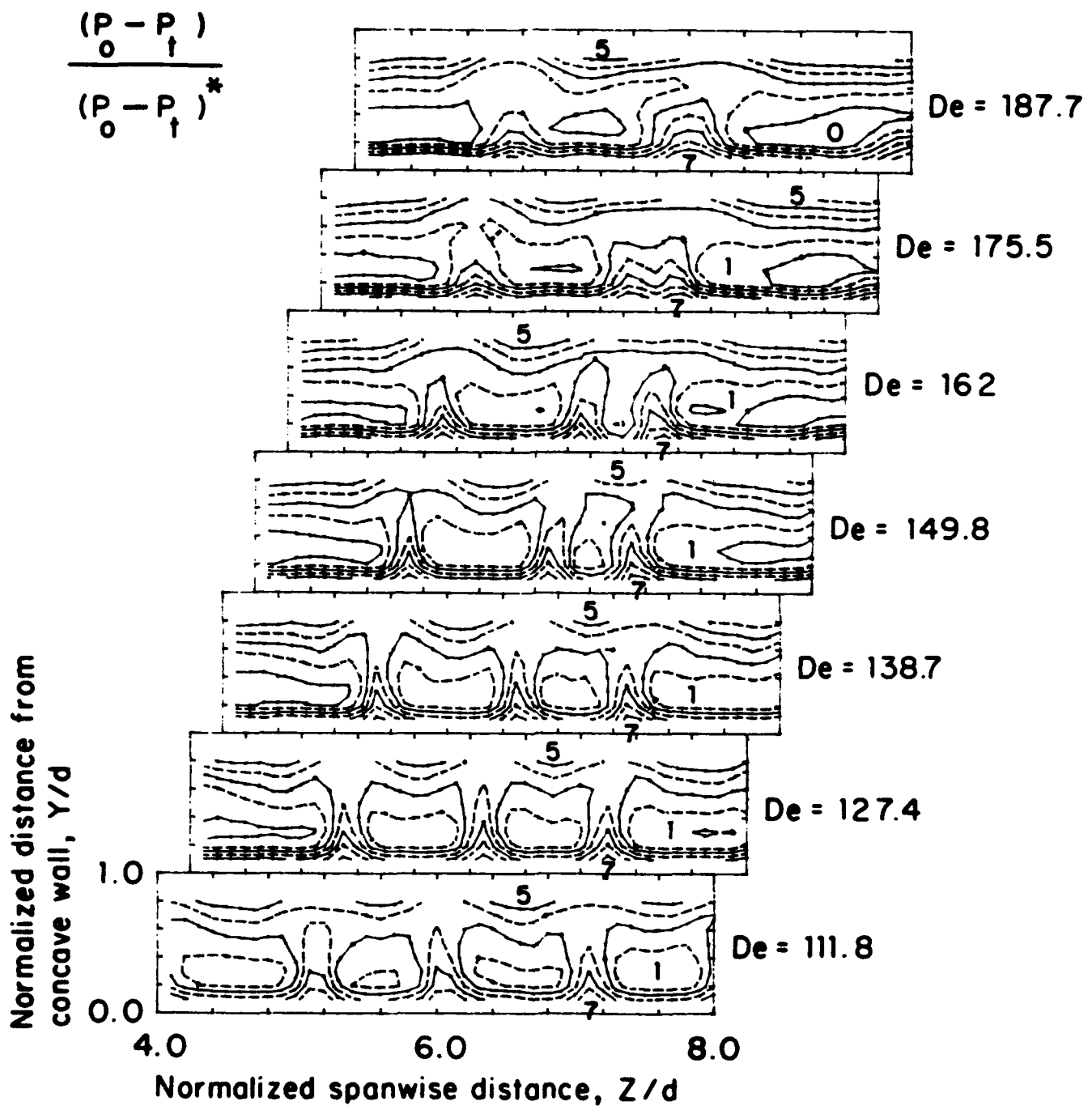


FIG. 25. Total pressure contours,  $De=111.8$  to  $De=187.7$ .

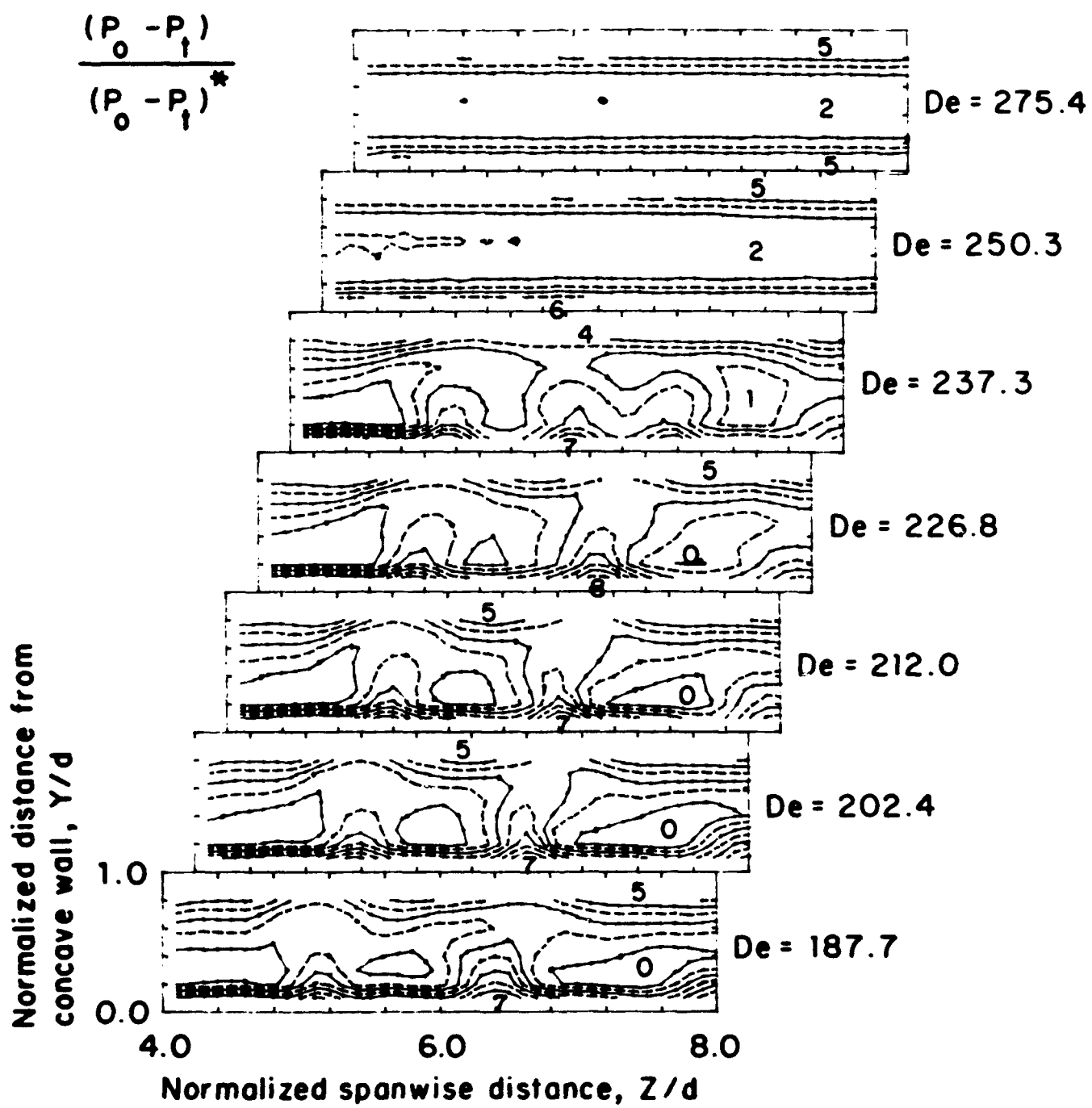


FIG. 26. Total pressure contours,  $De=187.7$  to  $De=275.4$ .

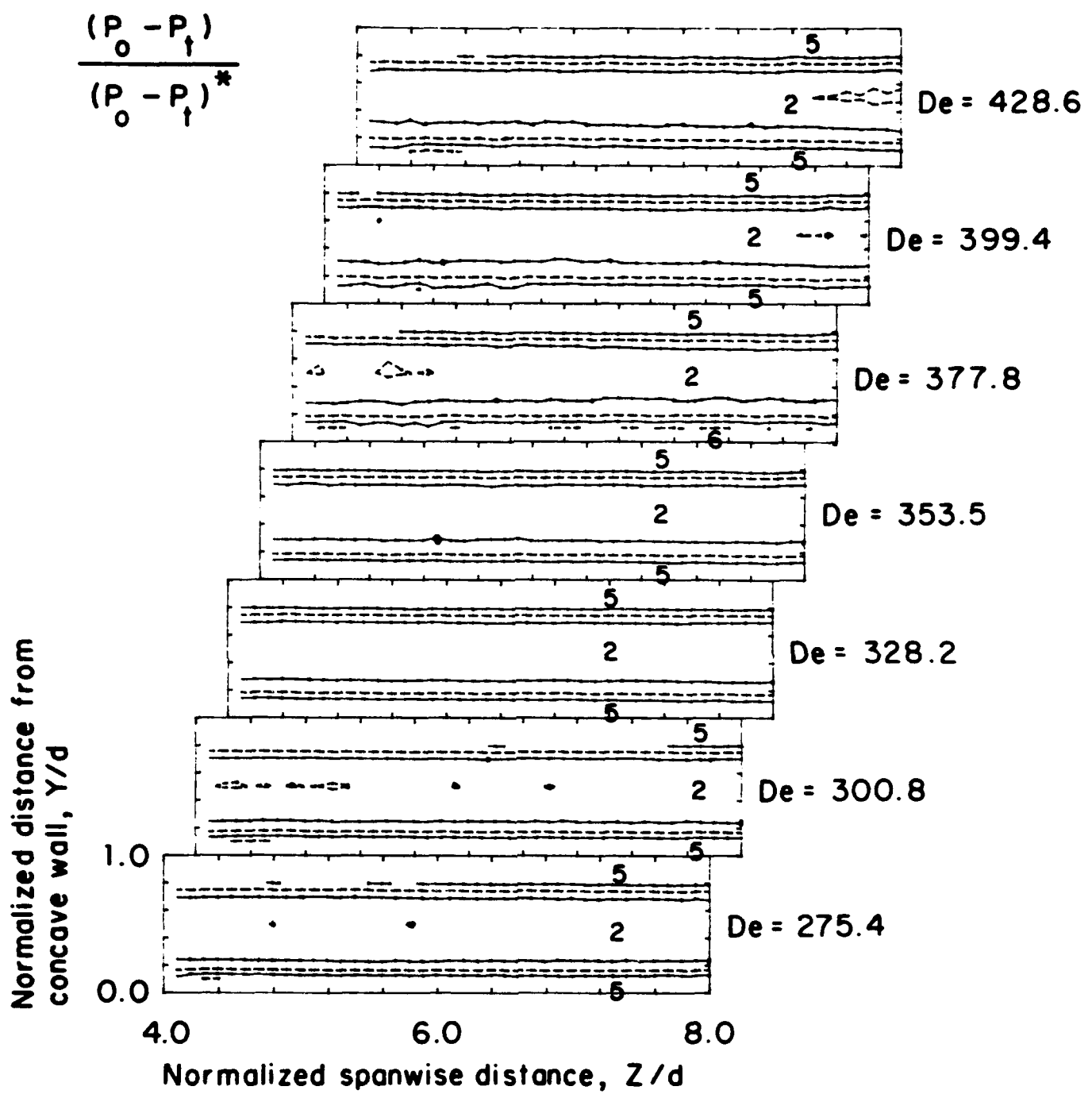


FIG. 27. Total pressure contours,  $De=275.4$  to  $De=428.6$ .

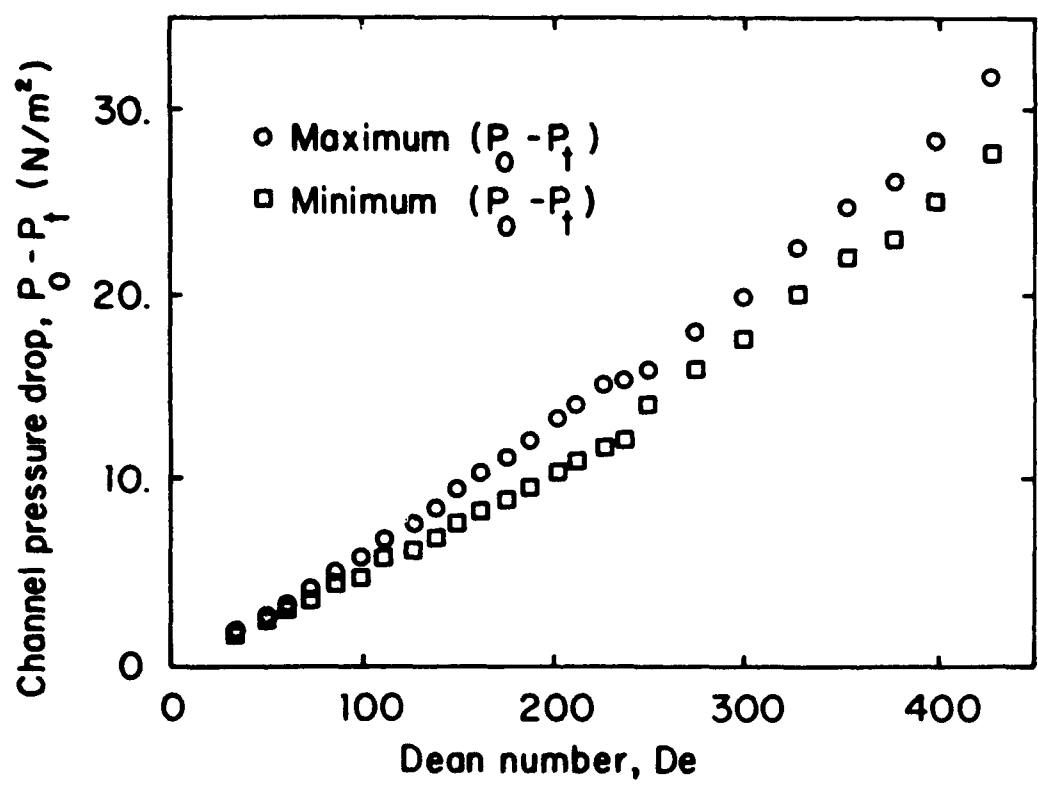


FIG. 28. Maximum and minimum values of the channel pressure drop.

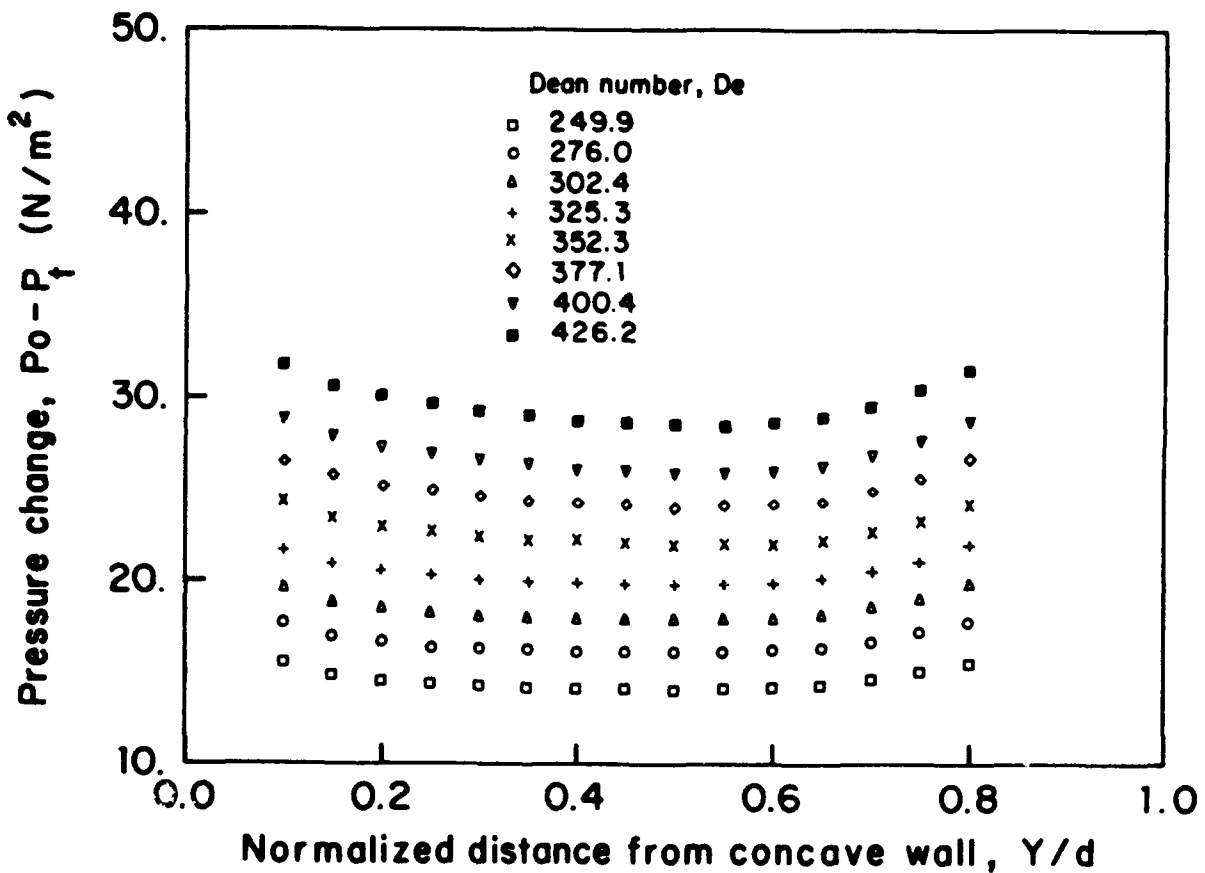


FIG. 29. Total pressure profiles,  $De=249.9$  to  $De=426.2$ .

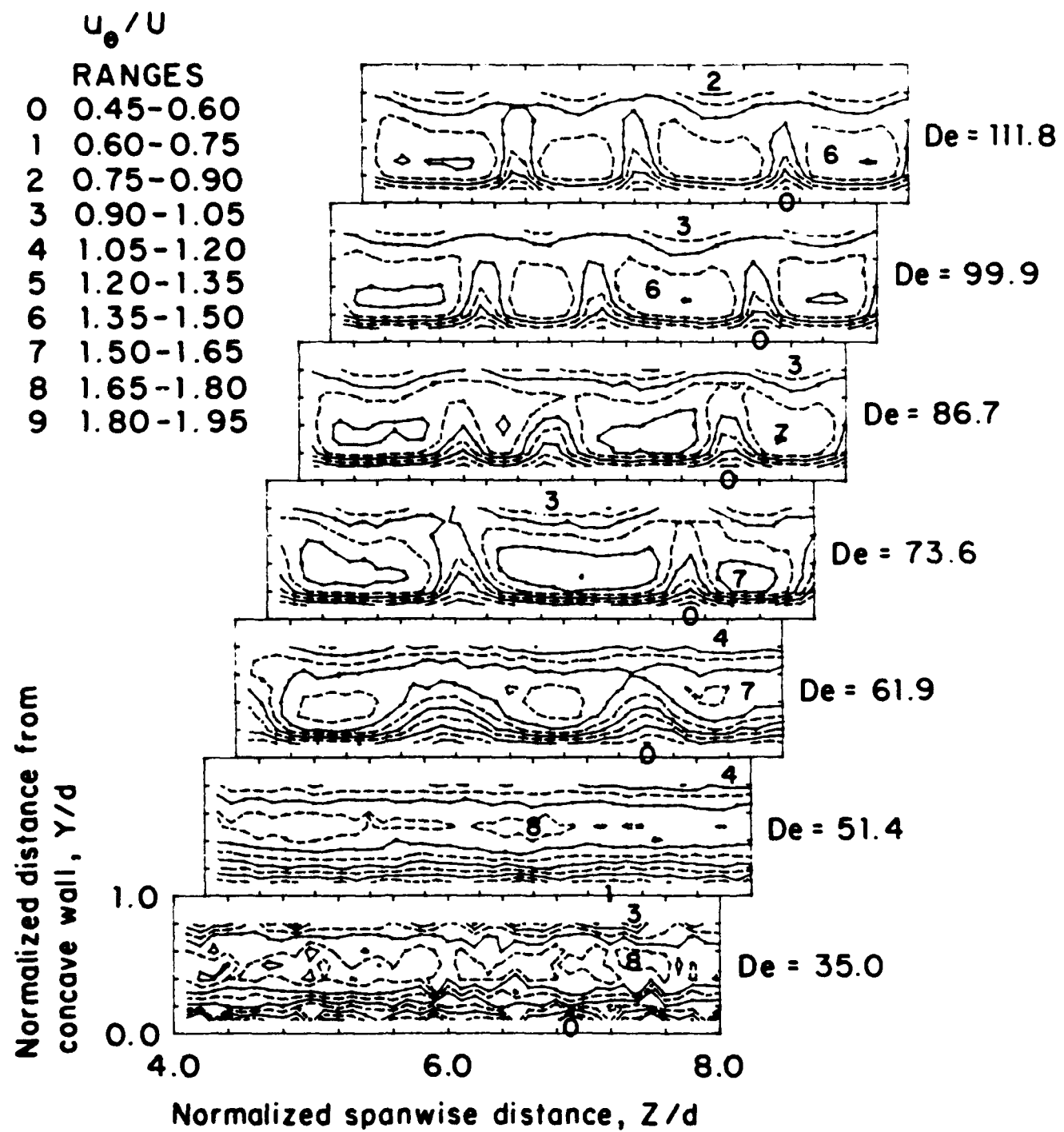


FIG. 30. Streamwise velocity contours,  $De=35.0$  to  $De=111.8$ .

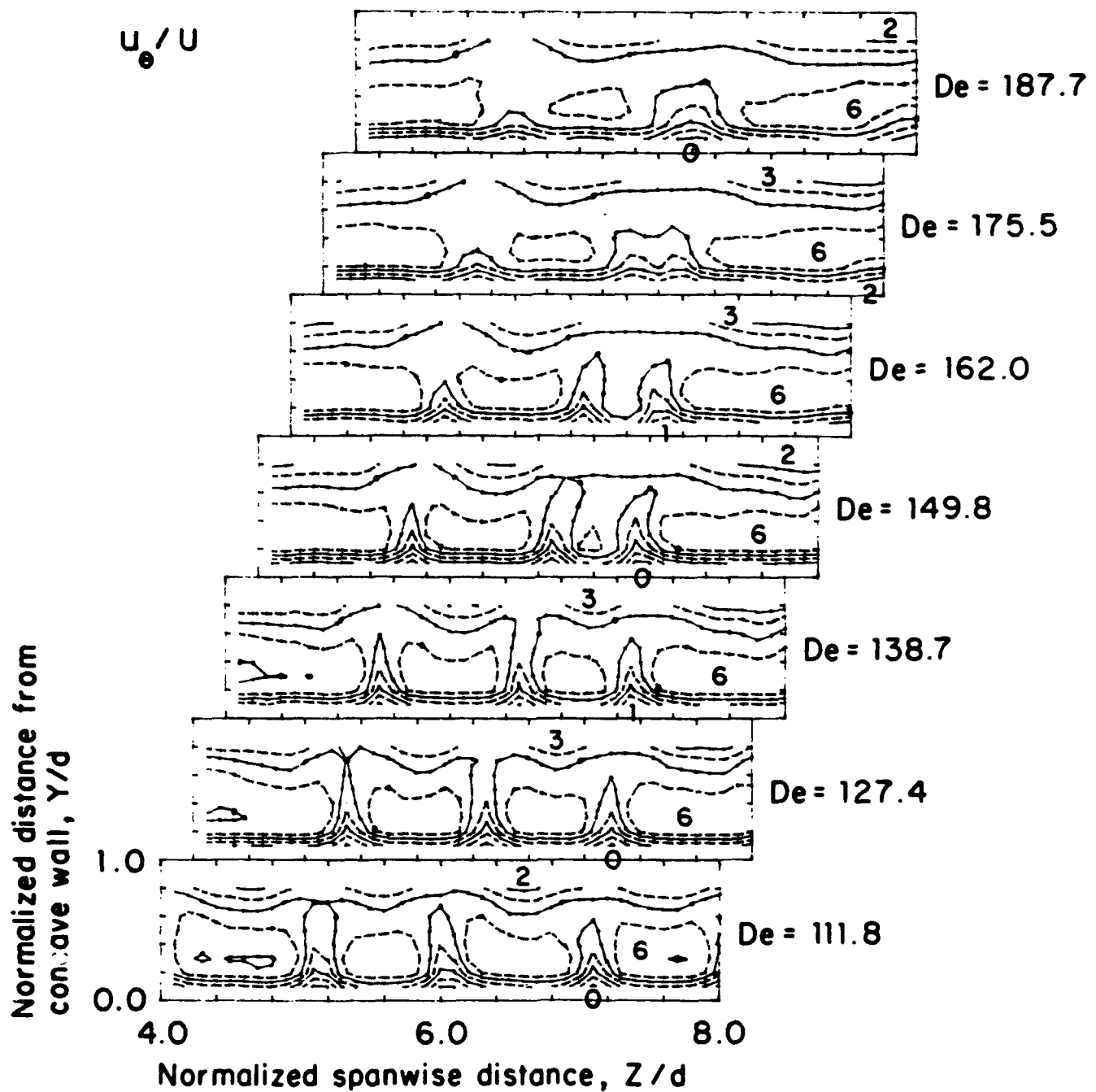


FIG. 31. Streamwise velocity contours,  $De=111.8$  to  $De=187.7$ .

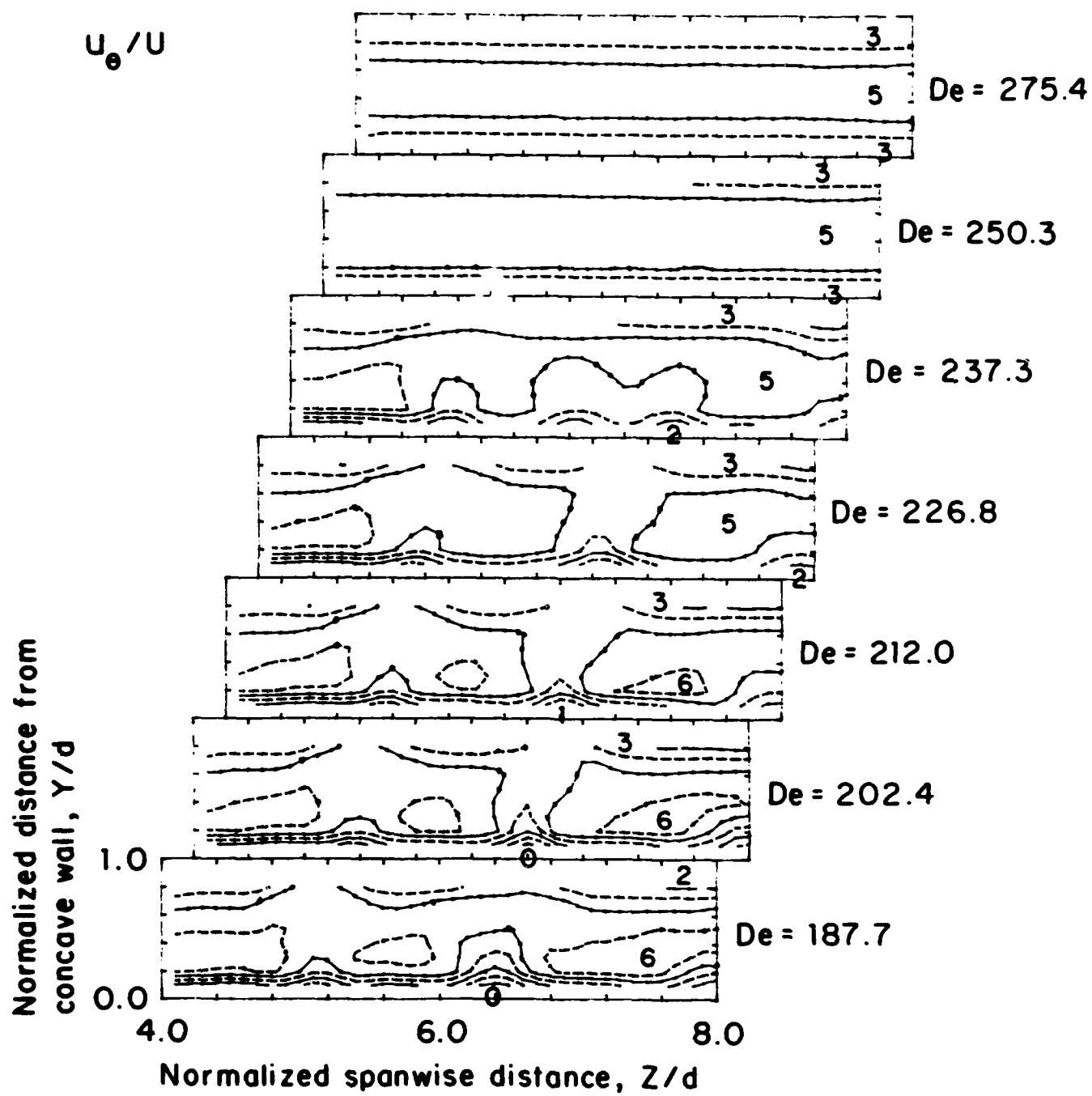


FIG. 32. Streamwise velocity contours,  $De=187.7$  to  $De=275.4$ .

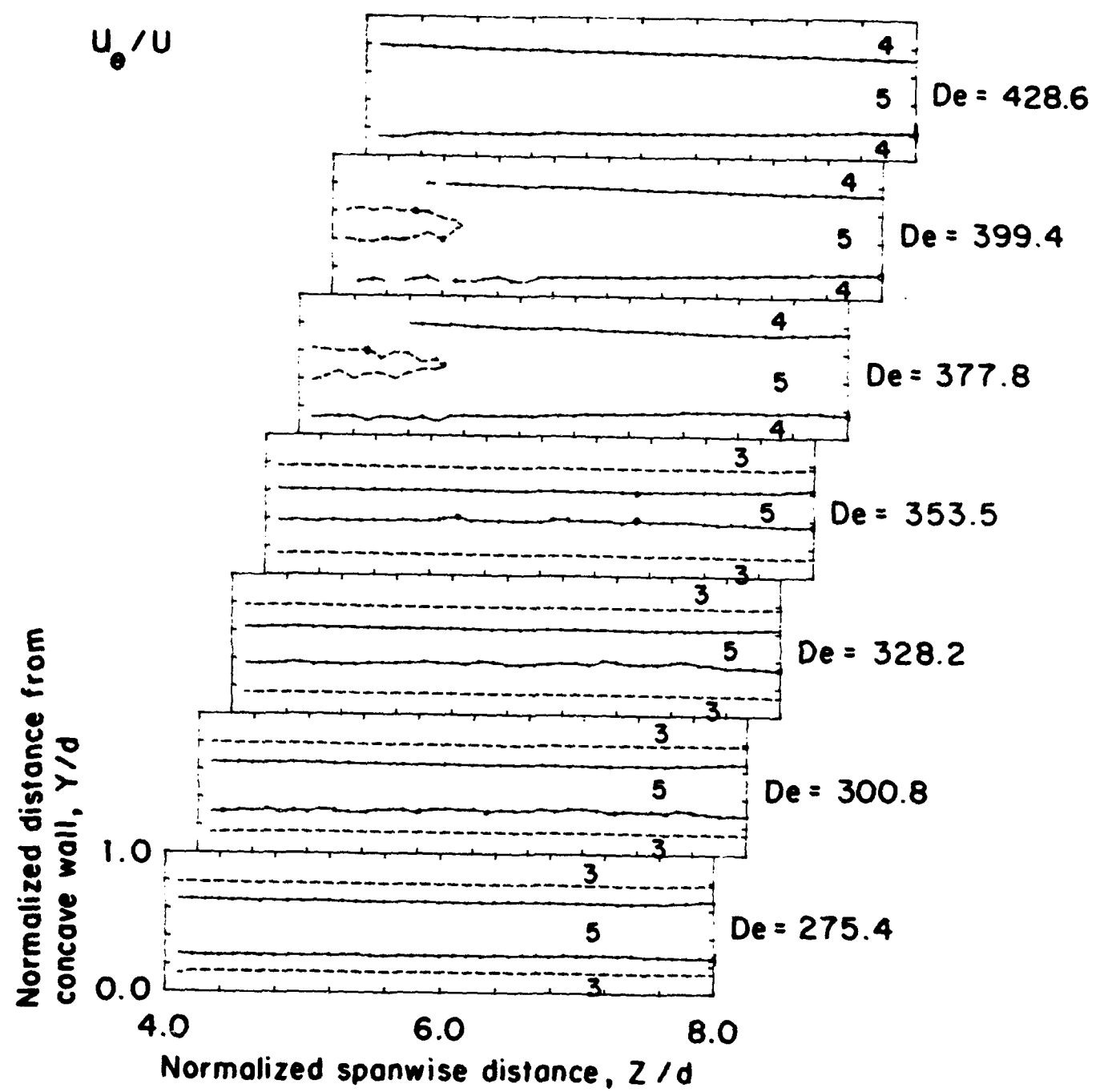


FIG. 33. Streamwise velocity contours,  $De=275.4$  to  $De=428.6$ .

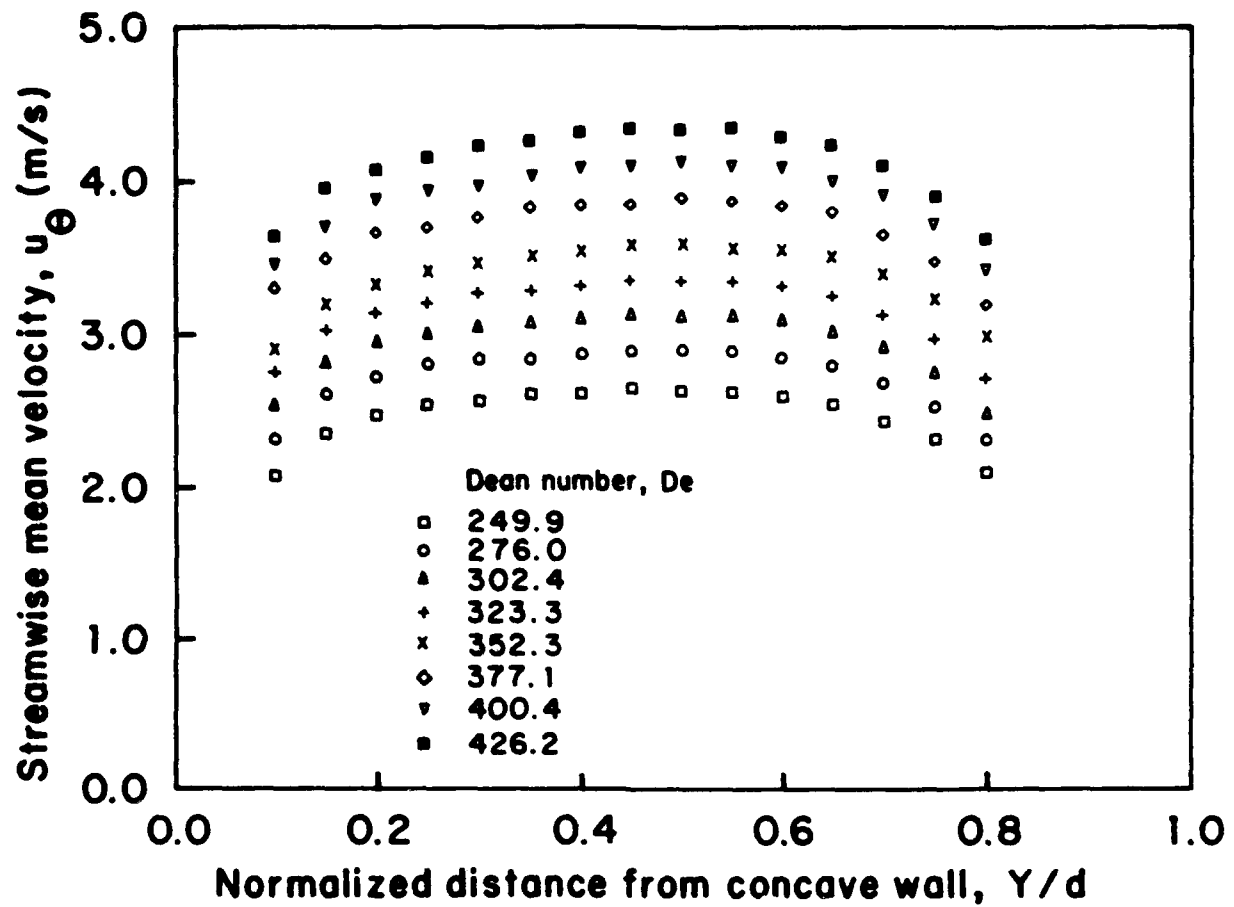


FIG. 34. Streamwise velocity profiles,  $De=249.9$  to  $De=426.2$ .

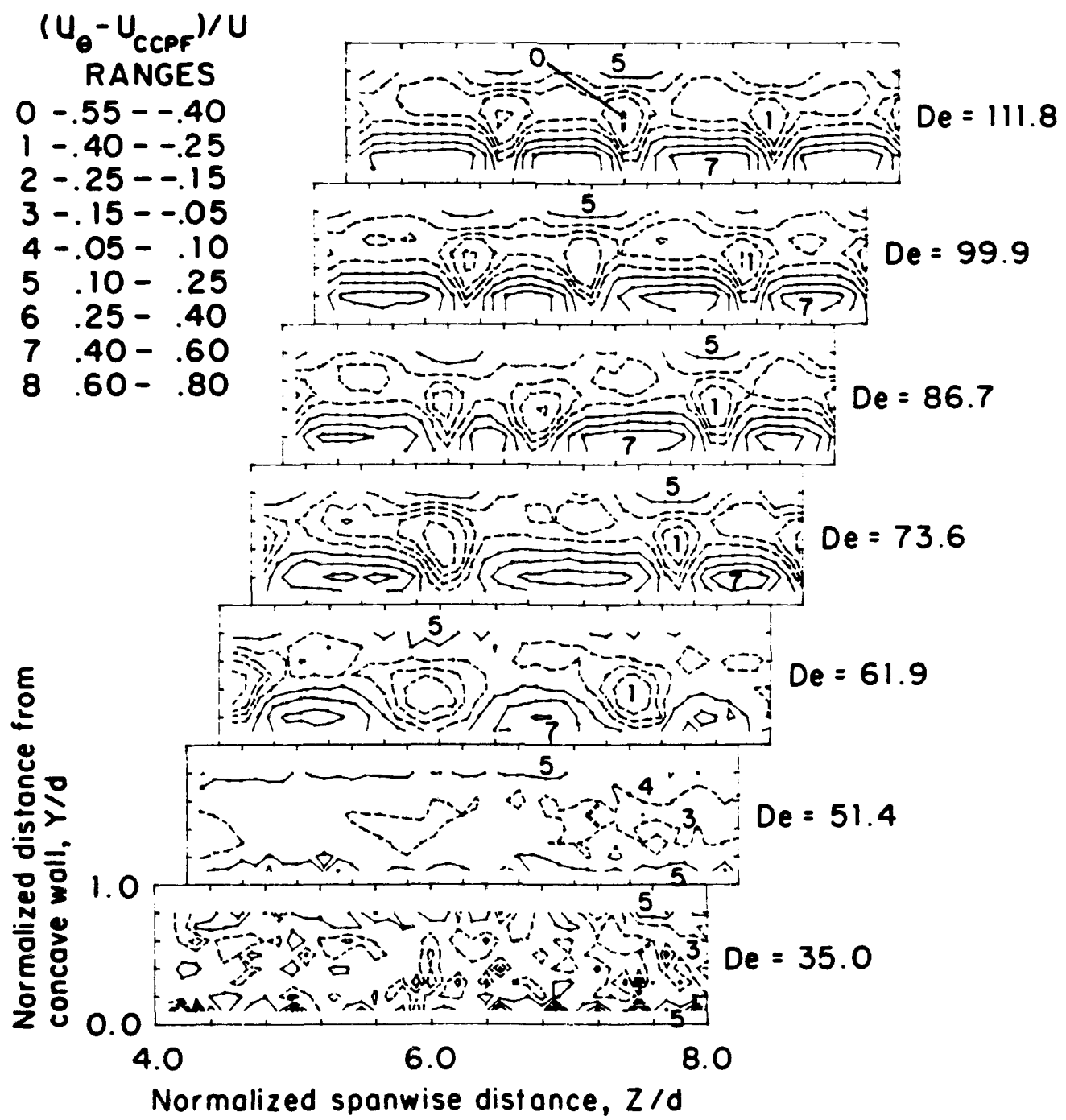


FIG. 35. Streamwise velocity perturbation contours,  $De=35.0$  to  $De=111.8$ .

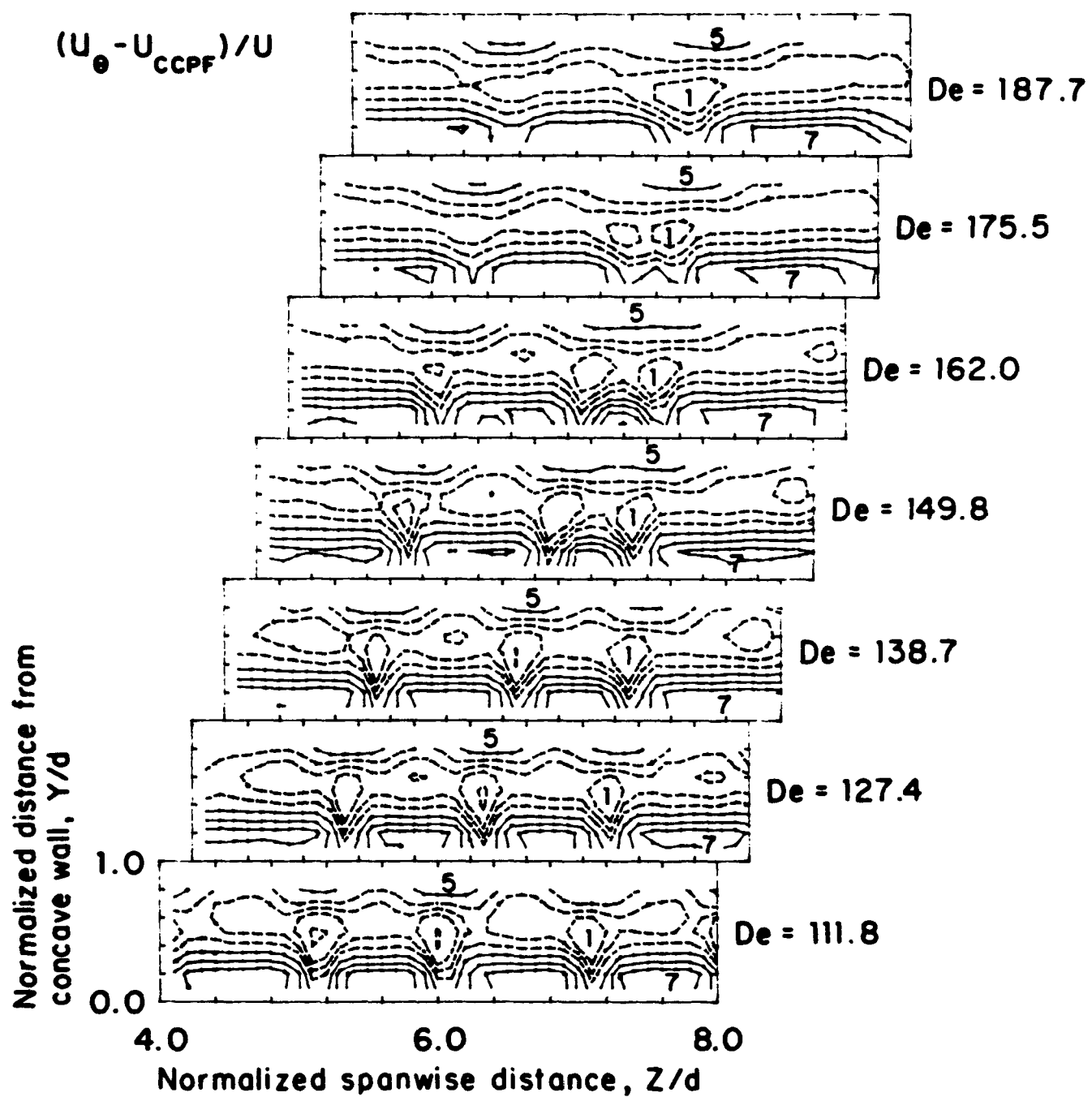


FIG. 36. Streamwise velocity perturbation contours,  $De=111.8$  to  $De=187.7$ .

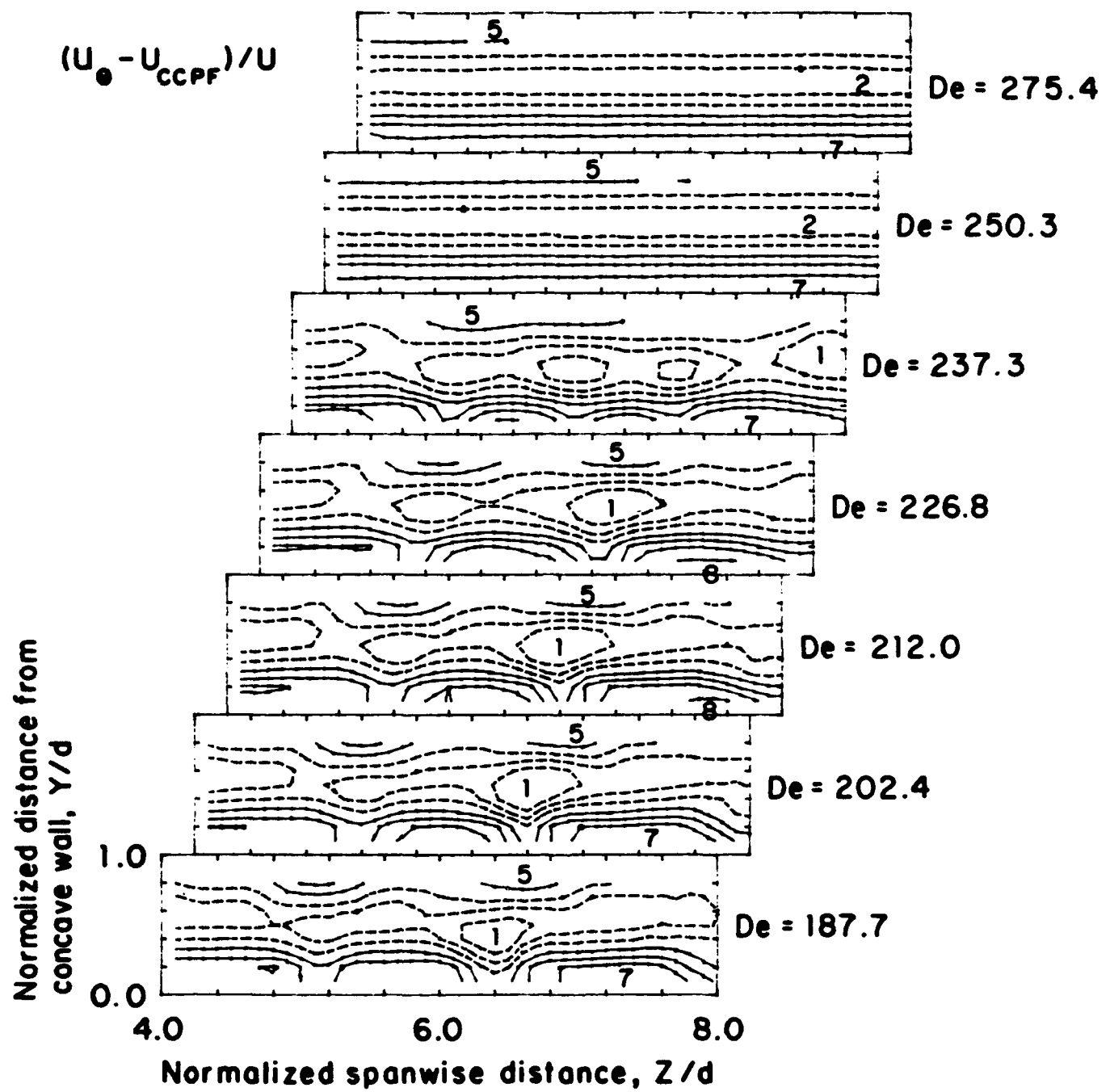


FIG. 37. Streamwise velocity perturbation contours,  $De=187.7$  to  $De=275.4$ .

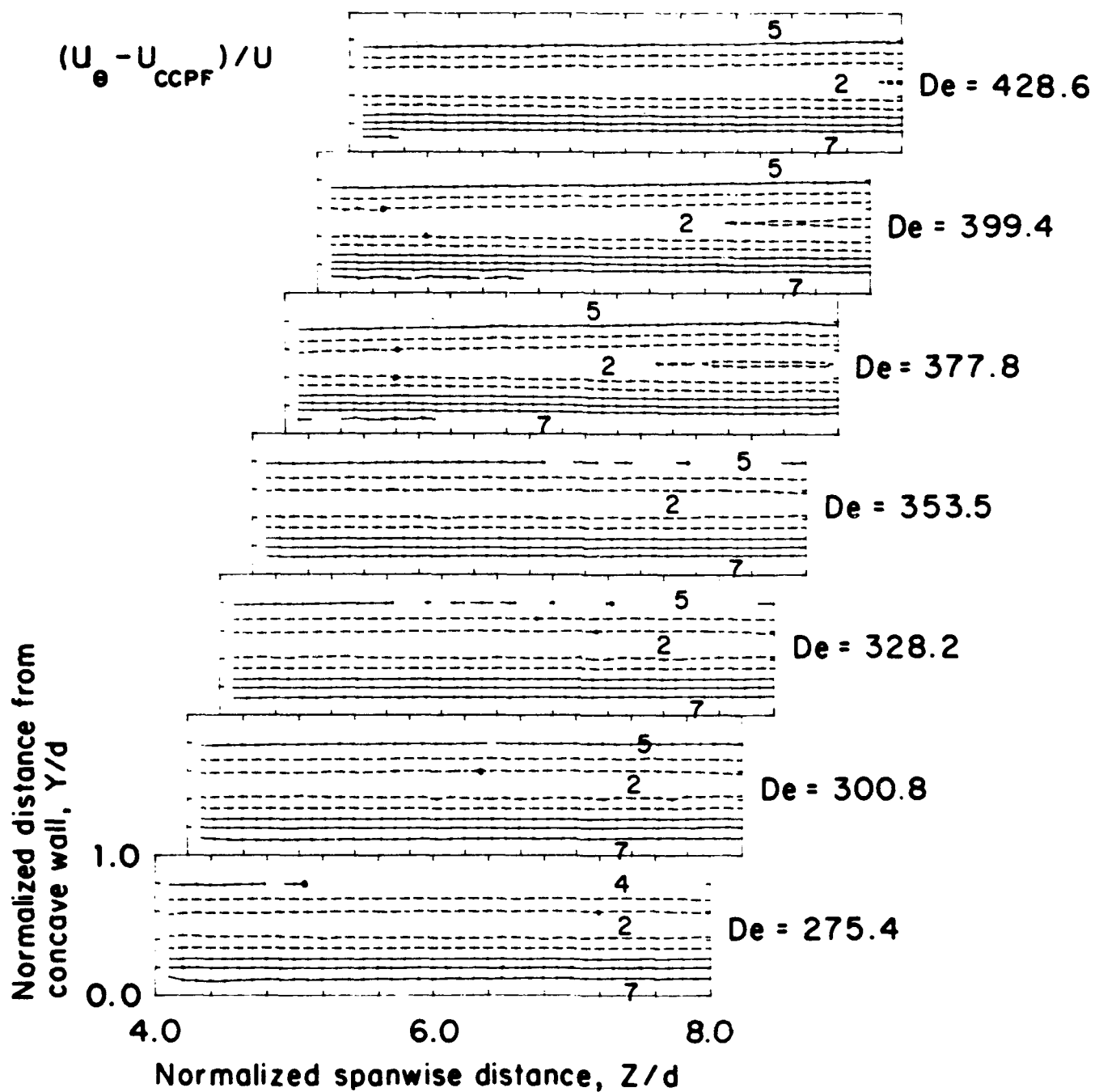


FIG. 38. Streamwise velocity perturbation contours,  $De=275.4$  to  $De=428.6$ .

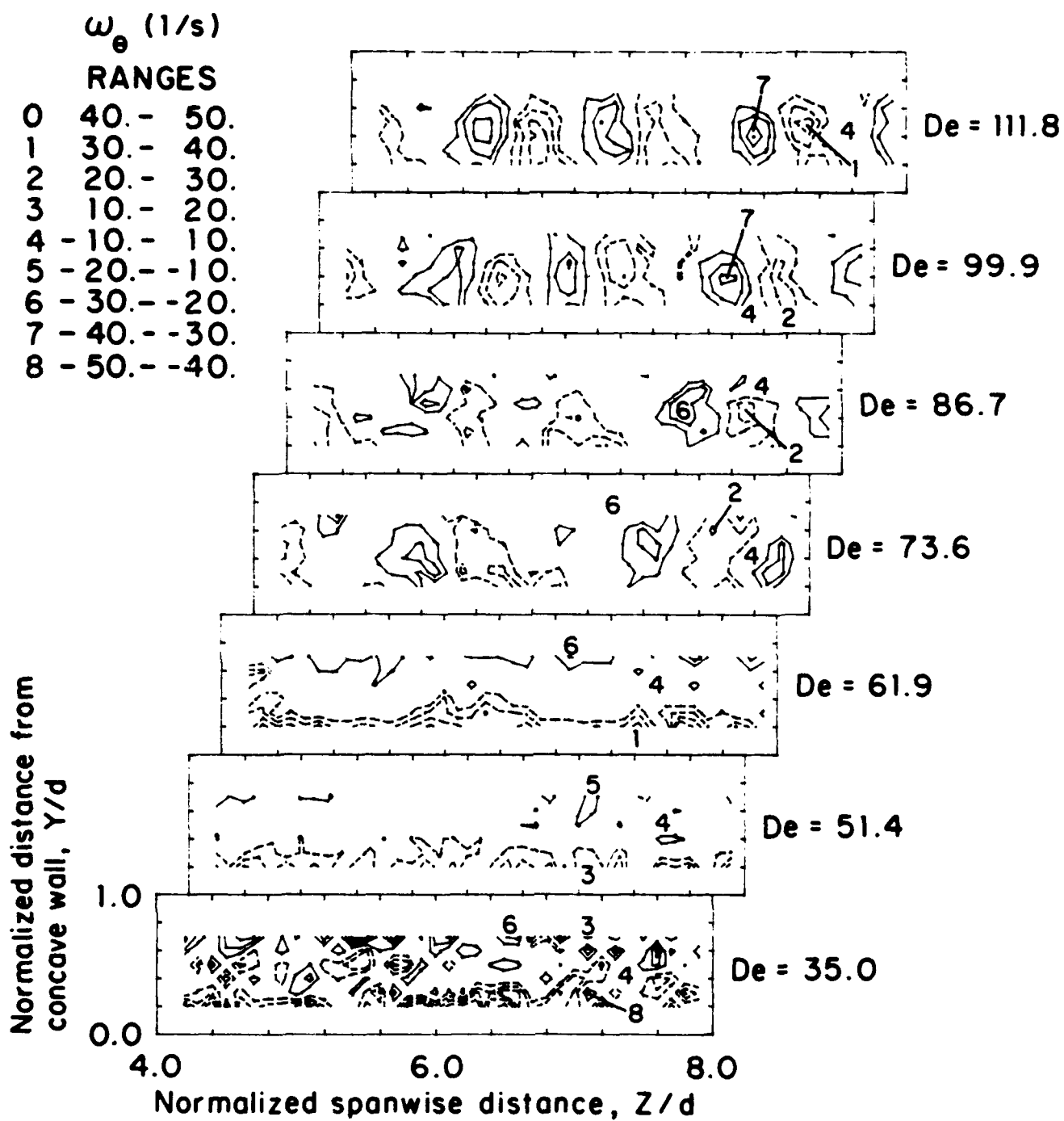


FIG. 39. Streamwise vorticity contours,  $De=35.0$  to  $De=111.8$ .

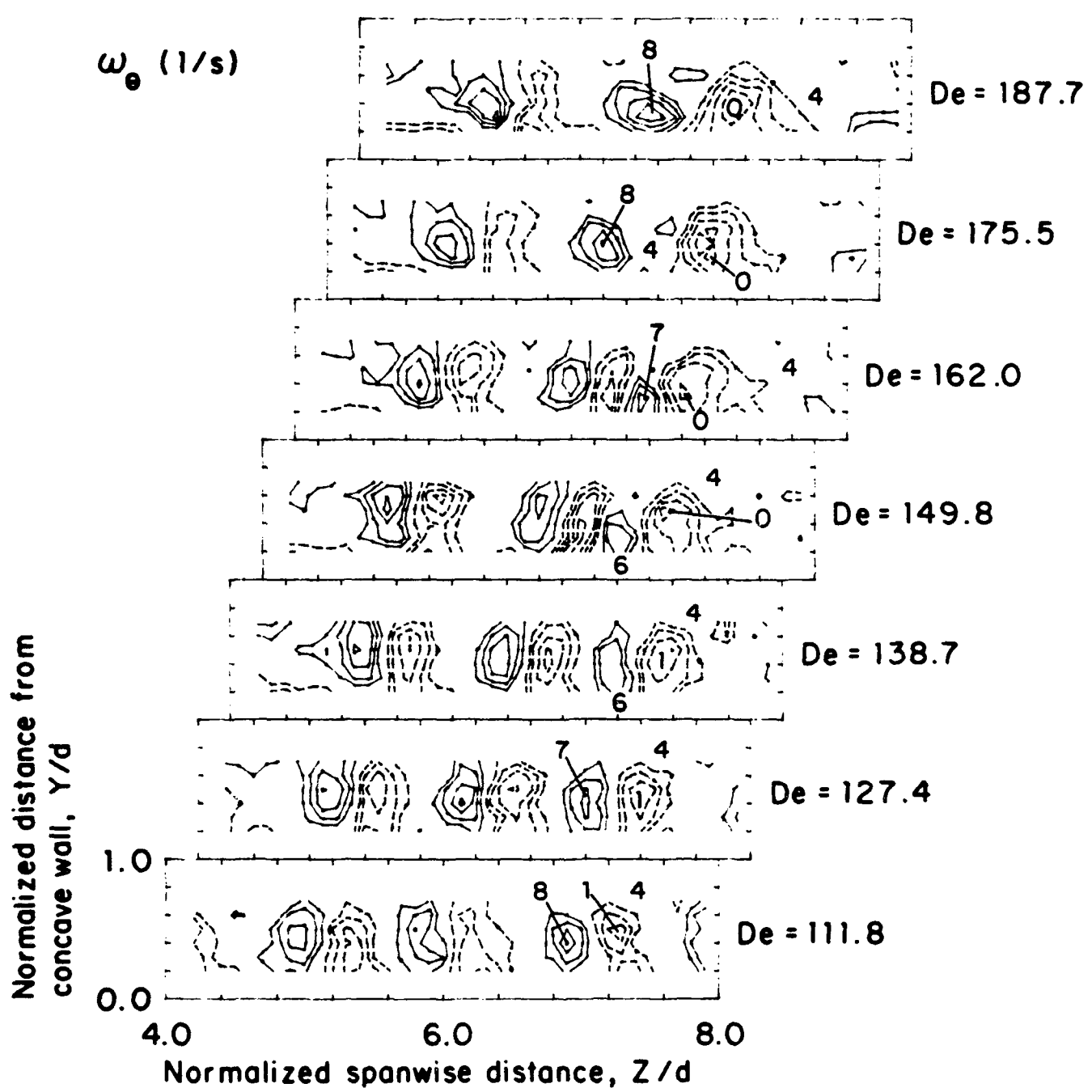


FIG. 40. Streamwise vorticity contours,  $De=111.8$  to  $De=187.7$ .

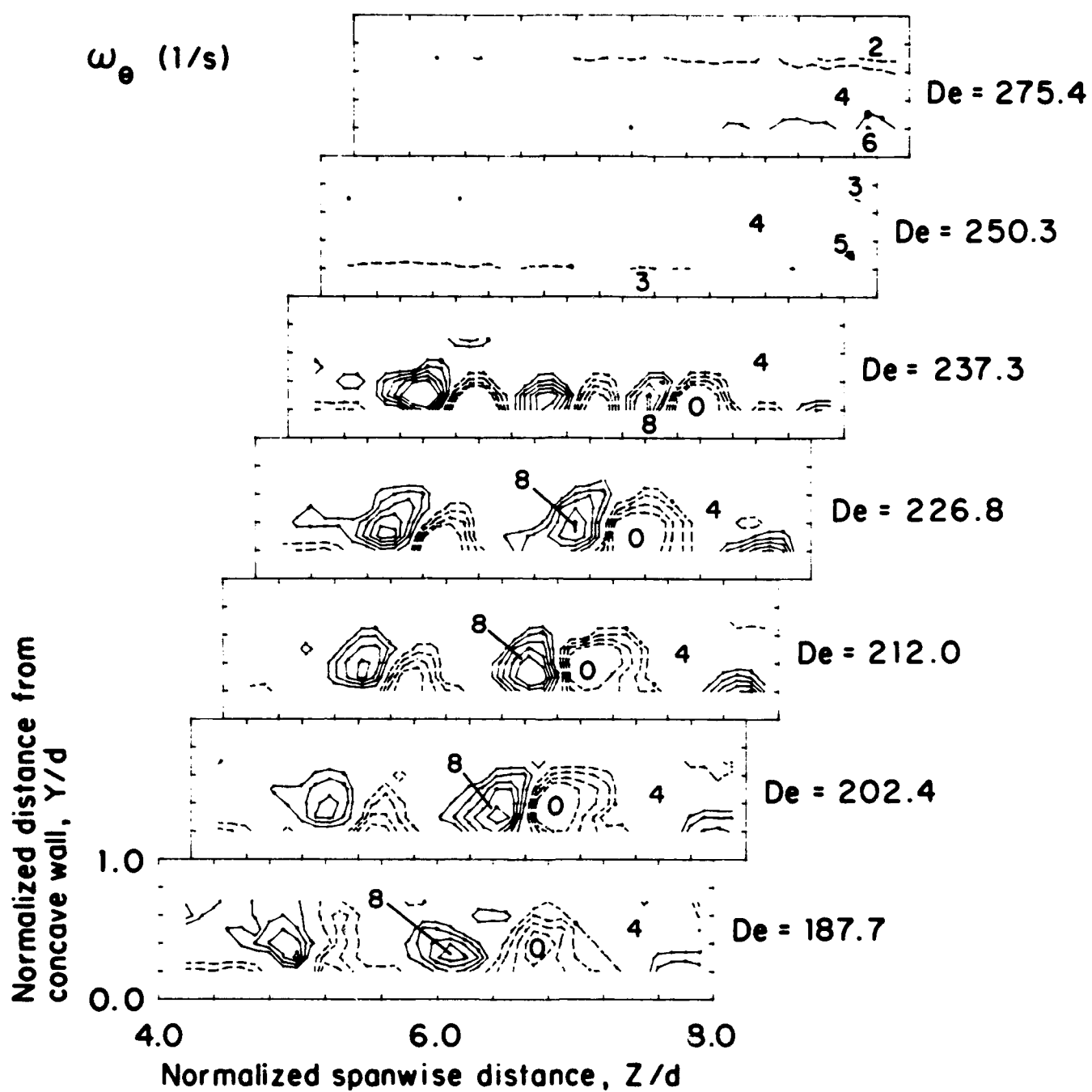


FIG. 41. Streamwise vorticity contours,  $De=187.7$  to  $De=275.4$ .

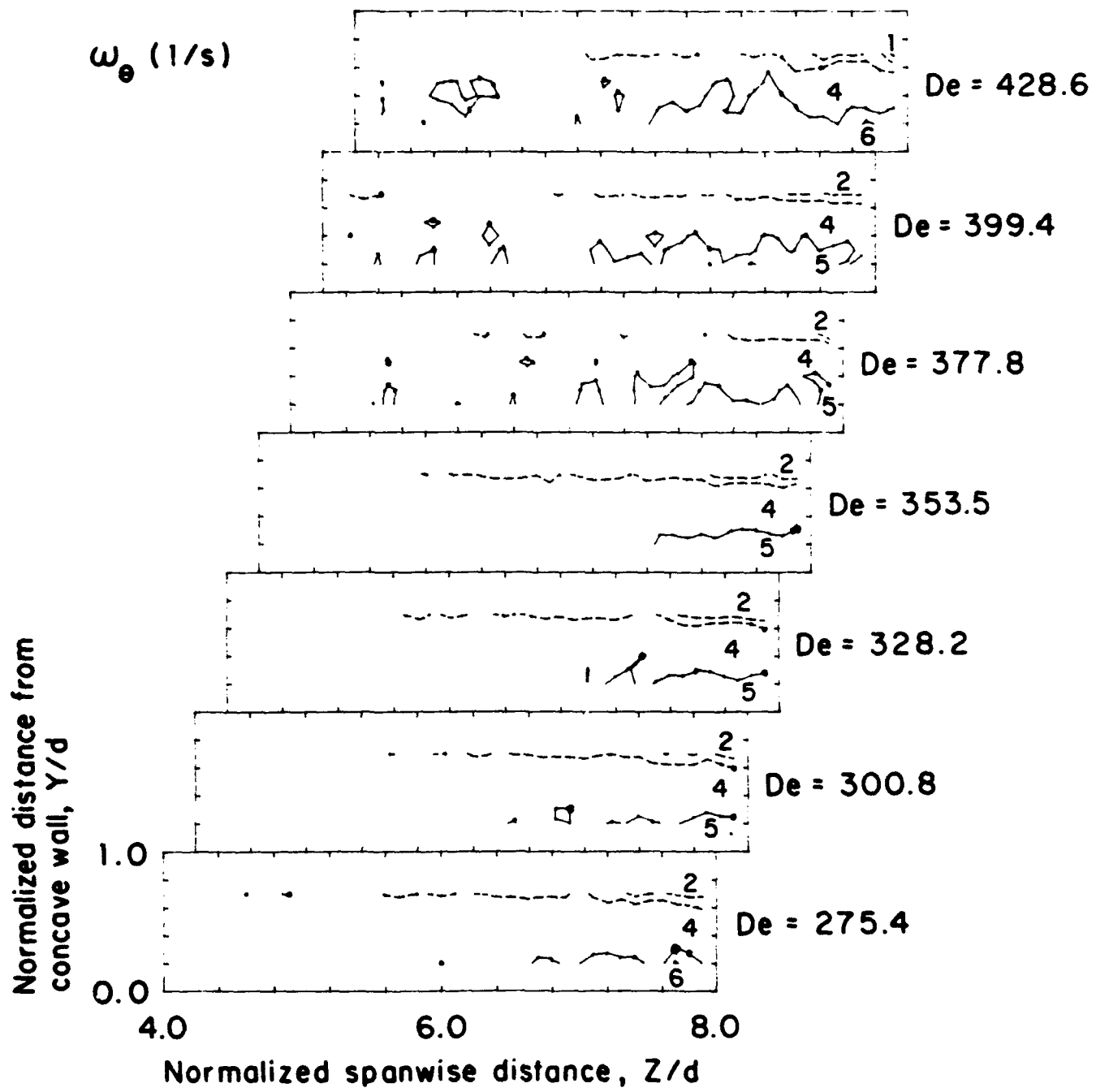


FIG. 42. Streamwise vorticity contours,  $De=275.4$  to  $De=428.6$ .

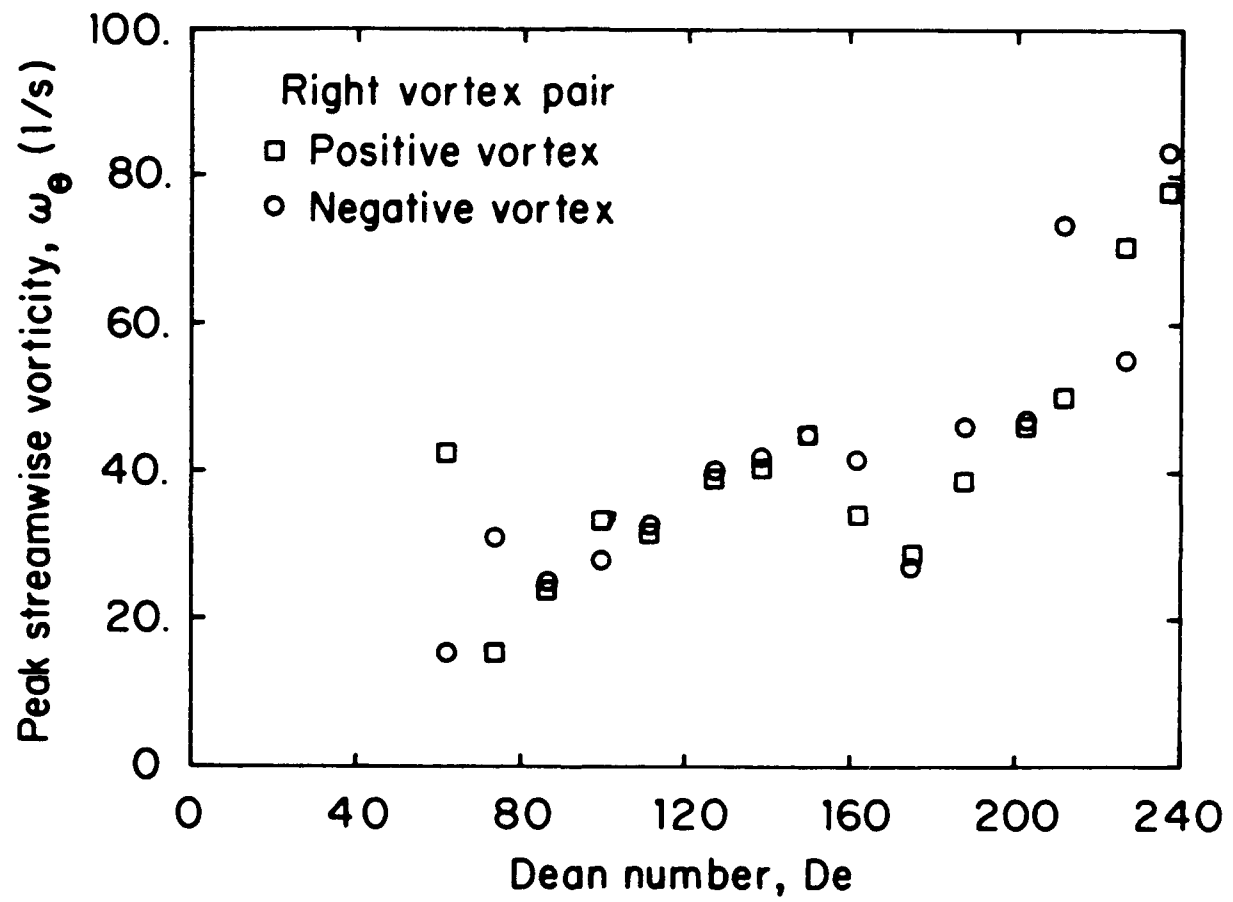


FIG. 43. Peak streamwise vorticity versus Dean number, right vortex pair.

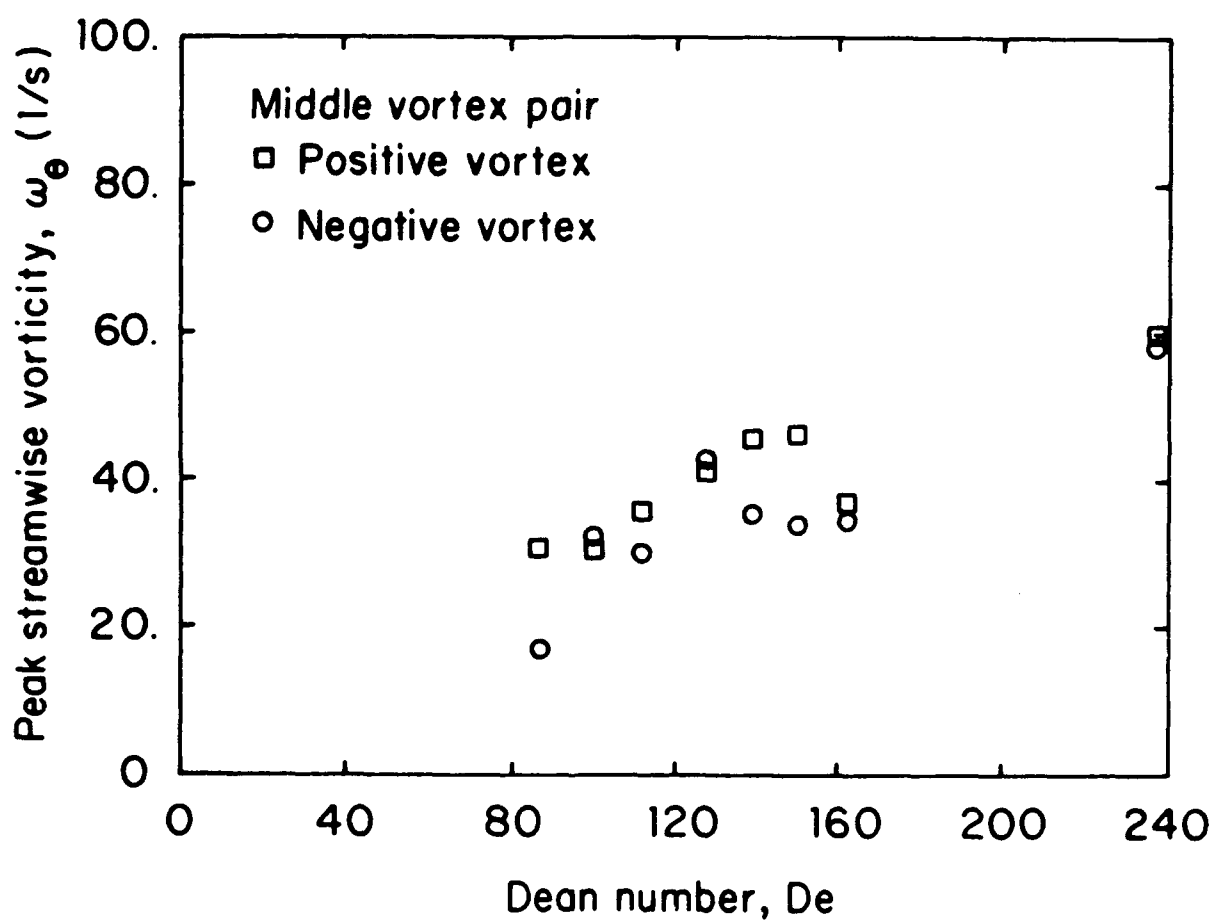


FIG. 44. Peak streamwise vorticity versus Dean number, middle vortex pair.

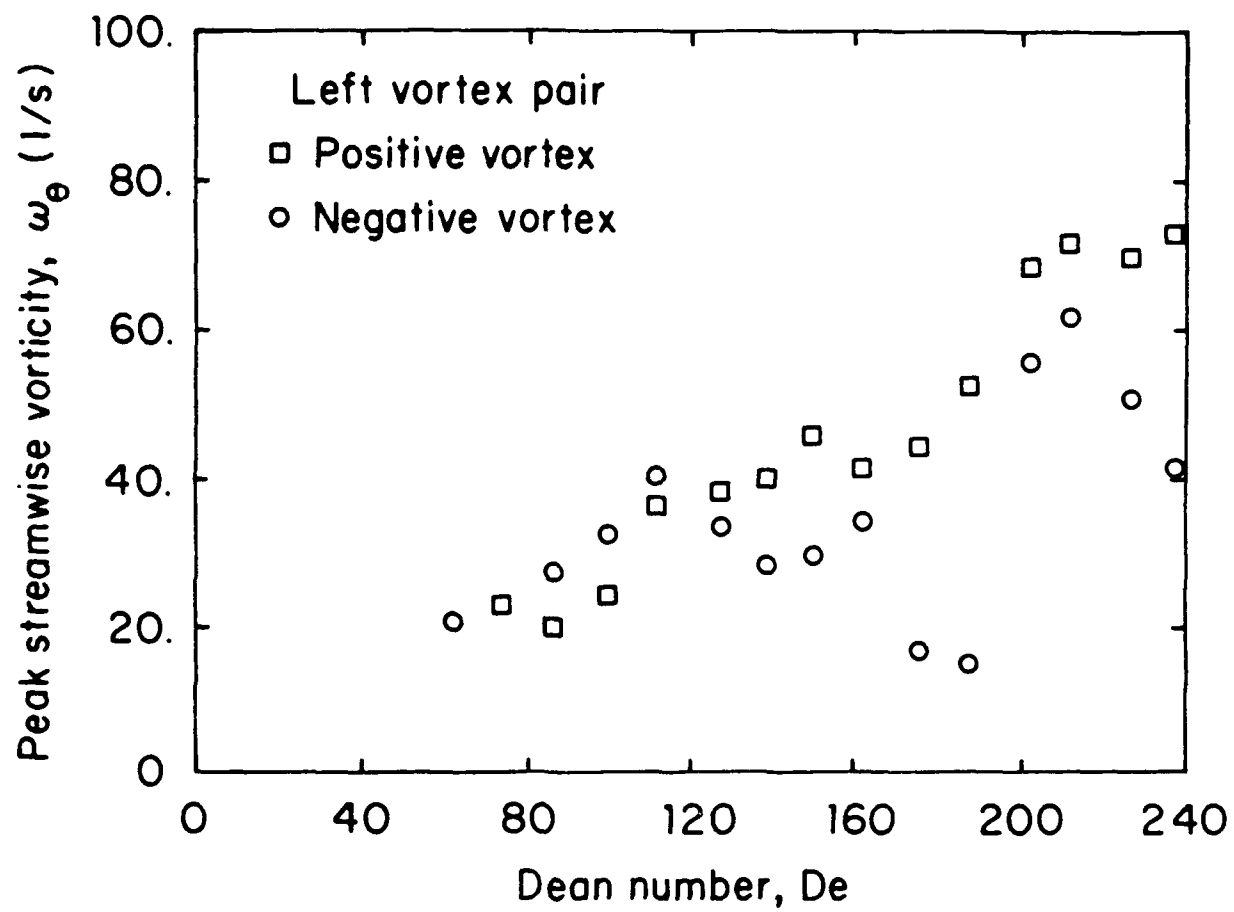


FIG. 45. Peak streamwise vorticity versus Dean number, left vortex pair.

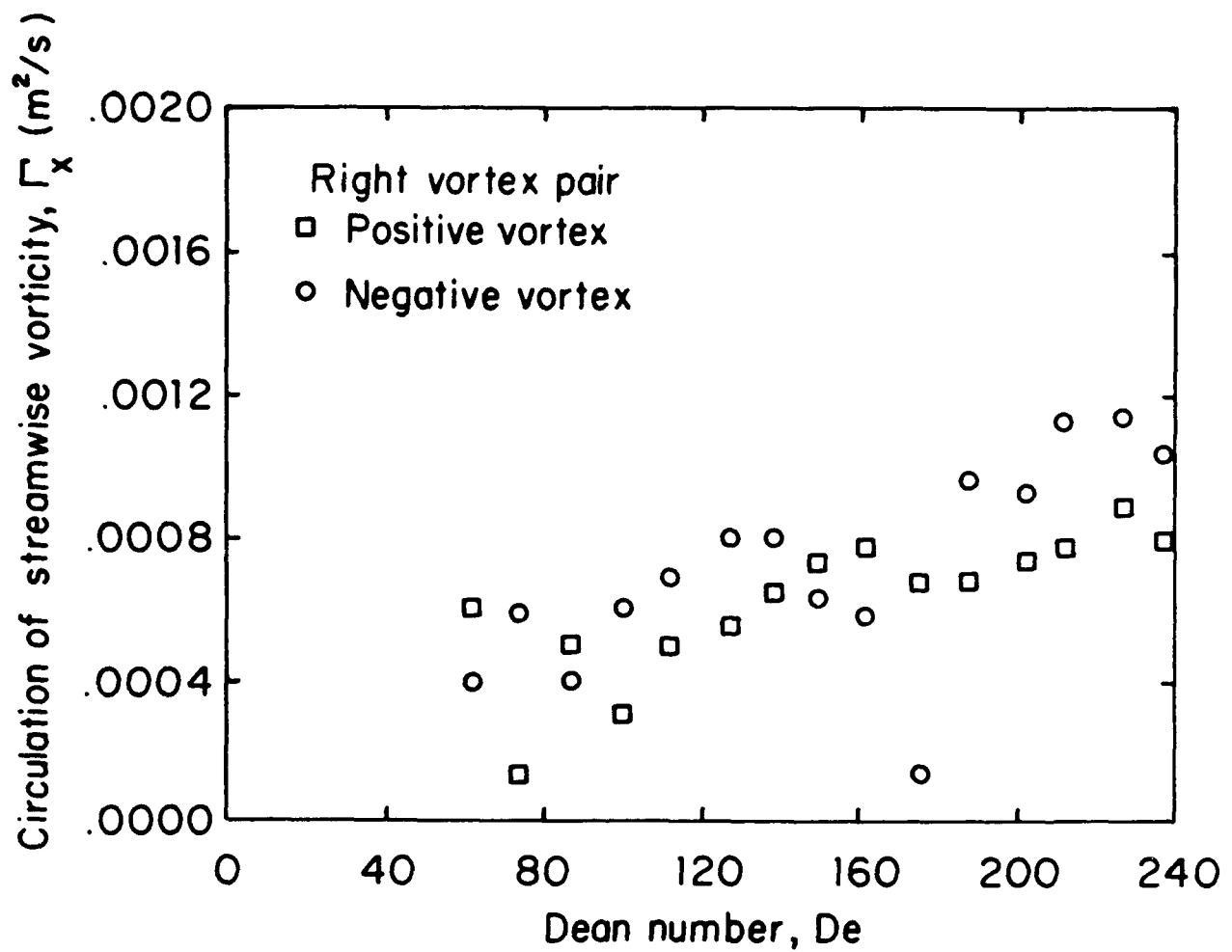


FIG. 46. Vortex circulation versus Dean number, right vortex pair.

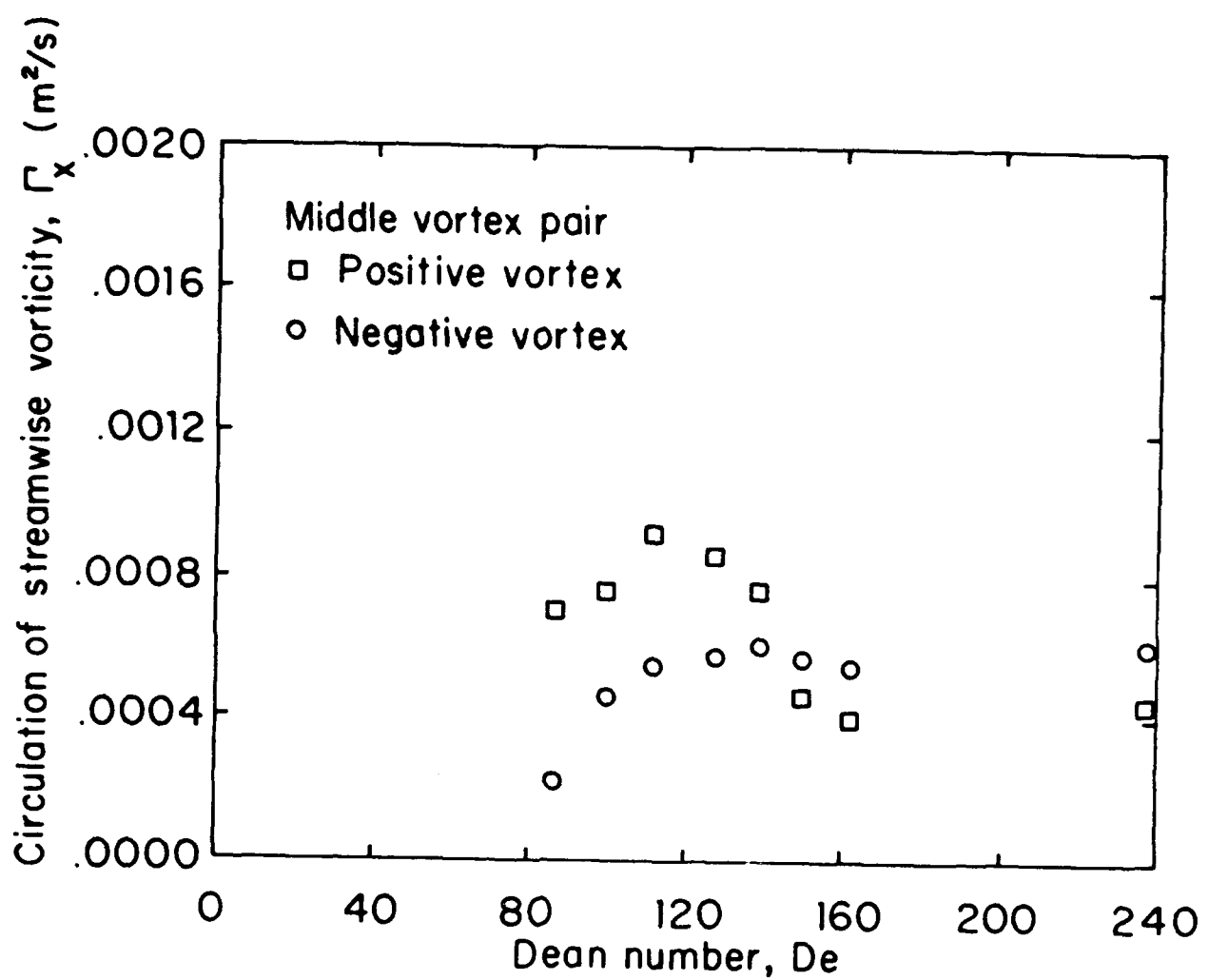


FIG. 47. Vortex circulation versus Dean number, middle vortex pair.

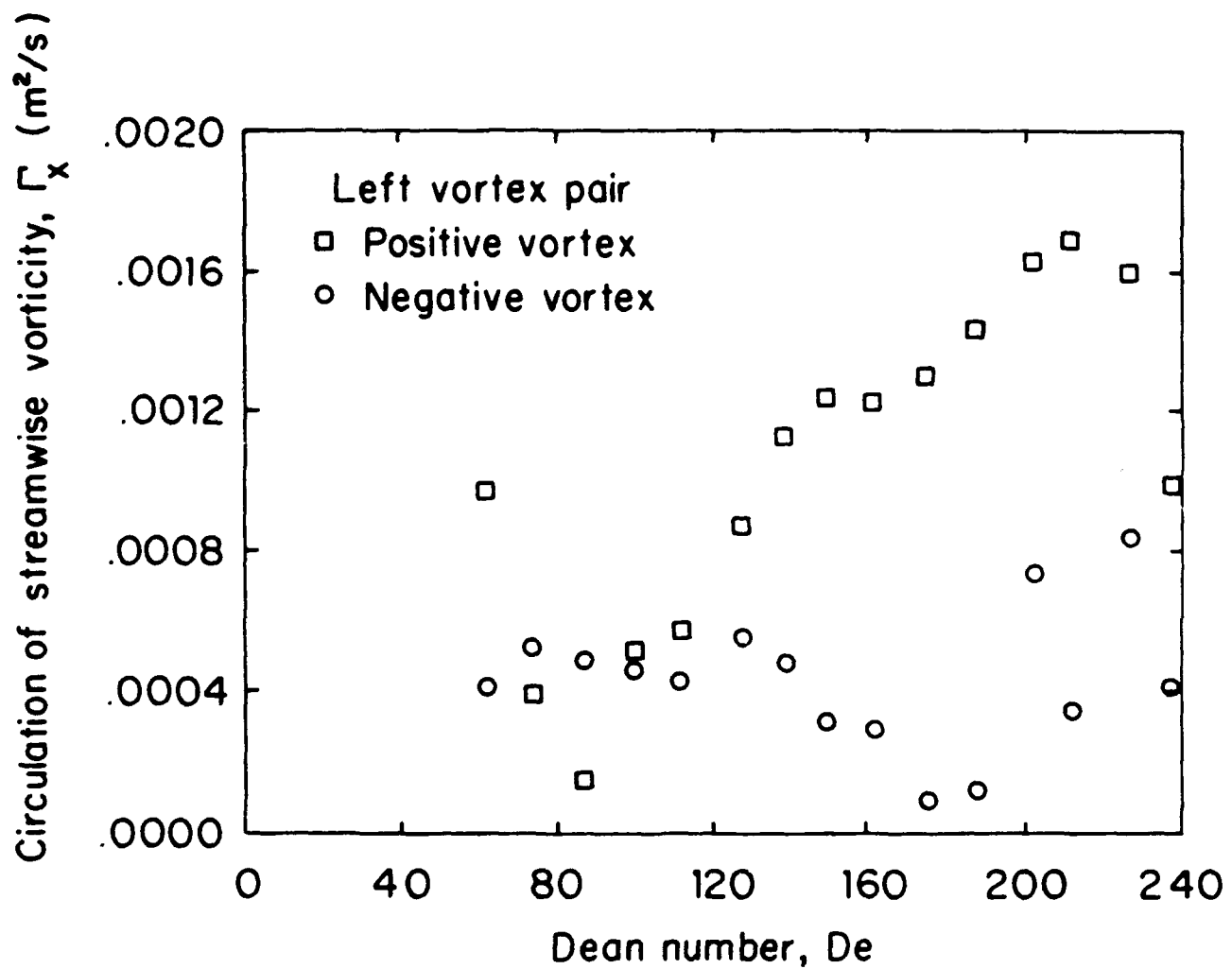


FIG. 48. Vortex circulation versus Dean number, left vortex pair.

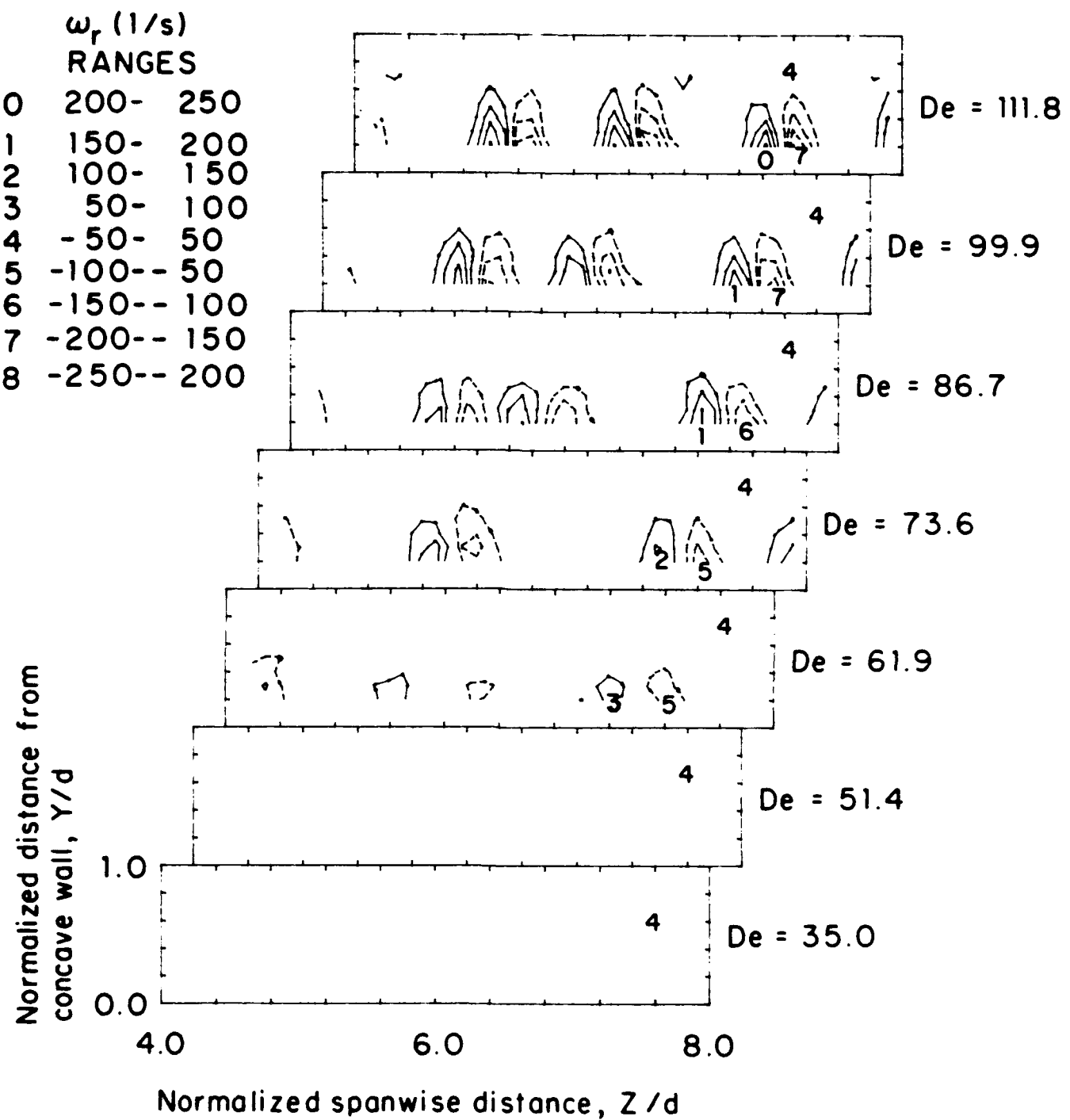


FIG. 49. Radial vorticity contours,  $De=35.0$  to  $De=111.8$ .

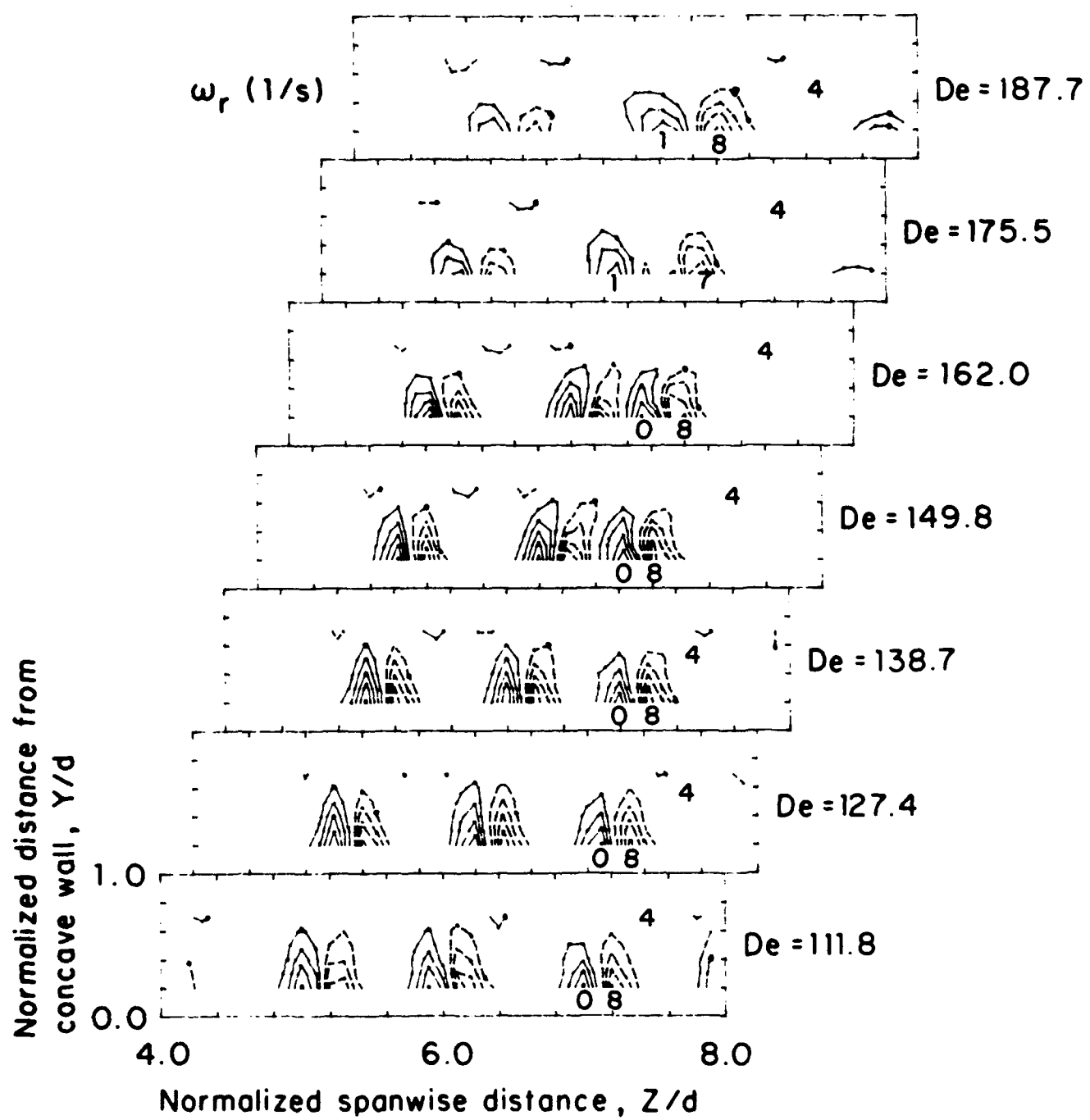


FIG. 50. Radial vorticity contours,  $De=111.8$  to  $De=187.7$ .

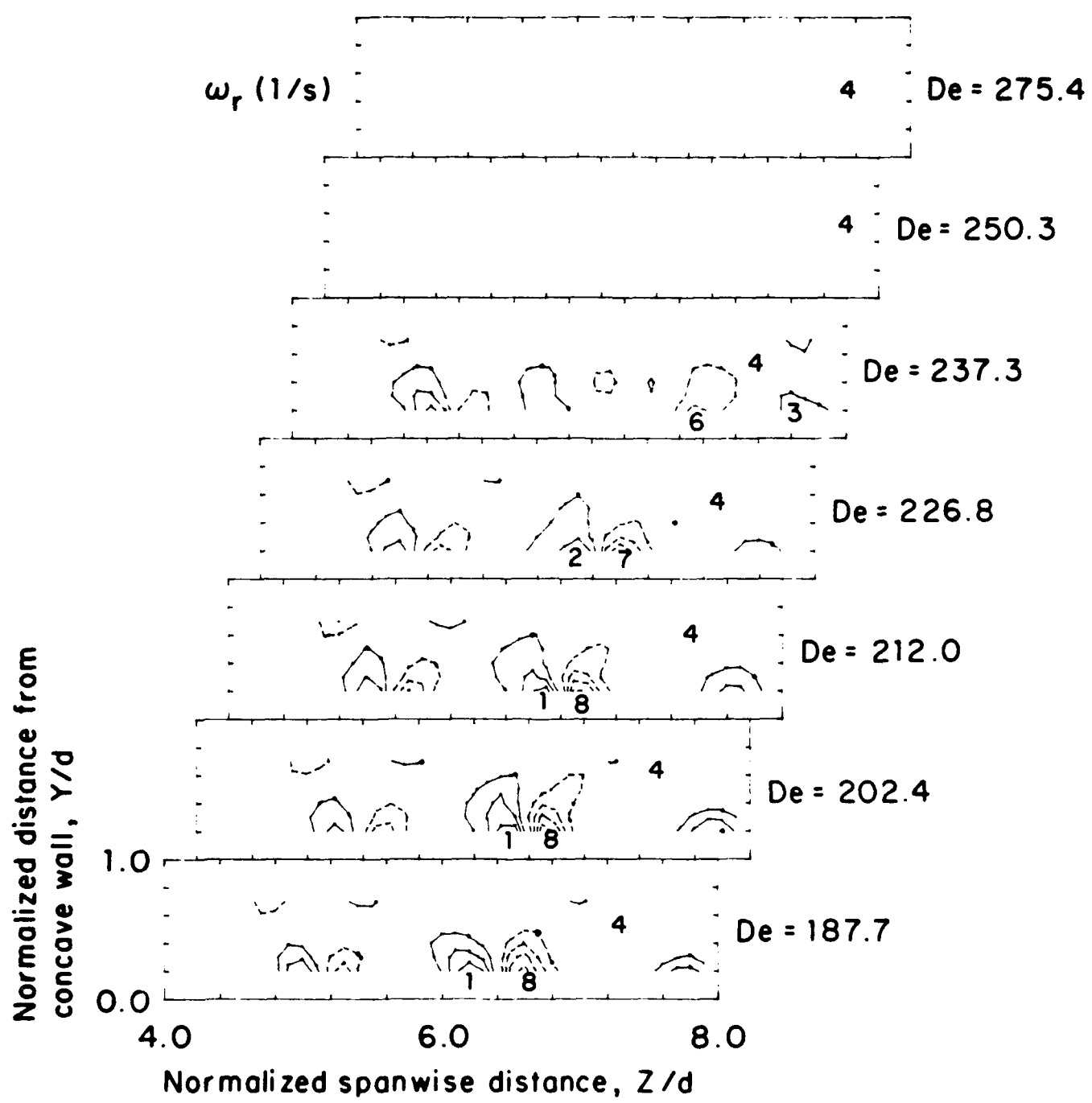


FIG. 51. Radial vorticity contours,  $De=187.7$  to  $De=275.4$ .

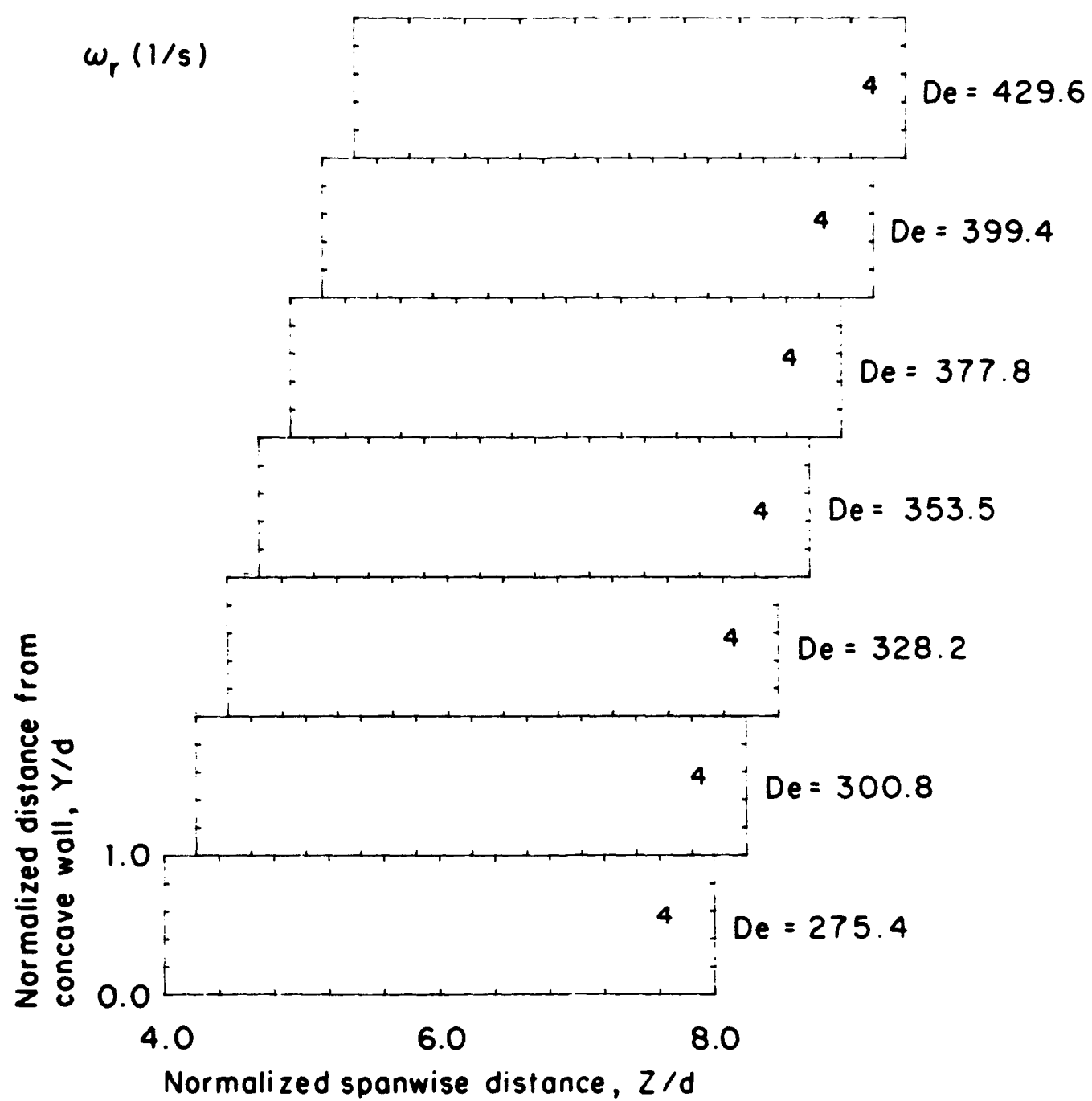


FIG. 52. Radial vorticity contours,  $De=275.4$  to  $De=428.6$ .

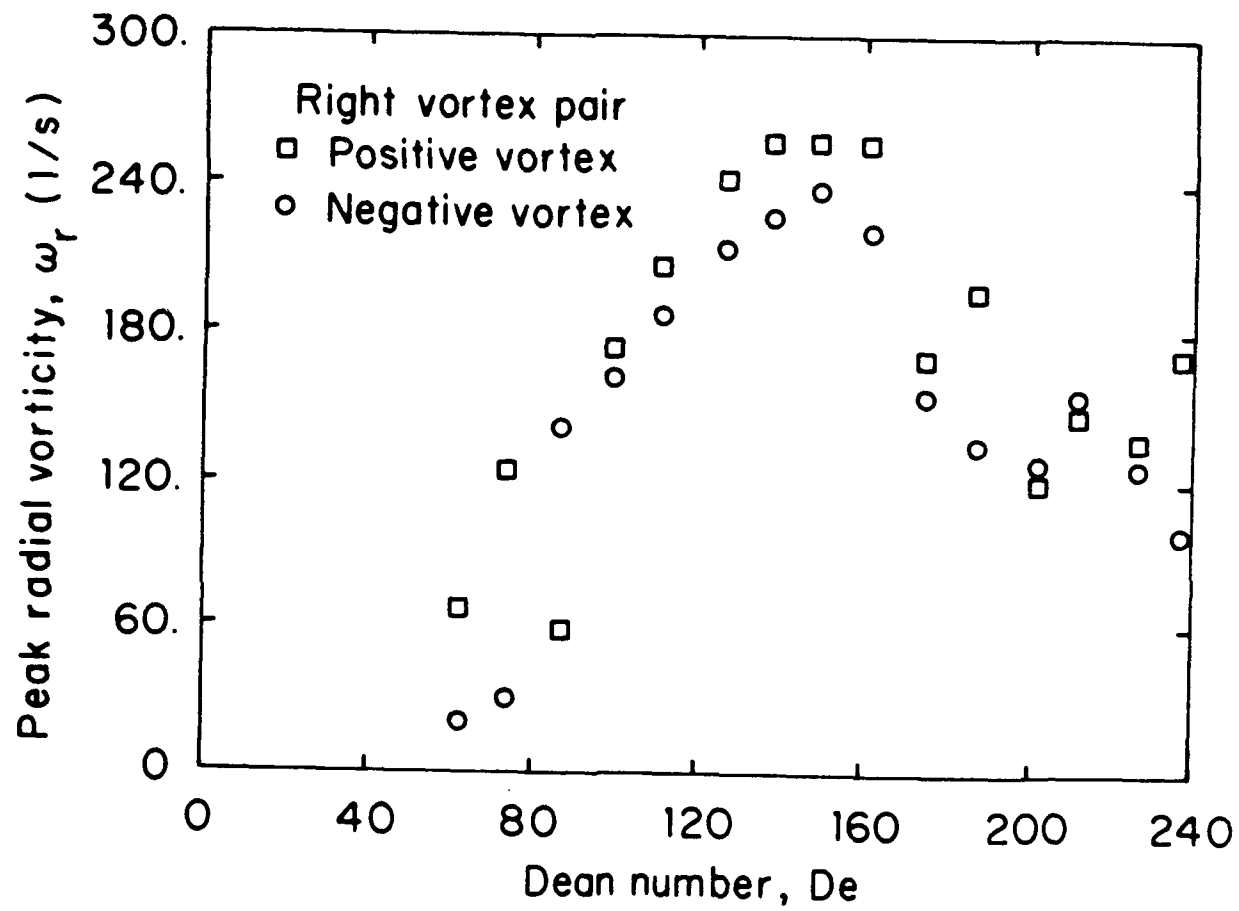


FIG. 53. Peak radial vorticity versus Dean number, right vortex pair.

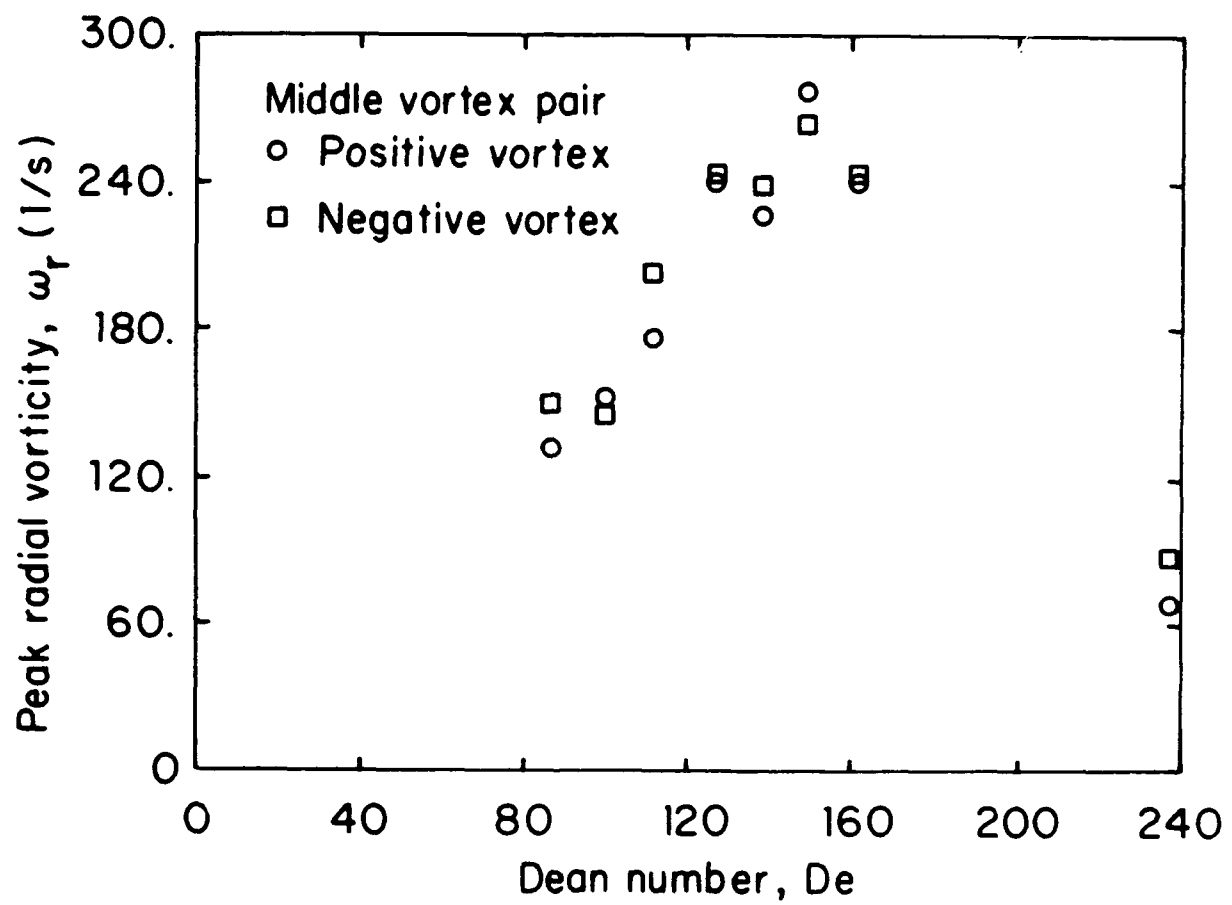


FIG. 54. Peak radial vorticity versus Dean number, middle vortex pair.

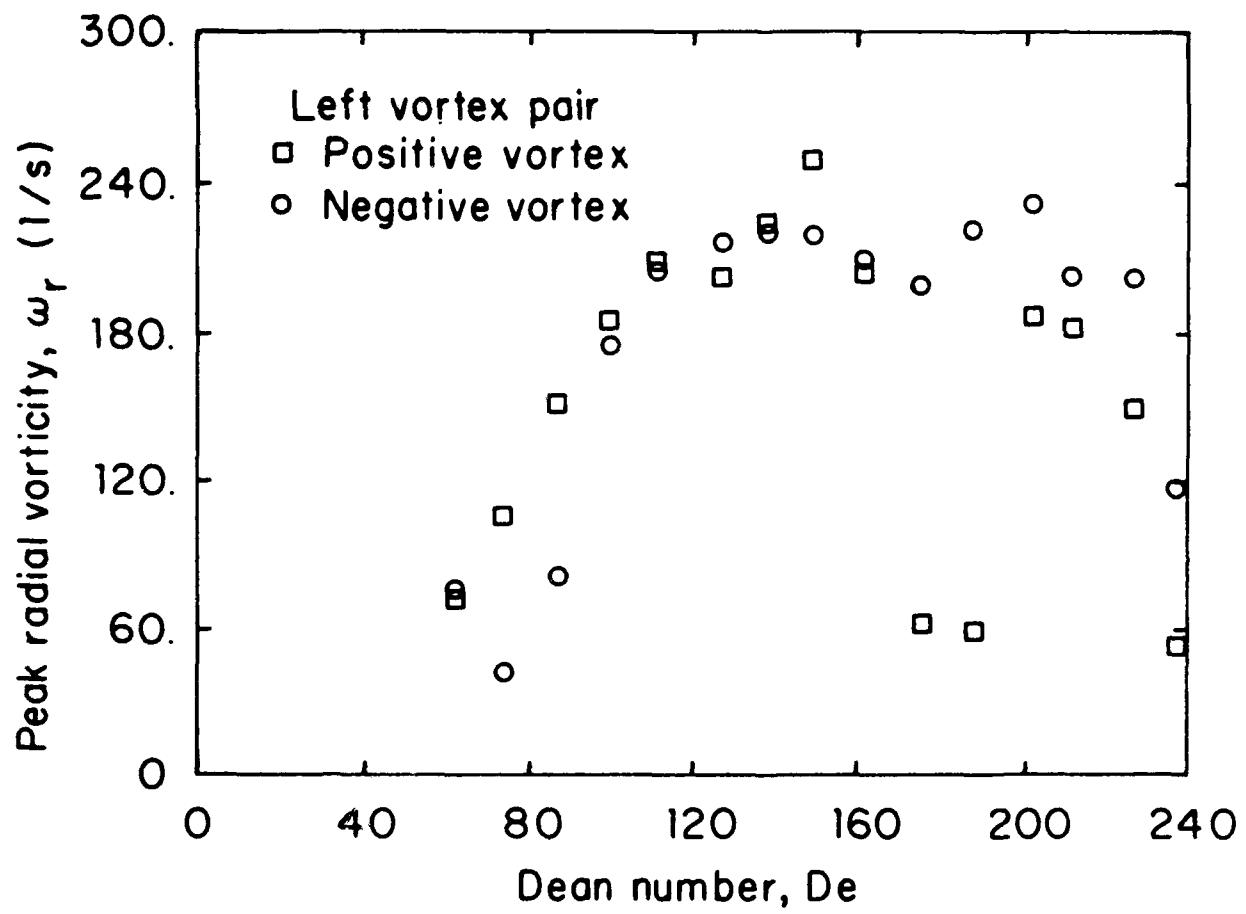


FIG. 55. Peak radial vorticity versus Dean number, left vortex pair.

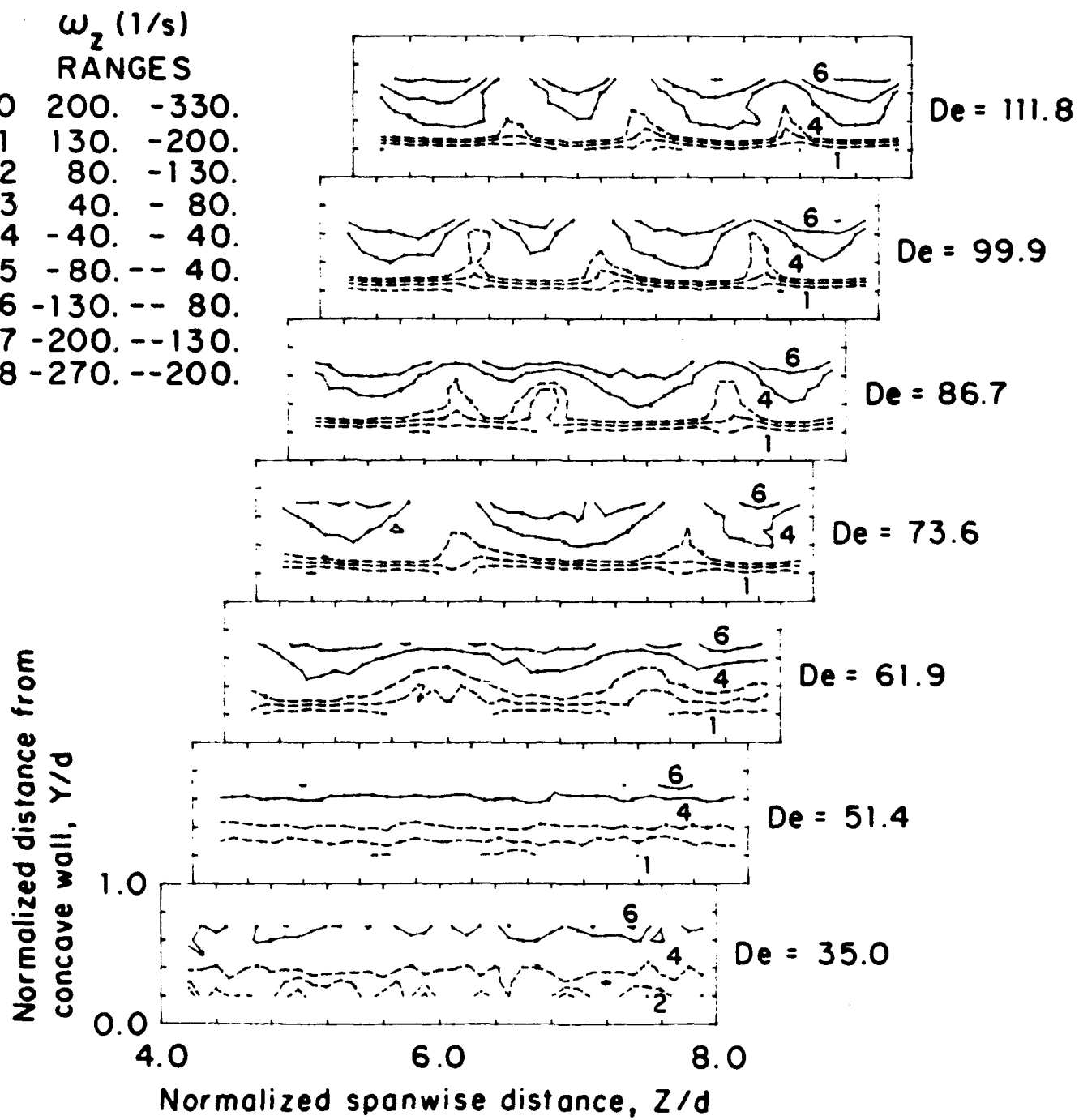


FIG. 56. Spanwise vorticity contours,  $De=35.0$  to  $De=111.8$ .

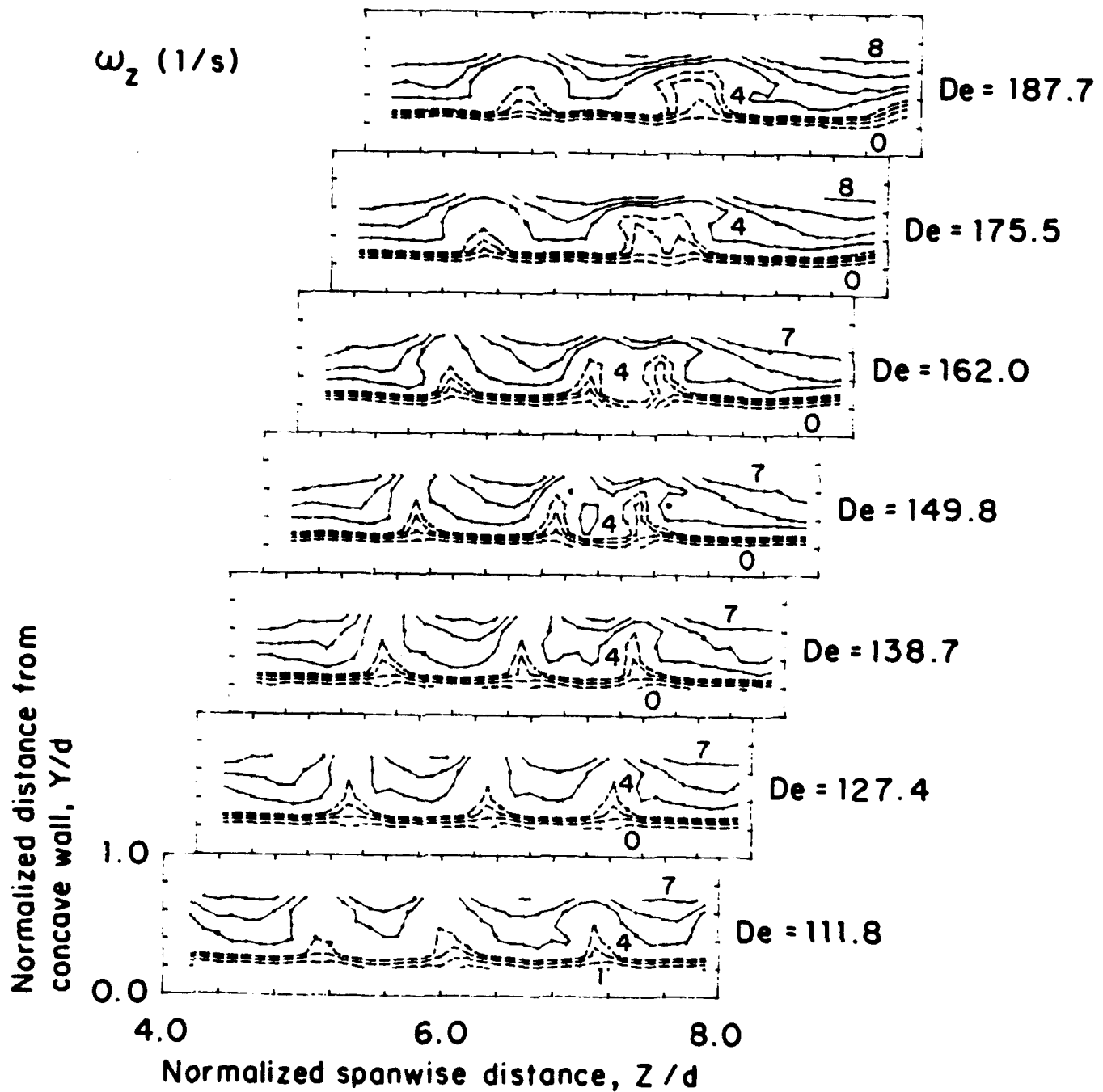


FIG. 57. Spanwise vorticity contours,  $De=111.8$  to  $De=187.7$ .

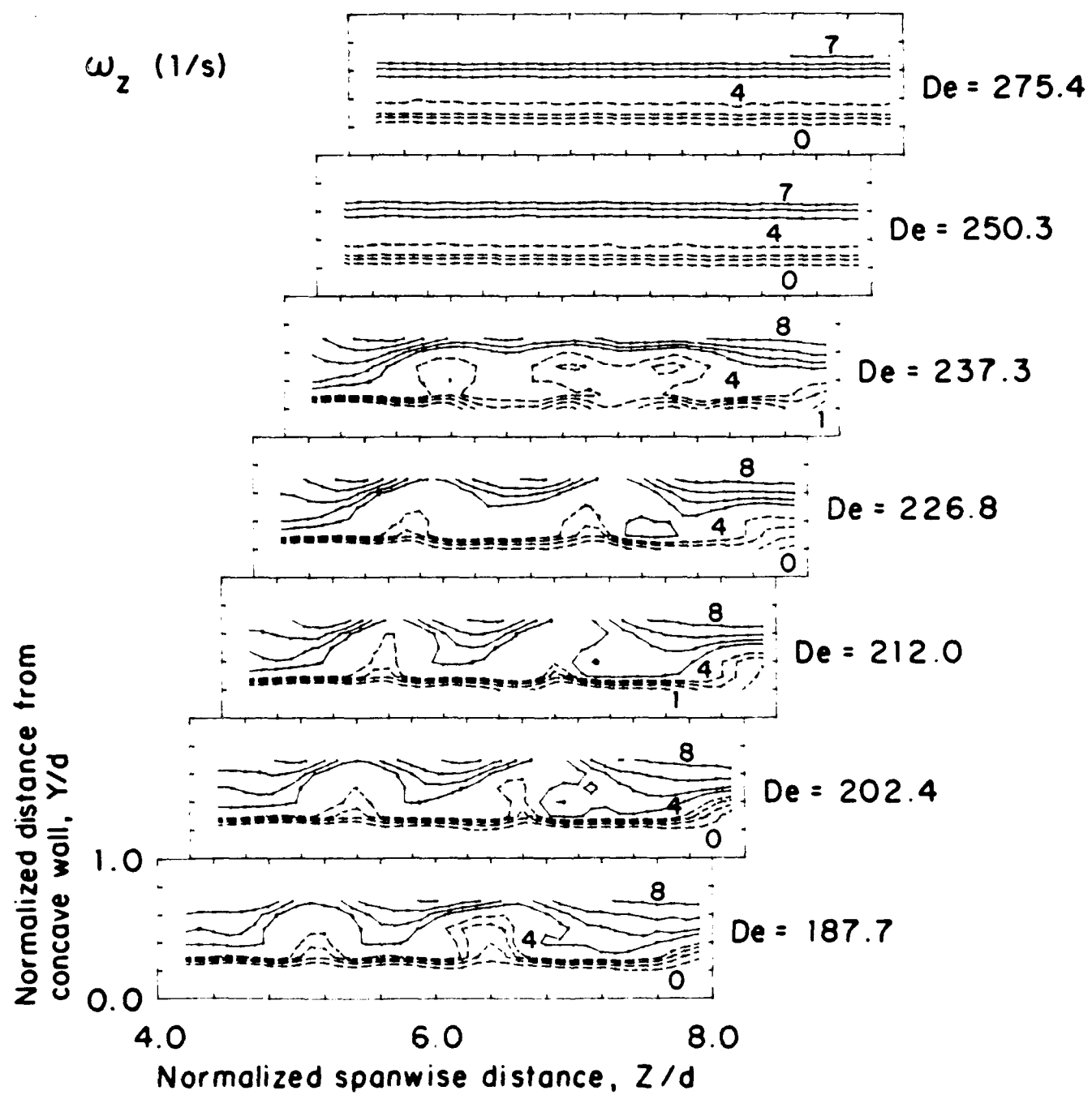


FIG. 58 Spanwise vorticity contours,  $De=187.7$  to  $De=275.4$ .

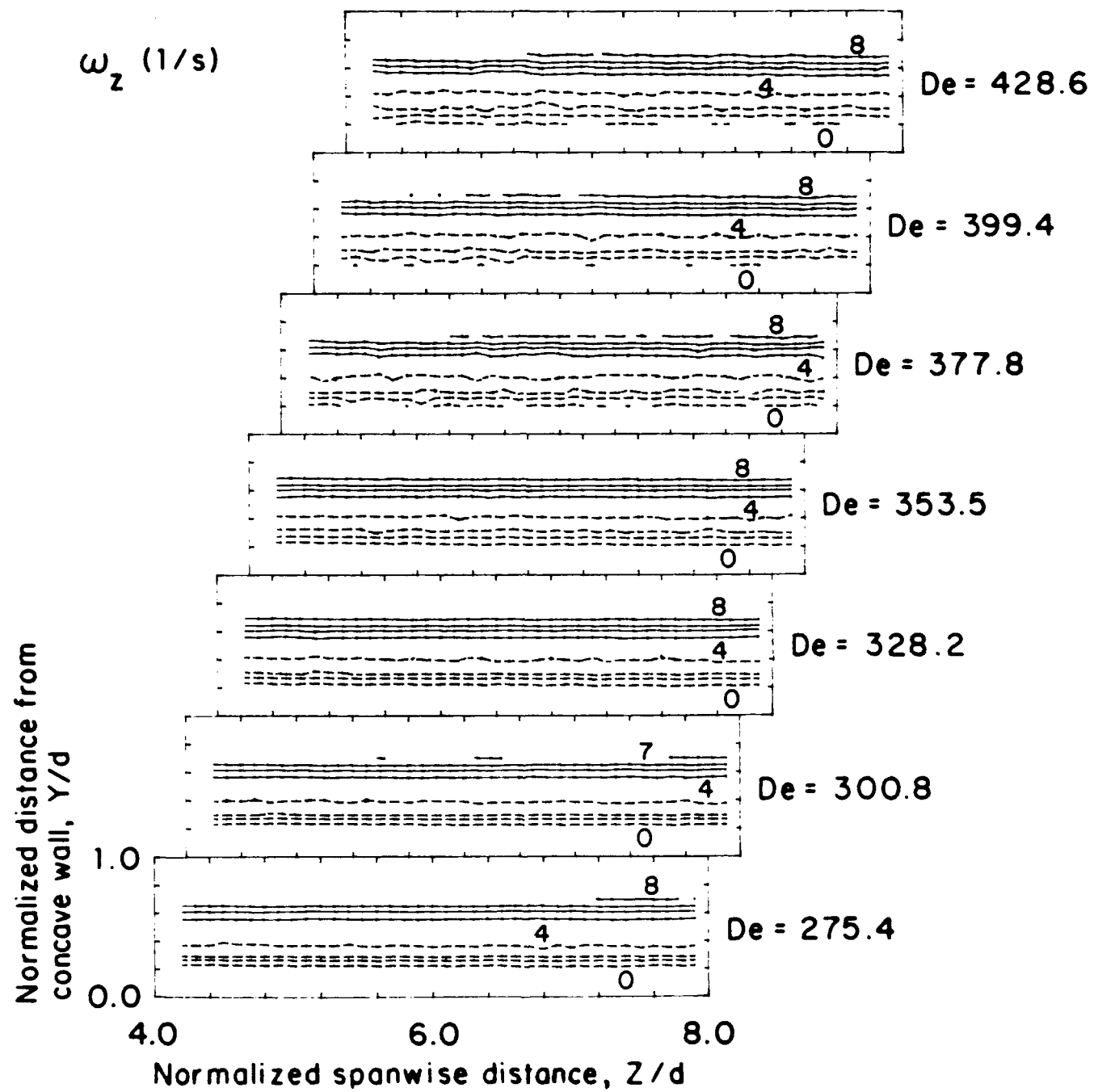


FIG. 59. Spanwise vorticity contours,  $De=275.4$  to  $De=428.6$ .

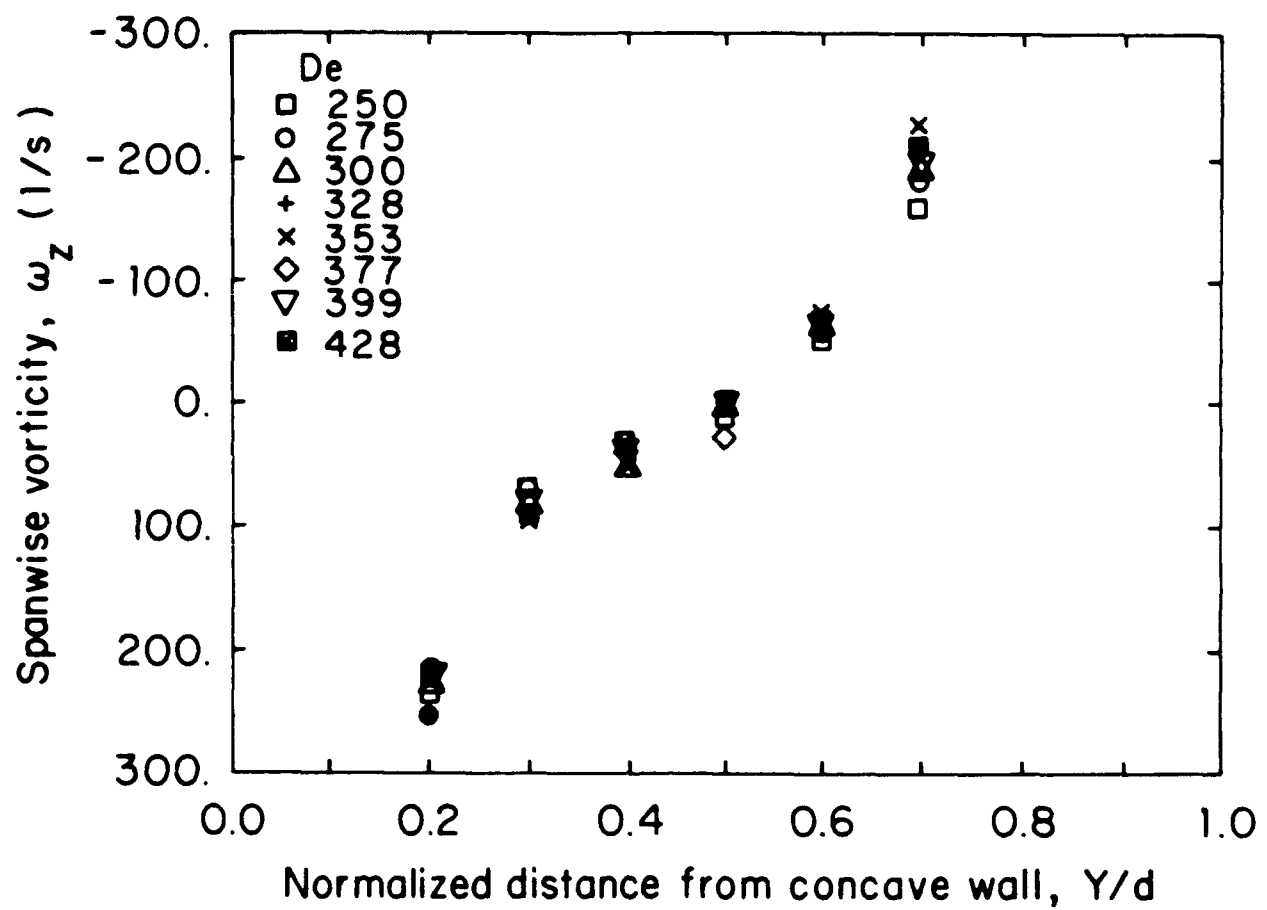


FIG. 60. Spanwise vorticity profiles,  $De=250$  to  $De=428$ .

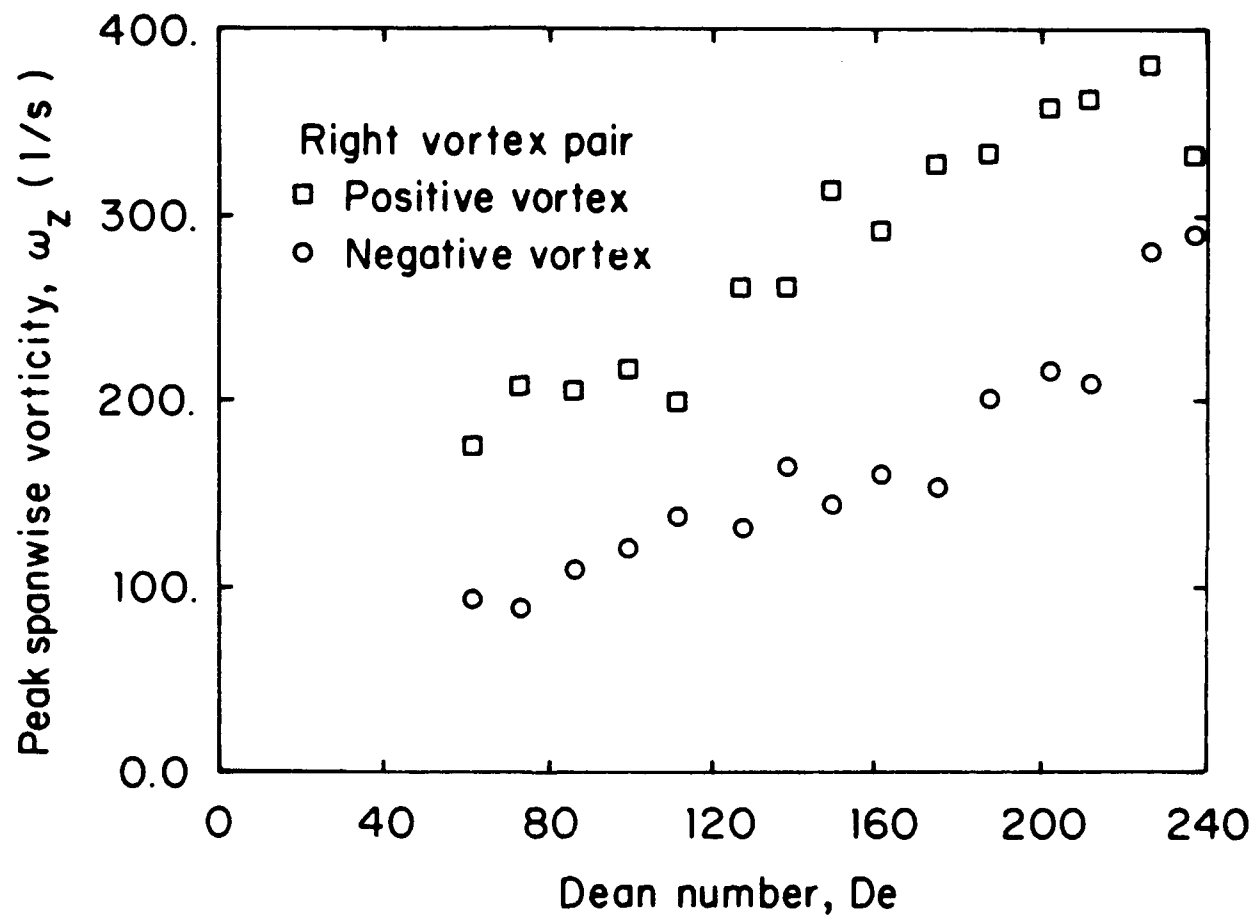


FIG. 61. Peak spanwise vorticity versus Dean number, right vortex pair.

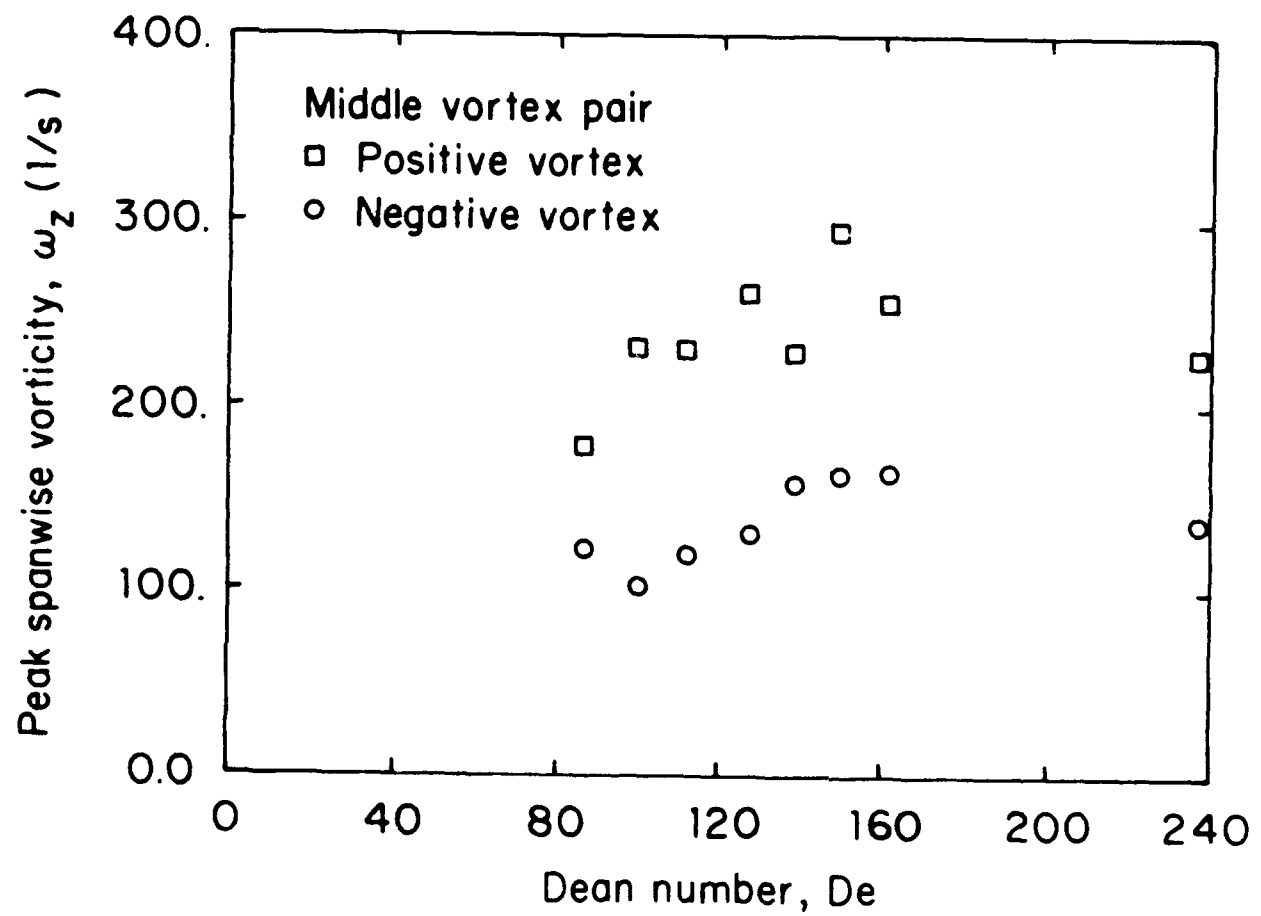


FIG. 62. Peak spanwise vorticity versus Dean number, middle vortex pair.

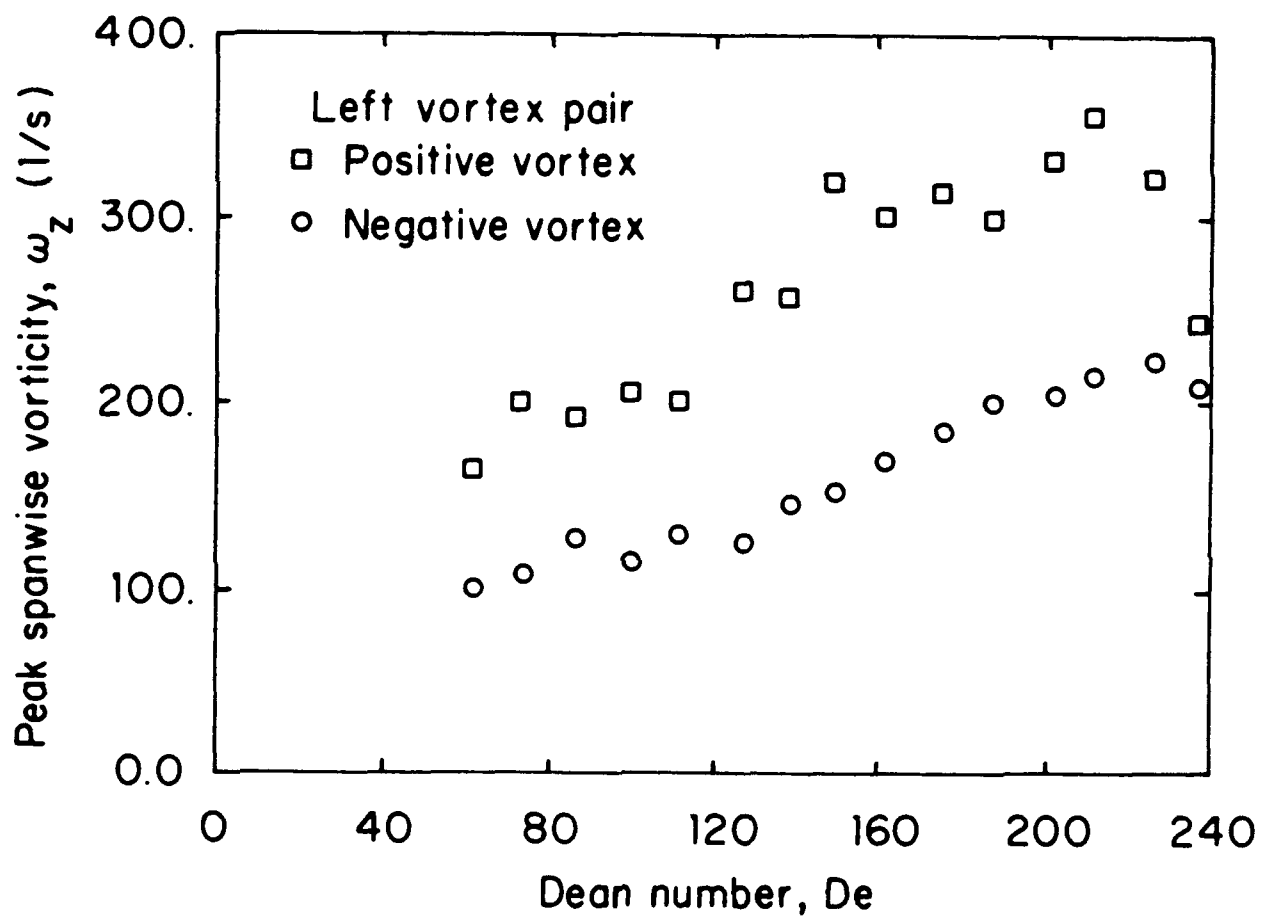


FIG. 63. Peak spanwise vorticity versus Dean number, left vortex pair.

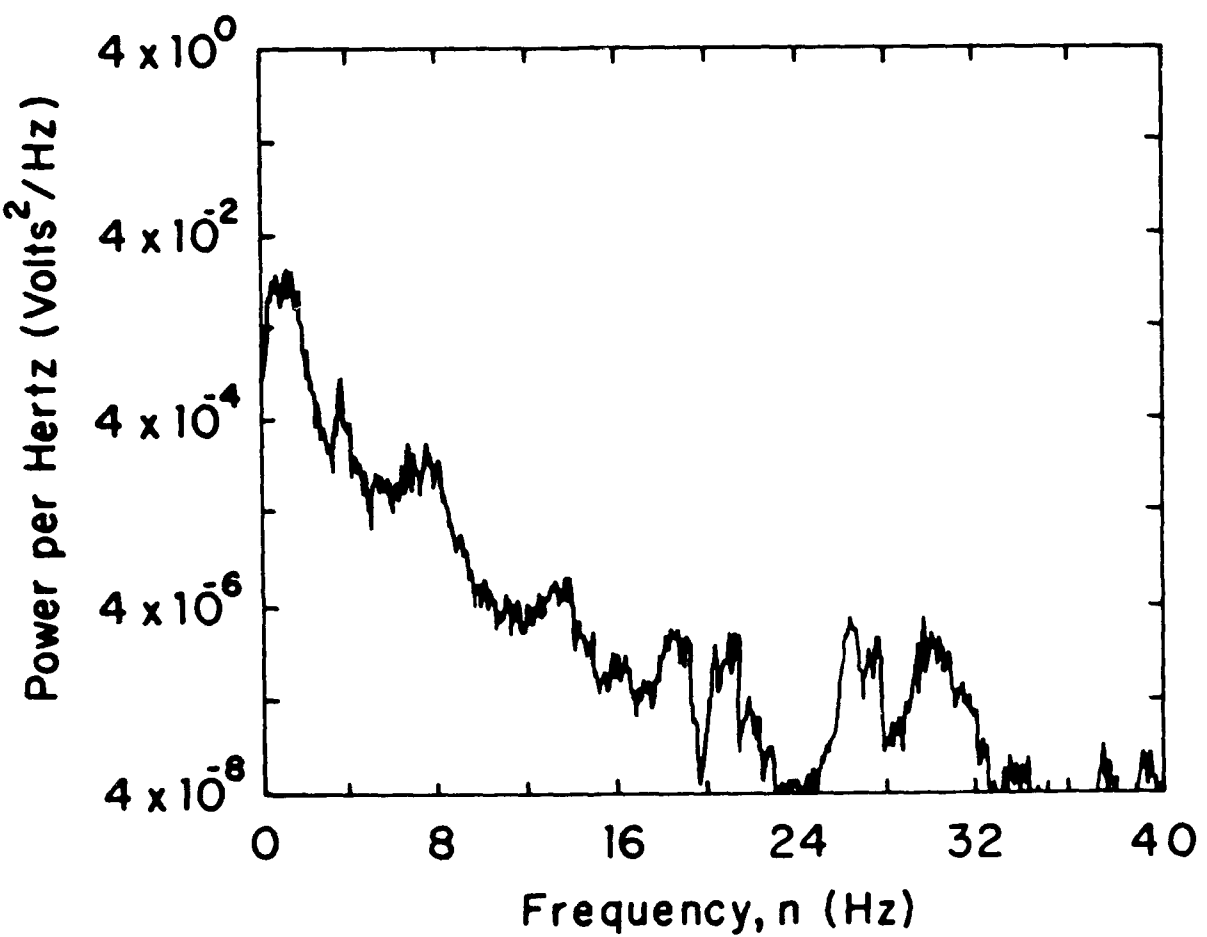


FIG. 64. Spectrum obtained at  $De=60$  at a location 112 degrees from the start of curvature at  $Z/d=12.2-12.4$  and  $Y/d=0.5$ . (a) Signal detected using a subminiature hot-wire sensor and analyzed using the signal analyzer.

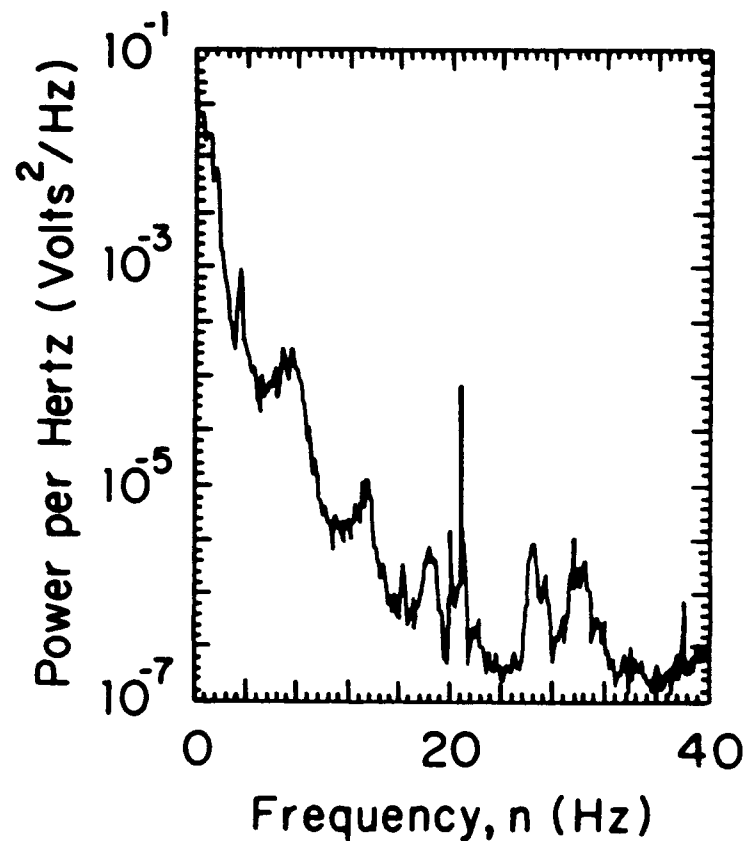


FIG. 64. Spectrum obtained at  $De=60$  at a location 112 degrees from the start of curvature at  $Z/d=12.2-12.4$  and  $Y/d=0.5$ . (b) Signal detected using a subminiature hot-wire sensor and analyzed using fast Fourier transforms of the digitized time varying signals.

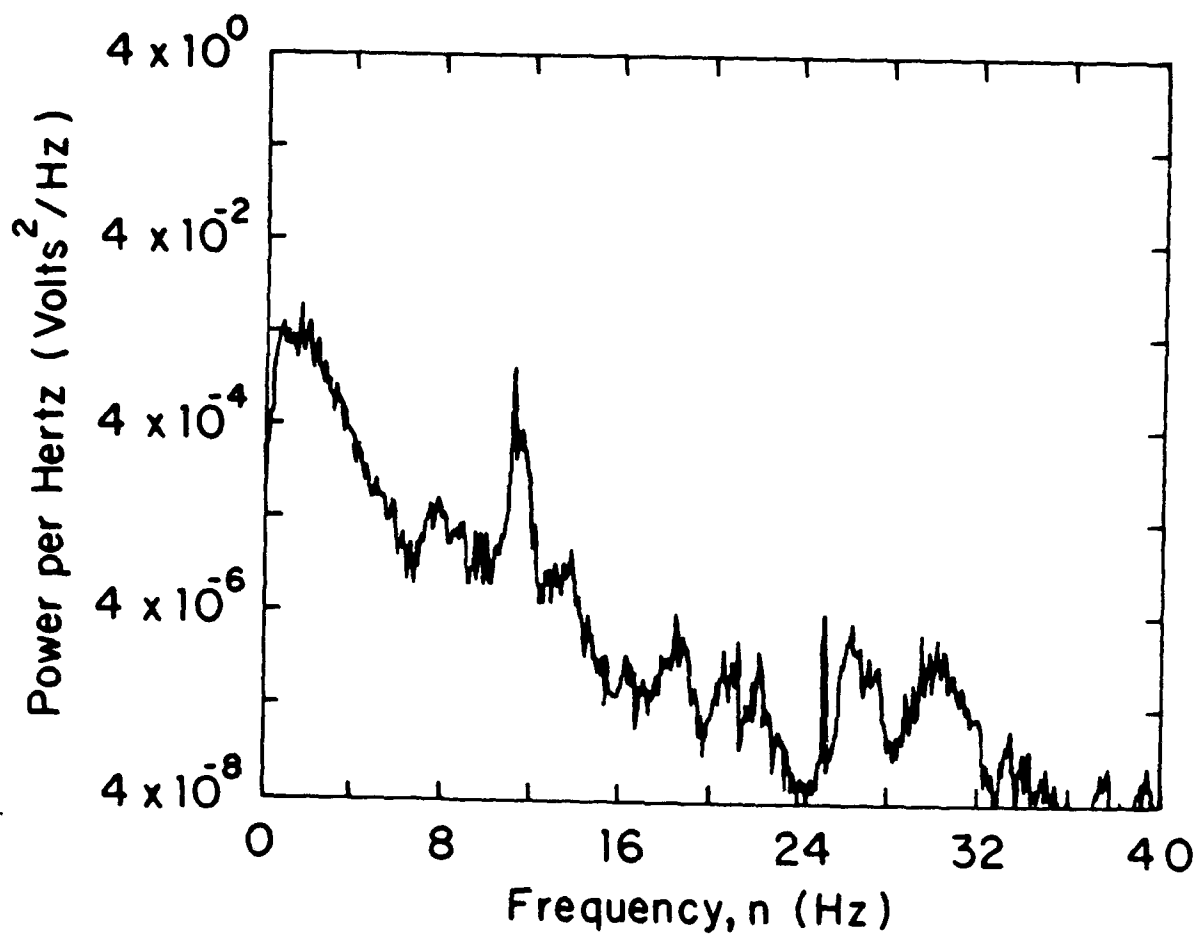


FIG. 65. Spectrum obtained at  $De=100$  at a location 112 degrees from the start of curvature at  $Z/d=12.2-12.4$  and  $Y/d=0.5$ . (a) Signal detected using a subminiature hot-wire sensor and analyzed using the signal analyzer.

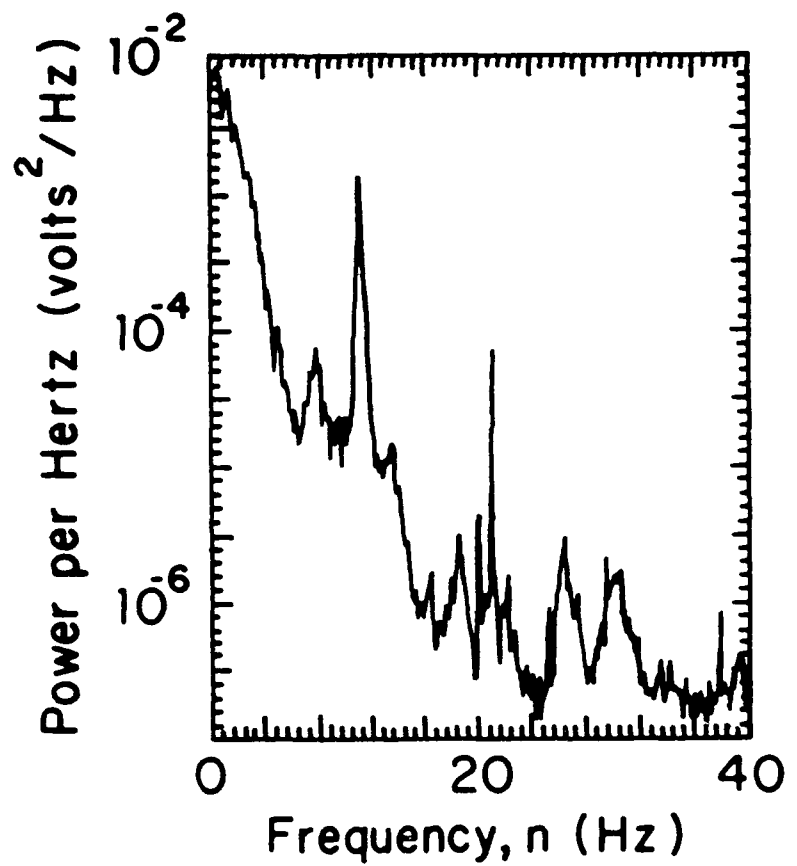


FIG. 65. Spectrum obtained at  $De=100$  at a location 112 degrees from the start of curvature at  $Z/d=12.2-12.4$  and  $Y/d=0.5$ . (b) Signal detected using a subminiature hot-wire sensor and analyzed using fast Fourier transforms of the digitized time varying signals.

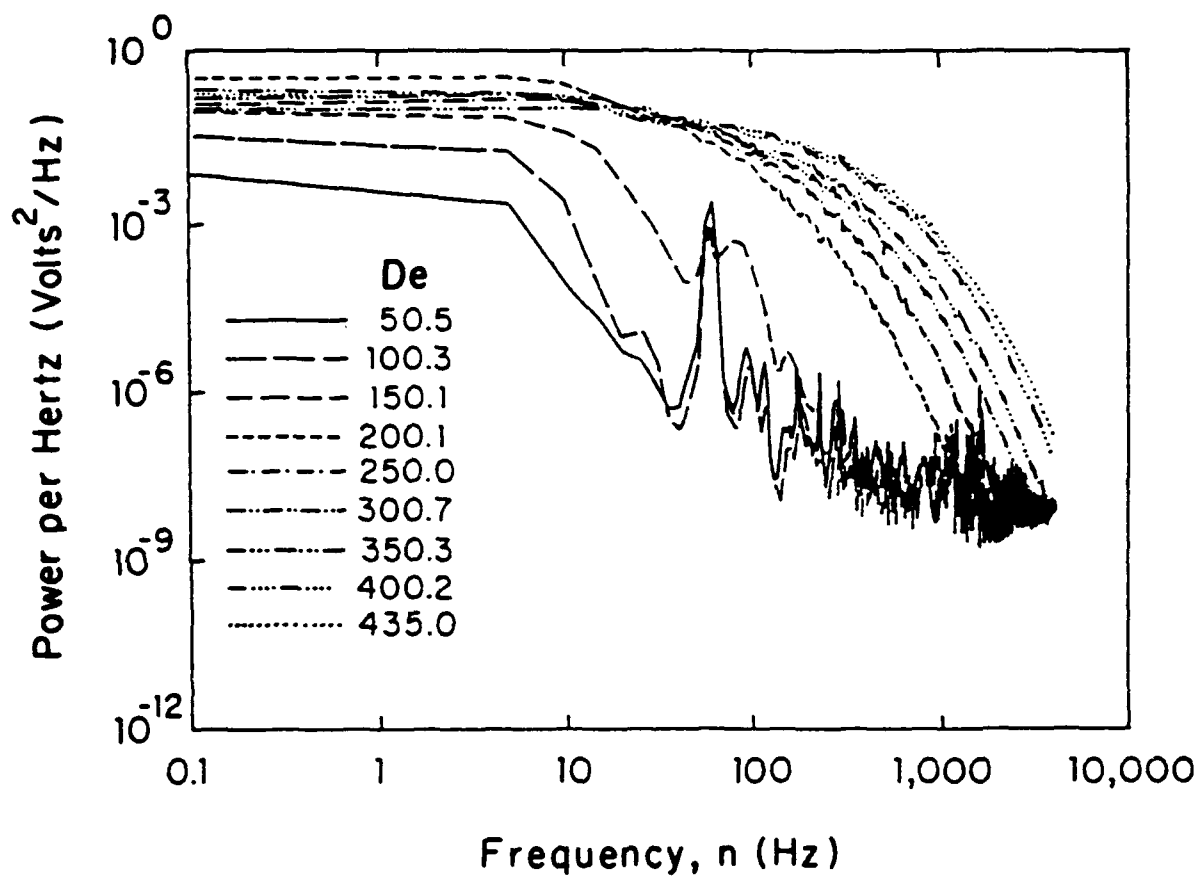


FIG. 66. Spectra at Dean numbers from 50.5 to 435.0 from voltage signals detected using an ordinary sized hot-wire probe and analyzed using the signal analyzer. To obtain the measurements, the probe was placed at a location 112 degrees from the start of curvature at  $Z/d=12.25$  and  $Y/d=0.5$ .

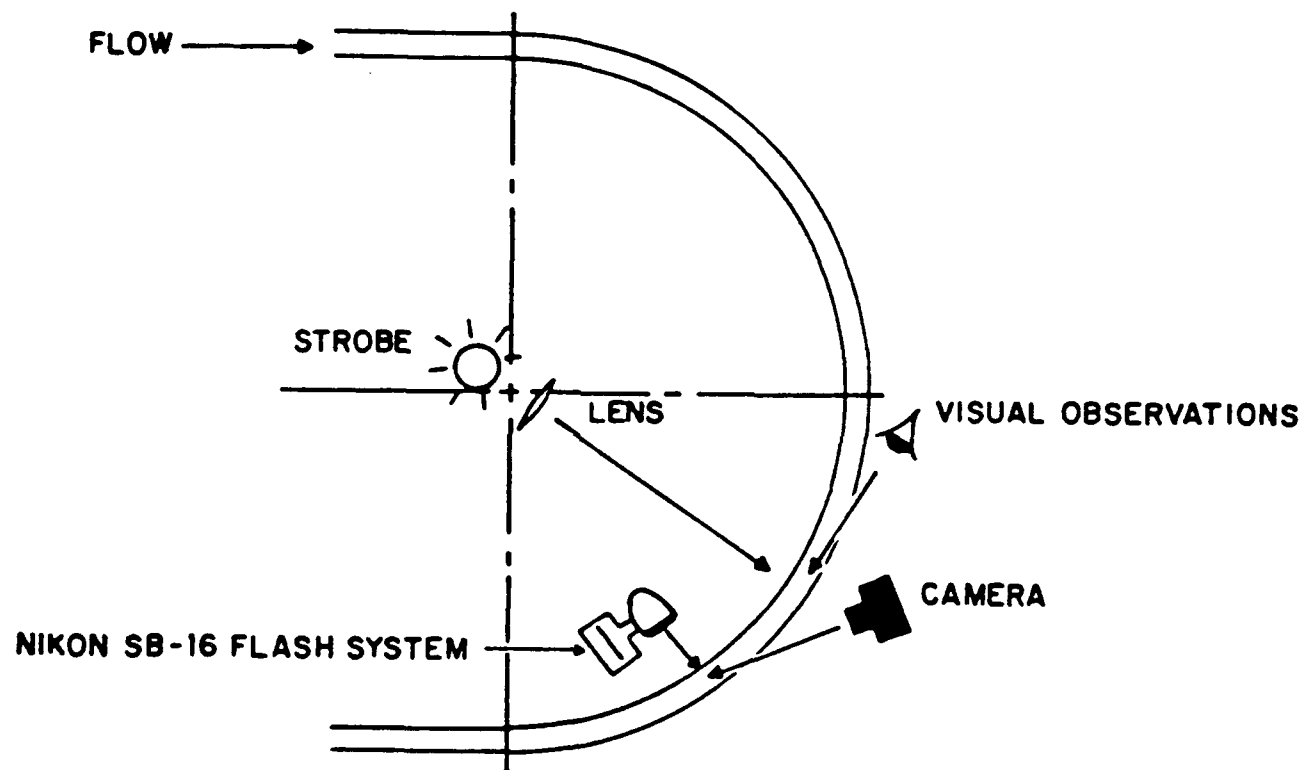


FIG. 67. Schematic showing arrangement of apparatus used for visualization of smoke patterns in spanwise/radial planes.

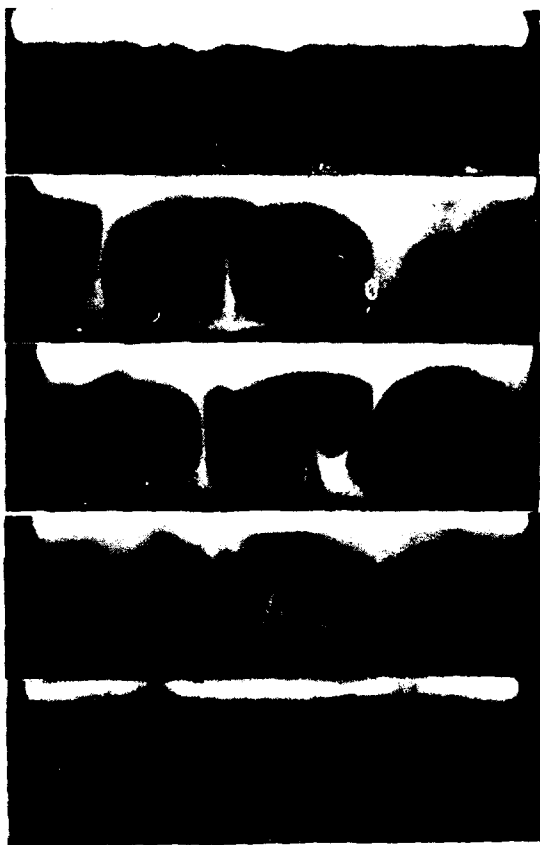
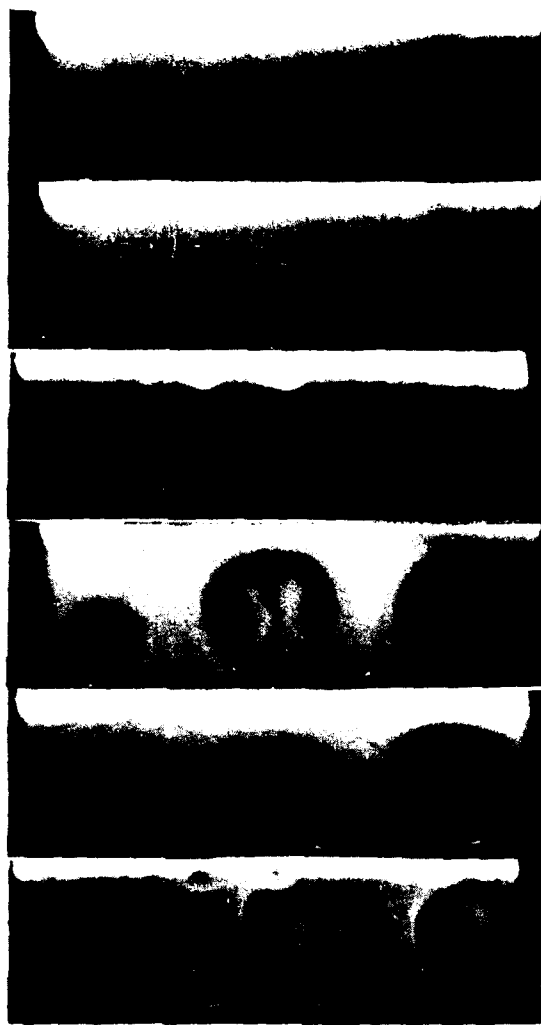


FIG. 68. Smoke patterns in a spanwise/radial plane located 115 degrees from the start of curvature for Dean numbers of 42, 53, 64, 73, 77, 90, 100, 123, 163, 192, and 218.

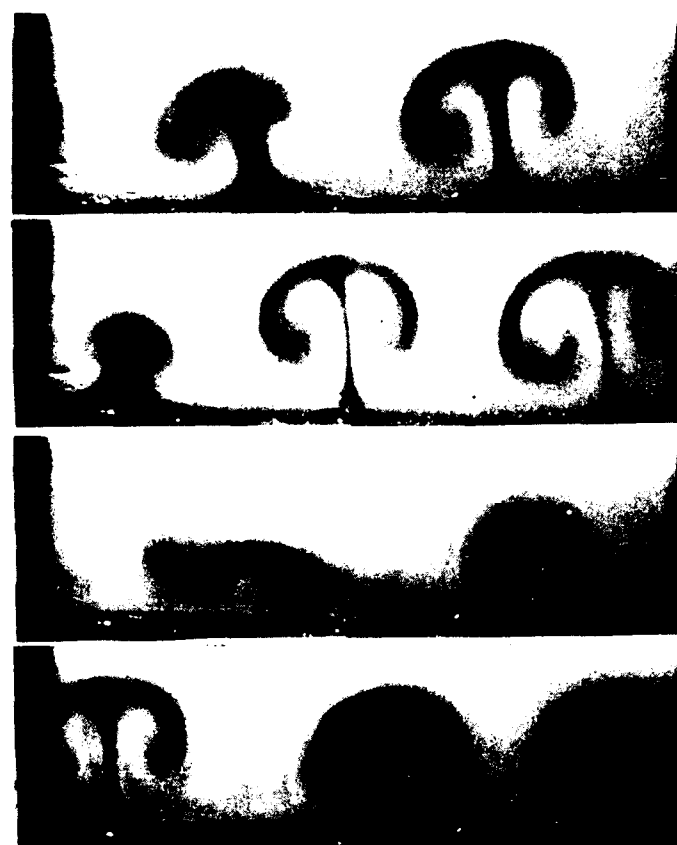


FIG. 69. Sequence of smoke patterns in a spanwise/radial plane located 115 degrees from the start of curvature timed approximately 1 sec. apart,  $De=73$ .

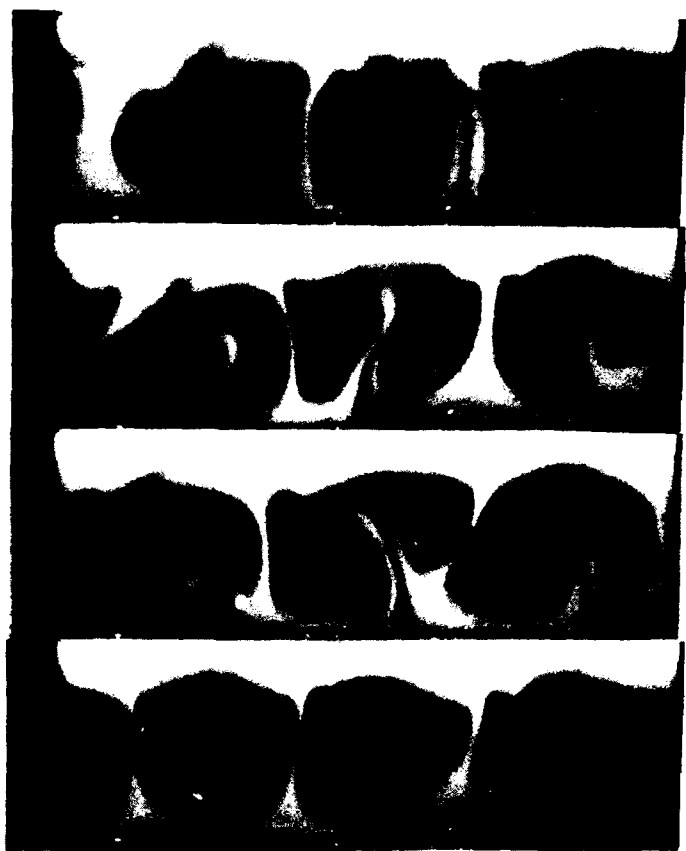


FIG. 70. Same caption as Fig. 69,  $De=163$ .

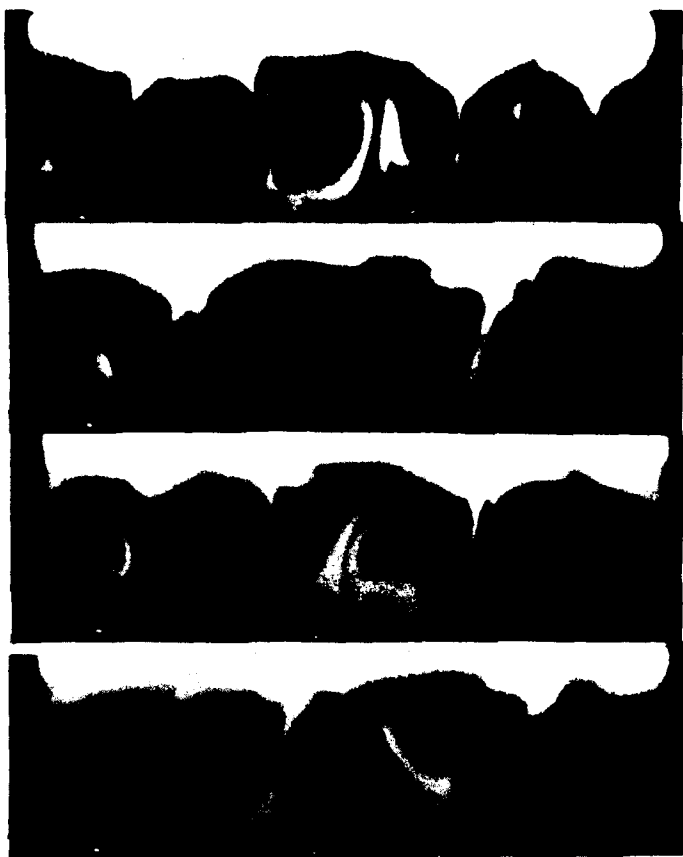


FIG. 71. Same caption as Fig. 69,  $De=192$ .

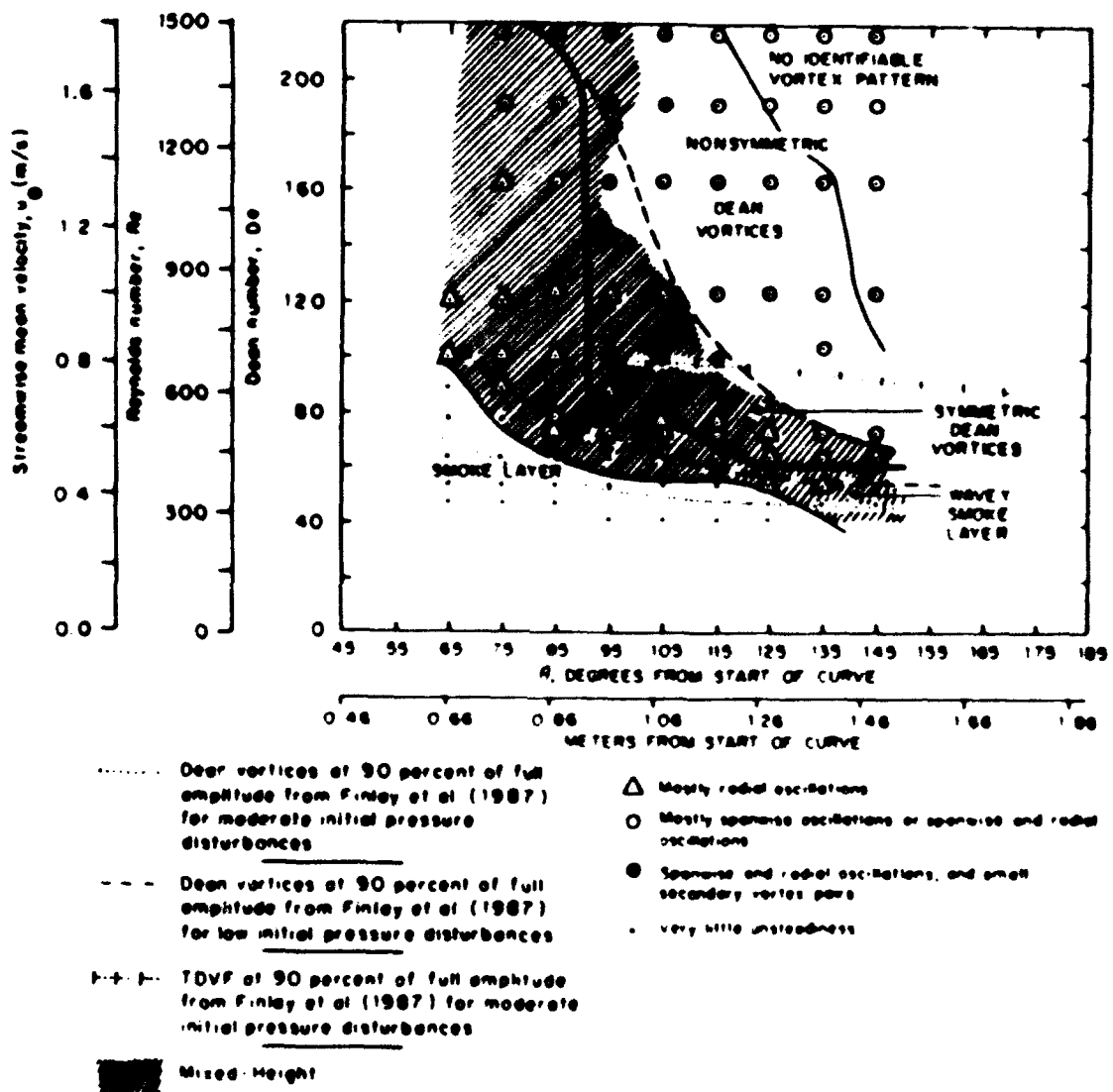


FIG. 72. Map showing observed types of smoke patterns at different Dean numbers and different radial positions around the curved channel test facility.

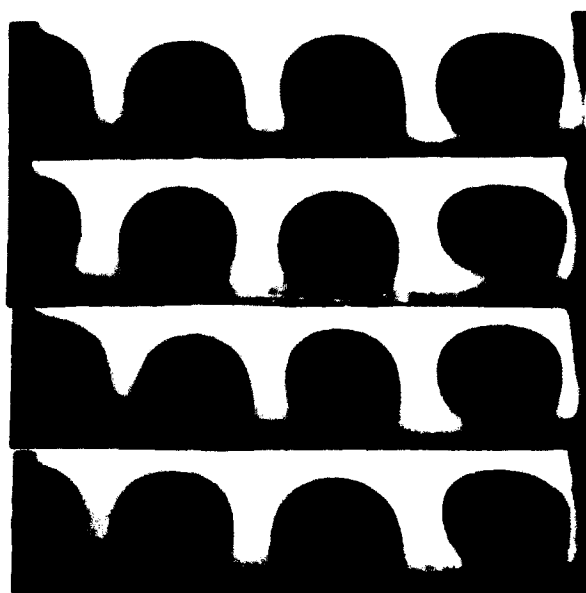


FIG. 73. Photographs timed about 1 sec. apart illustrating symmetric Dean vortex pairs with small amounts of unsteadiness in a spanwise/radial plane 95 degrees from the start of curvature for  $De=123$ .



FIG. 74. Photographs timed about 1 sec. apart illustrating small secondary Dean vortex pairs in a spanwise/radial plane 95 degrees from the start of curvature for  $De=100$ .

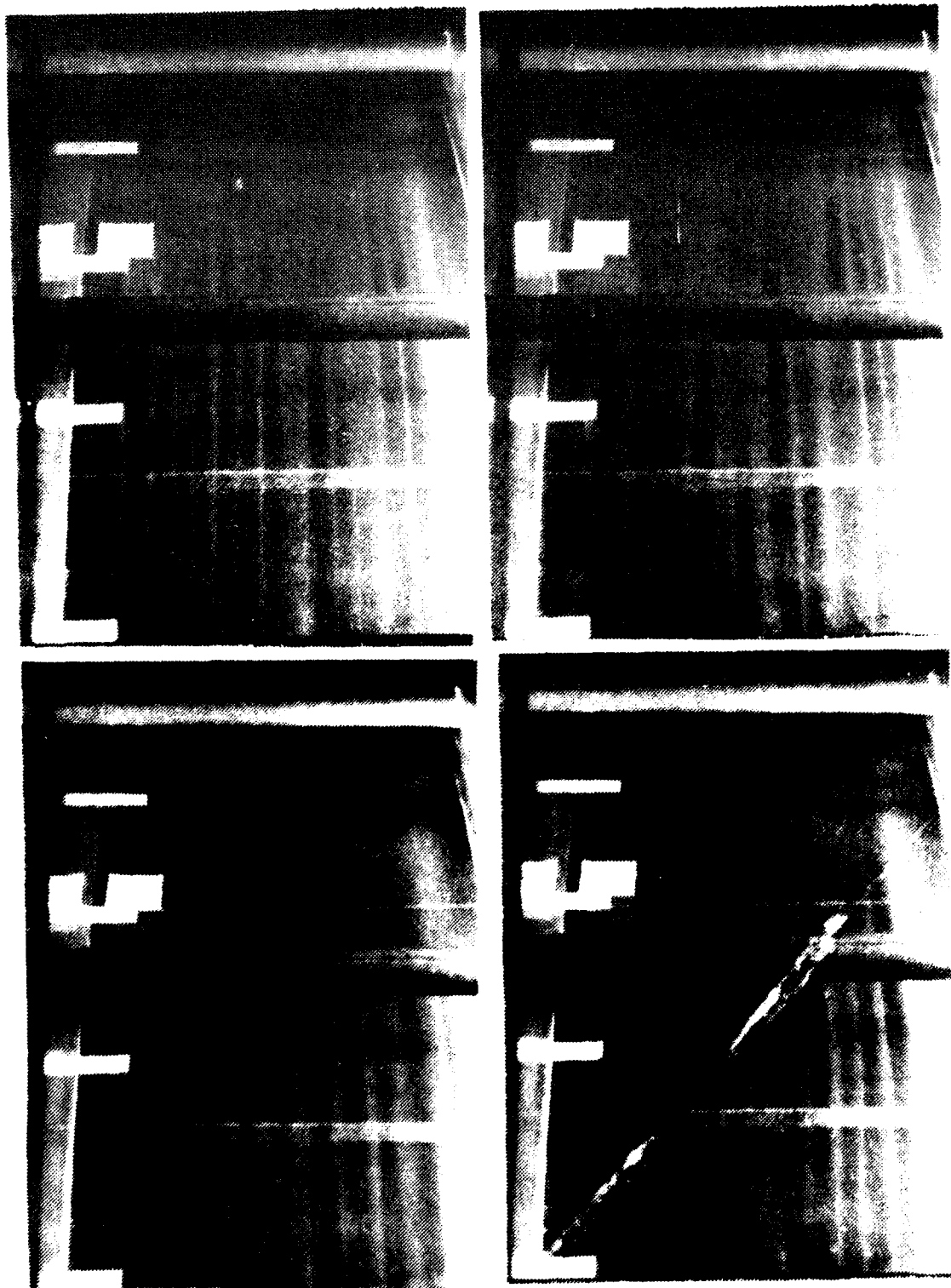


FIG. 75. Visualization of flow patterns as viewed from outside of the concave surface.  
 $De=145.2$ , 50-80 degrees from the start of curvature.

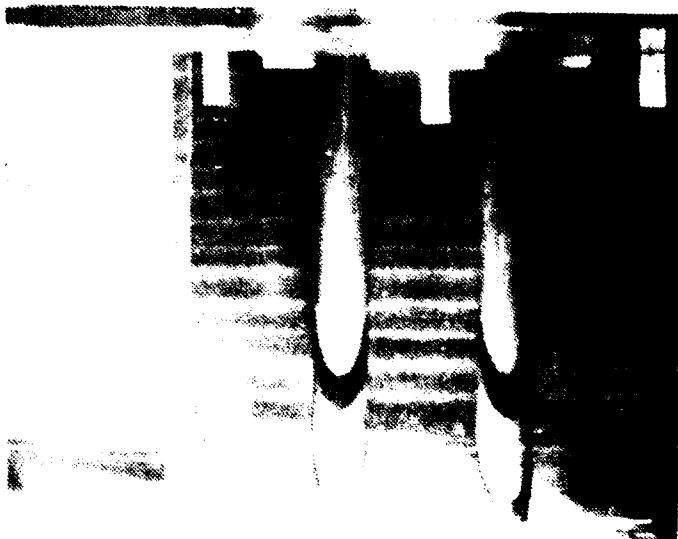
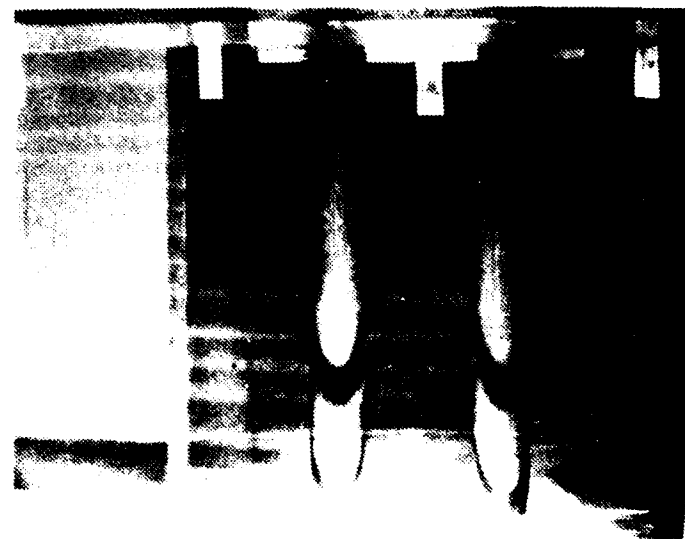
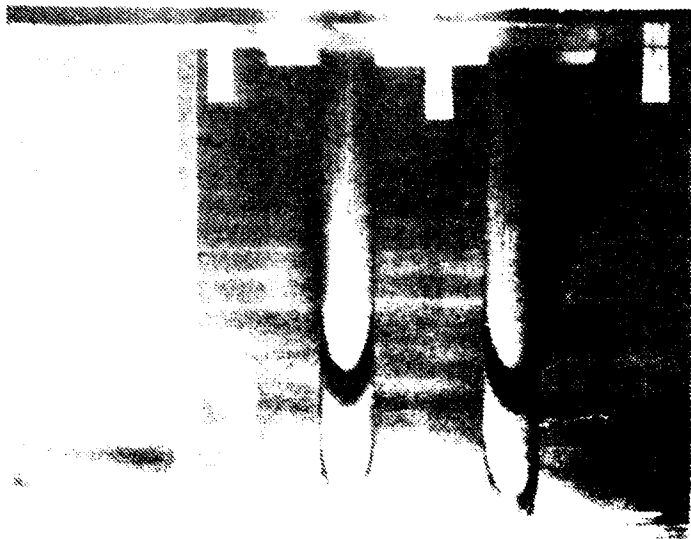
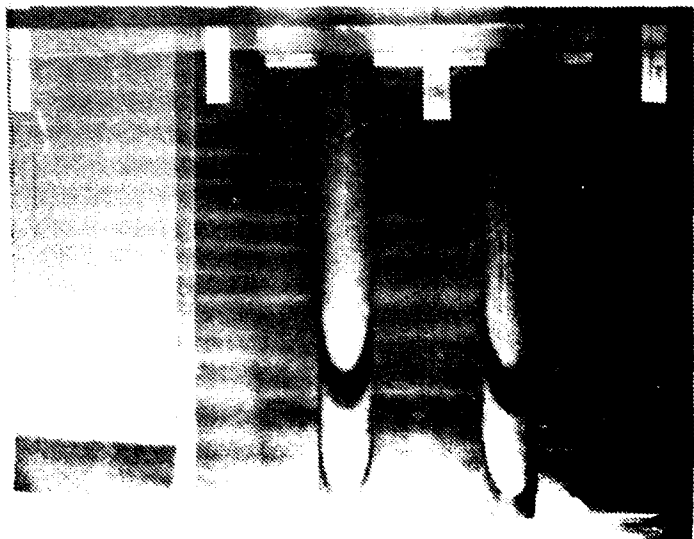


FIG. 76. Visualization of flow patterns as viewed from outside of the concave surface.  
 $De=104.8$ , 80-110 degrees from the start of curvature.

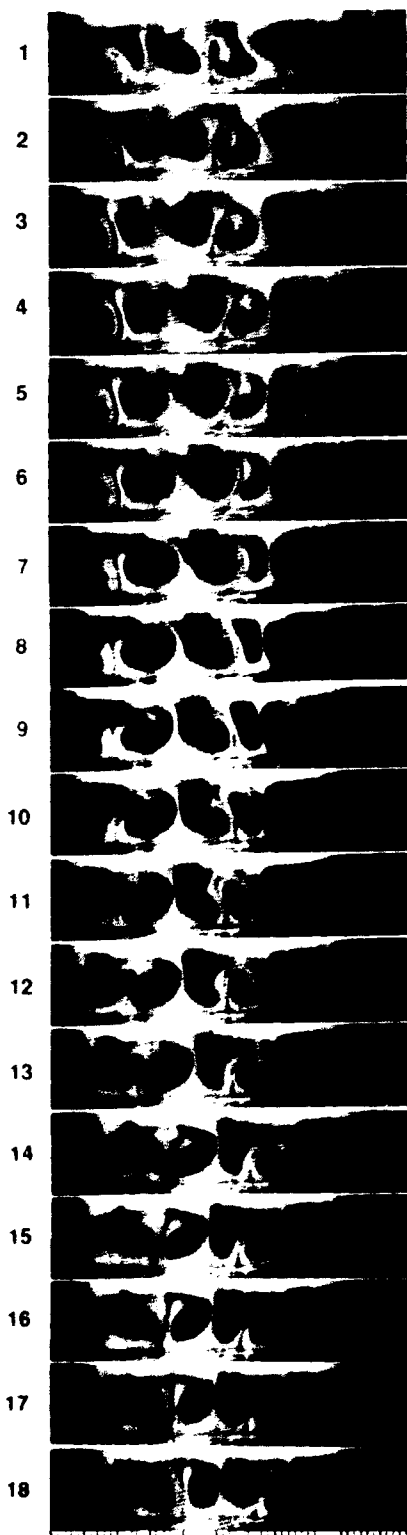


FIG. 77. Shown is a time sequence of eighteen smoke visualization photographs of experimental undulating vortices taken at 1/30 second (0.0333 sec.) intervals for  $De=3.4De_C$  at a streamwise location  $115^0$  from the start of curvature. The streamwise direction is into the plane of the plot, the concave surface is on the bottom of each photograph, and the convex surface is on the top of each photograph.

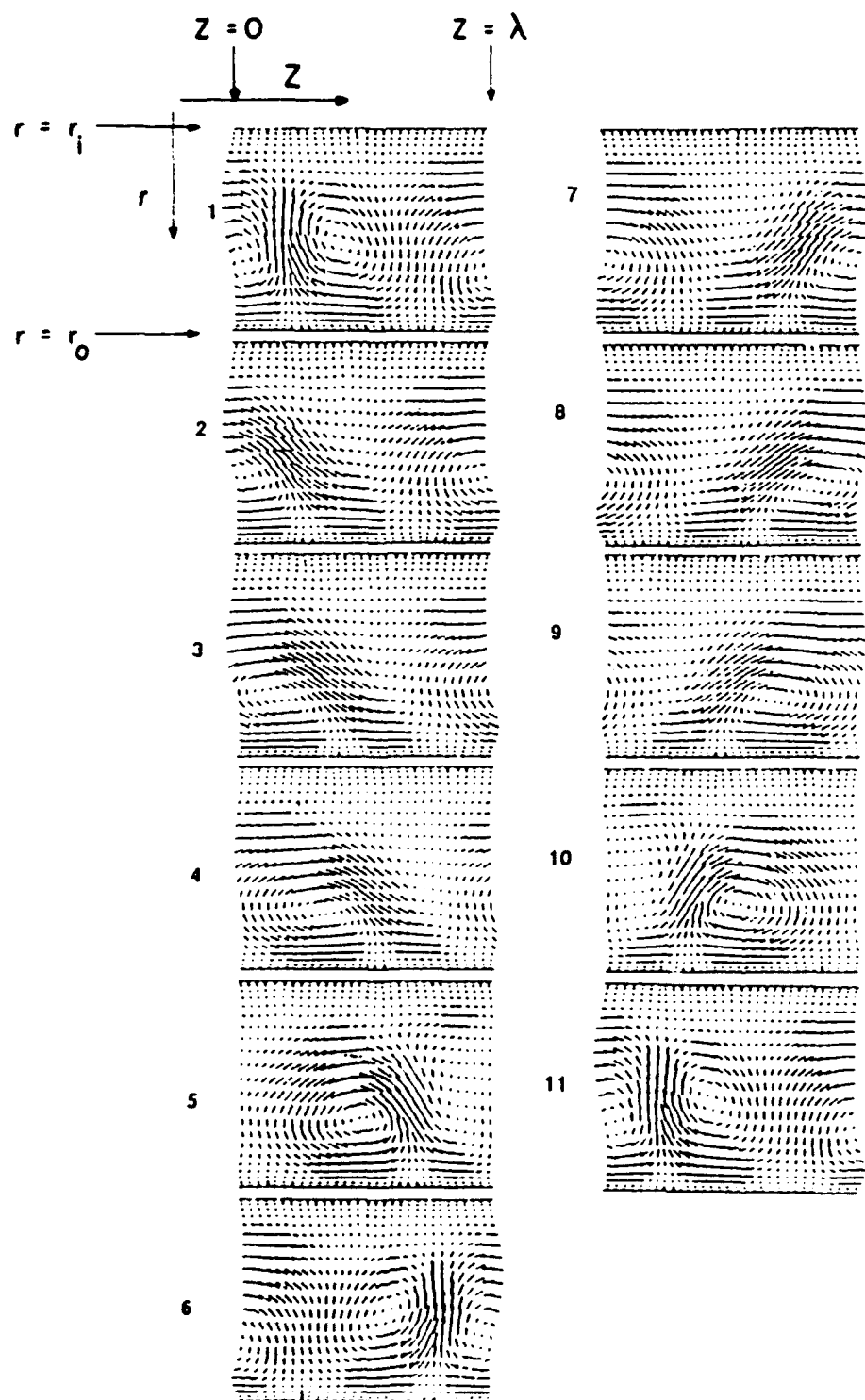


FIG. 78. Undulating Dean vortices obtained by numerical simulation are shown at  $De=1.776$ ,  $\alpha=2.5$ ,  $\eta=0.979$ , and streamwise wavenumber  $\beta=15$ . The flow is projected onto an  $(r, Z)$  plane at one streamwise location at times separated by one-tenth of one period of oscillation where 0.372 sec. is the period of oscillation.

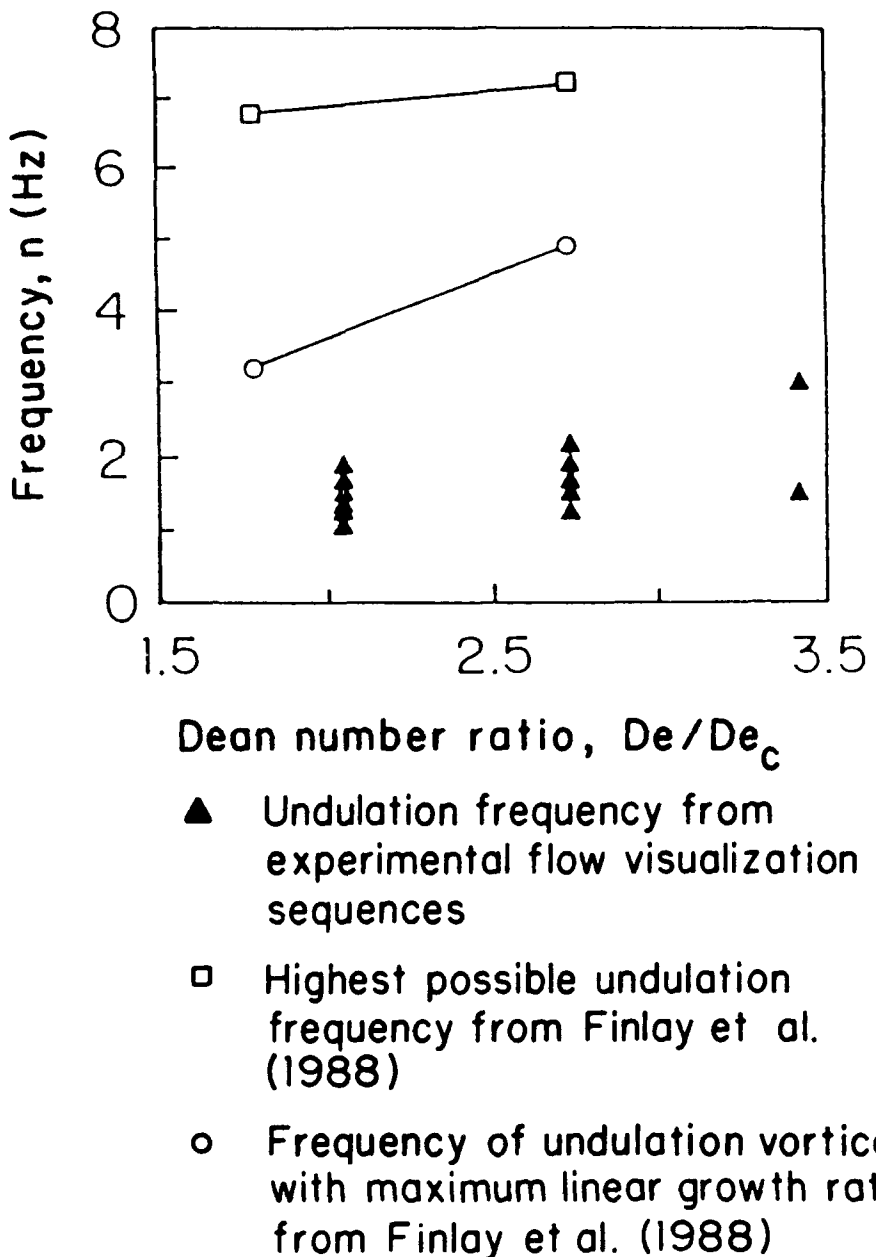
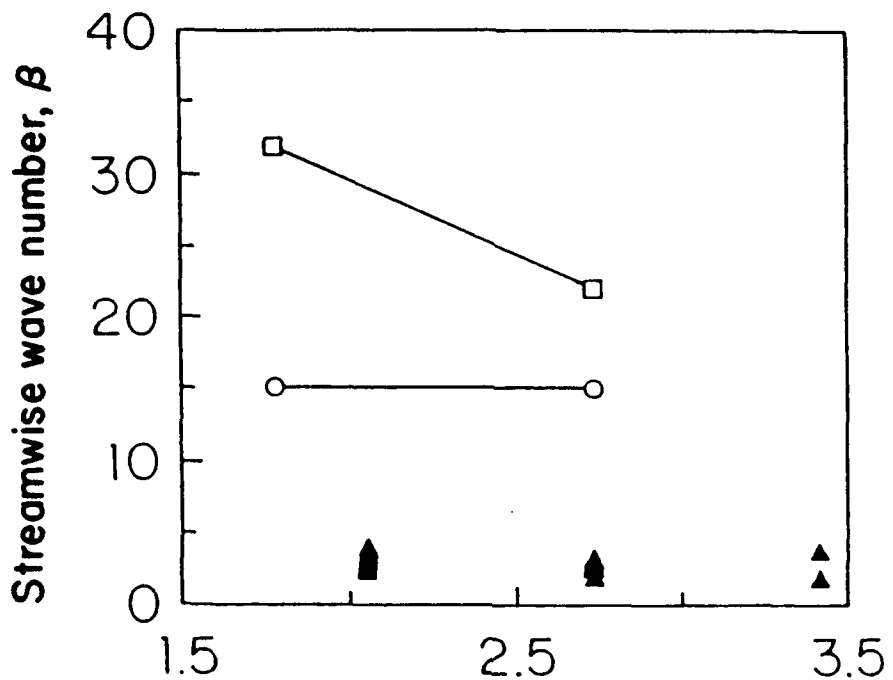


FIG. 79. The frequency of undulating vortices in Hz obtained from experimental flow visualization sequences is shown. Also given are results from linear stability analysis of axisymmetric vortices to wavy disturbances (Finlay et al. 1988) showing the highest possible frequency of undulating vortices and the frequency of undulating vortices that have the maximum linear growth rate for  $\eta = 0.975$ .



Dean number ratio,  $De/De_c$

- ▲ Undulation frequency from experimental flow visualization sequences
- Highest possible undulation frequency from Finlay et al. (1988)
- Frequency of undulation vortices with maximum linear growth rate from Finlay et al. (1988)

FIG. 80. The frequencies shown in Fig. 79 are converted approximately into streamwise wavenumbers by assuming the undulating waves travel at streamwise angular speed  $0.0155 U/(d/2)$  radian/sec.

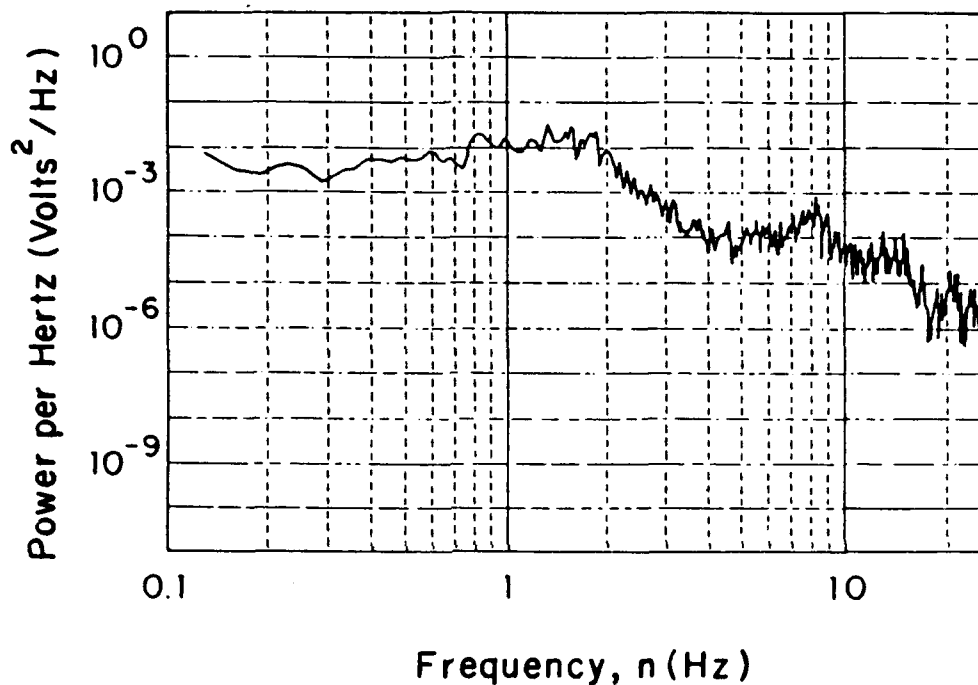


FIG. 81. Temporal power spectrum of the voltage signal from a hot-wire sensor placed within an upwash region at  $Y/d=0.1$  for  $De=1.35De_C$  and 120 degrees from the start of curvature shows several local maxima associated with low-frequency vortex oscillations.

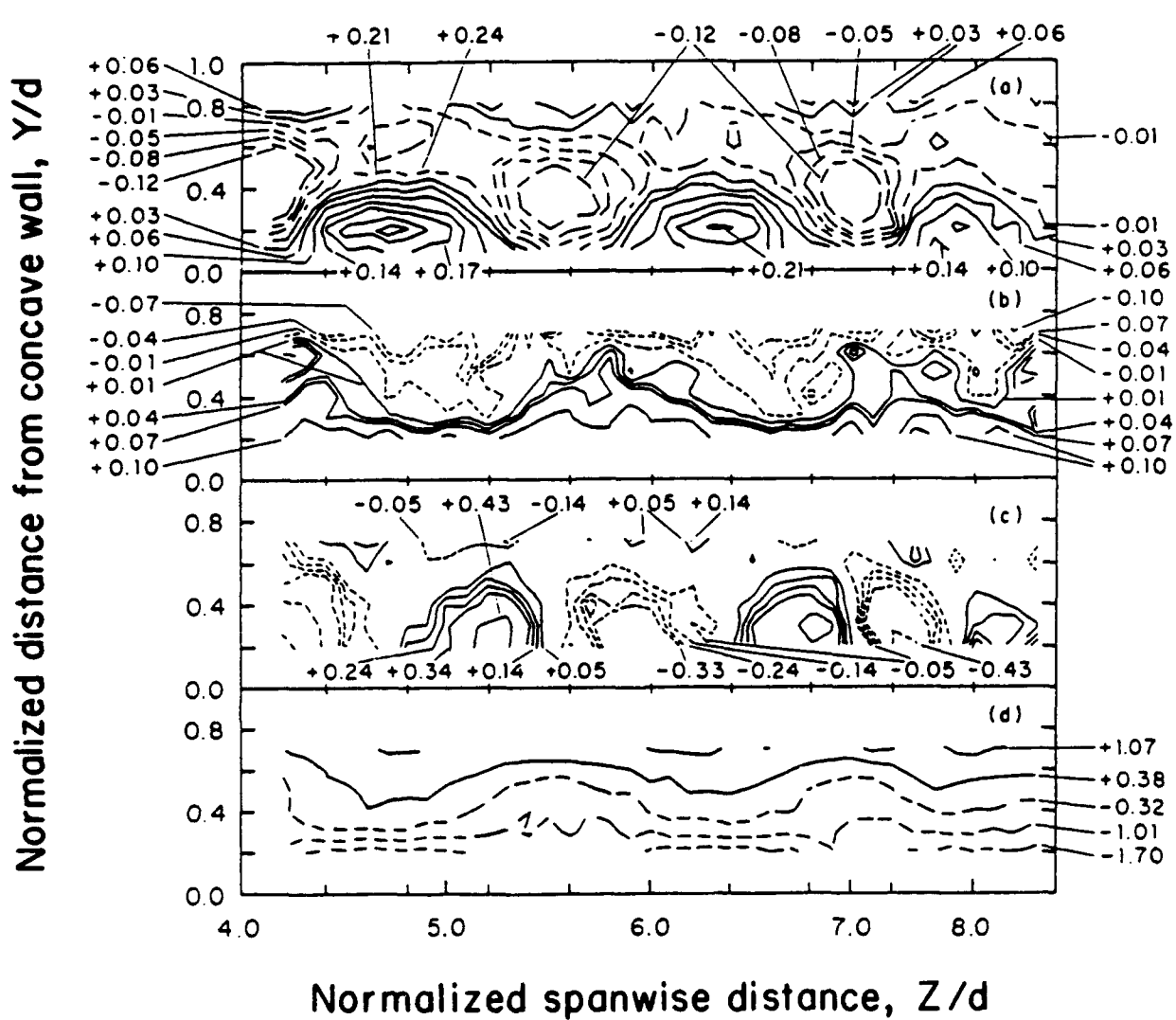


FIG. 82. Contours of (a) streamwise velocity minus the curved channel Poiseuille profile, (b) streamwise vorticity, (c) radial vorticity, and (d) spanwise vorticity as measured for  $De=1.75De_C$ ,  $\eta=0.979$ , and  $120^\circ$  from the start of curvature illustrating time-averaged flow field characteristics when Dean vortices are undulating.

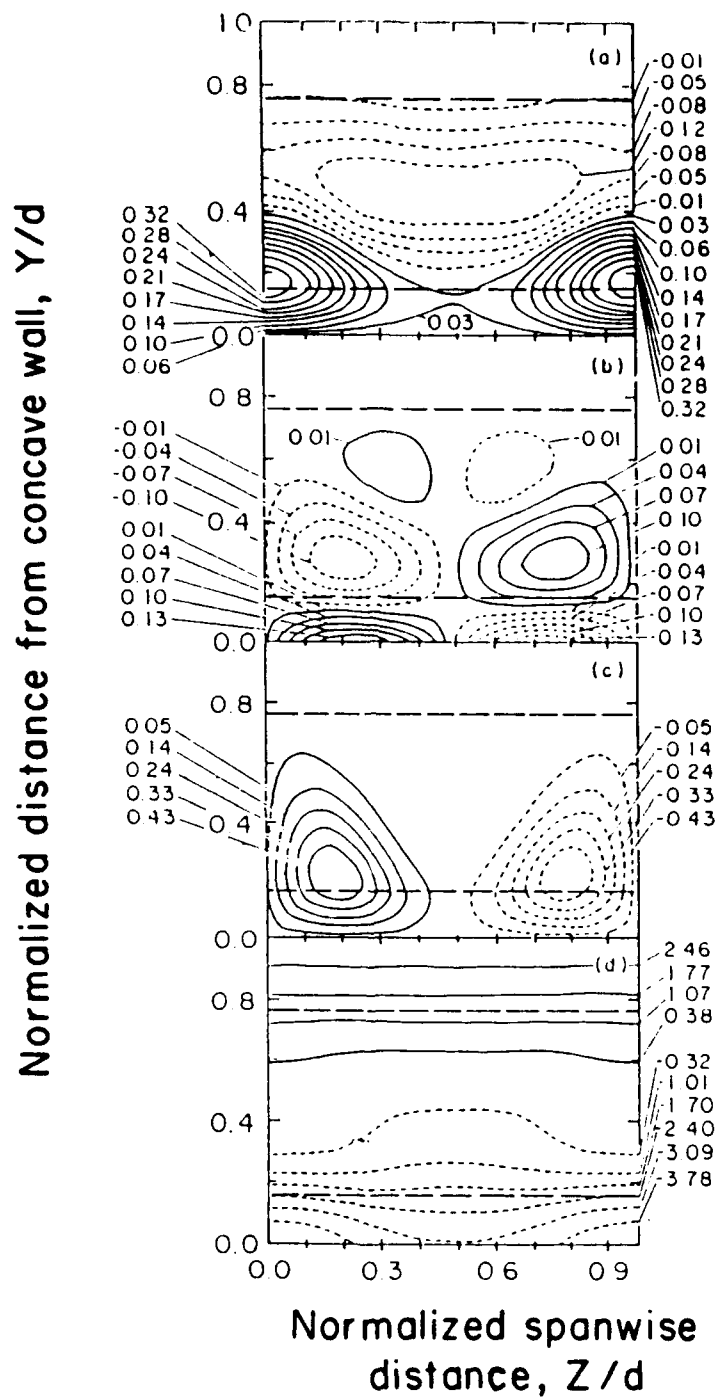


FIG. 83. Contours of (a) streamwise velocity minus the curved channel Poiseuille profile, (b) streamwise vorticity, (c) radial vorticity, and (d) spanwise vorticity as determined from a simulation for  $De=1.776De_c$ ,  $\alpha=2.5$ ,  $\eta=0.979$ , and streamwise wavenumber  $\beta=15$  illustrating time-averaged flow field characteristics when Dean vortices are undulating.

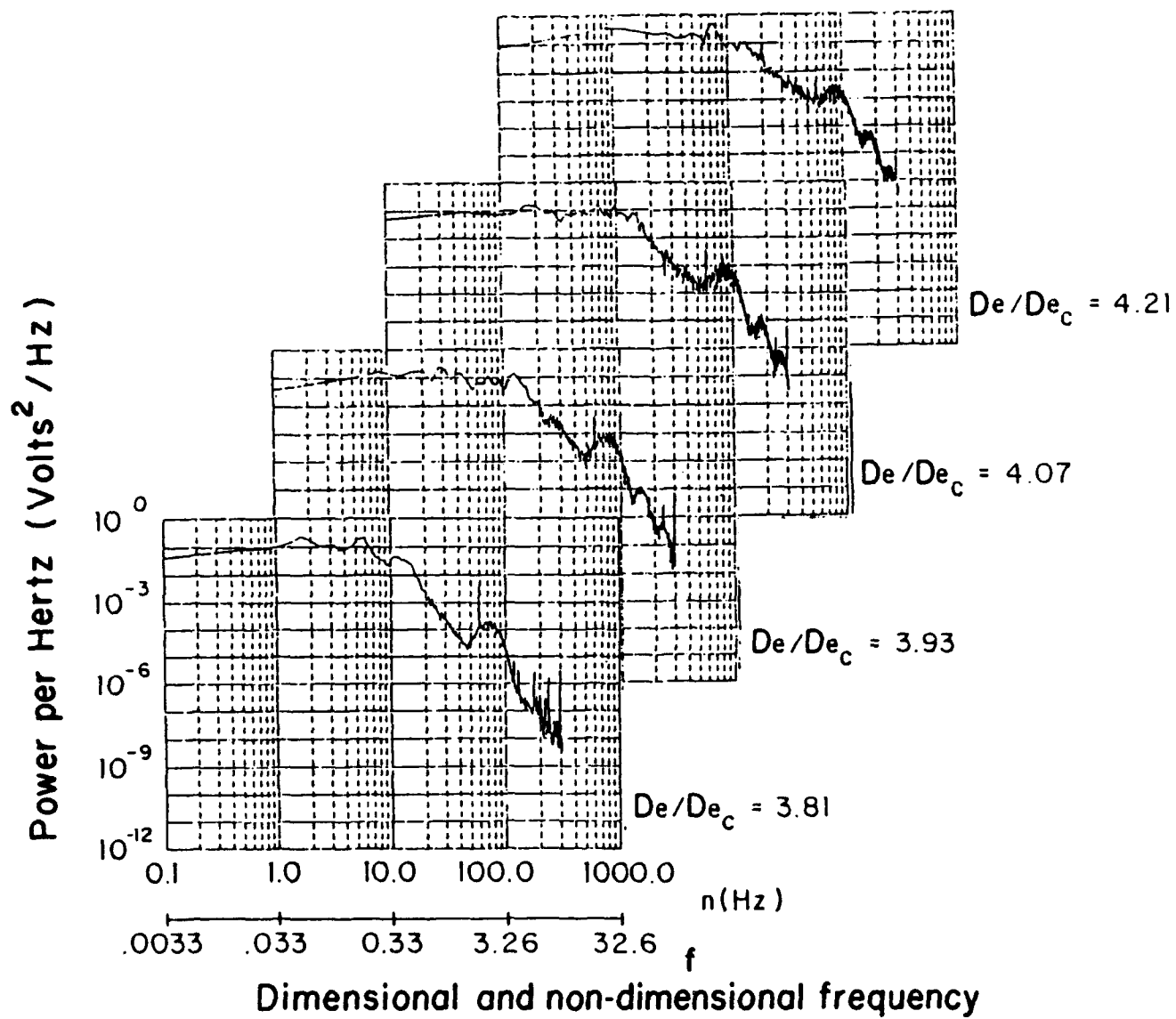


FIG. 84. Temporal power spectra of the voltage signals from a hot-wire sensor placed at  $Y/d=0.5$  and  $Z/d=12.25$  for  $De/De_c$  of 3.81, 3.93, 4.07, and 4.21 show the fundamental and two harmonic frequencies associated with twisting vortices.  $f$  values are computed for  $De/De_c$  of 3.93.

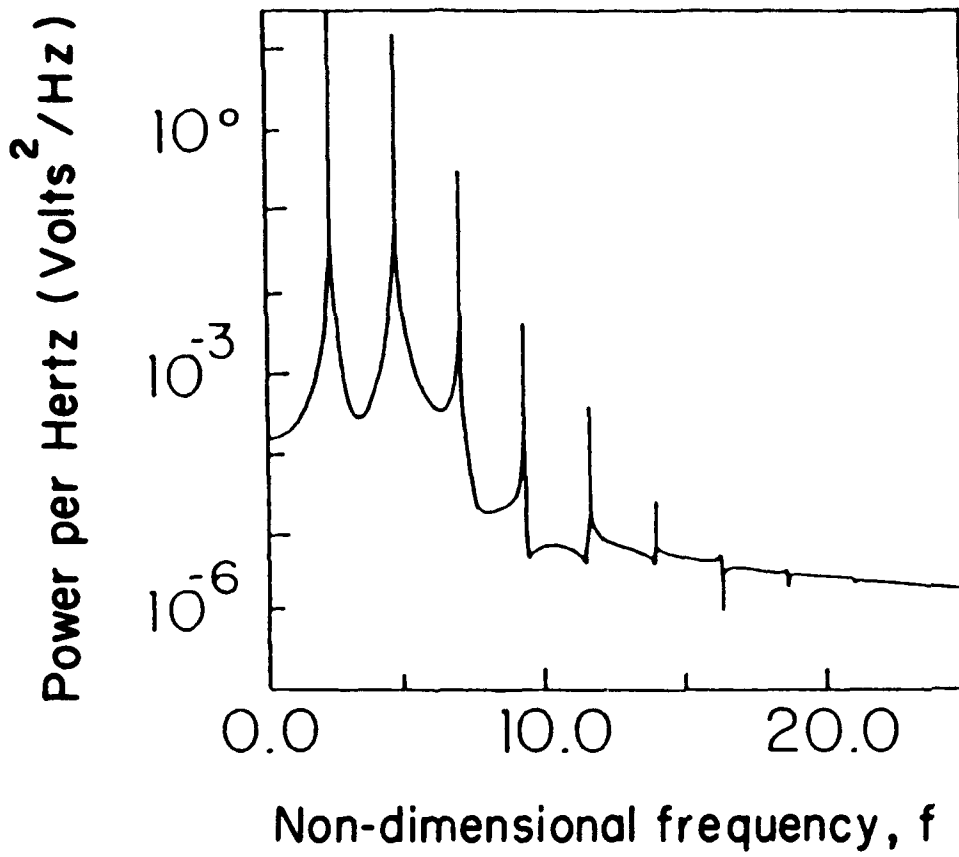


FIG. 85. Temporal power spectrum from a simulation of twisting vortices with  $\eta = 0.979$ ,  $\alpha = 3.0$ ,  $De = 3.580 De_C$ , and  $\beta = 200$ .

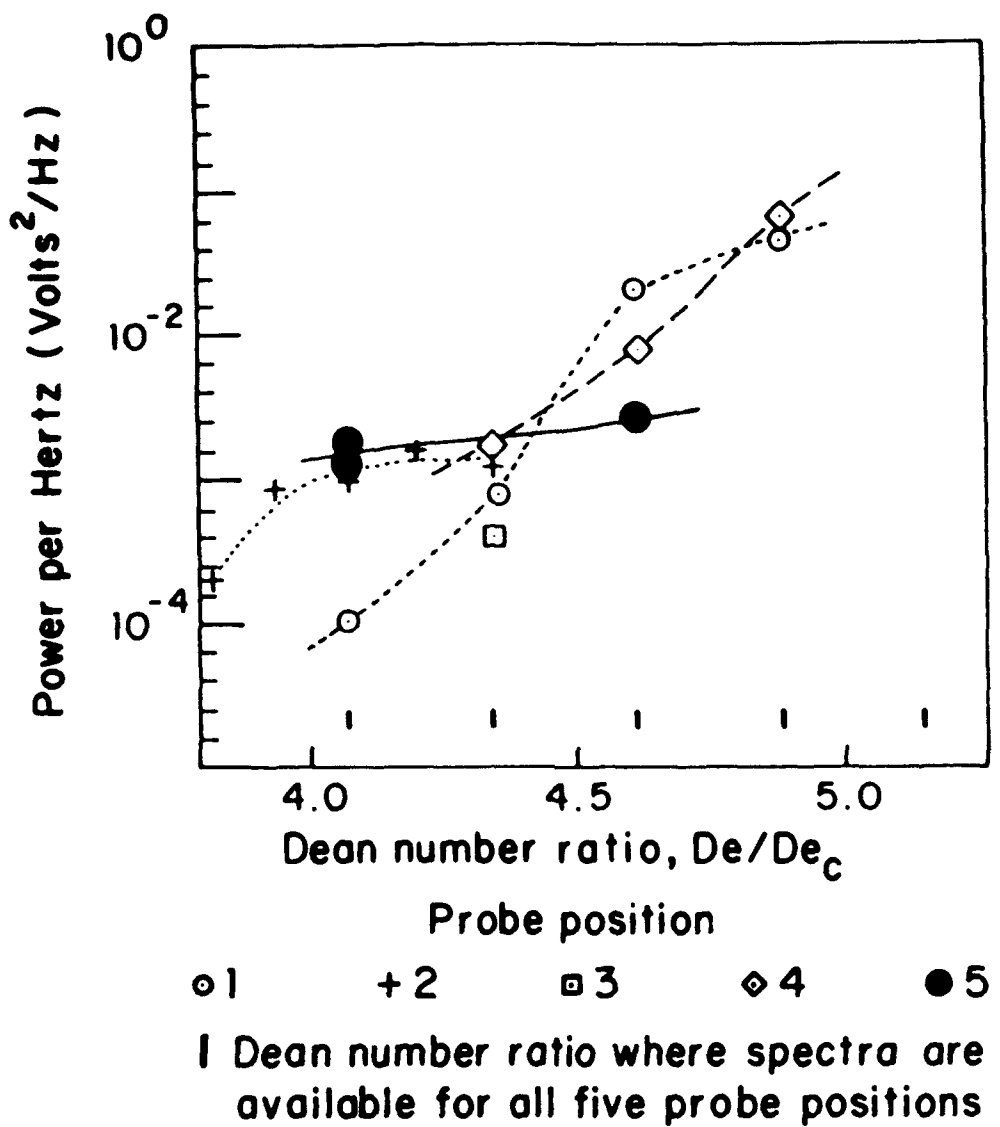


FIG. 86. Maximum amplitudes of principal peaks associated with twisting for different probe positions. Spectra are calculated from the voltage signals from a hot-wire sensor placed within a spanwise/radial plane located 120 degrees from the start of curvature.

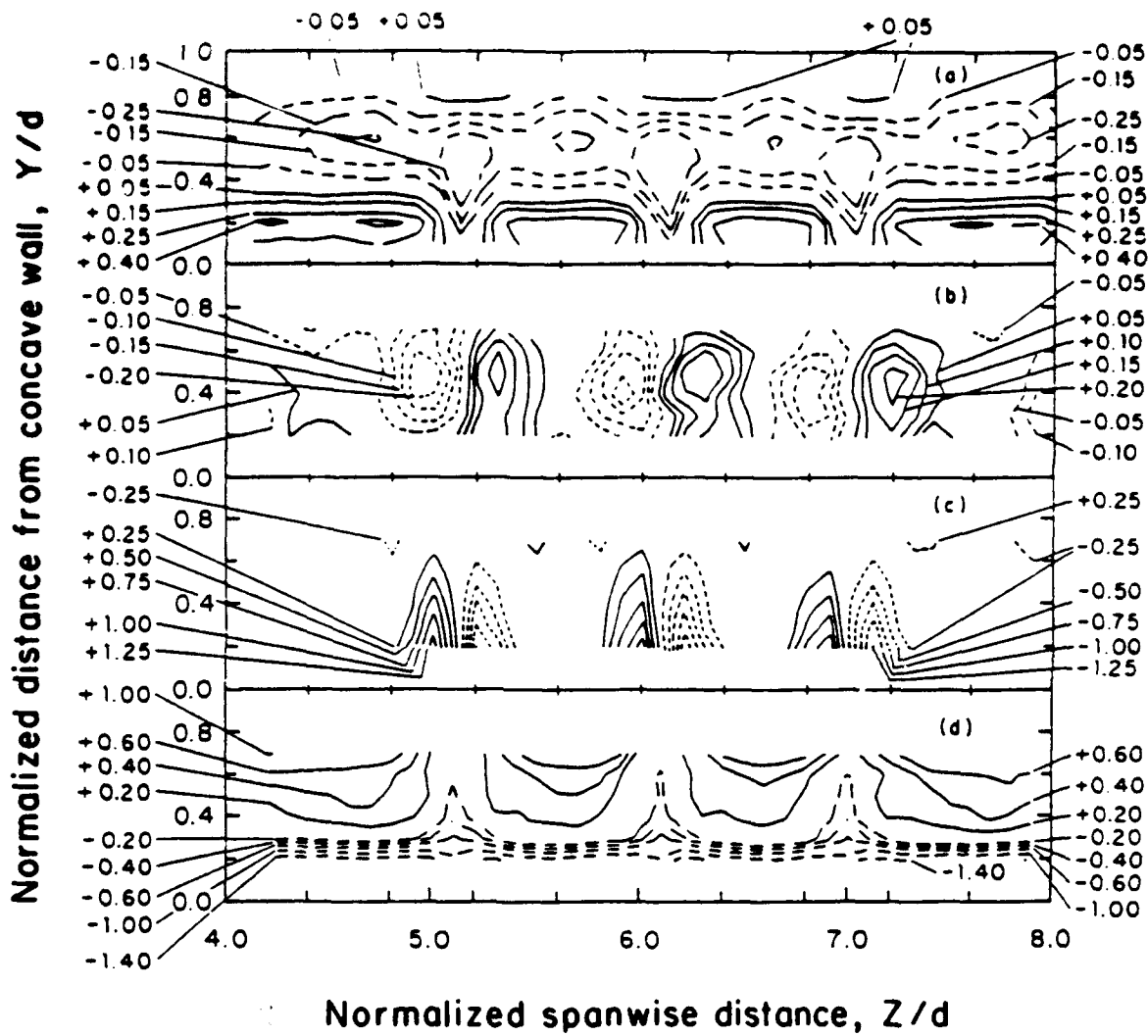


FIG. 87. Contours of (a) streamwise velocity minus the curved channel Poiseuille profile, (b) streamwise vorticity, (c) radial vorticity, and (d) spanwise vorticity as measured for  $De=3.56$   $Dec$   $\eta=0.979$ , and  $120^0$  from the start of curvature illustrating time-averaged flow field characteristics when Dean vortices are twisting.

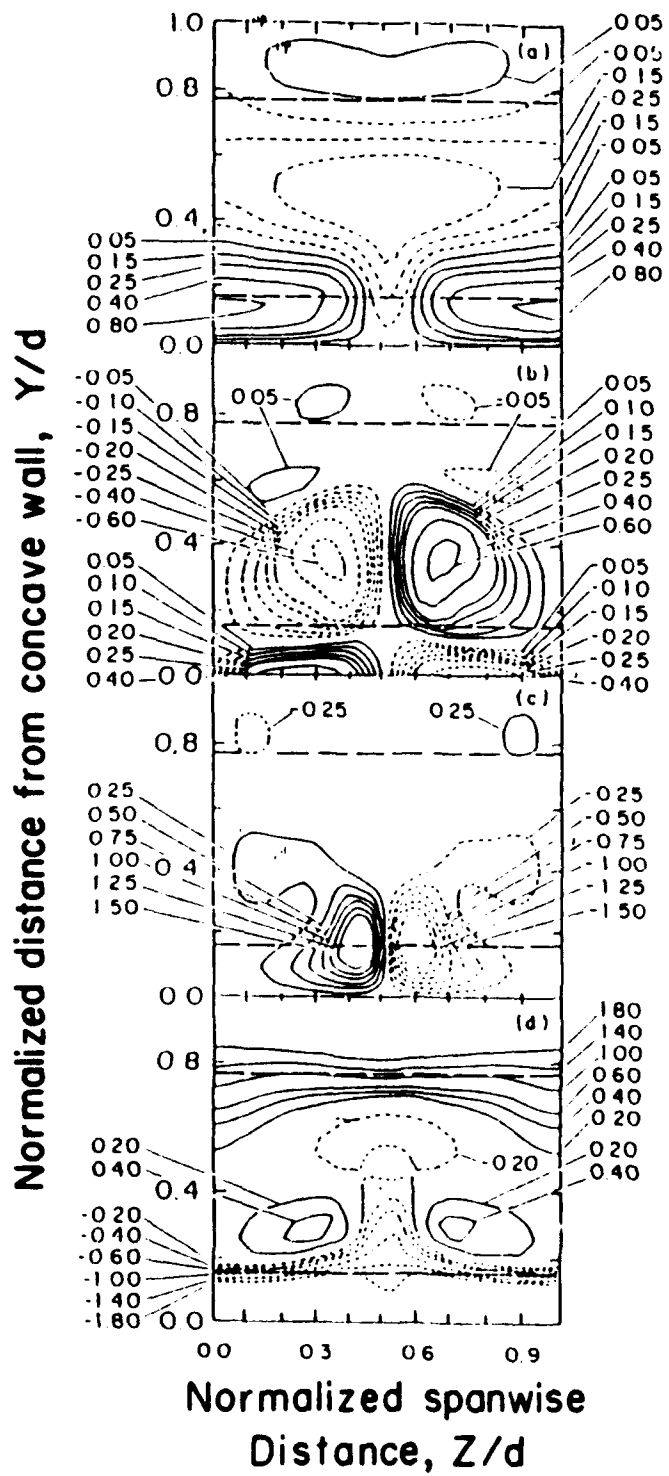


FIG. 88. Contours of (a) streamwise velocity minus the curved channel Poiseuille profile, (b) streamwise vorticity, (c) radial vorticity, and (d) spanwise vorticity as determined from a simulation for with  $\eta = 0.979$ ,  $\alpha = 3.0$ ,  $De = 3.580\text{Dec}$ , and streamwise wavenumber  $\beta = 200$  illustrating time-averaged flow field characteristics when Dean vortices are twisting.

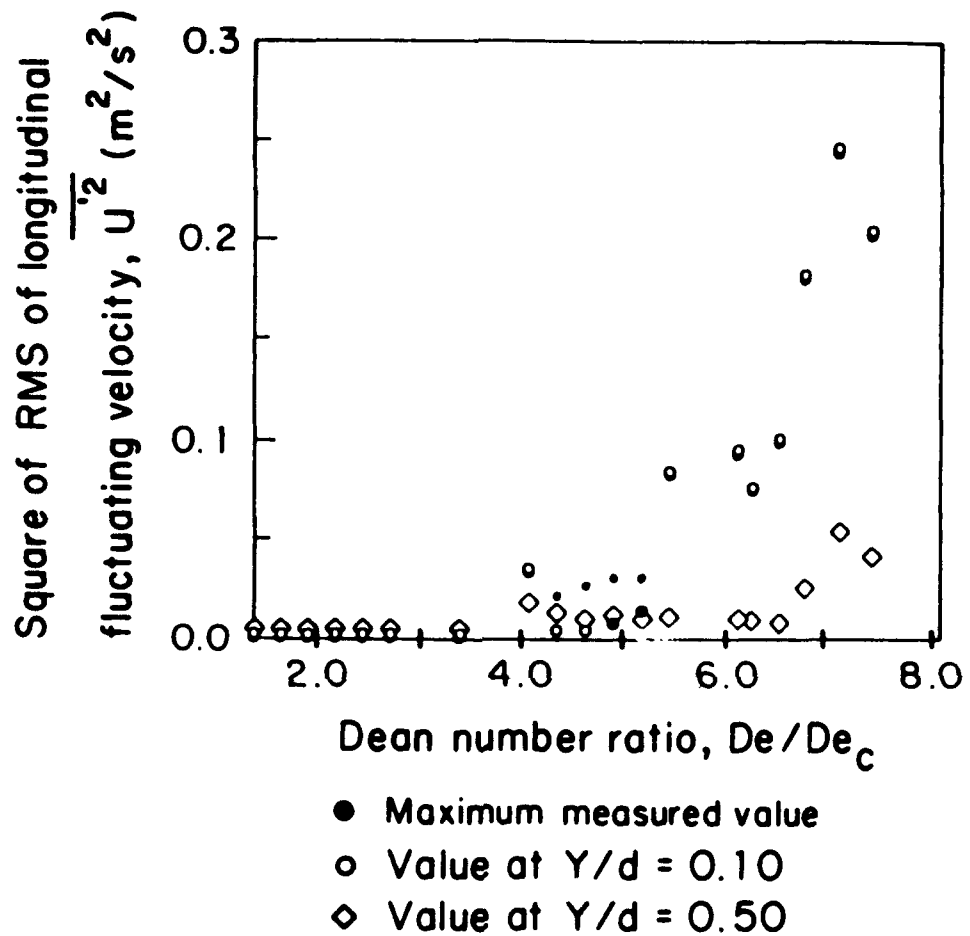
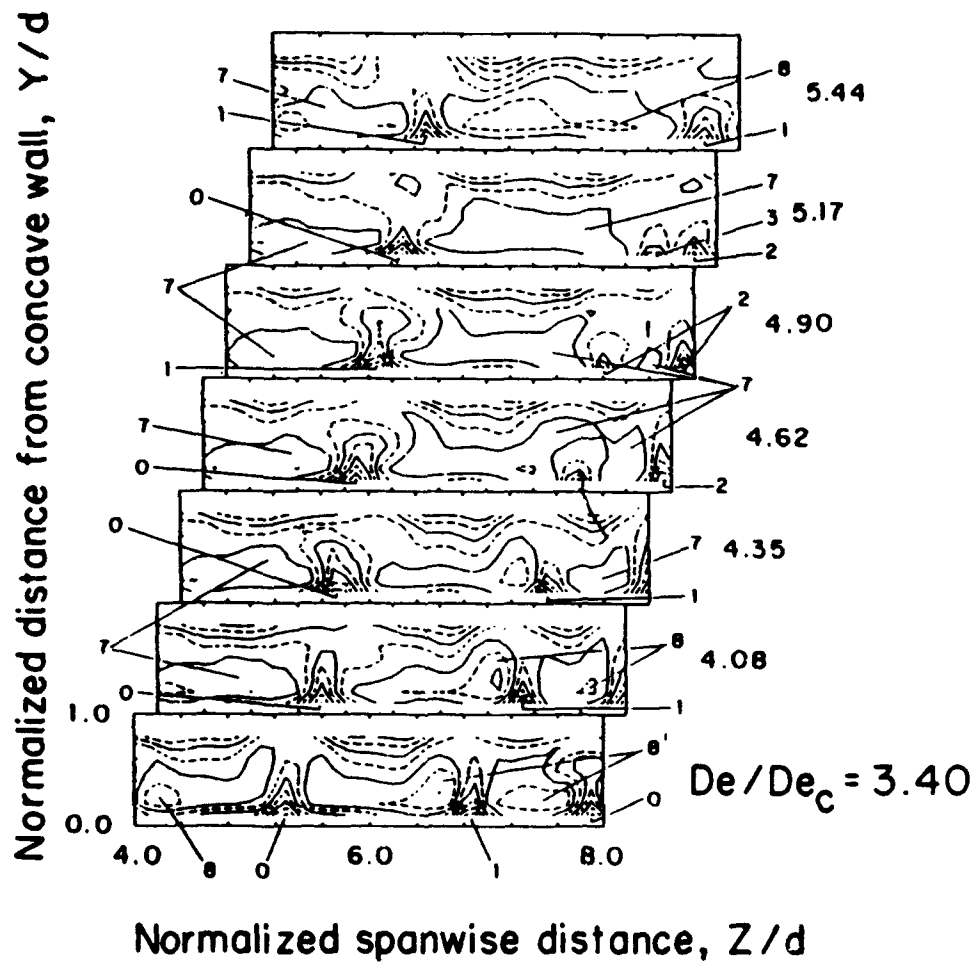


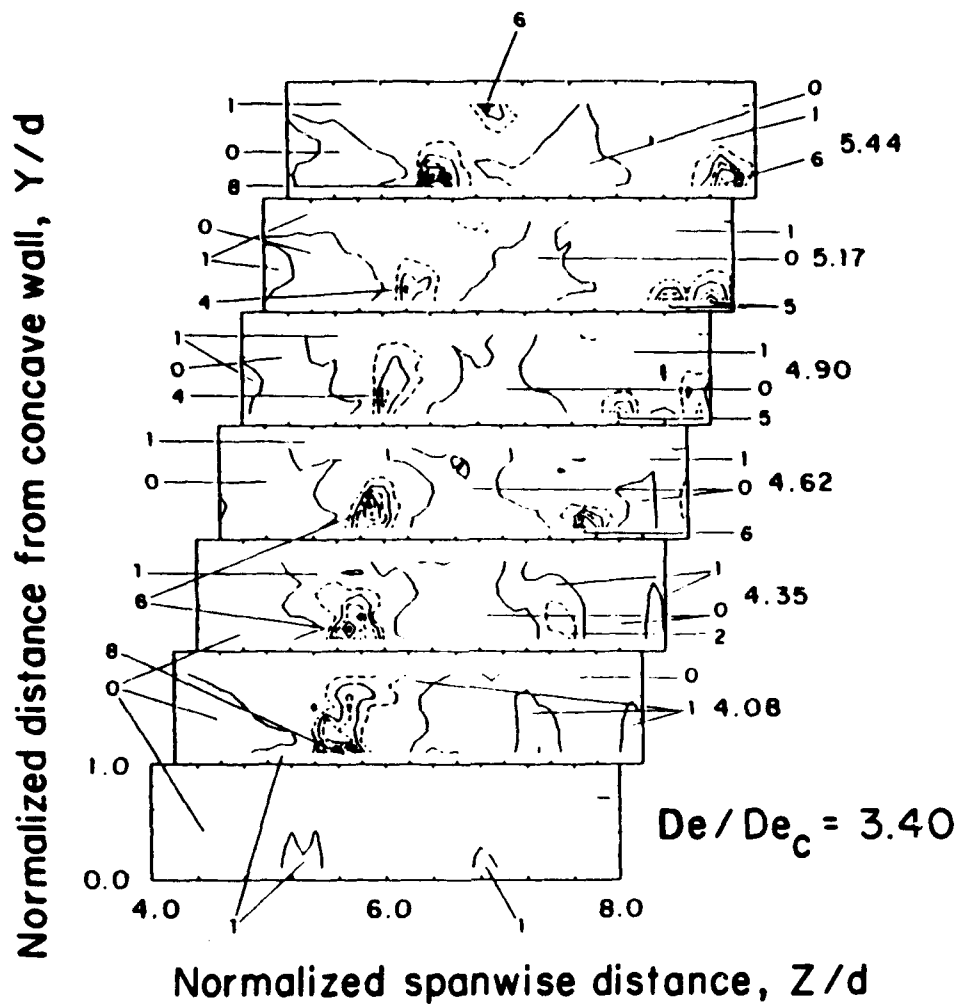
FIG. 89. Square of the root-mean-square (rms) of the longitudinal fluctuating velocity for the left-most-located upwash regions shown in Figs. 90 and 91, shown as dependent upon  $De/De_c$ . Data are given for three probe positions.



$U_e / U$  RANGES

0	0.35 - 0.45
1	0.45 - 0.55
2	0.55 - 0.65
3	0.65 - 0.75
4	0.75 - 0.85
5	0.85 - 0.95
6	0.95 - 1.05
7	1.05 - 1.15
8	1.15 - 1.25
9	1.25 - 1.40

FIG. 90. Surveys of the normalized streamwise mean velocity in a spanwise/radial plane located  $120^\circ$  from the start of curvature for  $\eta = 0.979$  and  $De/De_C$  from 3.398 to 5.439 when twisting vortex motions are present.



$\overline{u'^2}/u_\theta^2$  RANGES

0	.0001 - .0005
1	.0005 - .0050
2	.0050 - .0100
3	.0100 - .0150
4	.0150 - .0200
5	.0200 - .0250
6	.0250 - .0300
7	.0300 - .0350
8	.0350 - .0520

FIG. 91. Surveys of the square of the root-mean-square (rms) of the longitudinal fluctuating velocity in a spanwise/radial plane located  $120^\circ$  from the start of curvature for the same experimental conditions as the data presented in Fig. 90.

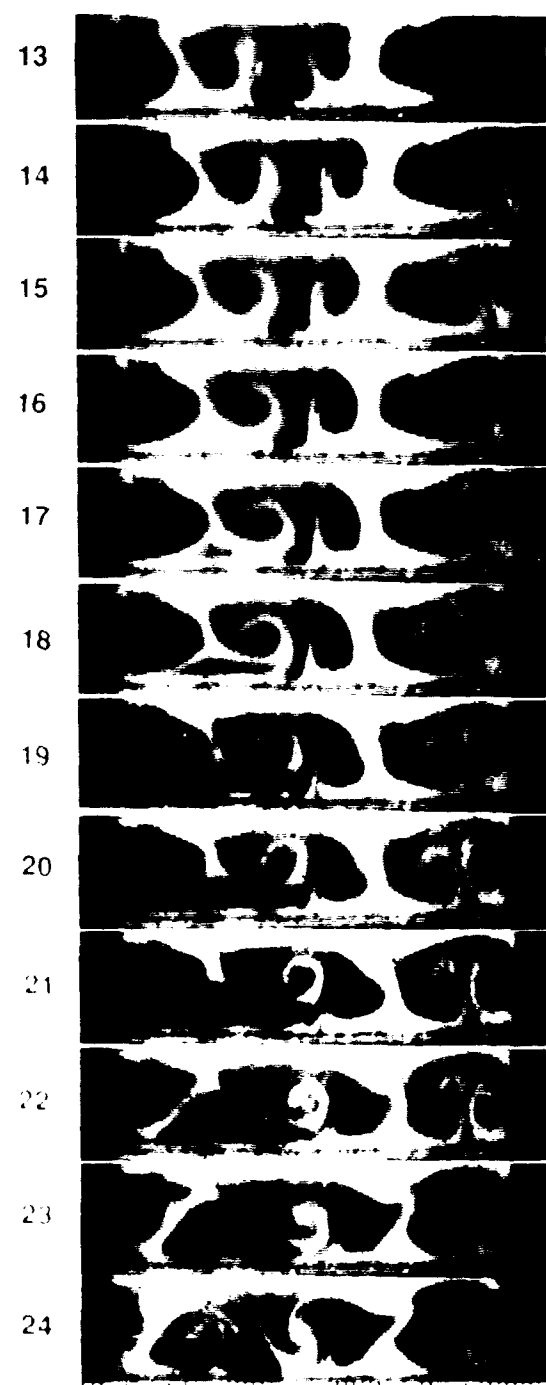
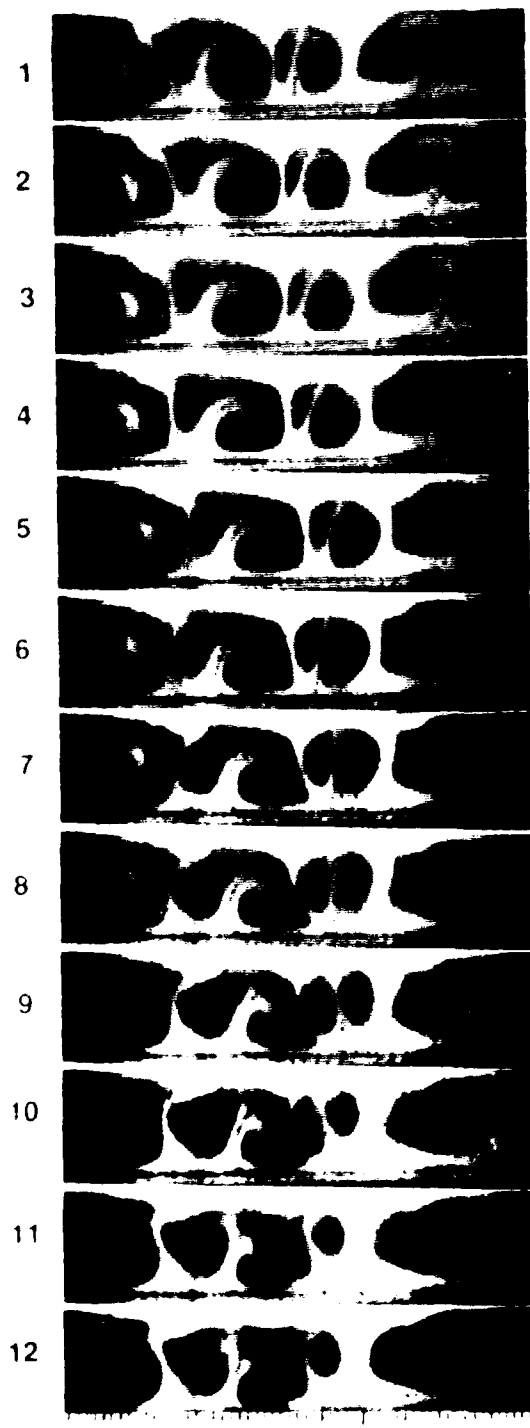


FIG. 92. Time sequence of twenty-four smoke visualization photographs illustrating how one vortex pair may be engulfed by an adjacent vortex pair followed by the emergence of a vortex pair from the near-wall region for  $De=100$  at a streamwise location  $125^0$  from the start of curvature. Photographs are spaced apart by  $1/30$  second (0.0333 sec.) intervals. The streamwise direction is into the plane of the plot, the concave surface is on the bottom of each photograph, and the convex surface is on the top of each photograph.

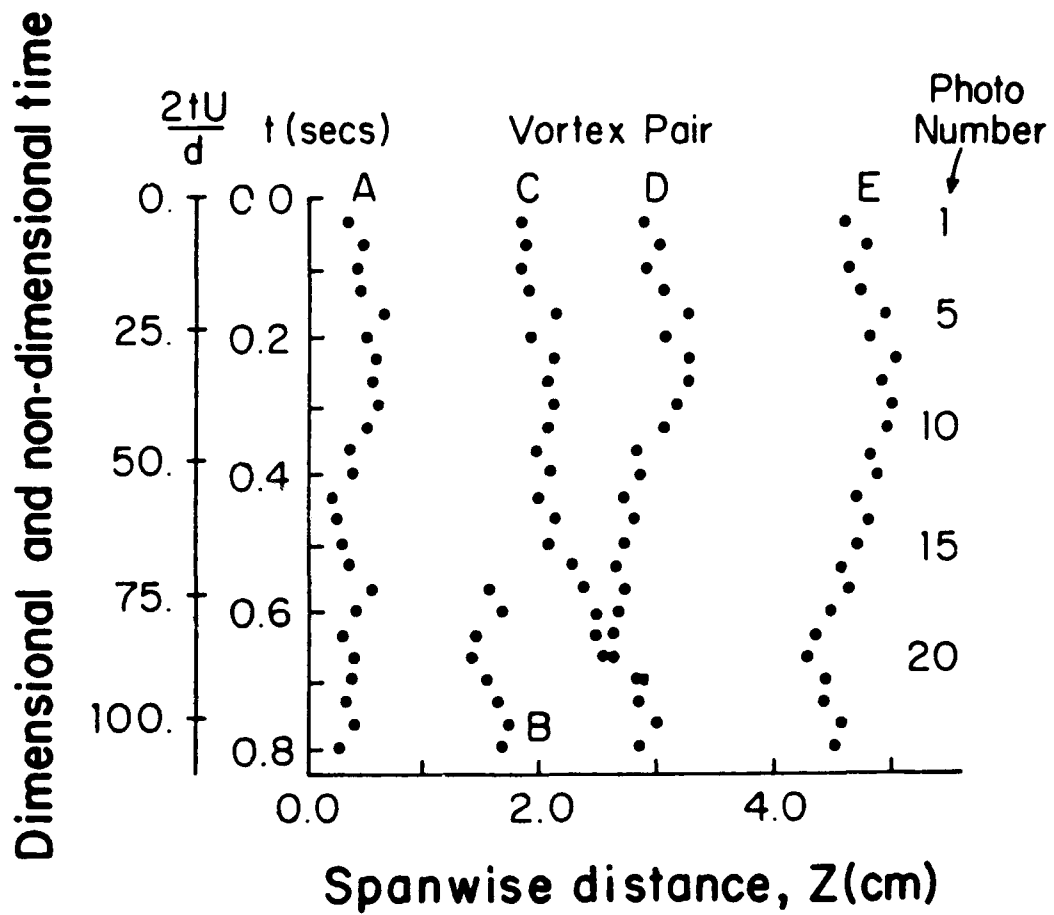


FIG. 93. For the same experimental conditions as for Fig. 92, results are presented which illustrate the spanwise locations of vortex pairs as a function of time.

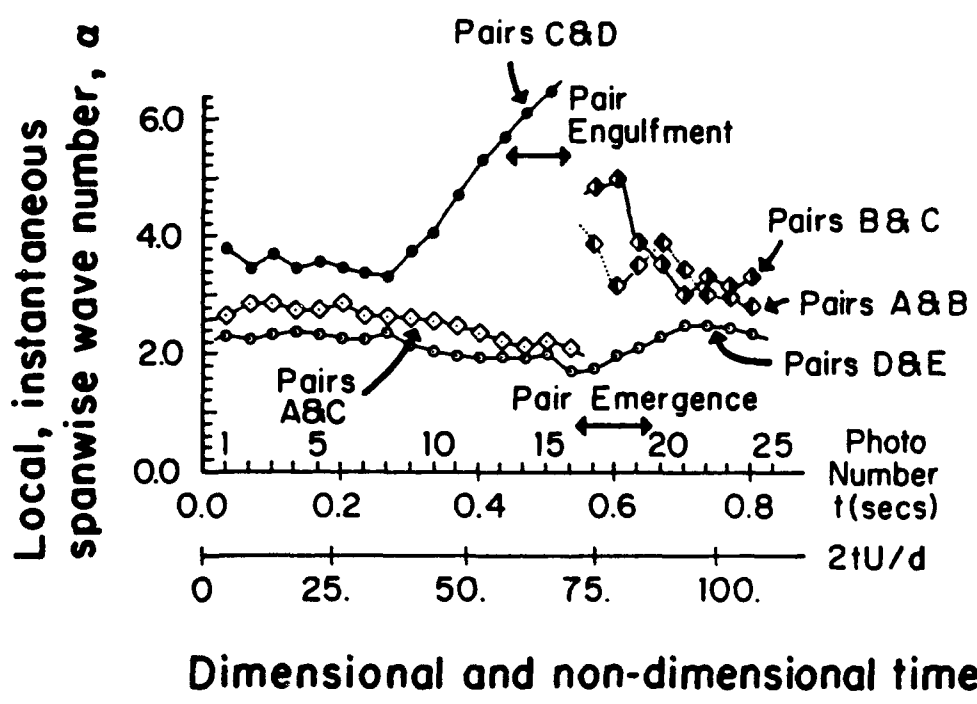


FIG. 94. For the same experimental conditions as for Fig. 92, results are presented which illustrate the local spanwise wavenumber variations with time between vortex pairs A, B, C, D, and E.



FIG. 95. Time sequence of thirty-seven smoke visualization photographs illustrating vortex pair engulfment for  $De=100$  at a streamwise location  $125^0$  from the start of curvature. All other figure details are the same as for Fig. 92.

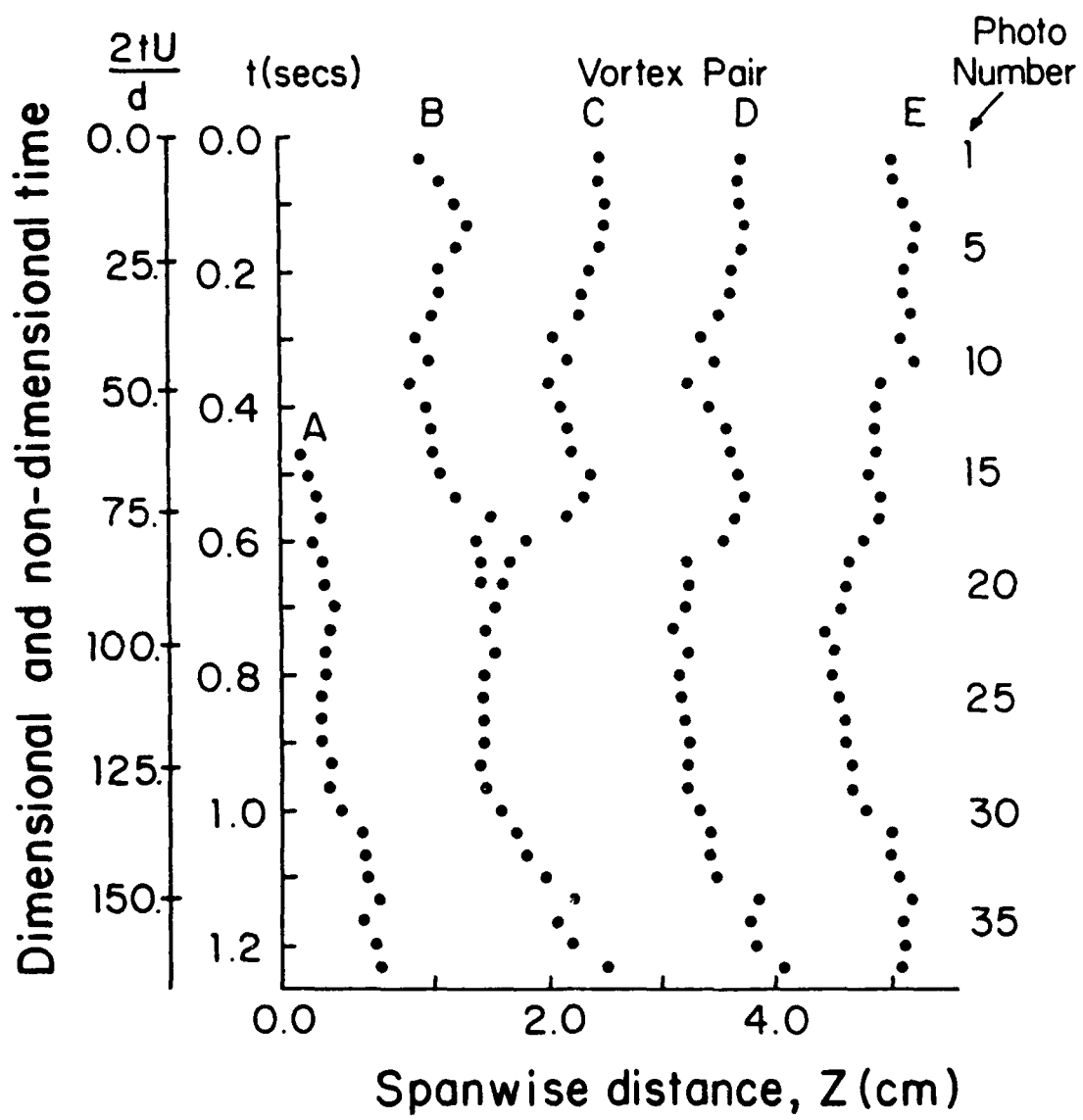


FIG. 96. For the same experimental conditions as for Fig. 95, results are presented which illustrate the spanwise locations of vortex pairs as a function of time.

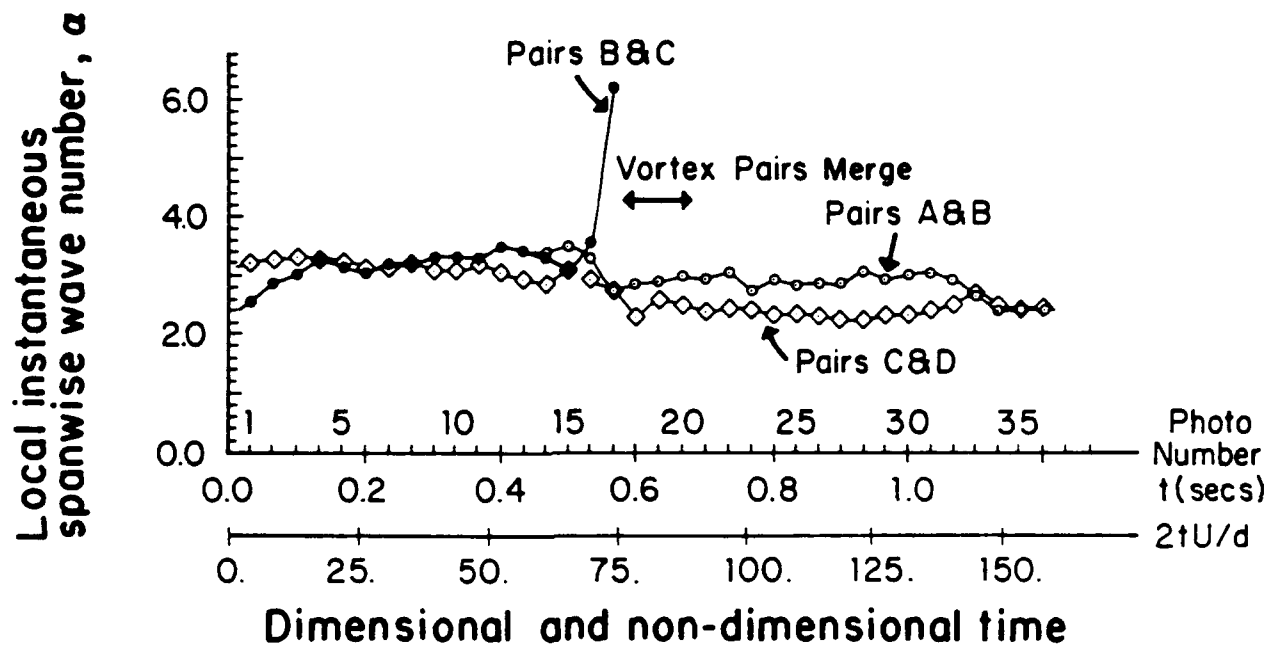


FIG. 97. For the same experimental conditions as for Fig. 95, results are presented which illustrate the local spanwise wavenumber variations with time between vortex pairs A, B, C, and D.

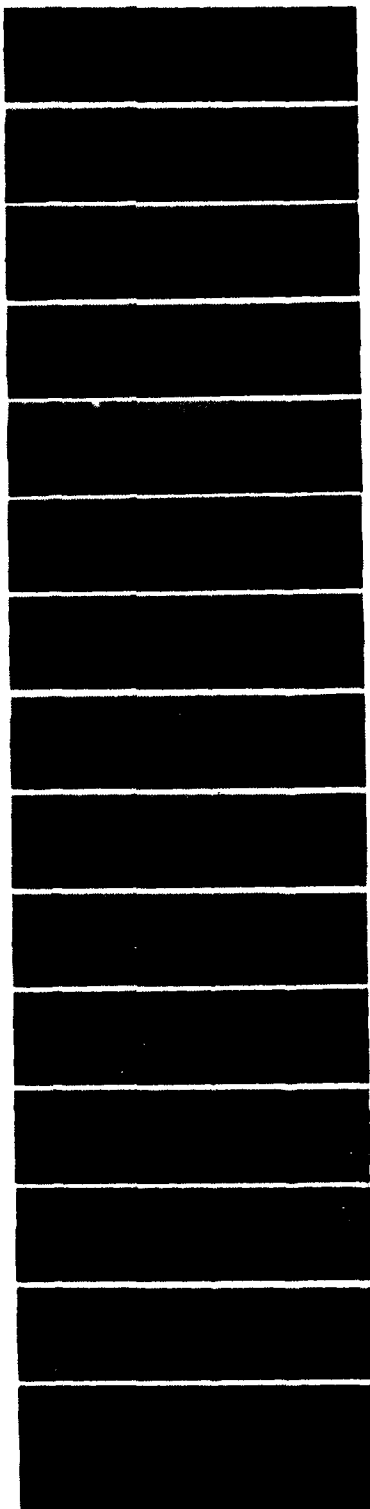


FIG. 98. Time sequence of fifteen smoke visualization photographs illustrating how one vortex pair may be swept into the upwash region of a neighboring vortex pair for  $De=75$  at a streamwise location  $135^0$  from the start of curvature. All other figure details are the same as for Fig. 92.

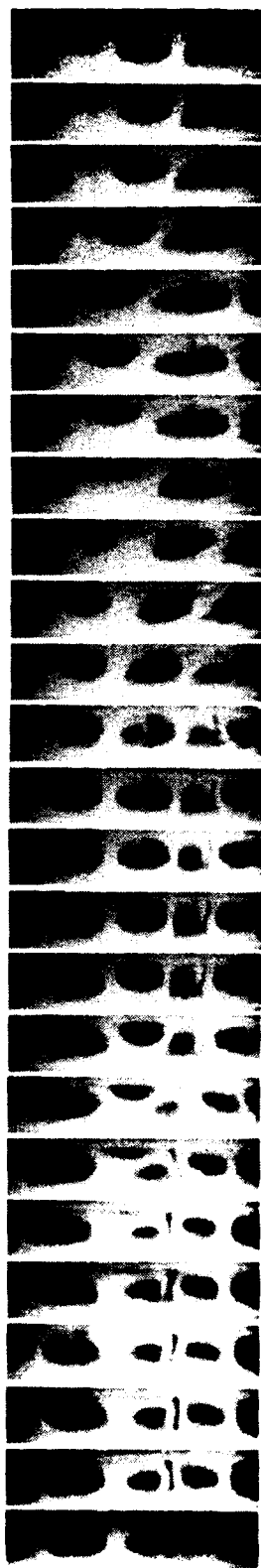


FIG. 99. Time sequence of twenty-five smoke visualization photographs illustrating the emergence of vortex pairs from near-wall regions for  $De=100$  at a streamwise location  $95^0$  from the start of curvature. All other figure details are the same as for Fig. 92 except that the time interval between photographs is 1/10 second.

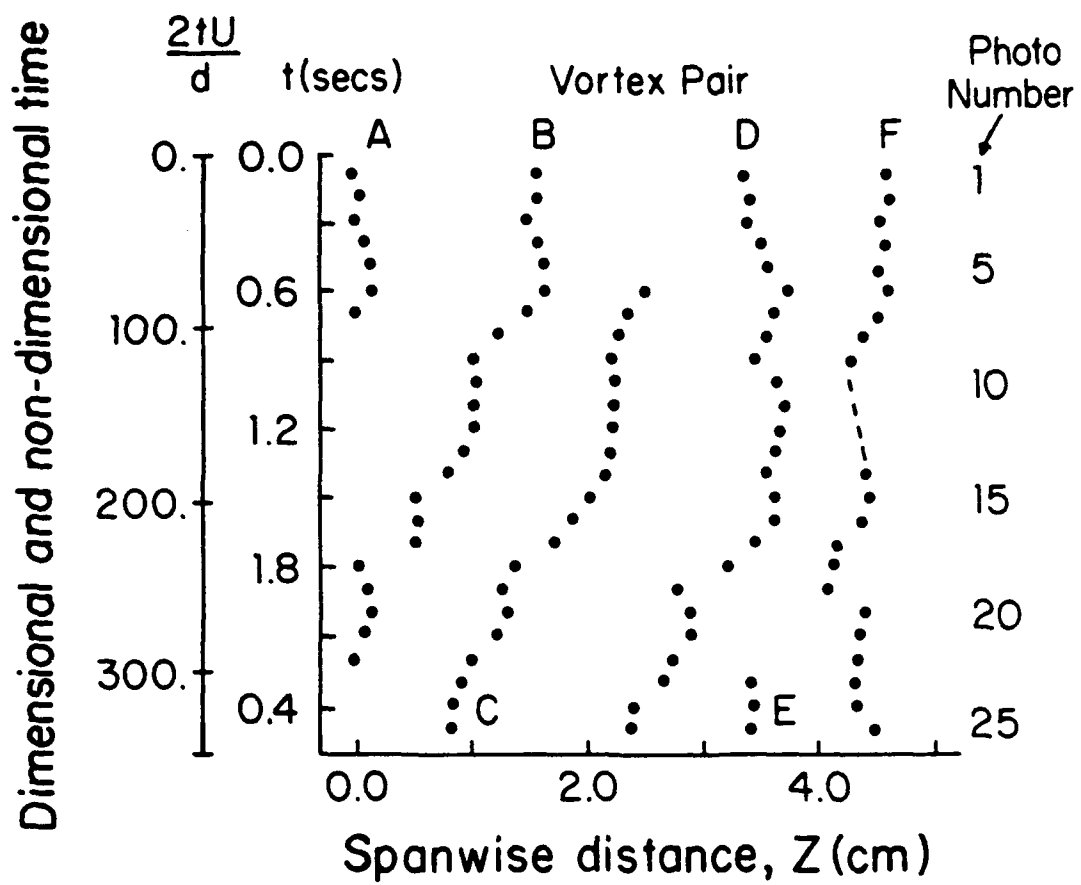


FIG. 100. For the same experimental conditions as for Fig. 99, results are presented which illustrate the spanwise locations of vortex pairs as a function of time.

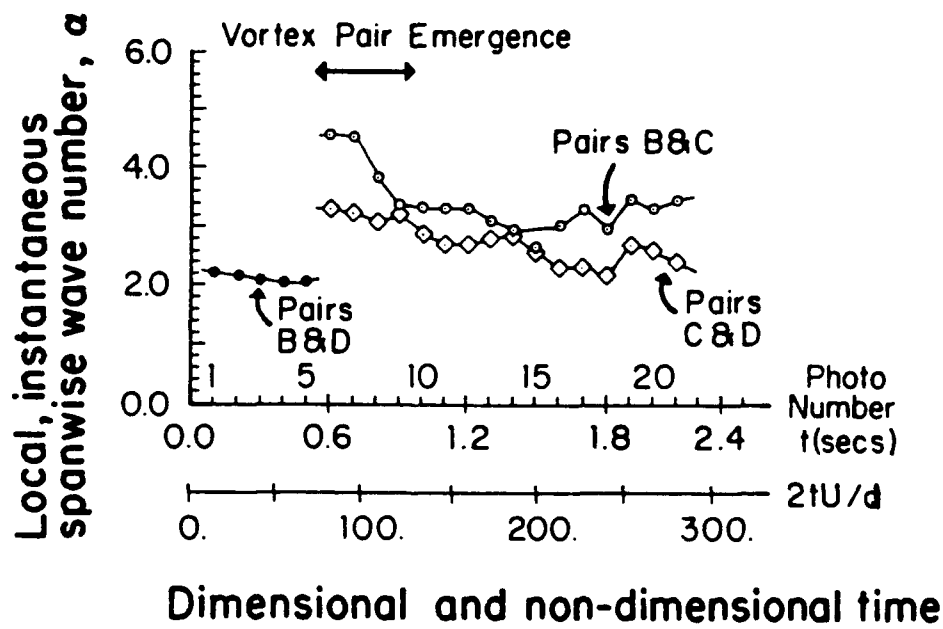


FIG. 101. For the same experimental conditions as for Fig. 99, results are presented which illustrate the local spanwise wavenumber variations with time between vortex pairs B, C, and D.

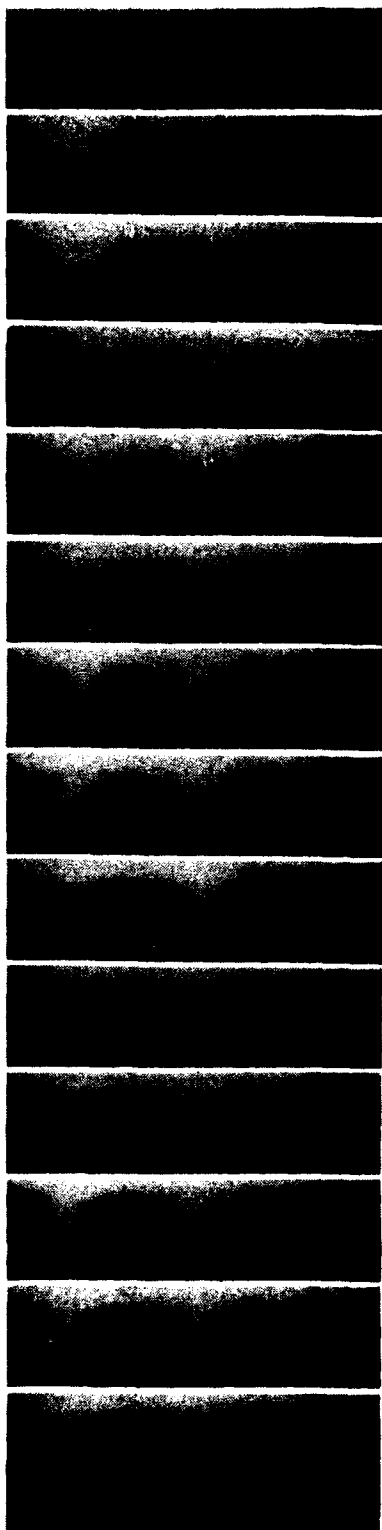
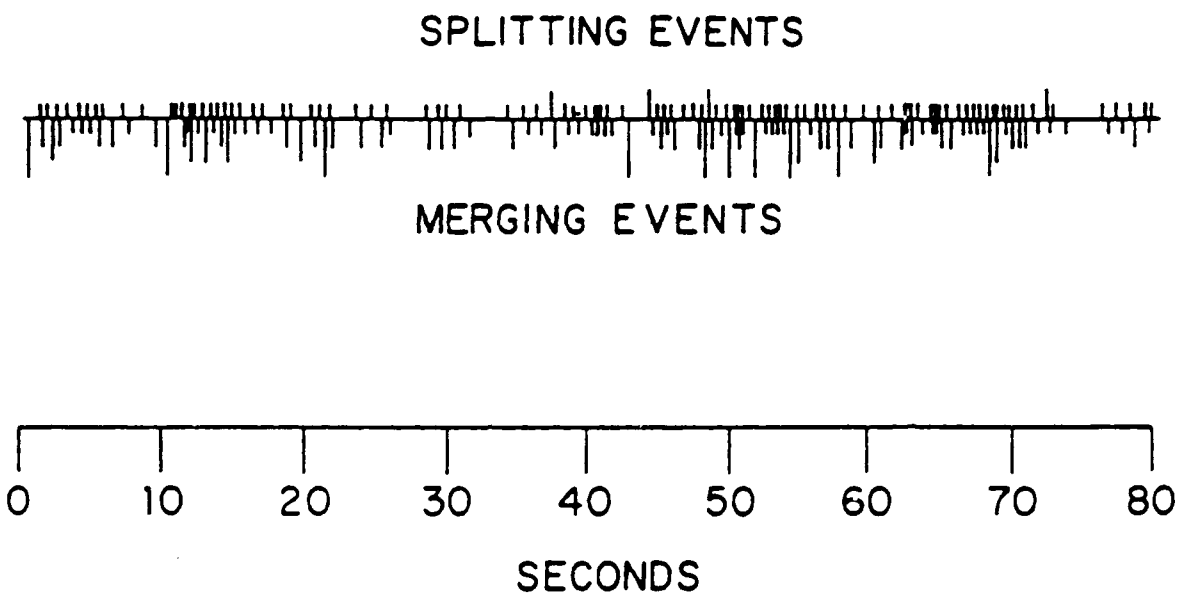


FIG. 102. Time sequence of fourteen smoke visualization photographs illustrating how one vortex pair is abruptly rearranged into two vortex pairs for  $De=75$  at a streamwise location  $135^0$  from the start of curvature. All other figure details are the same as for Fig. 92.



Splitting events: , emergence, | split.

Merging events: , collapse, | sweep,  
| engulfment, | cancellation.

FIG. 103. Time trace illustrating sequence and frequency of different types of splitting and merging events for  $De=100$  at a streamwise location  $115^0$  from the start of curvature.

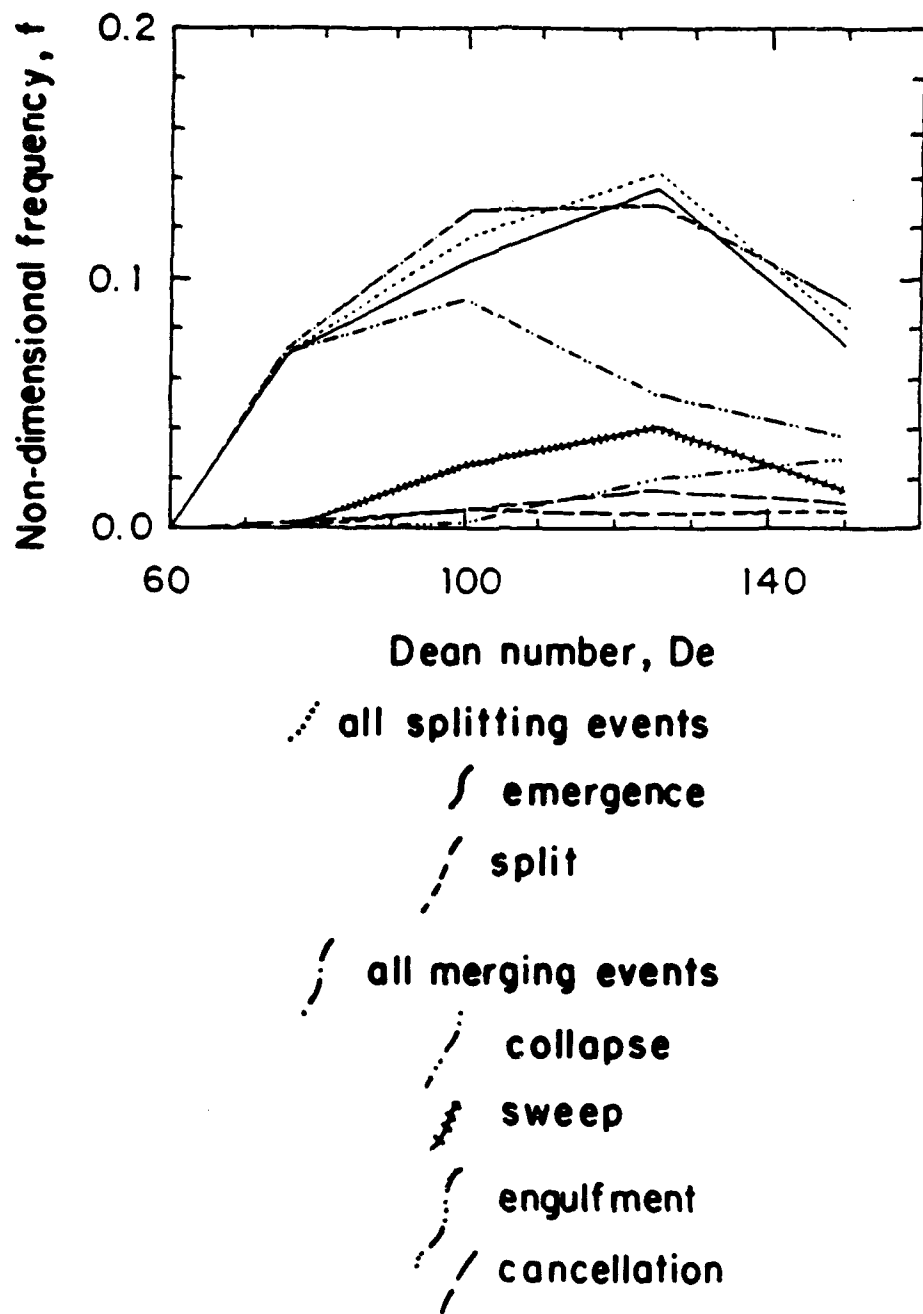


FIG. 104. Non-dimensional frequencies of different types of splitting and merging events as dependent upon Dean number as observed in a spanwise/radial plane at a streamwise location  $95^0$  from the start of curvature.

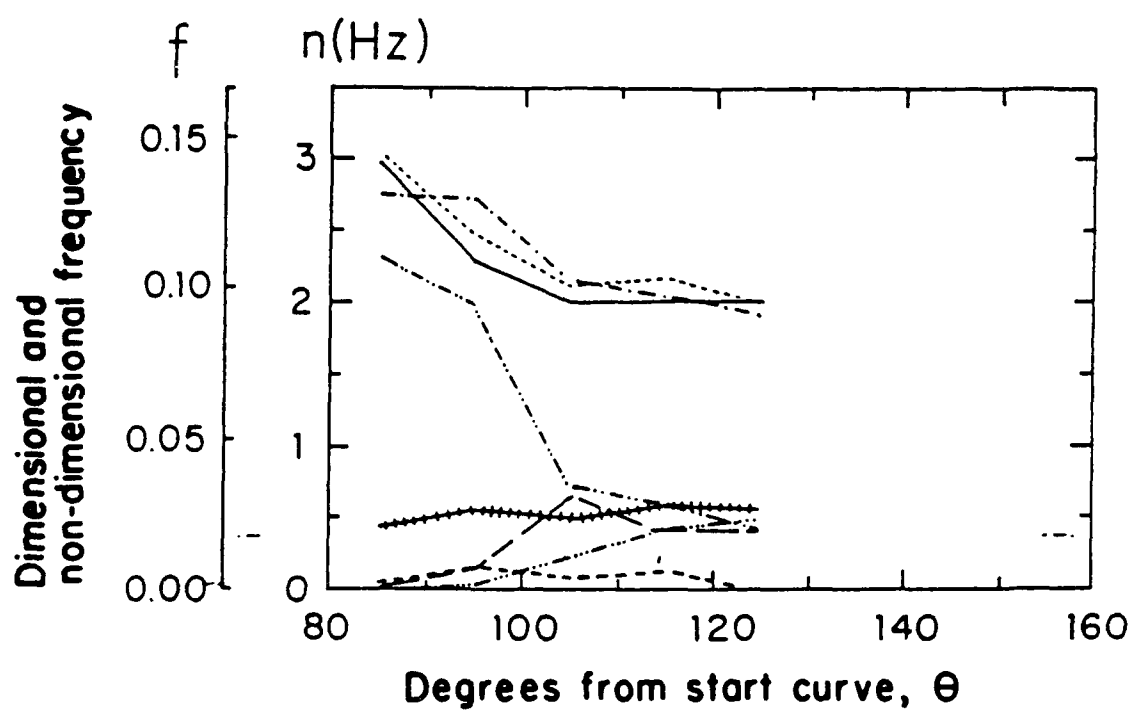
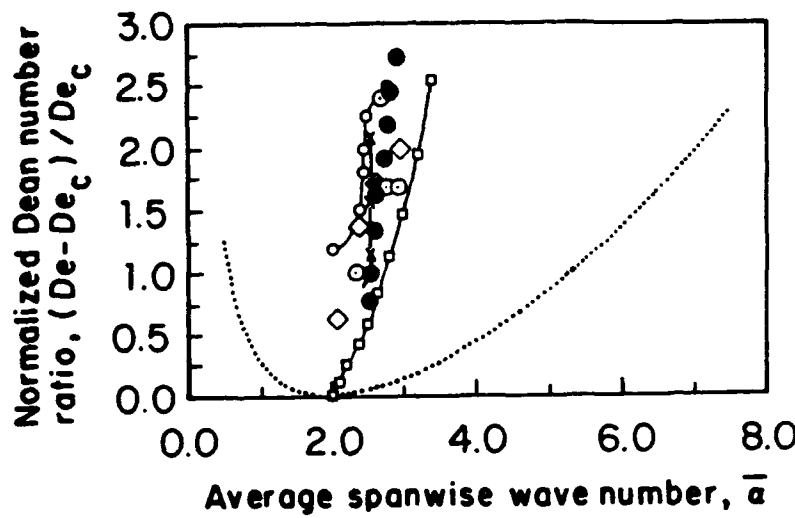
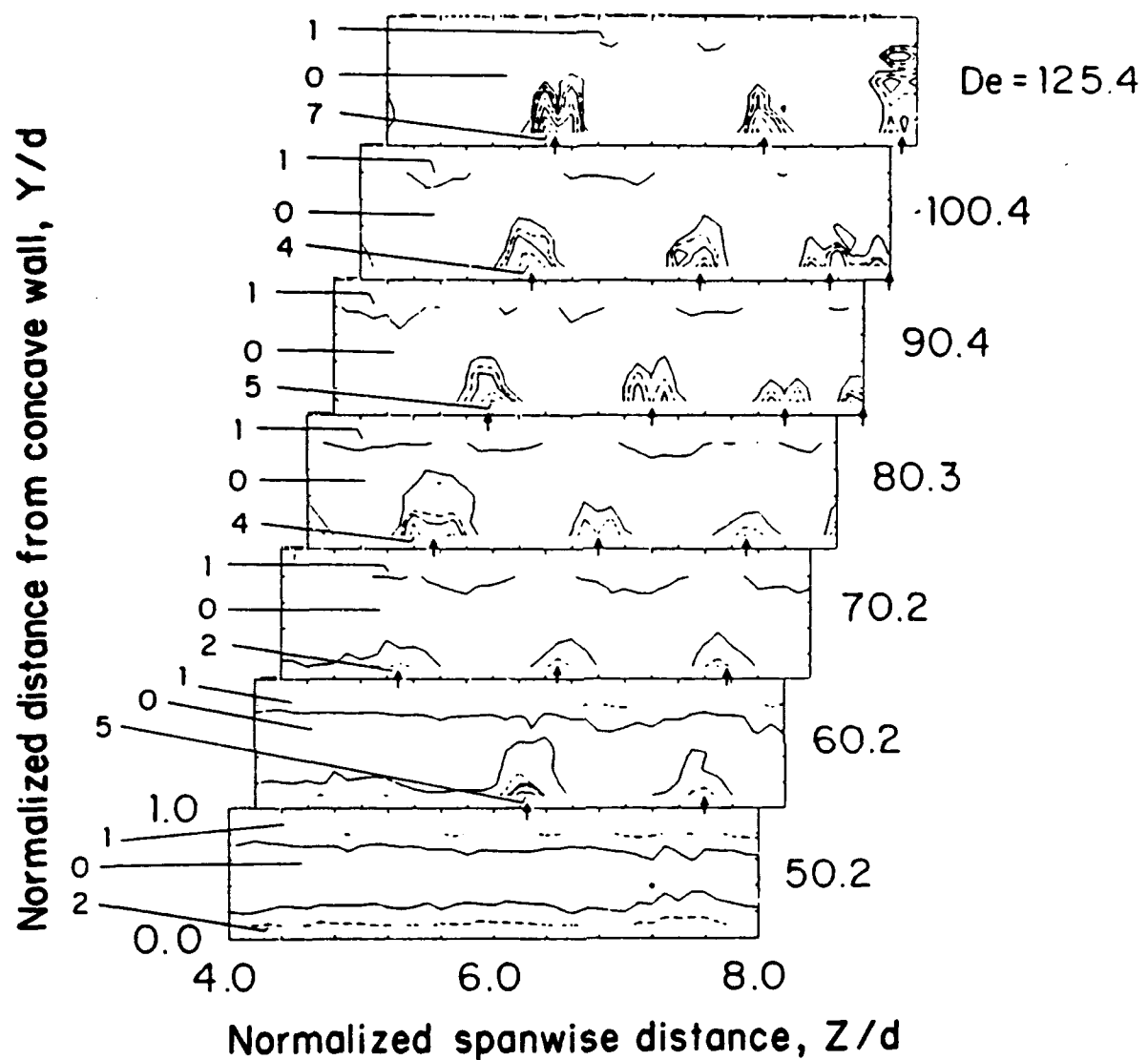


FIG. 105. Non-dimensional frequencies of different types of splitting and merging events as observed in different spanwise/radial planes for  $De=100$ . Symbols defined in Fig. 104.



- Spanwise wave number from flow visualization results
- ◇ Spanwise wave number from vorticity distributions from Fields (1990)
- Spanwise wave number from vorticity distributions from Baun (1988)
- ✗ Kelleher et al. (1980) experimental results
- ✗ Eckhaus stability boundary from Guo and Finlay (1991)
- ✗ Maximum linear growth rate of primary instability from Finlay et al. (1988)
- Primary stability boundary from Finlay et al. (1988)

FIG. 106. Average values of the spanwise wavenumber as dependent upon Dean number.



$\overline{u'^2} / \overline{u_\theta^2}$ RANGES	
0.	.0001 - .0002
1.	.0002 - .0003
2.	.0003 - .0004
3.	.0004 - .0006
4.	.0006 - .0008
5.	.0008 - .0010
6.	.0010 - .0012
7.	.0012 - .0016
8.	.0016 - .0032
9.	.0032 - .0048

FIG. 107. Surveys of the normalized square of the RMS of the longitudinal fluctuating velocity in a spanwise/radial plane located  $120^\circ$  from the start of curvature.

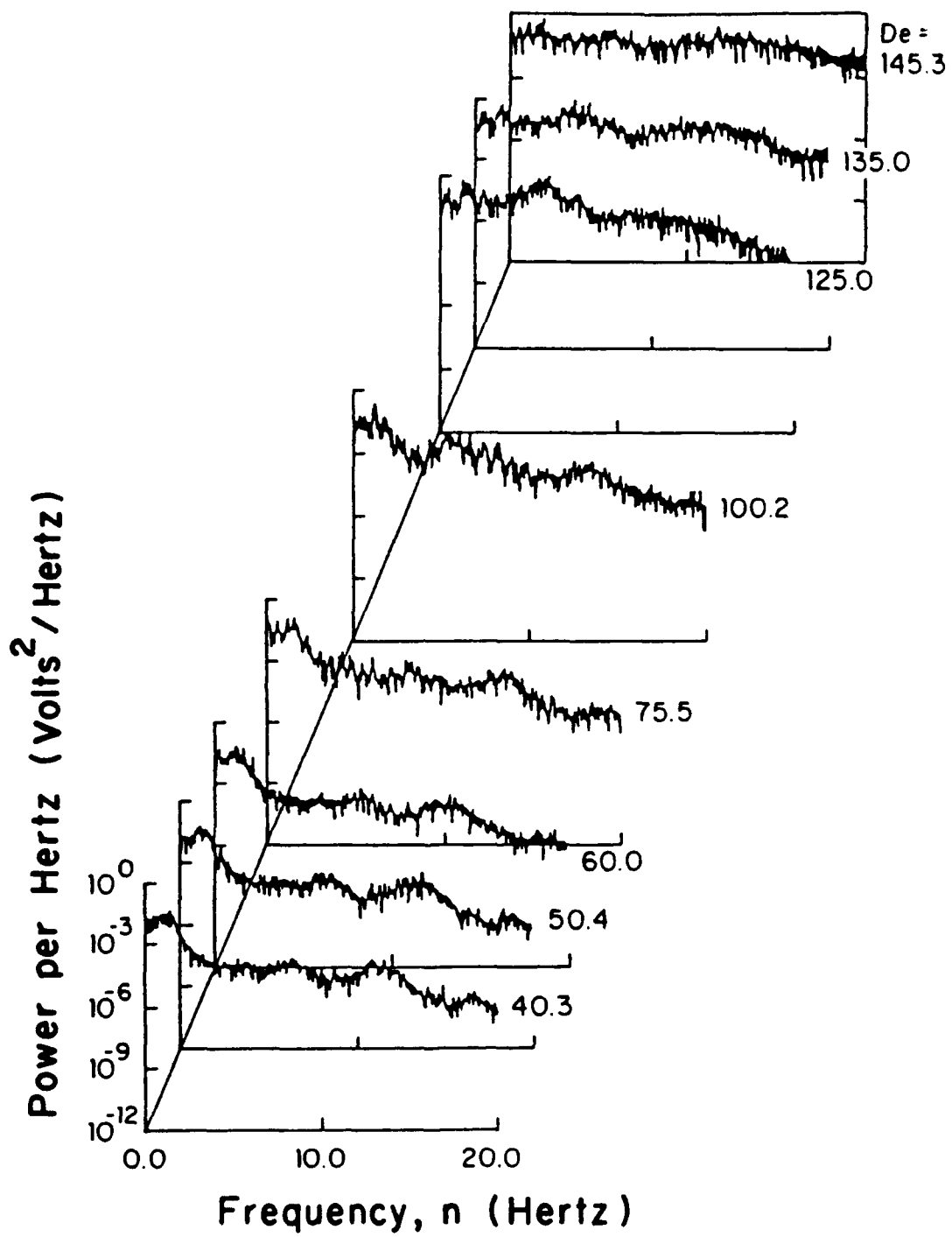


FIG. 108. Spectra of the voltage signal from a hot-wire sensing longitudinal velocity fluctuations located at  $\theta = 112^\circ$ ,  $Y/d=0.5$  and  $Z/d=12.25$  for Dean numbers from 40.3 to 145.3.

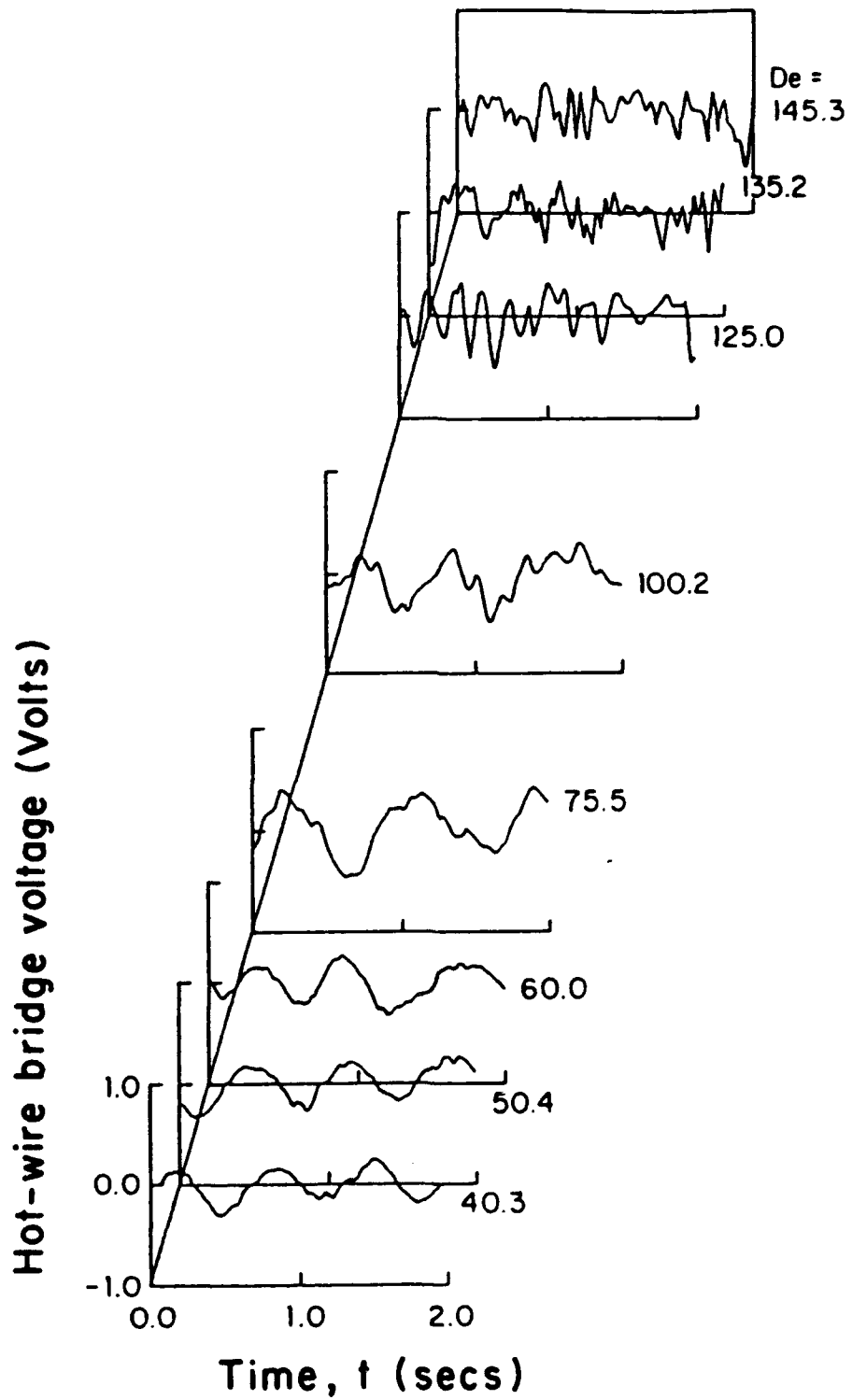


FIG. 109. Time traces of the voltage signal from a hot-wire sensing longitudinal velocity fluctuations located at  $\theta = 112^\circ$ ,  $Y/d=0.5$  and  $Z/d=12.25$  for Dean numbers from 40.3 to 145.3.

# REPORT DOCUMENTATION PAGE

Form Approved  
OMB No. 0704-0188

Public reporting burden for this collection of information is estimated to average 1 hour per response, including the time for reviewing instructions, searching existing data sources, gathering and maintaining the data needed, and completing and reviewing the collection of information. Send comments regarding this burden estimate or any other aspect of this collection of information, including suggestions for reducing this burden, to Washington Headquarters Services, Directorate for Information Operations and Reports, 1215 Jefferson Davis Highway, Suite 1204, Arlington, VA 22202-4302, and to the Office of Management and Budget, Paperwork Reduction Project (0704-0188), Washington, DC 20503.

<b>1. AGENCY USE ONLY (Leave blank)</b>			<b>2. REPORT DATE</b> July 1994	<b>3. REPORT TYPE AND DATES COVERED</b> Final Contractor Report
<b>4. TITLE AND SUBTITLE</b>  A Study of Dean Vortex Development and Structure in a Curved Rectangular Channel With Aspect Ratio of 40 at Dean Numbers up to 430			<b>5. FUNDING NUMBERS</b>  WU-505-62-0K 1L162211A47A	
<b>6. AUTHOR(S)</b>  Phillip M. Ligrani			<b>8. PERFORMING ORGANIZATION REPORT NUMBER</b>  E-8918	
<b>7. PERFORMING ORGANIZATION NAME(S) AND ADDRESS(ES)</b>  Naval Postgraduate School Department of Mechanical Engineering Monterey, California 94943-5000			<b>10. SPONSORING/MONITORING AGENCY REPORT NUMBER</b>  NASA CR-4607 ARL-CR-144	
<b>9. SPONSORING/MONITORING AGENCY NAME(S) AND ADDRESS(ES)</b>  Vehicle Propulsion Directorate U.S. Army Research Laboratory Cleveland, Ohio 44135-3191 and NASA Lewis Research Center Cleveland, Ohio 44135-3191				
<b>11. SUPPLEMENTARY NOTES</b>  Project Manager, Kestutis C. Civinskas, Propulsion Systems Division, NASA Lewis Research Center, organization code 2760, (216) 433-5890.				
<b>12a. DISTRIBUTION/AVAILABILITY STATEMENT</b>  Unclassified - Unlimited Subject Category 34		<b>12b. DISTRIBUTION CODE</b>		
<b>13. ABSTRACT (Maximum 200 words)</b>  Flow in a curved channel with mild curvature, an aspect ratio of 40 to 1, and an inner to outer radius ratio of 0.979 is studied at Dean numbers $De$ ranging from 35 to 430. For positions from the start of curvature ranging from 85 to 145 degrees, the sequence of transition events begins with curved channel Poiseuille flow at $De < 40-64$ . As the Dean number increases, observations show initial development of Dean vortex pairs, followed by symmetric vortex pairs which, when viewed in spanwise/radial planes, cover the entire channel height ( $De=90-100$ ). At $De$ from 40 to 125-130, the vortex pairs often develop intermittent waviness in the form of vortex undulations. Splitting and merging of vortex pairs is also observed over the same experimental conditions as well as at higher $De$ . When Dean numbers range from 130 to 185-200, the undulating wavy mode is replaced by a twisting mode with higher amplitudes of oscillation and shorter wavelengths. The twisting wavy mode results in the development of regions where turbulence intensity is locally augmented at Dean numbers from 150 to 185-200, principally in the upwash regions between the two individual vortices which make up each vortex pair. These turbulent regions eventually increase in intensity and spatial extent as the Dean number increases further, until individual regions merge together so that the entire cross section of the channel contains chaotic turbulent motions. When Dean numbers then reach 400-435, spectra of velocity fluctuations then evidence fully turbulent flow.				
<b>14. SUBJECT TERMS</b>  Curved channel; Concave and convex curvature; Dean vortex pairs; Twisting and undulating vortices			<b>15. NUMBER OF PAGES</b> 237	
<b>16. PRICE CODE</b> A11				
<b>17. SECURITY CLASSIFICATION OF REPORT</b> Unclassified	<b>18. SECURITY CLASSIFICATION OF THIS PAGE</b> Unclassified	<b>19. SECURITY CLASSIFICATION OF ABSTRACT</b>	<b>20. LIMITATION OF ABSTRACT</b>	